PHASE TRANSFORMATIONS IN SHOCK COMPACTED MAGNETIC MATERIALS

A Thesis
Presented to
The Academic Faculty

by

Christopher Wehrenberg

In Partial Fulfillment
of the Requirements for the Degree
Doctor of Philosophy in the
School of Material Science and Engineering

Georgia Institute of Technology
May 2012

PHASE TRANSFORMATIONS IN SHOCK COMPACTED MAGNETIC MATERIALS

Approved by:

Naresh Thadhani, Advisor
School of Material Science and Engineering
Georgia Institute of Technology

Suryanaray Sankar
President and Director of Research
Advanced Materials Corporation

Thomas Sanders
School of Material Science and Engineering
Georgia Institute of Technology

Matthew Willard
Magnetic Materials and Nanostructures Section
Naval Research Laboratory

Hamid Garmestani
School of Material Science and Engineering
Georgia Institute of Technology

Date Approved: January 12, 2012

ACKNOWLEDGEMENTS

This work would not possible with out the help and support of many people who have given their time and effort. I would like to thank my advisor, Naresh Thadhani, for allowing me the freedom to explore my ideas while still finding time to answer questions, as well as Kit Neel, Phil Graham, Morgan Trexler, Dan Eakins, and Anthony Fredenburg for their mentoring and guidance in the lab. Brian Zande and S. G. Sankar from Advanced Materials Corporation and Matt Willard, Maria Daniil, and Matthew Brandes at the Naval Research Laboratory all generously volunteered their time to help with various aspects of this work. Discussions with Ken Beyerlein, Greg Kennedy, and Brady Aydelotte proved invaluable while developing my ideas. Many other people at Georgia Tech and in the High Strain Rate Lab group have helped me along the way, including Melanie Kirkham, Jung-Il Hong, Jonathan Lowder, Susan Bowman, Brad White, Jennifer Breidenich, Tyler Jackson, Sean Dixon, Paul Specht, Mike Tucker, Sean Kelly, Ricky Whelchel, Anna Alexander, Alex Stuart, Jim Painter, Phillip Draa, Jim Amato, and Chengda Dai. I would like to thank my family and friends for their support and encouragement while writing this thesis, especially Sarah Boak for making me sandwiches and making me laugh and my parents, Cathy Howard and Andy Wehrenberg, who have helped me in too many ways to count.

TABLE OF CONTENTS

LIST OF TABLES

LIST OF FIGURES

SUMMARY

Shock compaction experiments were performed on soft magnetic phases Fe_4N and $Fe_{16}N_2$, and hard magnetic phases $Nd_2Fe_{14}B$ and $Sm_2Fe_{17}N_3$ in order to determine their thermo-mechanical stability during shock loading and explore the possibility of fabricating a textured nanocomposite magnet. Gas gun experiments performed on powders pressed in a three capsule fixture showed phase transformations occurring in Fe_4N, $Fe_{16}N_2$, and $Nd_2Fe_{14}B$, while $Sm_2Fe_{17}N_3$ was observed to be relatively stable. Shock compaction of *FCC* Fe_4N resulted in a partial transformation to *HCP* Fe_3N, consistent with previous reports of the transition occurring at a static pressure of ∼3 GPa. Shock compaction of $Fe_{16}N_2$ produced decomposition products α-Fe, Fe_4N, and FeN due to a combination of thermal effects associated with dynamic void collapse and plastic deformation. Decomposition of Nd-Fe-B, producing α-Fe and amorphous Nd-Fe-B, was observed in several shock consolidated samples and is attributed to deformation associated with shock compaction, similar to decomposition reported in ball milled Nd-Fe-B. No decomposition was observed in shock compacted samples of Sm-Fe-N, which is consistent with literature reports showing decomposition occurring only in samples compacted at a pressure above ∼15 GPa. Nd-Fe-B and Sm-Fe-N were shown to accommodate deformation primarily by grain size reduction, especially in large grained materials. Hard/Soft composite magnetic materials were formed by mixing single crystal particles of Nd-Fe-B with iron nanoparticles, and the alignment-by-magnetic-field technique was able to introduce significant texture into green compacts of this mixture. While problems with decomposition of the $Nd_2Fe_{14}B$ phase prevented fabricating bulk magnets from the aligned green compacts, retention of the nanoscale morphology of the α-Fe particles and the high alignment of the green

compacts shows promise for future development of textured nanocomposite magnets through shock compaction.

CHAPTER I

INTRODUCTION

Permanent magnetic materials have seen a steady improvement in their properties and applications since the start of the twentieth century. Increasing performance has occurred by discovery of a new material and then development of its magnetic properties to near theoretical limits. From hardened steels, to Alnico magnets, to samarium-cobalt, and now to neodymium-iron-boron magnets (Nd-Fe-B), each advance has allowed for a wider array of applications and more efficient use. Development of Nd-Fe-B, the best currently available magnetic material, is nearing its theoretical limit [1].

While Nd-Fe-B magnets have the highest energy product, which is the figure of merit for permanent magnets, several other materials have a higher magnetization but lack sufficient coercivity to be useful as permanent magnets. Nanocomposite magnets, in which nanoscale, magnetically soft grains are exchange coupled with a hard magnetic phase, have the potential to become the next generation of permanent magnets, possibly doubling the energy product of Nd-Fe-B magnets [2]. With ongoing problems related to the supply of rare earth materials [3], the lower neodymium content of iron-Nd-Fe-B composites provides an additional advantage for these materials.

There are several challenges to developing an exchange-coupled permanent magnet. The exchange length, the distance over which exchange coupling can take place, is very small and is typically estimated to be 5-10 nm for hard/soft composites [4]. This means that a hard-soft composite material needs to have all soft grains be neighboring a hard grain and be no more than 10-20 nm in diameter [5]. Such a fine grain size is not achievable using traditional processing techniques, such as sintering and

hot pressing. The high temperatures and extended heating times produce significant grain growth that can limit the effectiveness of exchange coupling [6]. Thus, creating full density bulk magnets from nanocomposite powders has been a serious challenge

In addition, the hard phase of an exchange coupled composite magnet must be highly textured in order to achieve very high energy products [7]. The *c*-axis serves as the easy direction of magnetization for $Nd_2Fe_{14}B$ and other magnetically hard crystal structures. Having a high degree of alignment of the easy magnetization direction dramatically increases the performance of a permanent magnet by increasing both the remanence and squareness of the magnetic hysteresis loop [8]. A well aligned magnet can potentially have an energy product four times greater than a typical isotropic magnet [4].

Many attempts to create texture in nanocomposite magnets have focused on hot-pressing and die-upsetting [9, 7, 10, 11]. For typical Nd-Fe-B magnets, uniaxial pressure is applied while at high temperature, creating an elongated grain structure perpendicular to the pressing direction and *c*-axis alignment along the pressing direction [12]. Die-upsetting of Nd-Fe-B depends on excess Nd to create a low melting point grain boundary phase. However, composites with excess iron lack this grain boundary phase and do not produce sufficient texture [13].

Shock compaction of powders provides several advantages to processing nanocomposite magnets. The energy of compaction is applied rapidly, such that any heating occurs over the course of a few microseconds [14]. Thus, a low porosity magnet can be made without extended heating times [15, 16]. While several studies have demonstrated the ability of the shock compaction technique to produce bulk magnets with nanocomposite structure, there have been very few attempts to control the texture of such magnets.

Therefore, the ultimate goal of this research is to develop a textured nanocomposite magnetic material through shock compaction. Two main problems are addressed

in working toward this goal: Which magnetic phases are suited for use in a magnet processed by shock compaction, and how can texture be created in a shock compacted nanocomposite material? Magnetic phases with high pressure phase transitions or with thermally or mechanically induced decomposition will have limited use in a shock compacted magnet. Additionally, the deformation behavior, occurring by plastic slip, twinning, fracture, or other method, will be important in developing or maintaining a textured microstructure during shock compaction. Thus, shock compaction experiments are performed on a variety of hard and soft magnetic phases in order to study their thermo-mechanical stability and mechanism of deformation. The problem of creating texture is addressed by adapting the two techniques used on conventional materials, die-upsetting and magnetic field alignment, for use on shock compacted materials. The study of each technique seeks to determine the conditions and extent of texture development.

This dissertation will begin with background information on the theory of magnetic materials, exchange coupling, and nanocomposite magnetic materials described in Chapter 2. A literature review is provided for both techniques commonly used to develop texture in magnets: die-upsetting and magnetic-field-alignment. The fundamentals of shock waves are discussed, followed by a review of previous shock compaction studies on permanent magnetic materials and nanocomposites. Chapter 3 details the characteristic of the as-received materials studied, the characterization techniques employed, and an overview of the setup of shock compaction experiments and related numerical simulations. The models and parameters used to estimate the shock pressure and temperature are also presented. Chapter 4 presents the results of shock compaction experiments for each material system. Chapter 5 will discuss key results, paying particular attention to the phase transformations and deformation mechanisms observed in shock compacted samples. The possibility of producing texture by high rate deformation and magnetic field alignment is also discussed. A

summary and concluding remarks are provided followed by suggestions for future work in Chapters 6 and 7.

CHAPTER II

BACKGROUND

This chapter will provide background information on permanent magnetic materials and shock compaction fundamentals. The two most common methods of processing magnetic materials to produce texture, die-upsetting and field-alignment-and-sintering, are discussed. A literature review of prior studies on shock compaction of magnetic materials is also provided.

2.1 Magnetic Materials

2.1.1 Magnetic Theory

The hysteresis curve provides many important characteristics of a magnetic material. The curve is measured by recording the magnetic induction, B, or magnetization, M, in a magnetic field, H.[1] These field parameters are related by Equation 1, where μ_0 is a constant, the permeability of free space, equal to 1.26 x $10^{-6} \frac{Tm}{A}$.

$$B = \mu_0(H + M) \tag{1}$$

It is often useful to think of H as the field applied to a magnet and B as the total field (sum of the applied field and the magnetization) as measured by the magnetometer. This is not technically accurate, since an external field, H_e, will produce a field anti-parallel and proportional to the magnetization inside the material called the demagnetizing field, $H_d = -DM$. The demagnetization factor, D, is a number between 0 and 1 and is dependent mainly on the geometry of the magnet. Demagnetization factors cannot be computed exactly for shapes other than ellipsoids of rotation. For

[1]There is a disagreement between physicists and material scientists over what terms should be used to describe various aspects of magnetic fields (e.g. whether the B or H field is referred as the "magnetic field"). The following discussion will use the terms common among material scientists.

Table 1: Magnetic terms and corresponding symbols in SI and cgs units

Magnetic Term	Alternate Name	Symbol	SI Unit	cgs Unit	Conversion Factor
Magnetic Induction	Magnetic Flux Density	B	Tesla (T)	Gauss (G)	$1\,T = 10^4\,G$
Magnetic Field	Applied Field	H	$\frac{A}{m}$	Oersted (Oe)	$1\frac{A}{m} = 4\pi \text{ x} 10^{-3}\,Oe$
Magnetization		M	$\frac{A}{m}$	$\frac{emu}{cm^3}$	$1\frac{A}{m} = 10^{-3}\frac{emu}{cm^3}$
Mass Magnetization		σ	$\frac{Am^2}{kg}$	$\frac{emu}{g}$	$1\,\frac{Am^2}{} = 10^3\frac{emu}{g}$
Magnetic Moment	Moment	m	Am^2	emu	$1\,Am^2 = 10^3\,emu$
Magnetic Constant	Permeability of Free Space	μ_0	$\frac{Tm}{A}$	none	$1.26\text{x}10^{-6}\frac{Tm}{A} = 1$
Energy Product		BH_{max}	$\frac{kJ}{m^3}$	$MGOe$	$8\frac{kJ}{m^3} = 1\,MGOe$

a sphere, the demagnetization factor is 1/3. Demagnetization factors are cited in the literature [17].

There are a few alternate ways of describing and naming magnetic units. Occasionally, magnetic properties may be measured by the polarization, J, where $J = \mu_0 M$, so that $B = \mu_0 H + J$. In CGS units, μ_0 is set equal to one and Eq 1 becomes $B = H + 4\pi M$. Table 1 lists the names and relationships between various magnetic terms and their units.

A typical $M - H$ curve is shown for a generic material in Figure 1(a). A material often begins in the demagnetized state at the origin of the hysteresis curve. As the applied field increases the magnetization reaches a maximum value M_s, which is a property intrinsic to the magnetic phase of the material. When the applied field is removed, the magnetization falls to the value M_r, called the remanence. H_c, called the intrinsic coercivity,[2] is the applied field required to bring the magnetization

[2]Intrinsic coercivity is a misnomer, since the coercivity is not an intrinsic property of the magnetic phase. It is dependent upon several microstructural factors.

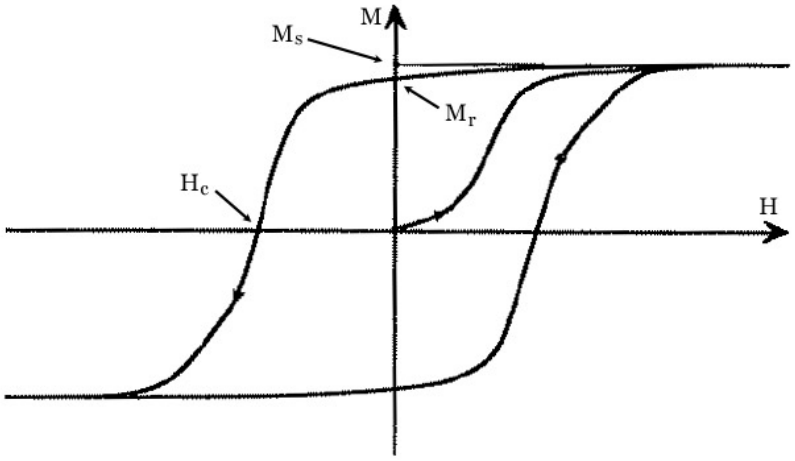

(a) A generic $M - H$ hysteresis curve for a hard magnetic material with the magnetization saturation, M_s, remanence, M_r, and intrinsic coercivity H_c marked on the graph [4]

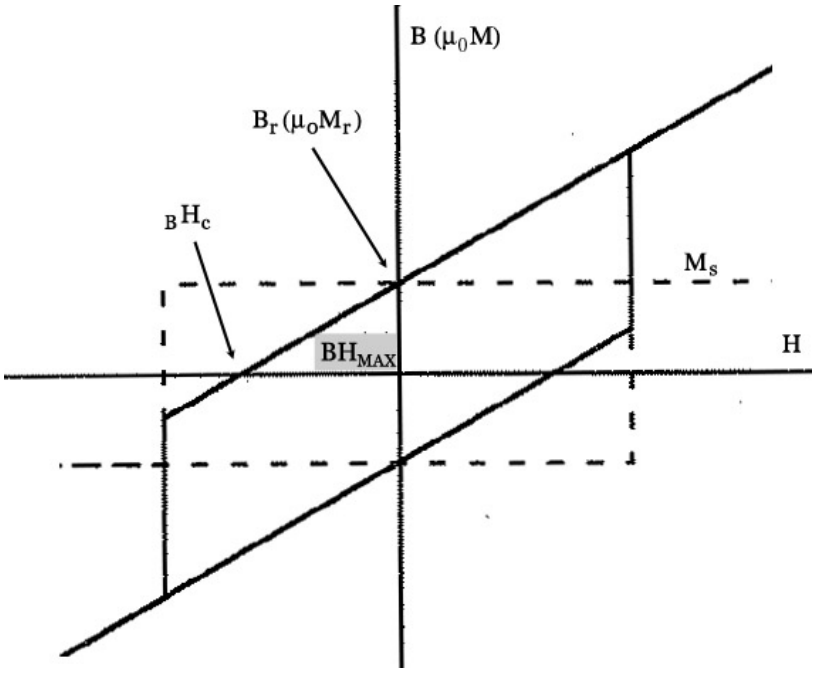

(b) Idealized hysteresis curves for a hard magnetic material. $B - H$ curve is shown with a solid line. $M - H$ curve is shown with a dotted line. [4].

Figure 1: Example hysteresis curves illustrating (a) generic behavior and (b) ideal behavior. The saturation, remanence, and coercivity are indicated in each plot.

back to zero. As the applied field continues to increase anti-parallel to the original magnetization, the material will saturate in the opposite direction.

Both the $M-H$ and $B-H$ curves are shown for an *ideal* hard magnetic material in Figure 1(b). The ideal hard magnetic material will have M_r equal to M_s and will hold that value of magnetization up to the intrinsic coercivity. At this point the magnetization completely reverses. When viewed in relation to Equation 1, it is easy to see that the remanence will be the same on both curves, $\mu_0 M_r = B_r$. Also, the coercivity, ${}_BH_c$, on the induction curve must necessarily be smaller than the intrinsic coercivity, H_c, since ${}_BH_c$ will occur when $M = -H$, instead of when $M = 0$.

The energy product is the figure of merit for engineering permanent magnets, and it is defined as the area of the largest rectangle that can be inscribed in the second quadrant of the $B-H$ curve. This is usually represented as BH_{max}. For an ideal material, with $B_r = \mu_0 M_s$, the energy product is then given by Equation 2.

$$BH = (B_r - \mu_0 H)H = B_r H - \mu_0 H^2 \tag{2}$$

Simple calculus shows that the maxima occurs at $H = \frac{B_r}{2\mu_0}$, yielding Equation 3 for the maximum energy product.

$$BH_{max} = \frac{B_r^2}{4\mu_0} = \frac{\mu_0 M_s^2}{4} \tag{3}$$

Since the maximum energy product occurs at $H = \frac{M_s}{2}$, an intrinsic coercivity larger than $\frac{M_s}{2}$ will not produce a higher energy product in an ideal magnet.

The magnetization behavior in ferromagnetic materials arises from the tendency of atomic magnetic moments to align with each other. The atomic magnetic moments in a ferromagnetic material are held parallel by exchange forces, also known as the molecular field. For a pair of atoms, the exchange energy is given by Equation 4 [17].

$$E_{ex} = -2J_{ex} S_i S_j cos\phi \tag{4}$$

The energy will the be minimized when ϕ is zero, or when the atomic moments are aligned parallel or anti-parallel. A first principle calculation of the exchange

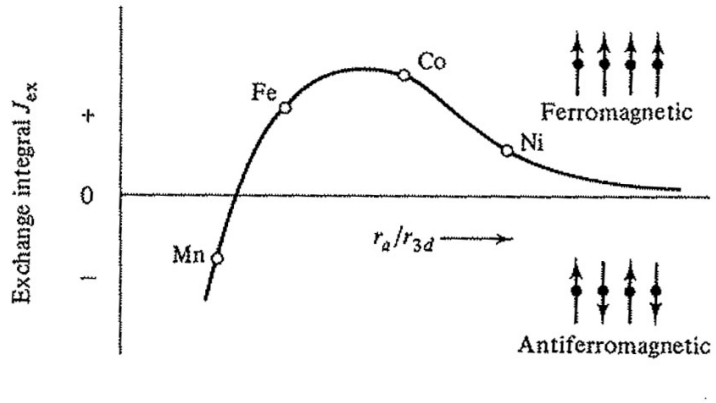

Figure 2: The Bethe-Slater curves shows a postulated dependence of the exchange integral upon the ratio of the atomic radius to the radius of the $3d$ shell. Ferromagnetic ordering is differentiated from antiferromagnetic ordering by the sign of the exchange integral. [17]

integral, J_{ex}, has not been developed; however, the Bethe-Slater curve approximates the integral's dependence on the ratio of the atomic radius to the radius of its $3d$ shell, $\frac{r_a}{r_{3d}}$. The Bethe-Slater curve, shown in Figure 2, provides an explanation for ferromagnetic ordering in simple systems, such as iron, nickel, and cobalt; however, applications of this theory to other materials are limited. Ferromagnetic ordering is differentiated from antiferromagnetic ordering by the sign of the exchange integral.

Ferromagnetic ordering is disrupted as the temperature of a material increases. M_s will decrease as the material is heated, reaching zero at the Curie temperature. Above the Curie temperature a ferromagnetic material will become paramagnetic. The Curie temperature is related to the strength of the exchange coupling between atomic moments, and so the Bethe-Slater curve has also been presented as a Curie temperature dependence on $3d$ orbital size [18].

Since exchange forces create magnetic alignment between atoms, these must be necessarily dependent on atomic arrangement and spacing. Magnetization behavior will vary greatly for different crystallographic directions. To reach saturation, a single crystal of cobalt requires a field an order of magnitude greater when applied along a

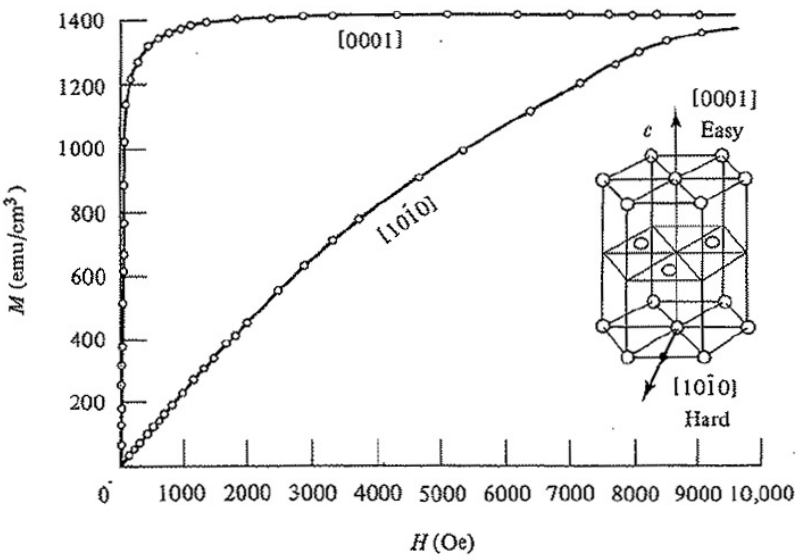

Figure 3: Magnetization curves for a single crystal of cobalt along the easy axis, [0001], and along a perpendicular direction [10$\bar{1}$0] [17].

basal direction than along the c-axis [17]. Thus the c-axis is termed the "easy" axis of magnetization. Some materials may have multiple easy directions or easy planes of magnetization, but all materials for practical use as hard magnetic materials have a single easy axis. Figure 3 shows the magnetization curves for a single crystal of cobalt along the easy magnetization direction and along a perpendicular, basal direction. The energy difference in magnetizing the material in a direction other than the easy direction is called the anisotropy energy, and it can be modeled as a series expansion of direction cosines of the angle between the easy axis and the magnetization axis, as shown in Equation 5.[3]

$$E_a/V = K_1 sin^2\theta + K_2 sin^4\theta + \ldots \tag{5}$$

For many high-anisotropy non-cubic materials, such as those used as permanent magnets, the K_1 term serves as a good approximation for anisotropy energy [19].

A high magnetic anisotropy is a critical element to achieve high performance and approach ideal hard magnetic behavior. While the shape of the grains has been used

[3]Typically a substitution is made to show the expansion in terms of $sin\theta$.

in the past to produce anisotropy (e.g. AlNiCo magnets), the anisotropy present in current high performance magnets is due mainly to magneto-crystalline anisotropy, which can be orders of magnitude higher.

The anisotropy energy is important in understanding magnetization reversal and coercivity in magnetic materials. The Stoner-Wohlfarth theory [20] assumes coherent rotation of magnetization of single domain particles, since this mode keeps the atomic moments aligned and minimizes the exchange energy. For a small ellipsoidal particle with uniform magnetization, the energy required to rotate all atomic magnetic moments together is given by Equation 6, in which only the angular dependent part is shown.

$$E = K_1 sin^2\theta - \mu_0 \vec{M} \cdot (\vec{H}_c + \frac{1}{2}\vec{H}_d) \tag{6}$$

H_e and H_d refer to the external field and the demagnetizing field, as defined previously (p.5). For a particle with its easy axis aligned along the major axis of the ellipsoid, Equation 6 will have two minima at 0 and 180 degrees, with an energy barrier in between. As H_e increases, the size of the barrier will decrease and eventually vanish. At this point, the magnetization of the particle is unstable and completely reverses. This point, equivalent to the coercivity for this model, is given in Equation 7.

$$H_c = \frac{2K_1}{\mu_0 M_s} + \frac{1}{2}(1 - 3D)M_s \tag{7}$$

Very few materials experience magnetization reversal by coherent rotation alone. As a result, the coercivity of most materials is several times smaller than what is predicted by the Stoner-Wolhfarth model [19].

For particles of a large enough size, a lower energy state can be achieved by the creation of separate magnetic domains, or areas in which the atomic moments are aligned. In the case of hard magnetic materials with strong uniaxial anisotropy, the domains will be aligned along the easy magnetization axis of the local grain, but individual domains will be anti-parallel to each other. There will be a finite region

between domains, called the domain wall, in which the alignment of atomic moments transitions between the opposing alignments of the neighboring domains.

Formation of multiple domains occurs when the decrease in energy from having multiple domains outweighs the energy cost of the domain wall. The size at which this begins to occur is dependent on the anisotropy, saturation magnetization, and the exchange interactions of the material. The critical size is a few hundred nanometers in diameter for most hard magnetic materials but only a few tens of nanometers or less for soft materials [4, 21].

Stoner-Wohlfarth theory can not be applied to multi-domain materials, since all the atomic moments can not be assumed to rotate together. Instead, magnetization reversal in many multi-domain materials is attributed to nucleation of reverse magnetic domains and movement of domain walls such that reverse domains grow. Reverse domains will typically nucleate at defects or inclusions in the grain. Hence, coercivity can be increased in some magnets through removal of defects or the addition of inter-granular phases that smooth over irregularities on the grain surface. Certain defects can be beneficial, by acting as pinning centers that hinder movement of the domain walls [4]. The field at which reverse domains begin to nucleate is called the nucleation field, H_N.

During the magnetization process of a material with strong uniaxial anisotropy, grains will initially have multiple domains with anti-parallel magnetization directions. As the applied field increases, grains will become single domain with the magnetization remaining aligned along the easy axis of the local grain. As applied field increases further and the material approaches saturation, the magnetization will move off of the easy axis and align with the applied field. In this high field region, a magnetic material will follow a well known behavior called the law of approach, as shown in Equation 8,

$$M = M_s(1 - \frac{a}{H}) + \chi_{hf} H \tag{8}$$

where χ_{hf} is the susceptibility at high fields. For materials well below the Curie temperature the $\chi_{hf}H$ term can be ignored. This equation can be used to to determine M_s in cases where the applied field is not strong enough to reach full saturation by plotting M versus $\frac{1}{H}$.

When the applied field is removed the magnetization will tend to return to the local easy axis, but leave a net magnetization, the remanence. Thus, the remanence can be seen to be heavily dependent upon the degree of alignment of the easy axis of the grains. While the remanence can also be affected by the presence of non-magnetic phases, porosity, and temperature, these factors also lower the saturation magnetization, and so the remanence ratio, $\frac{M_r}{M_s}$, also called the squareness, is often studied. For non-interacting grains, $\frac{M_r}{M_s}$ can be described by Equation 9.

$$\frac{M_r}{M_s} = \frac{\int P(\psi) cos(\psi)\, \mathrm{d}\psi}{\int P(\psi)\, \mathrm{d}\psi} \tag{9}$$

In the above equation, $P(\psi)$ is the probability that the easy axis of a particular grain will make an angle ψ with the magnetization direction. For a perfectly isotropic material, $P(\psi)$ =sinψ and $\frac{M_r}{M_s} = 0.5$. For this reason, $\frac{M_r}{M_s}$ is often used as a measurement of the degree of alignment of the grains. For textured samples with magnetization parallel to the alignment of the easy axes of the grains, the remanence ratio can approach 1 for well aligned materials.

2.1.2 Hard Magnetic Materials

The Nd-Fe-B material system, and other rare earth-iron intermetallics, represent the latest class of permanent magnets to be commercially realized. With $Nd_2Fe_{14}B$ as the primary magnetic phase, these magnets have significantly higher magnetic saturation than previous classes of magnets and sufficiently high coercivity. The tetragonal structure, $P4_2/mnm$ space group, of $Nd_2Fe_{14}B$ was first established by Herbst [22]. This structure is shown in Figure 4(a) along with the calculated X-ray diffraction profile (using Cu-K_α radiation) in Figure 4(b) [23]. $Nd_2Fe_{14}B$ has served as the

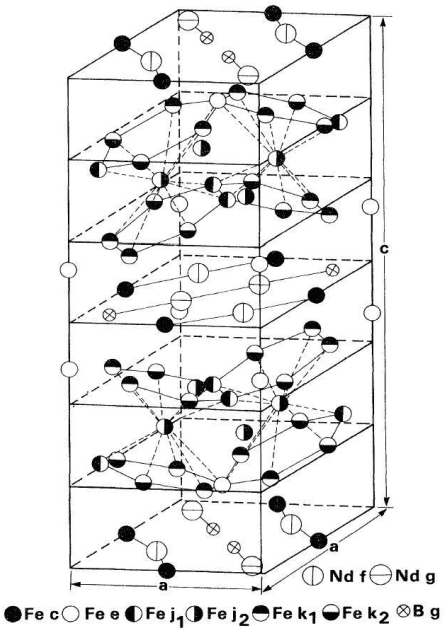

(a) Crystal structure of $Nd_2Fe_{14}B$

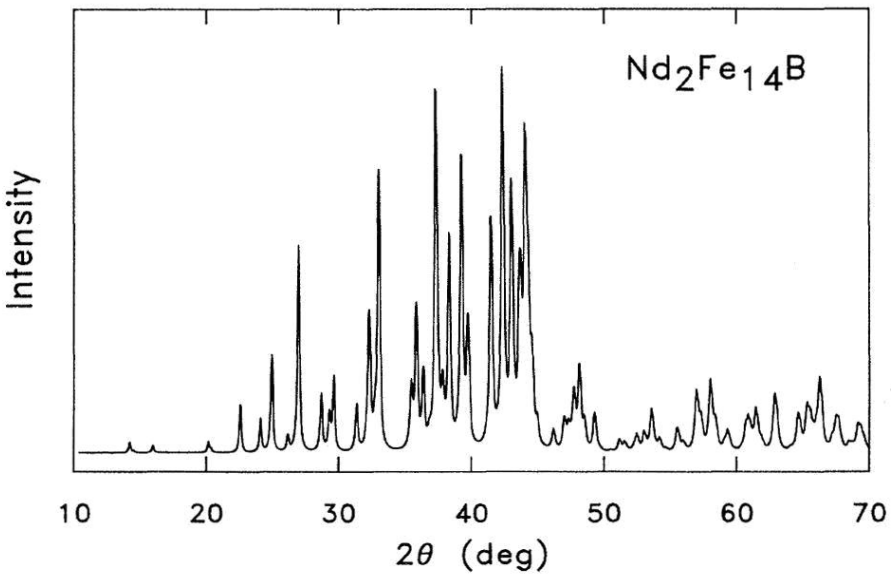

(b) X-ray diffraction pattern

Figure 4: (a)The crystal structure of $Nd_2Fe_{14}B$ showing atomic positions. (b) Calculated X-ray diffraction pattern for copper $K_{\alpha 1}$ radiation. [23]

prototypical material for this class but has roughly equivalent magnetic properties and structure to $Pr_2Fe_{14}B$ [23]. Lattice parameters for $Pr_2Fe_{14}B$ differ only slightly from $Nd_2Fe_{14}B$, so the $Pr_2Fe_{14}B$ XRD trace is similar to the one for Nd-Fe-B shown in Figure 4(b).

A vertical section of the ternary phase diagram for the Nd-Fe-B system is shown in Figure 5(a). The phase diagram follows the tie line that connects the 100% Fe point to the stoichiometric point for $Nd_2Fe_{14}B$. The system has three distinct Nd-Fe-B compounds. T_1 corresponds to the $Nd_2Fe_{14}B$ phase, the main magnetic phase in commerical Nd-Fe-B magnets. T_2 is another tetragonal phase with composition $Nd_{1+\epsilon}Fe_4B_4$. T_3 is a high boron phase not commonly found in high performance magnets [24]. Figure 5(b) shows that the Nd-Fe-B magnets with highest energy product will fall in the range of 14% to 17% Nd content. The excess Nd in this range is shown in the phase diagram in Figure 5(a) to melt at 938K. The Nd rich phase is the main grain boundary phase, and the relatively low melt temperature aides in liquid phase sintering.

$Sm_2Fe_{17}N_x$ represents the most promising of a new class of permanent magnetic materials in which improvement in magnetic properties is achieved through modification of interstitial sites. Nitrogenation of Sm_2Fe_{17} can produce an increase in the Curie temperature, magnetization, anisotropy, and a change from easy-plane to easy-axis magnetization behavior [25]. The improvement in magnetic properties is attributed largely to the increase in volume of the material's unit cell. Figure 6 shows the crystal structure of $Sm_2Fe_{17}N_x$, in which the octahedral interstitial sites are occupied by nitrogen. Nitrogenation of Sm_2Fe_{17} produces a gas-solid solution, not a true nitride compound [25]. This solution is not thermodynamically stable. The nitrogenation reaction, shown in Equation 10, is exothermic with $\Delta H = -181\frac{kJ}{mol}$ [19].

$$Sm_2Fe_{17} + \frac{3}{2}N_2 \rightarrow Sm_2Fe_{17}N_3 \tag{10}$$

The decomposition reaction, shown in Equation 11, is also exothermic, with $\Delta H =$

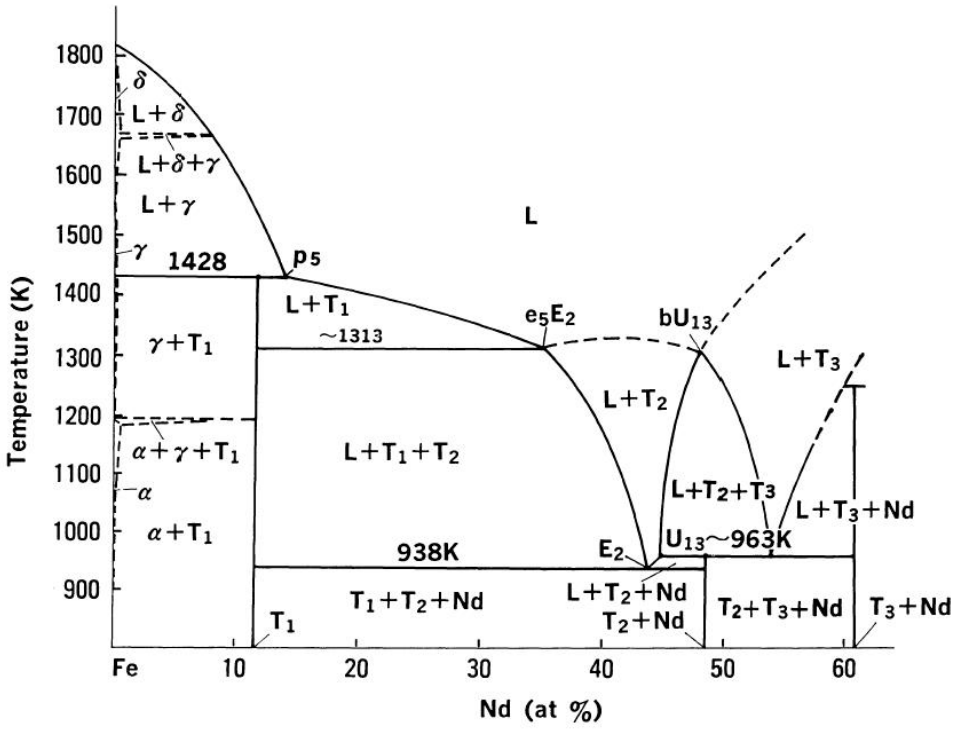

(a) Two-Dimensional Nd-Fe-B Phase Diagram

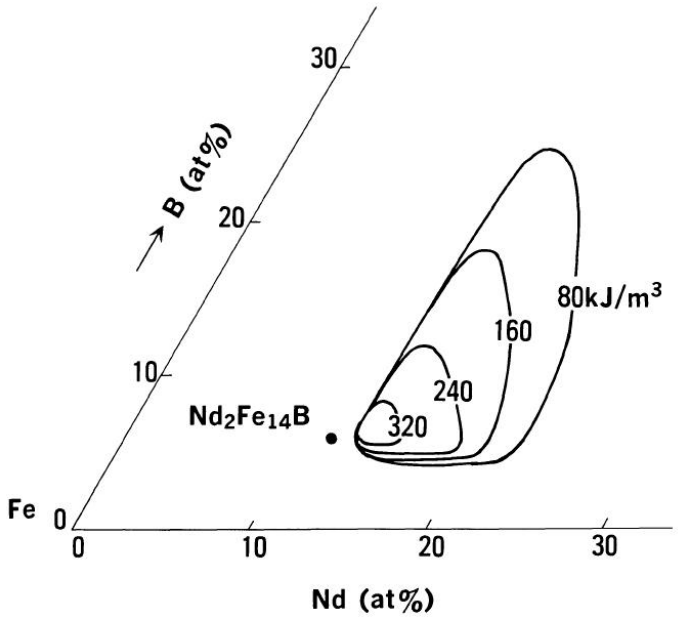

(b) Compositional dependence of Nd-Fe-B energy product

Figure 5: (a) Vertical section of the Nd-Fe-B ternary phase diagram along the tie line from 100% Fe to the stoichiometric point for $Nd_2Fe_{14}B$. $T_1 = Nd_2Fe_{14}B$. $T_2 = Nd_{1+\epsilon}Fe_4B_4$ (b) Ternary composition plot of the energy product of Nd-Fe-B sintered magnets following optimal annealing conditions. [24]

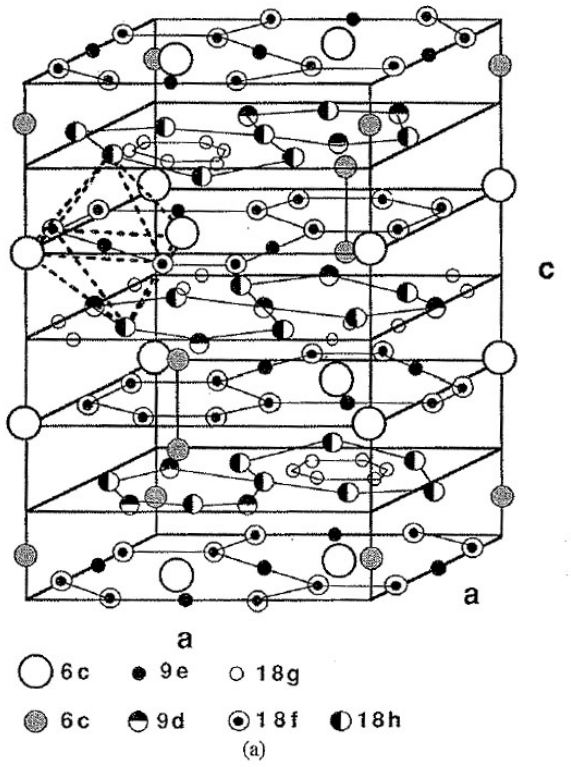

Figure 6: Rhombohedral crystal structure of $Sm_2Fe_{17}N_x$ and similar interstitially modified inter-metallics. Samarium atoms occupy the 6c sites. Nitrogen occupies the 9e sites. All other sites are occupied by iron. [25]

$-420\frac{kJ}{mol}$ [19].

$$Sm_2Fe_{17}N_3 \rightarrow 2SmN + Fe_4N + 13Fe \tag{11}$$

The nitrogenation and decompositional processes are controlled by the relative diffusion rates of iron and nitrogen. Figure 7 plots the diffusion distance, approximated as $2\sqrt{Dt}$, in Sm_2Fe_{17} for iron, nitrogen, and hydrogen There exists a window around 400-500^{o}C where nitrogen can diffuse into the bulk of a grain, typically a few μm in diameter, but no significant diffusion of iron is present, as shown by a diffusion distance smaller than the interatomic spacing. This window is the optimal range for nitrogenation of Sm_2Fe_{17} without subsequent decomposition into α-Fe and other phases [19].

Since decomposition is a diffusional process, the stability of the $Sm_2Fe_{17}N_3$ phase will be determined both by the temperature and the time it is held at temperature.

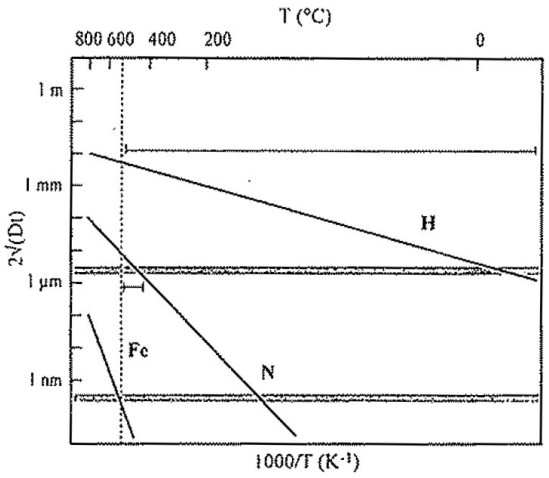

Figure 7: Diffusion distance, $2\sqrt{Dt}$, in Sm_2Fe_{17} as a function of inverse temperature. Shaded horizontal lines indicate the sizes of a typical grain, 1 μM, and the interatomic spacing of iron, 1 Å. [19]

One model developed by Skomski [25] assumes the material will no longer be suitable for use as a permanent magnet when α-Fe precipitates of 3 nm or larger have been formed. A temperature of 250-300^{o}C is identified as the point for long term stability, since growth of the α-Fe grains would take over 100 years at these temperatures [25]. However, other studies show that the magnetic properties begin to degrade at temperatures in the range of 400-475 ^{o}C, depending on nitrogen content [26]. Additionally DSC traces show an exothermic reaction, forming SmN and α-Fe, with an onset temperature 600-700^{o}C for a 40 C/min heating rate [26].

Table 2 compares properties of several high performance hard magnetic materials. Typical properties for Sm-Fe-N and Pr-Fe-B are not available because these materials are not commonly used in commercial applications.

2.1.3 Soft Magnetic Materials

As noted in Eq. 3, the maximum possible energy product is related to the saturation magnetization of a material. Since the saturation magnetization is an intrinsic property, the maximum energy product can only be increase by switching to a new

Table 2: Intrinsic magnetic properties and typical values of extrinsic properties of selected hard magnetic materials, . (a) O'Handley [27]. (b) Herbst [23]. (c) Lacheisserie [28]. (d) Skomski [25]. (e) Coey [4]

Material	M_s $(\frac{kA}{m})$	$T_c(^oC)$	$K_1(\frac{kJ}{m^3})$	H_c $(\frac{kA}{m})$	${}_BH_c$ $(\frac{kA}{m})$	$(BH)_{max}$ $(\frac{kJ}{m^3})$
$SmCo_5$	790_a	685-700$_a$	17000_c	1400_e	680_e	150_e
$Sm_2Fe_{17}N_x$	1220_d	476_d	8600_d			
$Nd_2Fe_{14}B$	1270_a	312_a	4900_c	1000_e	920_e	420
$Pr_2Fe_{14}B$	1240_b	292_b				

Table 3: Magnetic Properties of Selected Soft Magnetic Materials. (a) Lacheisserie [28]. (b) Hall [29]. (c) Coey [30]. (d) [31]. (e) [32].

Material	M_s $(\frac{kA}{m})$	T_c (^oC)	K_1 $(\frac{kJ}{m^3})$
Fe	1710_a	770_a	48_a
Co	1370_a	1121_a	530_a
Ni	480_a	212_a	-4.5$_a$
Fe_4N	1400_c	494_c	
$Fe_{16}N_2$	$\sim 1900_d$	537_c	780_d
FeCo	1940_b	980	$\sim 0_b$

material system or by making a composite material, such as a hard/soft composite. Traditional design of soft magnetic materials seeks to minimize coercivity and energy product, thereby reducing the energy loss per cycle, while maintaining a high magnetization. When designing hard/soft composites for use as permanent magnets, the coercivity of the soft phase, while potentially desirable, is considered negligible when compared with the hard phase. This allows the use of several high magnetization materials that would normally not be suitable as soft magnetic materials. Table 3 lists magnetic properties of selected soft magnetic materials.

α-Fe is one of the most commonly used soft magnetic materials. It combines a high magnetization with a very low cost. An alloy of iron and cobalt produces the among the highest magnetization of any material suitable for practical use. It should be noted that the iron-cobalt system shifts from $\langle 100 \rangle$ easy magnetization for low

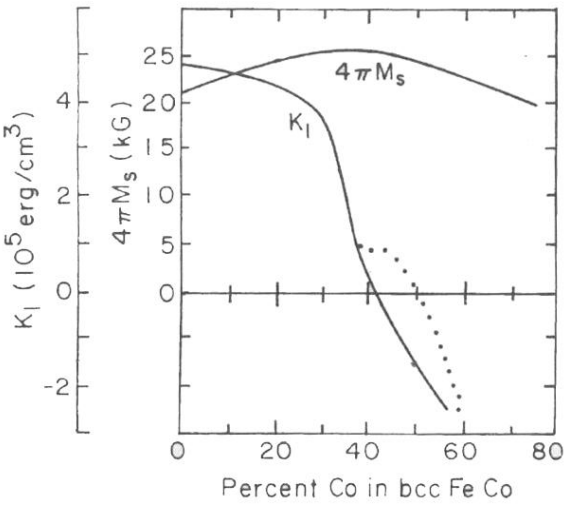

Figure 8: Graph of the dependence of magnetic saturation and anisotropy constant on composition in iron-cobalt alloys. The dotted line shows the ordered CsCl allotrope. After O'Handley [27].

cobalt content to $\langle 111 \rangle$ around 41% cobalt [29]. The saturation value for iron-cobalt remains high over a wide composition range, as shown in Figure 8.

The Iron-Nitrogen system contains multiple important magnetic phases. Figure 9 shows a portion of the Iron-Nitrogen phase diagram. The Fe-N system includes ferromagnetic structures γ'-Fe_4N, and α''-$Fe_{16}N_2$. Some other iron-nitride compounds, such as ϵ-Fe_3N and γ''-FeN, are paramagnetic. Of particular interest as a magnetic material is the α''-$Fe_{16}N_2$ phase which, while not the equilibrium phase in atmosphere, is meta stable at temperatures below $\sim 200^o$C. The α''-$Fe_{16}N_2$ phase is reported to have an unusually high saturation magnetization; however, the reports of the exact value have varied from 310 emu/g [34] to 240 emu/g [31]. Several difficulties have been highlighted in determining the magnetization of the α''-$Fe_{16}N_2$ phase. In many cases a pure sample of the phase can not be fabricated, so calculation of the magnetization requires an accurate knowledge of the relative amounts of each phase present and the magnetizations of non-α''-$Fe_{16}N_2$ phases. In addition to the presence of other ferromagnetic phases, such as α-Fe and γ'-Fe_4N, in many of the reported samples, formation of α''-$Fe_{16}N_2$ is frequently accompanied by α'-$Fe_{16}N_2$. α''-$Fe_{16}N_2$ can be

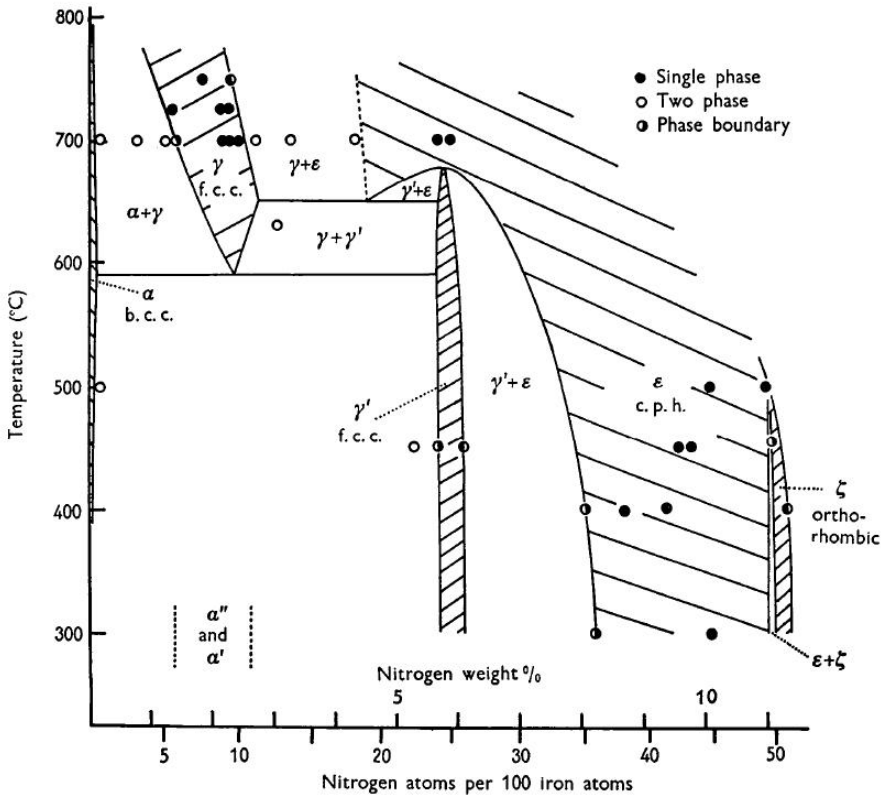

Figure 9: Iron-Nitrogen phase diagram. [33]

viewed as a face-centered tetragonal system with the nitrogen atoms occupying the body center octahedral sites in an ordered way so as to maximize the distance between nitrogen atoms [35]. The α'-$Fe_{16}N_2$ phase is a similar structure, but with nitrogen occupying the octahedral sites in a disordered manner. The two phases can be differentiated by the presence of super-lattice reflections in an XRD scan. Sugitay et al. [36] used the ratio of the integrated intensities of the $\alpha''(002)$ peak to the $\alpha''(004)$ + $\alpha'(002)$ combined peak as a measure of the N-site ordering in epitaxial thin films. They showed an increase in saturation magnetization as the ratio approached the value 0.125 for a perfectly ordered system; however, a similar effect could not be found by Takahashi et al. [37].

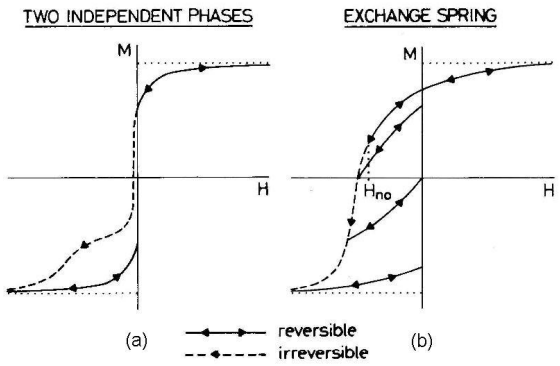

Figure 10: Example hysteresis curves of a permanent magnetic material with soft inclusions. The two phases act independently in part (a) and are exchange coupled in part (b). [38]

2.1.4 Exchange Coupling

In many cases, the presence of soft magnetic phases can severely limit the coercivity of a permanent magnet. Compared with the hard magnetic material, the soft inclusion can reverse its magnetization almost immediately as a reverse field is applied. This appears as a kink in the second quadrant of the hysteresis loop, as shown in Figure 10 (a). Under certain conditions the soft phase can be coupled to the hard phase, as shown in Figure 10 (b), and act similarly to a single phase hard magnet. With proper coupling between the phases, the overall performance of the material can be improved. As noted in Eq. 2, the maximum possible energy product is dependent on the square of the saturation magnetization. Comparing Table 2 and Table 3, one can see that the saturation magnetization of many soft materials exceeds that of current hard materials. Thus, with suitable coupling, a composite magnet may be able to achieve a larger energy product than the best currently available hard magnetic materials.

Over a short range, coupling between the hard and soft phases in a composite may be achieved by taking advantage of exchange forces. Exchange forces are described in §2.1.1, however, micromagnetic models often use a parameter called the exchange stiffness, A as an alternate means of describing exchange interactions. Skomski and

Zhou [39] assert that the exchange energy promotes coupling between magnetic moments over a characteristic length, as shown in Equation 12.

$$l_{exch} = \sqrt{\frac{A}{\mu_0 M_s^2}} \tag{12}$$

Estimates of the exchange length for most hard magnetic materials is only a few nanometers [4]. Thus, the ideal microstructure of an exchange-coupled nanocomposite magnet must have nanometer sized grains with no clustering of soft phases to ensure that the soft phase is within an exchange length of the nearest hard grain.

Since nanoscaled grains are generally too small to develop multiple domains, nanograined magnets are often modeled as a collection of non-interacting Stoner-Wohlfarth particles [4]. As noted previously, an isotropic material with non-interacting grains must have a remanence ratio, $\frac{M_r}{M_s}$, of 0.5. However, exchange-coupled grains interact by definition, and so the remanence ratio for these materials often exceeds 0.5, even though they are isotropic. Several studies have used the remanence ratio in nanograined magnets as a measure of the exchange-coupling, instead of the degree of easy axis alignment.

Critical to achieving high performance in exchange-coupled magnets is the small dimension of the soft phase. Skomski and Coey [2] used quantum mechanics analogies to magnetostatic interactions to estimate that alternating layers of 2.5 nm $Sm_2Fe_{17}N_3$ and 9 nm FeCo could achieve an energy product of $\sim 1000 \frac{kJ}{m^3}$. Soft inclusions significantly larger than the domain wall thickness, typically only a few nm, produces a very low coercivity [2]. Fischer et al. [40] used three dimensional micromagnetic calculations to simulate realistic microstructures of isotropic Nd-Fe-B/α-Fe composites. They found that for 10 nm iron grains, the remanence increases and the coercivity decreases as the volume fraction of iron increases up to 80% α-Fe, as shown in Figure 11. The 80% volume fraction point corresponds to the maximum energy product calculated and roughly corresponds with the volume fraction for the maximum energy product found in Skomski and Coey's [2] study. Fischer et al. [40] also found a

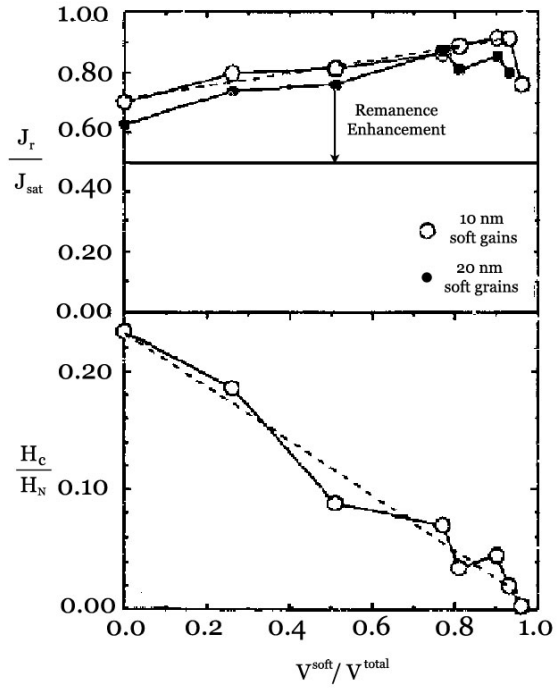

Figure 11: The dependence of reduced remanence, $\frac{J_r}{J_{sat}}$, and reduced coercivity, $\frac{H_c}{H_N}$, on the volume fraction of soft grains in an isotropic, exchange-coupled hard-soft nanocomposite magnet [40]

slight improvement in properties when a regularly shaped grain morphology was used. They observed that 10 nm iron grains produced slighly better remenance enchancement over 20nm soft grains. Lieneweber and Kronmüller [41] used a one dimensional analytical model to show a similar result: that the nucleation field decreases rapidly if the soft phase is much larger than the domain wall thickness of the hard phase, approximately 10 nm for Nd-Fe-B/α-Fe.

Recent reports have shown that single phase magnetic behavior can be achieved for soft phase inclusions much larger than the exchange length. Lee et al. [42] prepared a series of die-upset magnets by blending rare-earth-rich, melt-spun powder with micron sized α-Fe and Fe-Co particles. Adding these micron sized particles increased remanence and lowered coercivity, but produced a maximum energy product at low soft grain volume fractions of 3-8%. Initial reports suggested that coupling in large

soft grains is due to magnetostatic interactions; however, simulations of demagnetization behavior showed that incomplete exchange coupling must also be present to explain the experimental results [43]. The magnetostatic portion of the coupling was shown to be strongest when the soft phase inclusions where in a platelet morphology oriented perpendicularly to the magnetization direction. Samples using larger volume fractions of soft grains, up to 30%, have a siginfiicantly reduced energy product and coercivity, even though they had single phase demagnetization behavior [44].

2.1.5 Fabrication Techniques

Achieving the ideal microstructure for exchange-coupled permanent magnets, mainly a nanoscale, well-dispersed soft phase as described in §2.1.4, is a difficult challenge. The most common method is through phase separation of the hard and soft phases from a solid solution [45]. This can be achieved through heat treatment and crystallization of an amorphous material produced from melt-spinning or mechanical alloying, or melt spinning can be used to quench directly to the appropriate crystallite size [46, 47].

Melt-spinning is a prominent process for fabrication of isotropic nanocomposite magnetic ribbons which can be ground into powders. In melt spinning, a homogenized ingot of material is melted in a crucible, typically by an induction heater. The melt is rapidly quenched as it is poured on to a chilled, spinning wheel. The quench rate is dependent upon the speed of the wheel, the composition of the material, and rate of deposition of material onto the wheel, which itself can vary with ejection pressure and size of the hole in the crucible. For relatively modest cooling rates, heat flow occurs perpendicular to the wheel surface and thus creates crystal growth in that direction [48]. At lower wheel speeds, the process is growth dominated, ensuring that the fastest growing crystal orientations will dominate the solidification [49]. The resulting columnar structure typically has grains in the micron regime and a sharp

texture. Micron sized grains, however, are not suitable for nanocomposite magnets. More rapid cooling rates, corresponding to higher wheel speeds, result in amorphous structures or isotropic nanocrystallites[50].

The microstructure of melt spun R-Fe-B based materials will be dependent upon the quench rate and the composition of the material. Hard/soft nanocomposite materials can be fabricated through melt spinning by using a rare-earth lean composition. Chen et al. [51] fabricated such a material by over-quenching and creating an amorphous material that, with subsequent heat treatments, results in crystallite formation. The coercivity was highly dependent upon the size of the soft phase crystallites. The optimal coercivity was achieved for very short heat treatment times. Figure 12 shows the coercivity dependence on heat treatment time at three different temperatures. The alloys containing praesodymium as the rare-earth element achieved higher coercivities relative to neodymium for all heat treatments. The addition of Nb into the alloy further increased the coercivity by limiting growth of the soft phase crystallites [51]. Similar studies show that optimal quench rates and annealing conditions vary and must be optimized on a case by case basis [52, 47] However, the trends that annealing times remain on the order of minutes and small alloying additions can limit grain growth and increase coercivity hold true.

Mechanical alloying is another potential process for creating appropriate nanocrystalline powder. This technique employs various forms of ball milling to produce the alloy. A mixture of powder, mechanically hard balls, and milling media can be agitated in a variety of ways to achieve milling. The alloying is produced by a cycle of welding and fracturing of the alloyed materials. Varying the milling temperature or introducing specific liquid additives can provide some control over the welding-fracturing mechanisms [53]. The mechanical alloying technique often initially employs a simple mixture of starting powders to be alloyed. Refinement in particle and crystallite size is achieved through the process of repeated plastic deformation and

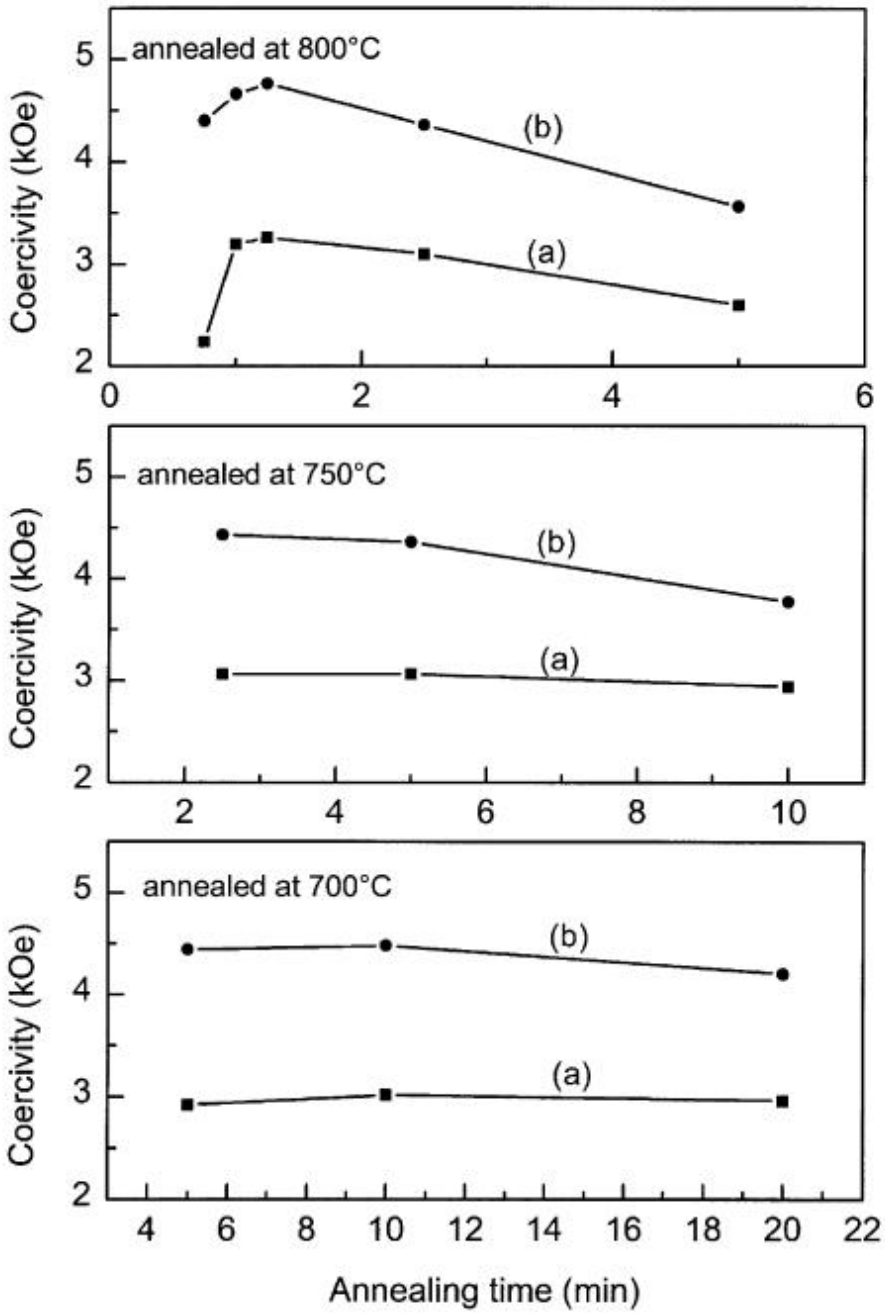

Figure 12: Coercivity dependence on heat treatment times for three different temperatures in RE-lean magnets. Composition (a) is $Nd_8Fe_{86}B_6$ and (b) is $Pr_8Fe_{86}B_6$. The optimal heat treatment is achieved after only a few minutes. Praesodymium containing alloys achieved higher coercivities for all heat treatments. [51]

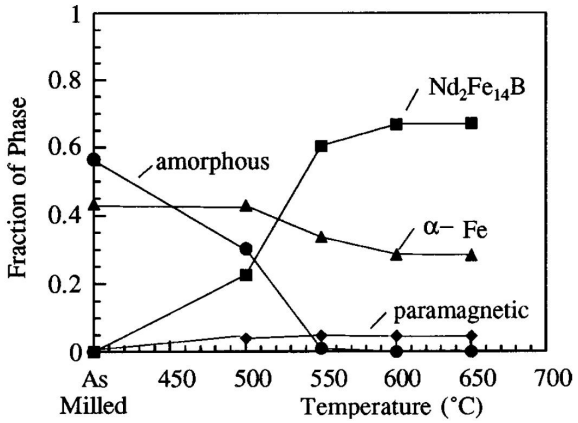

Figure 13: Phase Transformations in Nd-lean, mechanically alloyed powders under a range of heat treatment temperatures. [46]

fracture during milling.

During high-energy ball milling in most rare-earth based materials, the initial deformation mechanism has been assumed by some authors to be shear banding [46]. As milling time increases, the shear bands create sub grains with low-angle boundaries which then evolve with further milling into randomly oriented nanocrystallites. Depending upon the composition, additional milling can produce increasing disorder resulting in the formation of amorphous material, driven by the high surface energy of the nanocrystalline material [46]. Typically, the as-milled powder is magnetically soft and must be heat treated to produce a suitable hard magnetic material. The crystallization temperature increases from 550^o to 600^oC as the volume fraction of α-Fe increases [46]. At low heat treatment temperatures, the amorphous phase crystallizes into the $Nd_2Fe_{14}B$ phase with little change in α-Fe volume fraction, as shown in Figure 13. At higher temperatures, some of the α-Fe is incorporated into the $Nd_2Fe_{14}B$ phase. Despite the decrease in α-Fe volume fraction, the size of the α-Fe grains can increase. This results in a decreasing remanence and coercivity with increasing heat treatment time [46].

The mechanically alloyed powder can also be hot pressed to produce bulk samples. Wecker et al. [6] produced a series of mechanically alloyed Nd-Fe-B-Si powders that

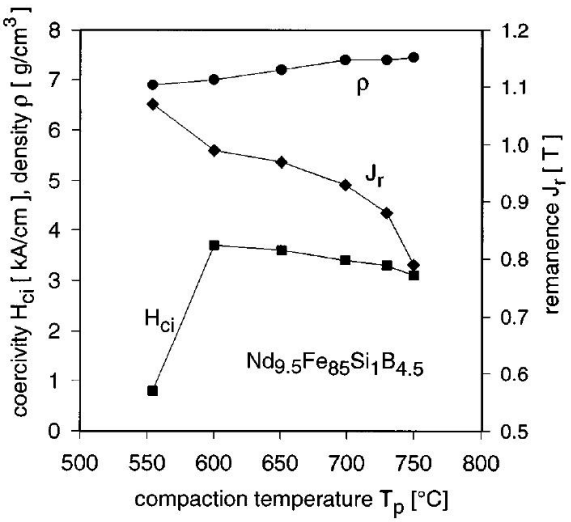

Figure 14: Dependence of density and magnetic properties on compaction temperature for hot pressed mechanically alloyed powder of composition $Nd_{9.5}Fe_{85}Si_1B_4.5$. [6]

were then hot pressed to produce bulk samples. Figure 14 shows the dependence of density and magnetic properties on compaction temperature for the alloy with the best magnetic performance, $Nd_{9.5}Fe_{85}Si_1B_{4.5}$. The figure shows that there is a trade off between density and magnetic properties. As the hot pressing temperature is increased, the density increases but the coercivity and remanence decrease. This is attributed to an increase in the soft grain size that degrades the exchange coupling.

The trade off between density and magnetic properties can be mitigated by using a warm compaction process, which is similar to hot pressing but uses a lower temperature (less than 700 ^{o}C) and a higher pressure (2.5-3.8 GPa) [54, 55]. Rong et al. [55] used the warm compaction technique consolidate ball-milled composites of SmCo/FeCo. Figure 15 shows the dependence of grain size, density and magnetic properties on compaction temperature. The compacts reach full density for compaction temperatures of approximately 550 ^{o}C, which corresponds to the temperature at which significant grain growth begins to occur. The energy product, however, reaches a maximum around 400 ^{o}C. Rong et al. [54] also used warm compaction to create an exchange coupled nanocomposite magnet by consolidating mixtures of FePt

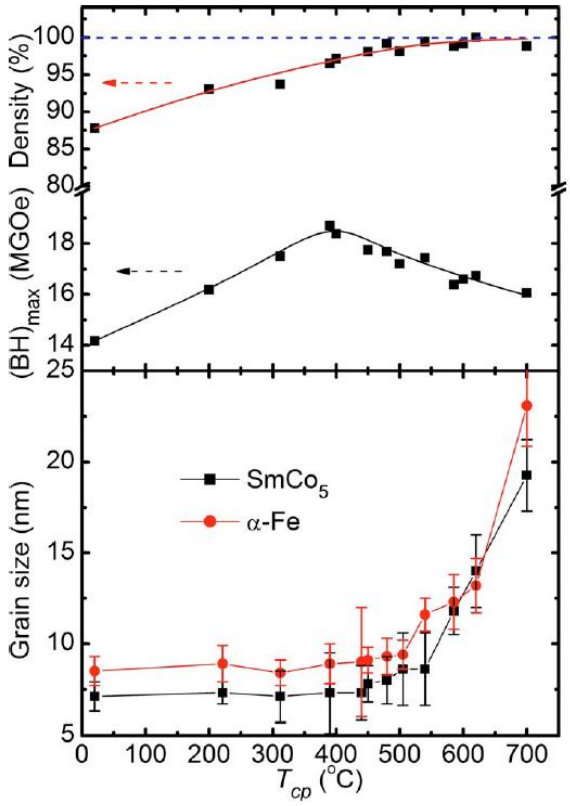

Figure 15: Dependence of grain size and magnetic properties on compaction temperature in warm compacted samples of $SmCo_5/\alpha$-Fe ball milled composite powder.[55]

and Fe_3O_4 nanoparticles. Difficulties in fabricating nanoparticles have limited the application of this technique to other more technologically important material systems, such as Nd-Fe-B; however, there has been some recent progress in producing Nd-Fe-B nanoparticles through surfactant assisted ball milling [56, 57].

The process of die-upsetting, in which a hot pressed magnet is removed from its die and then hot pressed in a larger die to create a radial expansion and a reduction in thickness, is an important technique for developing texture in some nanograined magnetic materials. This technique will be discussed in detail in §2.2.

2.2 Texture

As noted in Section 2.1.1, the remnant magnetization of a material is directly dependent upon the degree of alignment of the grains. Many engineering materials develop

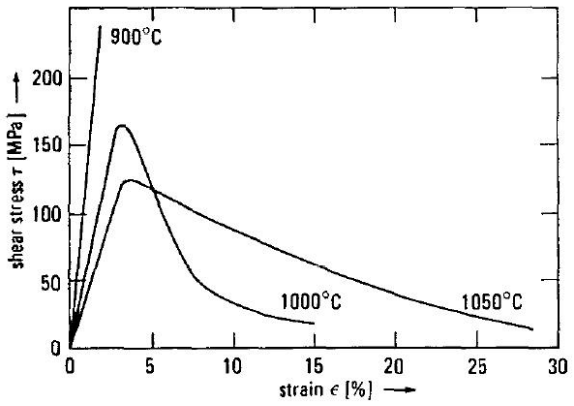

Figure 16: Shear stress - strain diagram for single crystal $Nd_2Fe_{14}B$ with its (001) plane oriented 45^o from the compression direction. [59]

significant anisotropy from texture created during bulk forming processes such as rolling, forging, or extrusion that rely on plastic flow of the material. Neodymium-Iron-Boron, and most rare earth permanent magnet materials, however, do not accommodate large amounts of plastic strain due to their limited dislocation mobility [58].

Studies on single crystals of $Nd_2Fe_{14}B$ indicate that dislocation motion is only possible at temperatures above 1000^oC [59]. Figure 16 shows the shear stress verses strain plot for a single crystal of $Nd_2Fe_{14}B$ with its (001) plane oriented 45^o to the compression direction. Since the (001) plane is the only active slip plane, this orientation maximizes the shear stress in the sample [59]. Below 1000^oC the stress-strain curve is purely elastic, indicating that the sample fractured before deforming plastically.

Limited plastic deformation makes the use of traditional bulk forming processes unsuitable for use on $Nd_2Fe_{14}B$. Instead, texture can be introduced into the material using a magnetic field to rotate single domain particles into alignment [24]. Alternatively, texture can be created through die-upsetting, a diffusional process in which properly oriented grains grow and misaligned grains shrink [60].

2.2.1 Descriptions and Measurement of Texture

In order to formulate a quantitative description of texture, such as the orientation distribution function (ODF), a rigorous method for representing orientation is needed. A common method is to state a particular orientation by specifying the crystallographic directions that are oriented with the bulk material axes, (hkl) [uvw], such as the normal to the plane of a rolled metal and the axis parallel to the rolling direction [61]. Real orientations are often idealized as the closest whole number index orientation [62]. A more precise method is the use of the Euler angles. The Euler angles represent a specific set of rotations relative to a specified sample axes. For instance, for a rolled material, we begin with the crystal axes parallel to the axes of the bulk material, such that [100], [010], and [001] axes are parallel to the rolling (x), transverse (y), and normal directions (z) [61]. The rotations, as shown in Figure 17, are about the [001] direction through an angle of α, about the [010] through β, and again about the [001] direction through γ. Together these rotations can represent any

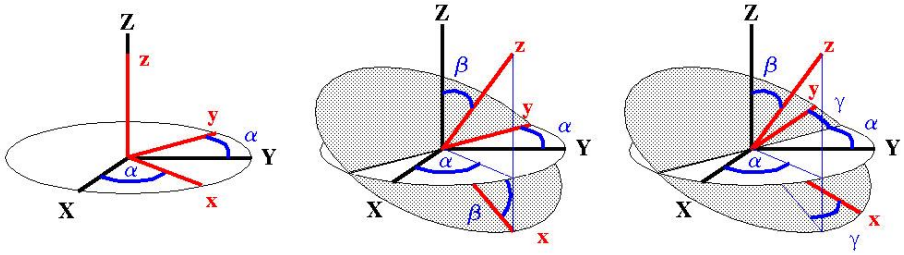

Figure 17: Diagrams illustrating the Euler transformations [63]

orientation, g, relative to the sample axes. The ODF, which describes the texture of a material, is a function of g and is given by the fractional volume of crystallites with an orientation from g to $g + dg$.

A particular crystallographic (hkl) plane only needs two parameters to be specified, β and γ. Thus, the orientation of the plane can be represented in a pole figure, a stereographic projection of the orientation of the poles relative the sample on a unit sphere. Alternatively, an inverse pole figure can be constructed from plotting

the specimen orientations relative to the crystal axes [62].

The most common method for measurement of pole figures is via x-ray diffraction. As the sample is rotated, the diffracted x-ray intensity is proportional to the number of diffraction planes oriented to satisfy the Bragg condition and are perpendicular to the plane of the incident and reflected beams. The proportionality constant will depend on experimental conditions [61]. The third orientation coordinate, however, remains undetermined by this method, thus, a single pole figure is insufficient to calculate an orientation distribution function. Several methods have been developed to calculate the ODF from multiple pole figures. Since all of these methods are complex, automated software can be used to perform the calculation. Because crystal symmetry can produce identical orientations with different Euler angles, the number of pole figures required will depend on the symmetry of the crystal system of the material. No exact analytical method for ODF calculation exists, and so most methods use more pole figures than is mathematically necessary. Cubic systems typically require 3 or 4 pole figures, while hexagonal materials usually need 5 or 6 [62].

Until recently, more detailed information linking orientation with microstructural features could only be obtained through selected area diffraction in a transmission electron microscope. This process is too time consuming to use to gather enough data to make any statistical analysis meaningful. Modern SEM and TEM techniques, however, have automated orientation measurement capabilities. Analysis of Kikuchi patterns using backscatter electrons in an SEM is the most prominent of these techniques. In addition to allowing direction measurement of the ODF, this technique also can provide information on local variations in texture, interfacial texture, morphological-texture relationships, as well as other microstructural-texture relationships [62]. The resolution of this technique, approximately 1 micron, prevents its use in studying nanograined materials, such as exchange-coupled nanocomposite magnets.

2.2.2 Texture by Alignment in a Magnetic Field

One main way texture is produced in rare-earth permanent magnets is through alignment in a magnetic field. The alloy is prepared by melting under vacuum and casting. The cast ingot is then crushed and milled to produce a small uniform particle size near the critical size for single domain behavior. For the Nd-Fe-B system, this is usually around 1 to 3 microns. This powder is then aligned in a magnetic field before being pressed and sintered, in order to achieve a very sharp fiber texture along the easy axis of magnetization [64, 24].

Texture is achieved as the particles rotate into alignment with the magnetic field. This requires that each particle have a single magnetic domain, since a multidomain particle will be magnetically isotropic and have no net torque. However, a magnetic particle does not need to be smaller than the critical size for a single domain. If the particle is slightly larger than the critical size, a strong enough field can first produce a single domain state in the particle and then produce a torque on the particle. However, if the particle is polycrystalline and isotropic, no texture will be created since the isotropic arrangement of grains will rotate together.

During the early stages of development of Nd-Fe-B magnets, the alignment and pressing were performed under static fields in a traditional die press set up. Applying an axial magnetic field during die pressing was the most common method used, since it allowed for the production of a wide variety of shapes [65]. In this setup, however, the deformation texture produced competed against the alignment from the magnetic field. Use of a transverse magnetic field produced better alignment but limited part shapes. In both cases, a static field is needed throughout the compaction process to maintain the alignment.

Isostatic pressing is able to surpass the alignment of both die pressing techniques [65]. Isostatic pressing does not significantly alter the texture of the material, thus no

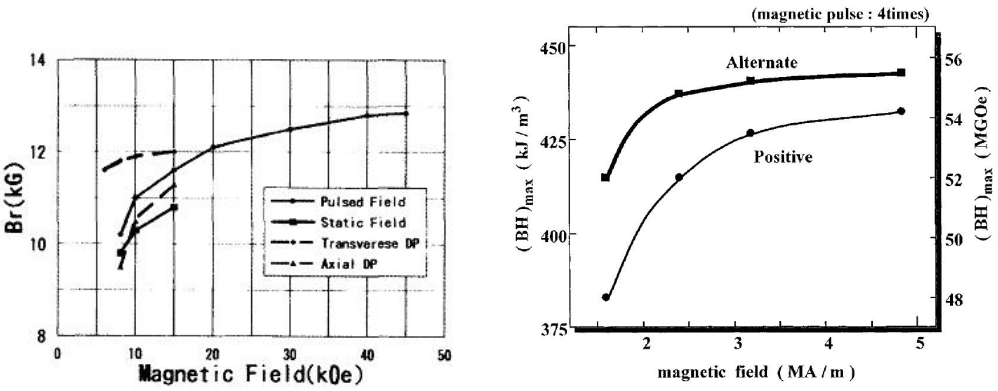

Figure 18: (a) Comparison of remanence as a function of the alignment field strength for rubber isostatic pressing versus several forms of traditional die pressing for Nd-Fe-B powder at 37% packing density [65]. (b) Energy product as a function of the alignment field strength for pulsed magnetic fields applied axially only and for alternating between axial and transverse [66]

field, or a relatively small field, is needed to keep the alignment . This allows the alignment step to be performed separately, creating the opportunity for the use of pulsed fields, which are much easier to create at high levels. The use of a strong magnetic pulse can also break up aggregates, creating a sharper alignment than a static field [64]. Sagawa and Nagata's [65] original investigation into pseudo-isostatic pressing using axially pressed rubber dies clearly demonstrated the advantage of the technique over conventional die pressing. Other investigations have found that alternating magnetic pulses between axial and transverse directions provides further improvement in the particle alignment [66]. Figure 18 compares the magnetic properties produced by the various techniques mentioned. In the case of materials with an easy plane of magnetization, where the c-axis is often the hard direction of magnetization, alignment is achieved by rotating the sample in a magnetic field [67, 68].

The powder alignment can also be affected by the initial packing density [65]. Interparticle friction will increase as packing density increases, limiting the ability of particles to rearrange and rotate. Use of pulsed fields, and especially alternating pulsed fields, allows for the use of a wider range of packing densities than conventional

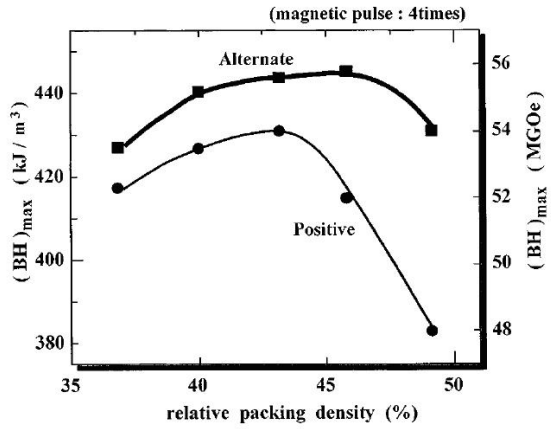

Figure 19: Energy product of magnets pressed at various initial packing densities. [66]

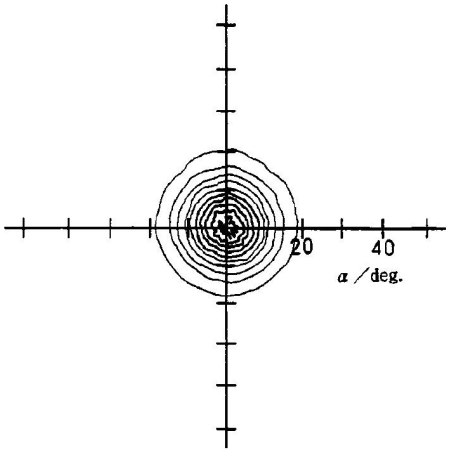

Figure 20: Pole figure for the easy axis, c-axis, of a very high energy product magnet. Contours are multiples of random intensity [66].

die pressing. Typically die pressing cannot exceed 20% packing density with out loss of particle rotation. Figure 19 shows the relationship between packing density and the resulting energy product of the magnets produced.

The degree of alignment needed to achieve very high energy products in $Nd_2Fe_{14}B$ is shown in the pole figure in Figure 20. Using very high pulsed fields with isostatic pressing, alignment coefficients of 99% can be reached [69]. Axial die pressing typically produces alignment coefficients of around 90% [70].

2.2.3 Texture by Die Upsetting

As noted in §2.2.2 polycrystalline powders are not suitable for alignment in a magnetic field. Texture can be produced in some polycrystalline magnetic materials by die upsetting. The die upsetting process consists of hot-pressing the magnetic powder in a die so that it reaches full density. The compact is then removed from the die and placed in a larger die so that it is not constrained around the circumference. The compact is heated and pressed so that its height is reduced and diameter increases. This process is typically used on melt-spun powders, whose isotropic and equiaxed grain structure becomes elongated perpendicular to the pressing direction during the die upsetting process.

Although the material is mechanically deformed during die upsetting, the process does not rely on typical mechanisms of plastic deformation such as dislocation motion or twinning. Instead alignment in die upsetting is a diffusional process. In the model put forth by Li and Graham [71, 60], the low melting point Nd-rich grain described in §2.1.2, serves as a fast diffusion path when in the liquid phase. Properly oriented grains, those with their *c*-axis parallel to the pressing direction, grow, becoming elongated and slightly thicker. Improperly oriented grains shrink and mass transport between the two occurs mainly through the grain boundary.

The driving force for diffusion is a concentration gradient in the liquid boundary phase. According to Li and Graham [71, 60], an isotropic sample of $Nd_2Fe_{14}B$ undergoing uniaxial strain during die pressing will have a certain fraction of grains with the *c*-axis aligned parallel to the pressing direction. Since the the *c* direction has the lowest elastic constant, these grains will have a lower strain energy than the surrounding grains [72, 60]. The difference in strain energy drives the diffusion between grains.

Figure 21 depicts Li and Grahams's model in which grains, idealized as 50 nm cubes, combine to form 250 nm X 250 nm X 50 nm platelet grains. In support of this model, the authors note that post die upsetting grains will have their *c*-axis aligned

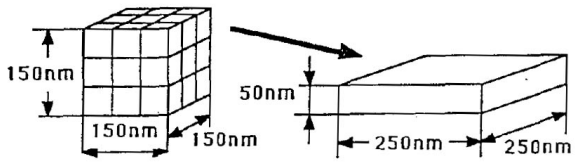

Figure 21: Schematic of recrystallization behavior in die upset magnets with approximately 50 nm initial grain size [60]

to within 15^o of the pressing direction. If properly aligned grains serve as the nucleus for recrystallization, then approximately 1 in 29 would be within this 15^o range. This loosely agrees with their model in which 1 in 27 serves as the nucleus. Additionally, when the die upset magnet has undergone a height reduction of 60% to 70% the alignment becomes saturated. This seems to agree with the model in which a 150 nm tall group of grains combines to from a 50 nm thick grain, producing a height reduction similar to the 60% to 70% limit [60].

This model also explains several of the features of die upsetting. During initial hot pressing, in which porosity is removed, the material is under hydrostatic pressure. This means there is no difference in elastic energy between grains, no driving force for diffusion, and no significant texture developed. The Hall-Petch relationship does not apply to die upsetting, since smaller grains result in a shorter diffusion distance and therefore the bulk is more easily deformed. Additionally, when temperature increases, the stress needed is lowered, since the diffusivity has increased and less driving force is needed [60].

The temperature-stress-strain rate relationship was investigated by Grünberg et al. [13] for two commonly used nanograined Nd-Fe-B powders, MQP-A (containing 14 atomic % Nd) and MQP-B (containing 12% Nd) produced by Magnaquench, Inc.. The authors first demonstrated that these materials do not work harden for strains below 50%, meaning that there is a single value of flow stress for a given strain rate and temperature. The flow stress verses temperature relationship, shown in Figure 22, follows the Arrhenius relationship and is linear on a log-log plot for temperatures

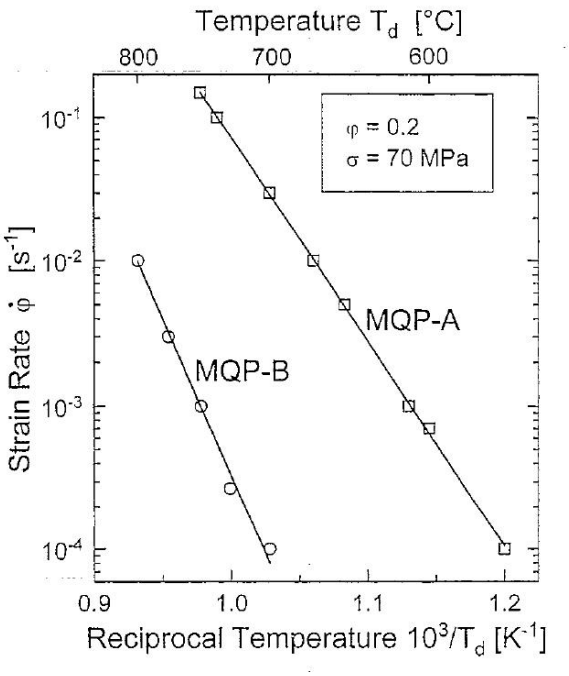

Figure 22: Plot of the strain rate verse temperature dependence of nanocrystalline Nd-Fe-B with two different amounts of Nd content. MQP-A = 14% Nd. MQP-B = 12% Nd. [13]

that extend below the melting point of the Nd-rich grain boundary phase. This indicates that the grain boundary phase does not have to be in the liquid phase to allow die upsetting. This was confirmed by studies of the diffusivity of Nd and Fe in the grain boundary phase using radioactive tracer atoms [73]. The diffusivity of Nd remained high at temperatures down to 600^{o}C, below the 665^{o}C melting point of the grain boundary phase. In addition, the diffusivity for Nd and Fe were similar, despite the large difference in atom sizes, suggesting that diffusion is not the rate limiting factor in die upsetting[73]. However, Grünberg et al., showed that the flow stress and temperature required for die upsetting at a particular strain rate decrease as Nd content increases, suggesting that the excess Nd aides the diffusion-deformation process [13].

Several studies have shown that low Nd content, below the stoichiometric point of 11.8%, reduces the ability of die upset material to produce texture. Leonowicz et

al. [74] developed a series of melt-spun alloys with varying Nd content. Figure 2.2.3 shows the dependece of various magnetic properties on Nd. All three graphs show significant differences between the Nd-rich (greater than 12%) region and the Nd-lean (less than 12%) region. In the Nd-rich region shown in Figure 23(a), increasing the Nd content lowers the remanence, since the fraction of $Nd_2Fe_{14}B$ is decreased. The coercivity increases because the additional Nd in the grain boundaries helps to inhibit nucleation of reversed magnetic domains. In the Nd-lean region, decreasing Nd content increases the fraction of α-Fe phase, thereby increasing the remanence. The magnetically soft α-Fe phase also reduces the coercivity. Even as the remanence increases with decreasing Nd, remanence values are still considerably lower than those found in the Nd-rich region. The reason for this can be seen in Figure 23(b) as being due to a lack of anisotropy in the Nd-lean region. The anisotropy, as measured by the ratio of the magnetization parallel and perpendicular to the die upset direction, is essentially 1 (isotropic) until the Nd-content is increased past the 12% mark. Since the stoichiometric point is 11.8%, samples above the 12% point will have significant amounts of excess Nd. As a result, the Nd-lean samples have low energy products, as shown in Figure 23(c).

Recently magnets have been fabricated with higher anisotropy in the Nd-lean region [9, 7]. In these samples the anisotropy decreases rapidly as the volume fraction of α-Fe phase increases past a couple of percent. Liu et al. [75, 76] showed that a slight c-axis texture can be produced in samples with 9% Nd when intially amorphous powder is used. The authors suggest that under uniaxial pressure, the amorphous material will nucleate and grow crystals in a preffered direction. The alignment developed in these samples was very limited; the anisotropy ratio (J_z/J_x) for the best sample was approximately 1.25 [76].

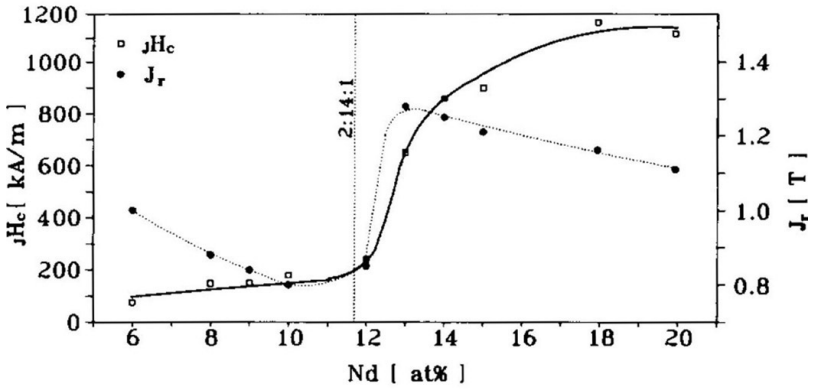

(a) Coercivity ($_JH_c$) and Remanence (J_r) verse Nd content

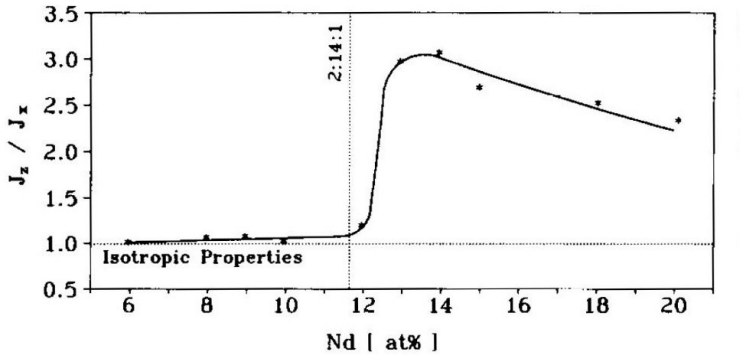

(b) Anisotropy (J_z/J_x) verse Nd content

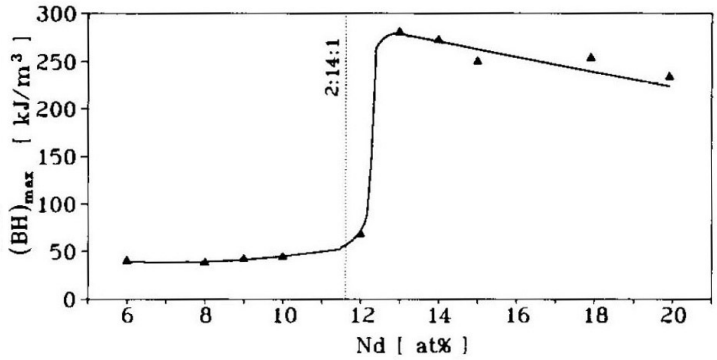

(c) Energy Product (BH_{max}) verse Nd content

Figure 23: Dependence of magnetic properties on Nd content for melt-spun and die upset magnets [74].

2.3 Shock Compression and High Strain Rate Deformation

As discussed in §2.1.4 and §2.1.5, conventional means of processing exchange-coupled magnets such as hot pressing requires precise control of temperature, heating time, and composition. Exchange-coupled magnets fabricated to date have been able to only match the magnetic properties of single-phase materials for isotropic magnets and techniques for developing significant texture are lacking. The use of shock compression and high strain rate deformation to process magnetic materials has the potential to provide a significant advantage to hot pressing by allowing consolidation of magnetic powders without extended heating times. The following section describes some basic concepts of shock compression.

2.3.1 Shock Compression Theory

Conventional mechanics of materials assumes quasi-static loading conditions such that at any point a volume element is assumed to be in mechanical equilibrium. A high speed impact between two bodies creates a non-equilibrium loading condition, producing large magnitude stress waves that propagate through the bodies involved. Low amplitude stress waves produce only elastic effects. If the amplitude of the wave is sufficiently large such that any instantaneous state of stress is much larger than the dynamic yield stress, then the material can be considered to flow freely, or hydro-dynamically. This assumption is equivalent to assuming the material is in a hydrostatic state of stress, or that $\sigma_x = \sigma_y = \sigma_z = -P$ [77]. The propagating disturbance is termed a shock wave, since it produces discontinuities in pressure, density, and particle velocity between the shocked and unshocked regions. The jump conditions describing conservation of mass (Eq 13), momentum (Eq 14), and energy (Eq 15) across the shock front, are expressed by the following equations.

$$\rho_0 U_s = \rho(U_s - U_p) \tag{13}$$

$$P = \rho_0 U_s U_p \tag{14}$$

$$E - E_0 = \frac{1}{2}P(V_0 - V) \tag{15}$$

The shocked material is at pressure P, internal energy E, and density ρ, while P_0, E_0, and ρ_0 represent the corresponding unshocked states. V is the specific volume, so that $V = \frac{1}{\rho}$. The shock front moves at velocity U_s, and the particles in the region behind the shock front move at a velocity U_p [77]. Equation 15 depends upon the approximation that no energy is lost to thermal conduction or radiation. This assumption is often valid since the microsecond time scale of shock events is much shorter than the time scale for thermal equilibration. One additional equation, the equation of state (EOS), also known as the Hugoniot, is required in order to relate all variables to a single input variable. The EOS is a material dependent empirical relationship, which for most solid, non-reacting material systems follows a linear behavior in $U_s - U_p$ space, as shown in Equation 16, [78]

$$U_s = C_0 + S_1 U_p \tag{16}$$

where C_0 is the sound speed and S_1 is a constant for the material.

The Hugoniot can be shown as a representation of any two of the shock parameters. Figure 24 shows an example of the Hugoniot for a solid material expressed as a pressure - specific volume, $P - V$, relationship. The Hugoniot represents the locus of all shock states, not necessarily the shock loading path. The material will instead follow the Rayleigh line from the initial state to the shock state, $P_1 - V_1 - T_1$. Unloading of the material is assumed to occur isentropically, and therefore the unloading path follows the release isentrope shown in the Figure 24. The process is an irreversible one, as the material will unload to a higher specific volume and temperature, V_2 and

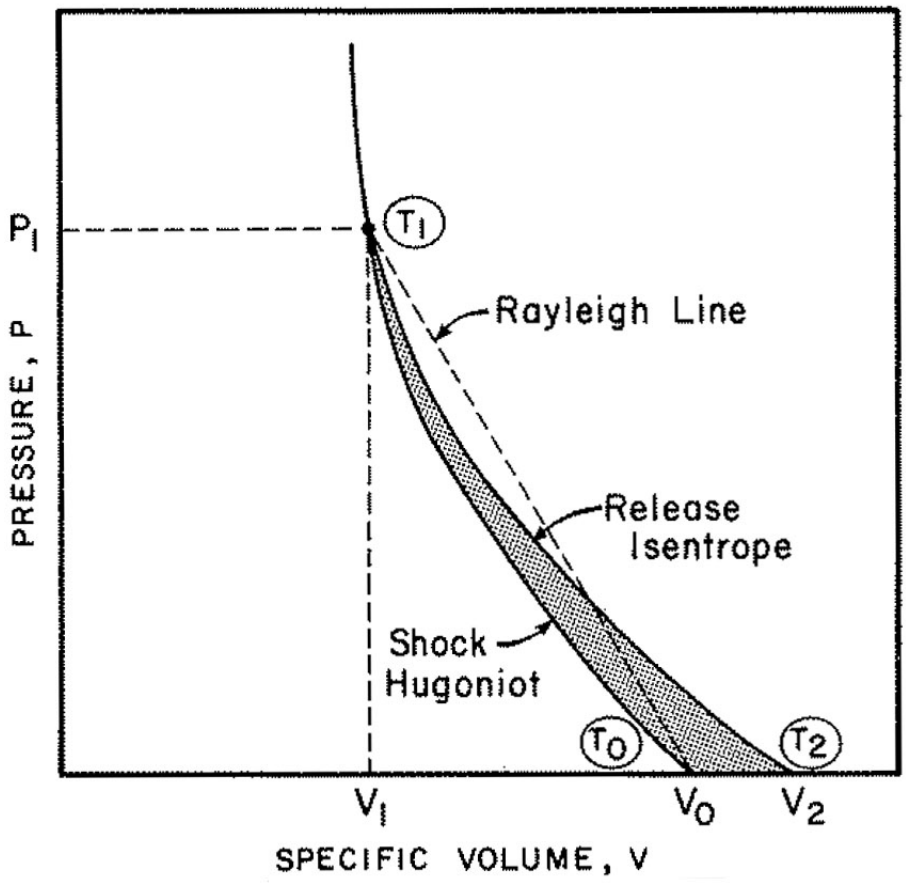

Figure 24: Example Hugoniot in P-V space. The material begins at ambient pressure and temperature, P_0 and T_0, and specific volume V_0 and is shocked to state P_1, V_1, T_1. Unloading follows the release isentrope back to ambient pressure but has expanded to specific volume, V_2 and T_2. [77]

T_2, than the initial state. T_1 and T_2 can be found from Equations 17 and 18 [77].

$$T_1 = T_0\, exp[(\frac{\gamma_0}{V_0})(V_0 - V)] + \frac{V_0 - V}{2C_v}P + \frac{exp[(\frac{-\gamma_0}{V_0})V]}{2C_v}\int_{V_0}^{V} P\, exp[\frac{\gamma_0}{V_0}V][2 - (\frac{\gamma_0}{V_0})(V_0 - V)]\,\mathrm{d}V \quad (17)$$

$$T_2 = T_1\, exp[\frac{\gamma_0}{V_0}(V_1 - V_2)] \quad (18)$$

Equation 17 is derived by combining Equation 15 with the combined first and second laws of thermodynamics. Additionally, a substitution is made for the Gruüneisen

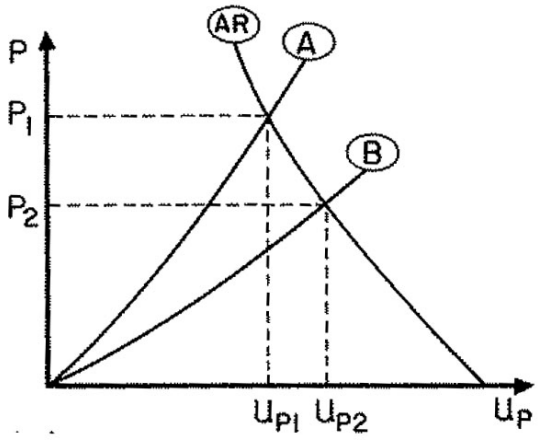

Figure 25: Graphical method for determining the pressure and particle velocity at the interface of two materials as a shock wave of amplitude P_1 moves from high impedance material A to low impedance material B. AR is the Hugoniot of material A reflected across the vertical line containing point $P_1 - U_{p1}$ [77]

parameter, γ, which is defined by Equation 19

$$\gamma \; = \; V(\frac{\delta P}{\delta E})_V \tag{19}$$

Calculation of both T_1 and T_2 is often practically limited by knowing the Gruüneisen parameter accurately.

When a shock wave passes from one material to another, the pressure, P, and particle velocity, U_p, must necessarily be equal at the interface. A graphical solution can be used for obtaining the pressure and particle velocity at the interface of two materials using a straight forward approach employing a $P - U_p$ graph, as shown in Figure 25. A shock wave of amplitude P_1 is transmitted from material A to material B. The reflected curve, AR, is constructed by reflecting the Hugoniot of material A about the vertical line containing the point $P_1 - U_{p1}$. A reflection is used to represent a change in reference frame from material A to material B. The $P - U_p$ point for the interface and for material B is found from the intersection of the reflected Hugoniot of A and the Hugoniot of B, $P_2 - U_{p2}$. The impedance, $\rho_0 U_s$, is equal to the slope of the line from the origin to the $P - U_p$ point. Therefore, a shock wave traveling from a high impedance material to a lower one, as shown in Figure 25 will have a

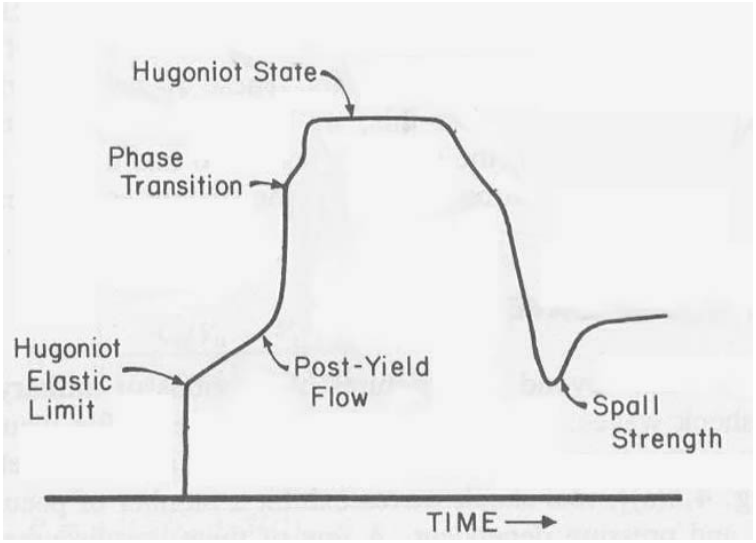

Figure 26: Generalized example of a VISAR trace showing particle velocity over time for a shock wave. [77]

faster particle velocity but a lower pressure. In addition, a release wave proportional in amplitude to the degree of impedance mismatch will reflect from the surface. The opposite will be true for transmission of a shock wave into higher impedance material: The pressure will increase, the particle speed will decrease, and an increased pressure will reflect from the surface.

As noted earlier, the above analysis is dependent upon the assumption that strength effects in the material can be ignored and that the stress state is equivalent to a hydrostatic stress state. Some materials have a high enough strength that the hydrodynamic assumption is not valid in a strict sense. In these cases a shock wave may be proceeded by an elastic wave equal in amplitude to the elastic limit of the material, called the Hugoniot Elastic Limit (HEL). Figure 26 shows generalized example of a Velocity Interferometer System for Any Reflector (VISAR) trace, which measures the particle velocity (or pressure, if the Hugoniot is known) of the shock wave over time. Initially, the velocity rises rapidly up to the point of the HEL. A shoulder occurs at the HEL, and above this point, plastic deformation occurs. In some cases, a second shoulder may occur that represents a phase transformation.

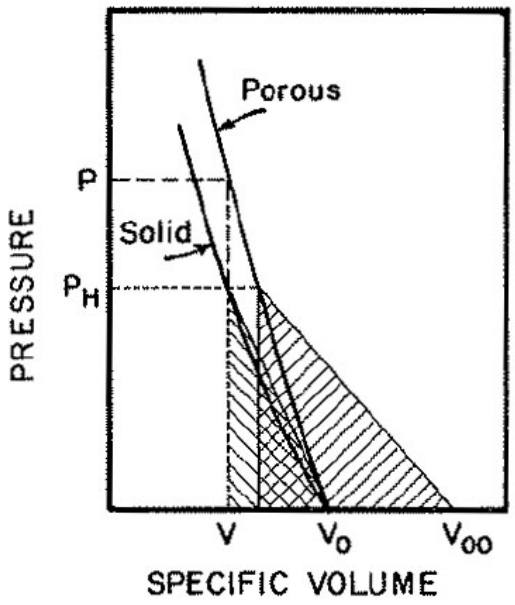

Figure 27: $P - V$ space Hugoniot for a solid and porous material. The shaded areas illustrate the amount of energy deposited by shock wave. [77]

Shock induced phase transformations will be discussed further in §2.3.4. Since the shock wave speed increases with pressure, a high enough amplitude shock will travel faster than the elastic wave, and the HEL will not be visible in a VISAR trace.

2.3.2 Shock Waves in Porous Media

A porous or distended material will have a lower density than its solid counterpart, and so, from Eq. 14, it must necessarily have a different Hugoniot. Figure 27 displays the differences in energy deposited by a shock wave of equal pressure for a solid and porous material as calculated by Eq. 15. The Mie-Grüneisen equation, shown in Equation 20, is one way of estimating the difference between the solid and porous Hugoniot. This equation can be seen to follow naturally from the definition of the Grüneisen parameter shown in Eq. 19. A $P - V$ relationship, as shown in Equation 21, can be developed by combining Eq. 20 with the jump conditions, Equations 13,14,

and 15, and a linear EOS.

$$P = P_S + \frac{\gamma}{V}(E - E_S) \tag{20}$$

$$P = \frac{[2V_S - \gamma(V_0 - V_S)]C^2(V_0 - V_S)}{[2V_S - \gamma(V_{00} - V_S)][V_0 - S(V_0 - V_S)]^2} \tag{21}$$

The subscript s refers to properties of the solid material, and V_{00} is the initial volume of the porous material. The Mie-Grüneisen equation ignores any strength effects. It basically assumes that a porous material will crush up to solid density at a negligible pressure. This assumption is reasonable when using very high shock pressures or for materials with a low crush strength.

The temperature rise associated with shock compression of porous materials can be estimated by assuming that the total shock energy, represented by the shaded area in Figure 27 is converted into internal energy. The temperature rise can then be estimated if the specific heat of the material is known. If the temperature rise is not large, the specific heat can be assumed to be constant. Therefore, the temperature rise is given by Eq. 22.

$$\Delta T = \frac{1}{2}P(V_{00} - V_S)/C_p \tag{22}$$

The temperature calculated using Eq. 22 can be viewed as an upper bound to the shock temperature, since portions of the shock energy must inevitably be stored as defects created by mechanical deformation. However, in many cases the defect energy is a small portion of the total energy. Schwarz et al. [14] conducted shock compaction experiments on a combination of copper and constantan powder that provided a thermocouple effect and allowed for in situ temperature measurements. Figure 28(a) shows the setup of the experiments. A shock temperature verse shock energy plot is shown in Figure 28(b). The authors use an equation similar to Eq. 22 to calculate the shock energy, with the main difference being that the specific heat is integrated over the temperature range. The calculated temperature is marked by the solid line in the figure and a good correlation is shown with the measured

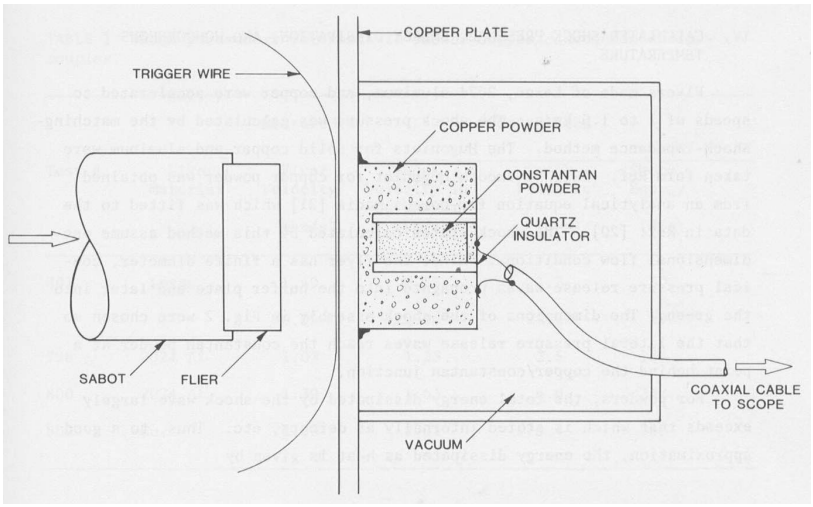

(a) Schematic of shock temperature measurements

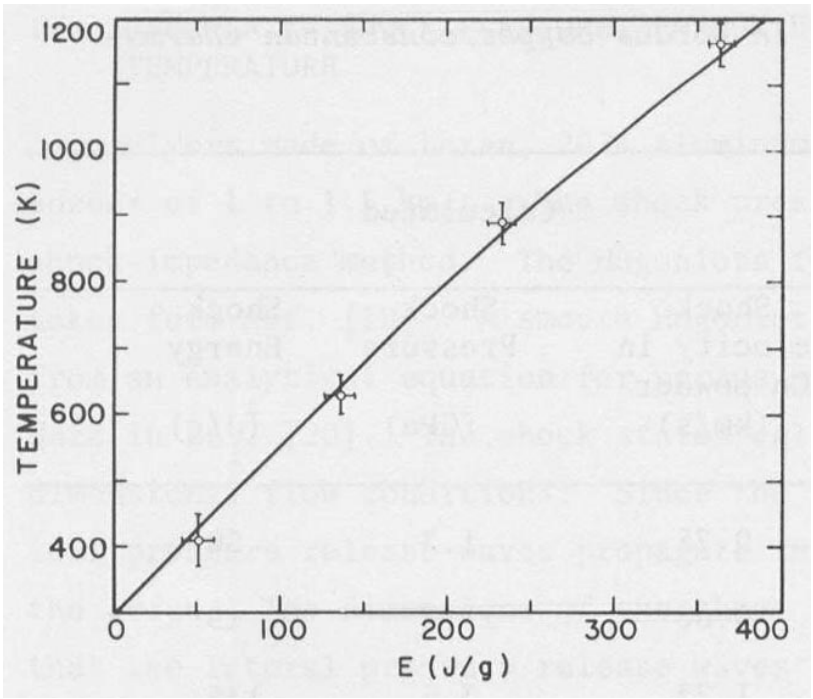

(b) Shock temperature verse Shock Energy

Figure 28: (a) Schematic of shock compaction experiments on copper and constantin powder that provide in situ measurements of temperature and (b) corresponding plot of shock temperature verse shock energy. [14]

temperatures.

The temperature calculated using Eq. 28 is the mean bulk temperature rise. Significantly higher temperature spikes are expected at the point contacts between particles. The timescale of a temperature spike is typically on the order of the rise time of the shock wave, tens of nanoseconds, and the temperature equilibrates to the bulk temperature calculated from Equation 22 after a few hundred nanoseconds [14].

The P-α model is commonly used to estimate strength effects on the porous Hugoniot [79]. The P-α model uses the α parameter to model the distention of the system, as shown in Equation 23.

$$\alpha = \frac{V}{V_S} \tag{23}$$

V is the specific volume of the porous material, and V_s is the specific volume of the material after complete crush up, which can be calculated using Eq. 21. The α parameter separates compression of the material from collapse of the pores. A third order series expansion of the α parameter has been commonly employed [80]. This formulation simplifies to the form shown in Equation 24.

$$\alpha = 1 + (\alpha_P - 1)\left[\frac{P_c - P}{P_c - P_e}\right]^n \tag{24}$$

P_e is the pressure at which the porous material no longer behaves elastically, and α_P is the corresponding distention. P_c is the crush strength. The constant n is typically set to 2.

A common practical challenge in implementing the P-α model is determining the crush strength of a porous material. The Fishmeister-Artz relationship [81], which models compaction of homogeneous spheres of similar size, can be used as an estimate. A simplified version was developed by Helle et al. [82] for relative densities below 90%, as shown in Equation 25.

$$P_y = \frac{3D^2\sigma_Y(D - D_0)}{1 - D_0} \tag{25}$$

P_y is the pressure needed to achieve a relative density D, starting from an initial relative fractional density of D_0. The powder mixture has an effective yield strength of σ_0. Although this model was developed for quasi-static loading of material, it can be used as a lower bound for approximating the the crush strength. The method employs fitting a $P - D$ curve to measured data points under quasi-static conditions such as die-pressing.

The Fischmeister-Artz model for use in the D 90% regime approaches full densification assymptotically. In practice, one can assume full density is reached at some value of D near, but less than 1; however, the crush strength then becomes very sensitive to the value of D chosen. Alternatively, the simplified version of Helle et al. [82] can be extended to full compaction, implying that the crush strength is aproximately 3 times the yield strength. This can serve either as a rough estimate of the crush strength or the lower bound of the crush strength.

2.3.3 Deformation and Bonding Mechanisms

The previous sections described the behavior of shock loaded materials on a continuum level, while this section will look at microstructural effects of shock compaction. For ductile materials, dislocation generation and motion is an important deformation mechanism. The model developed by Meyers [83, 77] holds that the shock wave generates dislocations through homogeneous nucleation at the shock front. The shock wave initially creates a uniaxial strain that necessitates a deviatoric component to the stress condition. Dislocations form to relieve the deviatoric stress, but move at a slower speed than the shock wave. Thus, additional dislocations are generated as the shock wave travels through the material. Metals with a high stacking fault energy energy (SFE) will have little separation of dislocations and closely spaced partial dislocations [77]. This will result in pockets of high dislocation density. Metals with a higher SFE will also have a higher critical pressure needed for twinning [84]. Low

SFE metals will tend to have more planar arrays of dislocations and more twinning faults [77].

The deviatoric stress component to the shock wave loading condition can also generate point defects. Shock loading can produce vacancy and interstitial defect concentrations several times higher than cold rolling [85, 77]. Meyers and Murr [86] attributed the high concentration of vacancies in shock loaded materials to nonconservative motion of dislocation jogs. The authors demonstrate that the jogs provide less resistance to dislocation motion as the velocity of the dislocation increases. Shock loading will produce high velocity dislocations that essentially "drag along" the jogs, creating many point defects[77].

Deformation in low ductility materials, such as ceramics, will often involve significant cracking; however, there are several other important mechanisms for deformation in low ductility materials. At high shock pressures, alumina exhibits extensive twinning, and microcracks form at the intersection of twins with grain boundaries [87]. Shock loading of alumina has been observed to create bands of dislocations and generate additional dislocations near twins and microcracks [88]. Shock compaction has been shown to create plastic deformation in a range of ceramic powders [89]. Figure 29 shows the residual lattice strain, as measured from size-strain analysis of XRD patterns of shock compacted ceramic powders. It can be seen that not only ceramic oxides, but also nitrides, carbides, and borides, have been shown to exhibit residual lattice strain due to plasticity associated with the formation of dislocations. Certain materials, such as alumina (Al_2O_3), begin to show residual lattice strain at relatively low pressure ($\sim$ 1 GPa); however, titanium carbide (TiC) and titanium diboride (TiB_2) have a high critical pressure (12 GPa) in order to initiate plastic deformation [89].

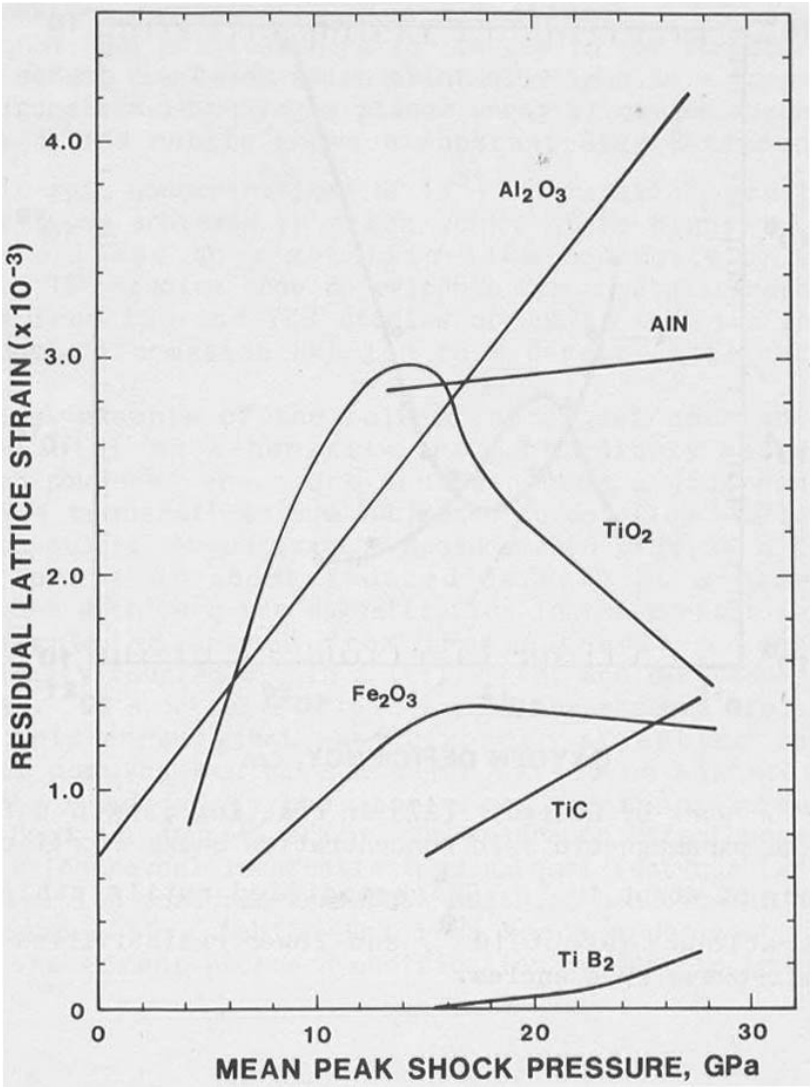

Figure 29: Plot of lattice strain verses shock pressure for a range of shock compacted ceramic powders. [89]

The previous section described how the Fischmeister-Artz model can be used to estimate the crush strength of a porous material; however, a powder compact which has been shock loaded up to its crush strength may not necessarily have bulk strength due to lack of interparticle bonding. Bonding between particles is driven by localized deposition of shock energy at the particle surface [90]. The shock energy is assumed to be preferentially deposited at particle surfaces during the rise time of the shock wave [91]. For porous materials that are shocked to near the solid density, the shock width will be approximately equal to average particle diameter, D. Therefore, the rise time is given by $\tau \sim D/U_s$.

For shock compaction of metal powders, extensive plastic deformation occurs at interparticle surfaces, creating localized heating. This may lead to melting and strong interparticle bonding. Figure 30(a) shows an optical micrograph of shock consolidated Inconel powder [92]. The micrograph also shows shrinkage voids (D) which can form after resolidification of melted regions and parachute shaped grains (A) that form through plastic deformation.

Shock compaction of ceramic materials is dependent upon both plastic deformation and fracture [90]. Particle fracture helps to create clean surfaces that aide in solid state bonding [93]. The micrograph in Figure 30(b) shows an example of shock compacted silicon carbide with extensive particle fracture [92]. For materials with fracture as the dominant deformation mechanism, a significant amount of particle size reduction is expected [90]. Samples with significant amount of plastic deformation will see an increase in residual lattice strain, while those undergoing fracture will reveal crystallite size reduction.

The deformation mechanism (plastic or fracture) has been shown to be dependent upon pressure and initial particle size for some low plasticity materials. Figure 31 shows the results of shock compaction experiments performed on differing grades of

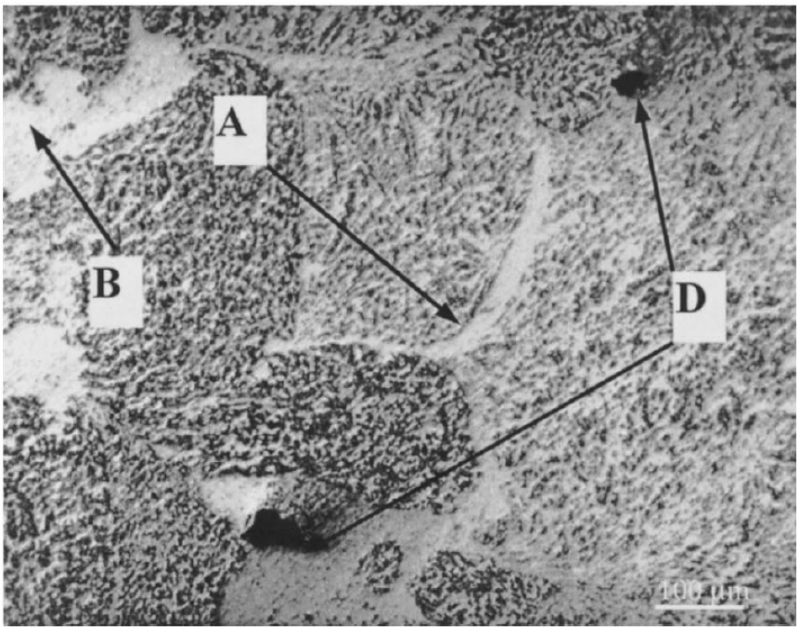

(a) Optical micrograph of shock compacted Inconel powder

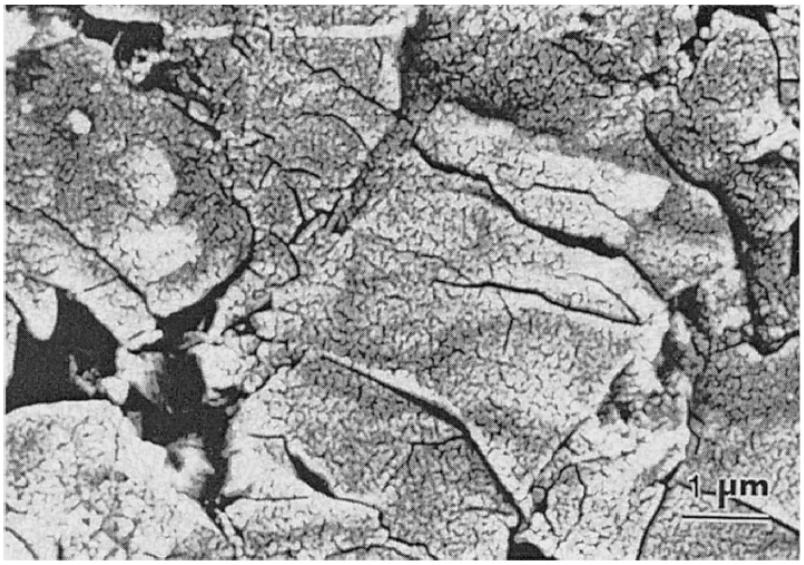

(b) Micrograph of shock compacted silicon carbide

Figure 30: Micrographs showing microstructural features typical for shock compacted metal powders (a) and ceramic powders (b). Bonding between metal particles occurs mainly by melting at the particle surface, marked by "B". Also marked are shrinkage voids "D" and parachute shaped grains "A" which form from plastic deformation of the original grains. Bonding between ceramic particles is aided by particle fracture, as shown in the micrograph in part (b). [92]

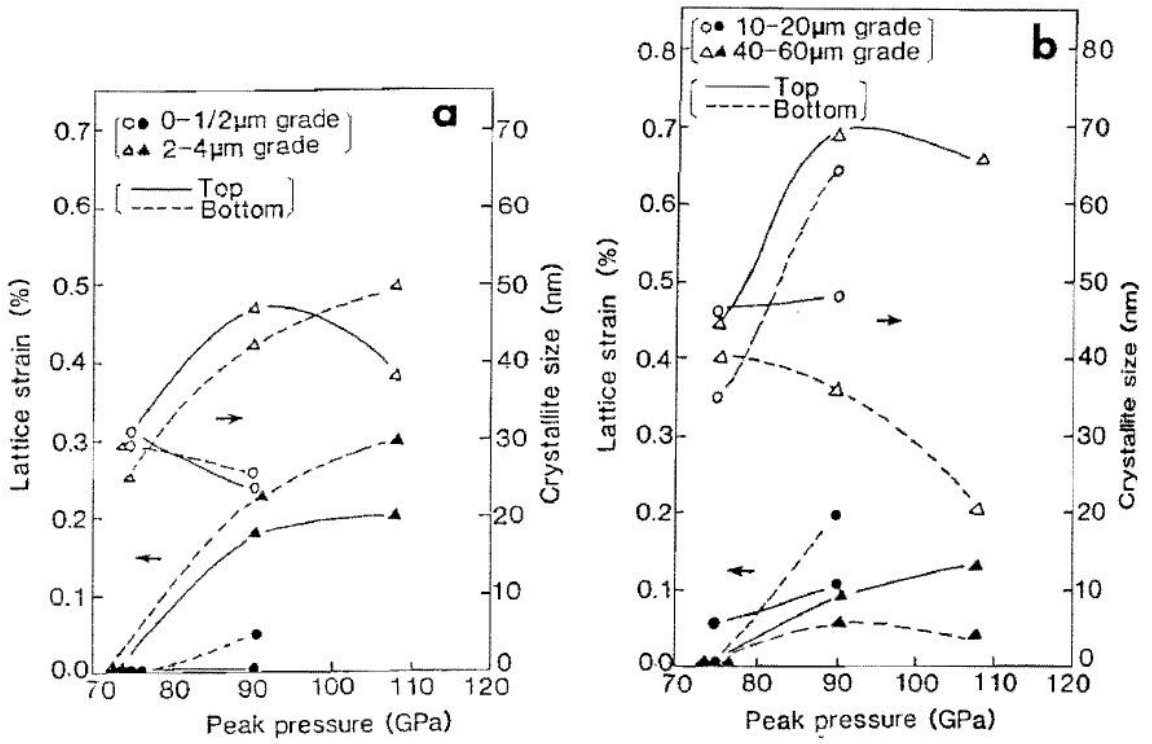

Figure 31: Plot of lattice strain and crystallite size versus peak shock pressure for different grades of diamond particles. Crystallite size plots are marked with open symbols and lattice strain is marked with filled symbols. [90]

diamond powder [90]. The graphs show the relationship of lattice strain or crystallite size with peak shock pressure. In most diamond samples, increasing the shock pressure increases both the lattice strain and the crystallite size. This means the deformation mechanism shifts from fracture to lattice strain as pressure increases. At lower pressures (peak pressure < 80 GPa), there is little difference between the behavior of large and small diamond particles. The recovered samples had very little lattice strain and had crystallite sizes in the range of 25-45 nm for all initial particle sizes. As pressure increases, certain grades (2-4 μm and 10-20μm) have increased lattice strain and crystallite size, while the largest (20-40 μm) and smallest (0-0.5 μm) grades show relatively little increase in lattice strain. In all cases, increases in the amount of lattice strain correlate with increases in grain size. This indicates that fracture and plastic deformation are competing mechanisms.

2.3.4 Mechanisms of Phase Transformations in Shock Compacted Materials

Phase transformations in shock compacted materials can take place by a variety of different mechanisms. Allotropic phase transformations are often driven by a shift to a higher density phase under high pressure, such as the formation of diamond from graphite [94, 95] or the BCC to HCP (α to ϵ) transition in iron [96]. Tensile waves can create an phase transition to a lower density phase, as in the case of martensitic transformations iron [97, 98].

Two types of reactions have been identified in shock compacted materials, shock assisted and shock induced reactions [99]. Shock induced creations occur while the materials is in the shock compressed state, while shock assisted reactions occur after unloading and are thermally activated by the heat generated from mechanical compression and deformation. While allotropic phase transformations serve as one example of shock induced reactions, decomposition reactions [100] and reactions forming intermetallic compounds [101] and have also been classified as shock induced reactions. As noted in §2.3.1, shock induced reactions may appear as a shoulder (transition point) in a VISAR trace, since they occur while in shock compressed state.

Chemical reactions can be added by the deformation associated with shock compaction. Dremin and Breusov [102] developed the ROLLER model, in which mixing and alloying of occurs as particles slide past each other, to describe reactions in shock compacted mixtures of metal particles. Nucleation of the new phase occurs at the particle interfaces and mass transport is accomplished by plastic flow around the nucleation sites. Batsanov [103, 104] has theorized that crystalline to amorphous transitions in shock compressed materials such as SiO_2 occur when the grain size has been reduced to such an extent that the surface energy exceeds the heat of melting.

Shock assisted reactions, occurring after the passage of the shock wave, are generally driven by the temperature rise associated with shock compaction; however,

the deformation produced during shock compaction can alter the reactivity of the material. In shock compacted nickel-aluminum mixtures, the generation of addition defects, such as vacancies and grain boundaries, increases the available paths for mass transport, creating a shock-modified material with defect enhanced solid state diffusion [101, 99]. Certain materials, such as Nd_2O_3 and Sm_2F_3, form a lower density material during shock compaction [105]. These transformations are thought to undergo a crystalline to amorphous transition while under high pressure, followed by crystallization of the lower density phase after unloading of the shock wave due to thermal effects.

2.4 Shock Compaction of Magnetic Powders

There have been few published reports of shock compaction studies performed on permanent magnetic materials. The following discussion provides a thorough review of the literature available at the time of this writing. Unless otherwise noted, the studies in each subsection are presented in chronological order for each magnetic material investigated.

2.4.1 Shock Compaction of Nd-Fe-B

An early study on shock compaction of Nd-Fe-B melt-spun powder attempted to perform shock equation of state measurements and recovery experiments [106]. An unusual method of measuring the shock speed through the powder was used. The authors used a piston setup to produce the compaction and measured the shock arrival time through the wall of the die. No explanation was given as to how the impact event produced a lateral shock wave through the die wall. As a result, the Hugoniot data shows a large scatter in the data, including non-overlapping shock speed measurements for the same shock pressure.

Recovery experiments were performed over a range of low shock pressures, which were calculated from the unusual Hugoniot measurements. Figure 32 shows the etched

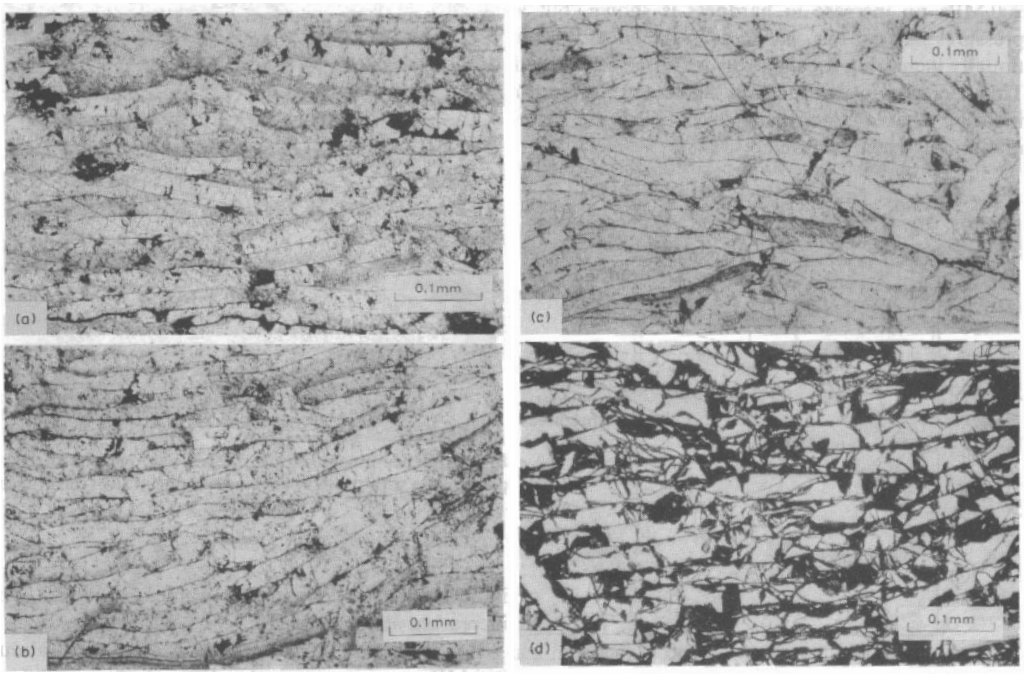

Figure 32: Optical micrographs of etched Nd-Fe-B recovered compacts subjected to primary shock pressures of (a) 850 (b) 1100 and (c) 2050 MPa. A micrograph of a compact loaded quasi-statically at 850 MPa is shown in part (d) for comparison. [106]

micrograph of compacts with primary shock loading pressures of 850, 1100, and 2050 MPa. Additionally, a compact loaded under 850 MPa of quasi-static pressure is shown for comparison. Micrographs of the three shock loaded samples show lower porosity and less fracture as compared with the quasi-statically loaded compact. The authors [106] assert that plastic flow can be observed in the shock loaded particles. Hardness tests of shock compacted powder showed no significant change from the uncompacted hardness of 900 HV up to a shock pressure of 2050 MPa. The authors attribute the increase in hardness to the onset of plastic deformation in the material.

A compaction study of ball milled Nd-Fe-B was performed in the higher pressure range or 5-20 GPa by Chandramouli et al. [107]. Powders composed of Nd-Fe-B and Nd-Fe-B mixed with 10% aluminum were pressed into capsules to an approximate density of 60% theoretical maximum density (TMD). After compaction, the unmixed

Nd-Fe-B powder compacts reached ∼70% TMD. In addition, it was found that samples compacted at higher pressure, around 20 GPa, had formed α-iron as the main crystalline phase. The authors attributed this change to partial melting of the powder during the shock compression process. The addition of aluminum powder improved the compaction behavior such that 85% TMD compacts were produced.

Guruswamy et al. [108] performed a series of explosive compaction experiments on Magnaquench Powders MQP-A and MQP-B, similar to the powders discussed in §2.2.3. Both powders were compacted using an initial shock pressure of 6 GPa. The resulting compacts were approximately 95% dense and had energy products, 11-14 MGOe, superior to bonded magnets made from the same powder and equivalent to hot pressed magnets. The powders were initially isotropic and showed no significant anisotropy after shock loading.

Ando et al. [109] studied explosive compaction of amorphous Nd-Fe-B powder of composition $Nd_{13}Fe_{77}Co_5B_5$. While the initial density was not reported, the shock consolidated compacts achieved 97% TMD. The high density was achieved in part through reduction of reflected shock waves by the use of momentum traps. The detonation velocity of the explosive used was aproxiamtely 7 km/s, but the shock pressure in the compact was not reported. Additionally, no results were reported to show evidence of the amorphous structure of either the original powder or the shocked compacts. Melted regions were observed in SEM micrographs and the authors assume that these regions crystallize into the 2-14-1 phase. A slight increase in remanence, from 8.0 to 8.5 kG, was reported for the shock conslidated compacts as compared to the powder. Although not mentioned by the authors, this increase may be attributed to the crystallization of the material in the melted regions.

An explosive compaction study was performed by Liu et al. [110] on nanocrystalline Magnaquench powder MQLP-B. The powder was pressed to 67% TMD and the detonation velocity of the explosive used was 6.5 km/s, corresponding to a maximum

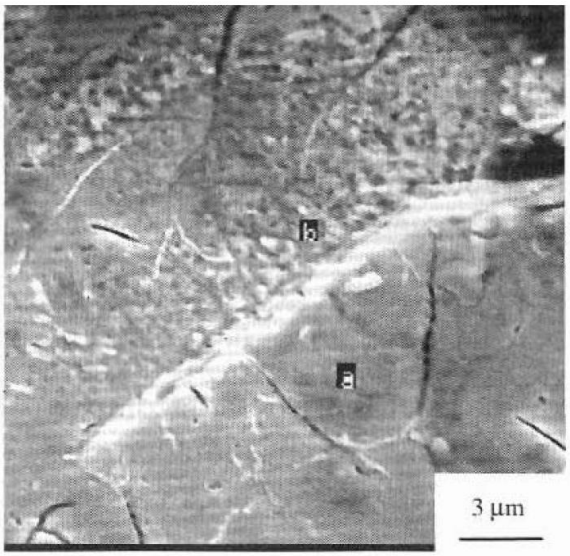

Figure 33: SEM micrograph of the melt regions in explosive compacted Nd-Fe-B melt-spun powder. [110]

pressure of 13 GPa. No momentum traps were used, and a compact density of around 88% TMD was produced. No significant grain growth was observed, however, large melted regions were formed between particles. Figure 33 shows the microstructure of the melted regions, called an "alveolate" microstructure by the authors.

Lin et al. [111] studied shock compaction of melt-spun Nd-Fe-B powders with Al, Si, and Zr alloying elements. Compacts of composition $Nd_{13}Fe_{80}B_6Zr_1$ produced significantly larger coercivity and energy products, as compared to those mixed with silicon and aluminum; however, comparing these results to other studies is difficult since the authors report unrealistic data, such as an intrinsic coercivity of 20T.

Kawano et al. reported an underwater shock compaction study of Nd-Fe-B, but provided few details of the material and its properties [112].

2.4.2 Shock Compaction of Hard-Soft Magnetic Nanocomposites

A study by Leonowicz et al. [113, 114] compared shock compacted Pr-Fe-B samples with high and low Pr content. The precursor powder materials were pressed into copper capsules for explosive compaction at 4.4 GPa. The compact densities for the

Pr-Fe-B samples were not reported other than to say that that the Pr-lean compacts were more porous than the Pr-rich samples. The average grain size of the shock compacted samples, 50 nm, was similar to that of the starting powder, although some grains over 100 nm were found. The Pr-lean shock compacted samples had a higher remanence, 0.96 T versus 0.91 T or less, but much lower coercivity, 200 kA/m versus 600 kA/m or higher, as compared to Pr-rich samples. In the same reports, the authors also studied Sm-Fe-N nitride samples; however, XRD scans showed large amounts of SmN and α-Fe in the starting powder, and the resulting magnetic properties were poor.

A study by Saito et al. [115] investigated shock compaction of amorphous $Nd_4Fe_{77.5}B_{18.5}$ melt-spun ribbons. A shock pressure of 21 GPa was generated using plate impact experiments, yielding shock compacts of 85% density. The amorphous phase was retained in the shock consolidated compacts. Subsequent annealing between 500^0C and 650^0C was performed, and the XRD traces of the annealed compacts are shown in Figure 34. The XRD pattern of the sample annealed at 500^oC is very similar to the pattern of the as compacted material (not shown). Annealing at temperatures of 550 to 650^oC crystallized the material, producing $Nd_2Fe_{14}B$ and Fe_3B phases. For the 700^oC and 800^oC temperature heat treatments, α-Fe became the dominant phase, with small amounts of the $Nd_2Fe_{14}B$, Fe_3B, and Fe_2B phases present. The maximum coercivity, 2.7 kOe, corresponded to the 600^oC sample, which had a larger relative amount of the $Nd_2Fe_{14}B$ phase as compared to the samples annealed at 700 and 800^oC.

A series of studies by Jin et al. [15, 116, 16, 117, 118] have characterized the shock compaction response and magnetic properties of melt-spun nanocomposite powders of composition 80% $Pr_2Fe_{14}B$ and 20%-Fe. The authors [15] estimated the $U_s - U_p$ EOS for this material by mass averaging to be $U_s = 4.056km/s + 1.446 * U_p$. Fully density compacts were created by parallel plate impact experiments at 880 m/s. Magnetic

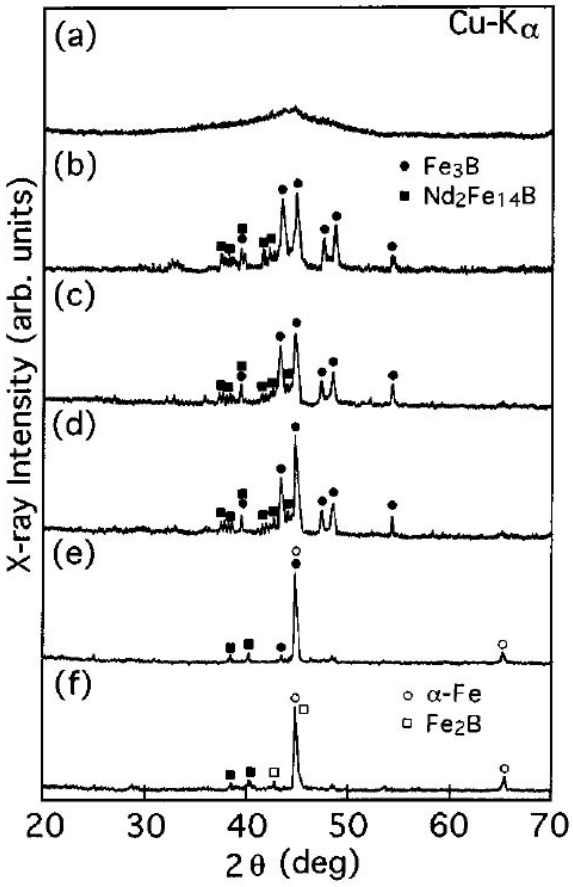

Figure 34: XRD traces of amorphous melt-spun ribbons of composition $Nd_4Fe_{77.5}B_{18.5}$ following shock compaction and annealing. The samples were annealed for 30 minutes at temperatures of a) 500^oC, b) 550^oC, c) 600^oC, d) 650^oC, e) 700^oC, and f) 800^oC.

characterization showed an energy product similar to those produced by Guruswamy et al. [108] for single phase powders, 11-14 MGOe. Varying initial packing density, from 64% to 78%, resulted in only small changes in compact density and coercivity, despite having different pressure-volume compressiblity behavior.

TEM micrographs showed that deformation in the shocked compressed compacts is localized into shear bands, as shown in Figure 35. The micrograph in part (a) shows the shear band passing through several Pr-Fe-B grains. The dark areas are α-Fe grains, as shown by the dark field image in the inset. The micrograph in part (b) shows the presence of an amorphous phase and small α-Fe crystallites in the shear band.

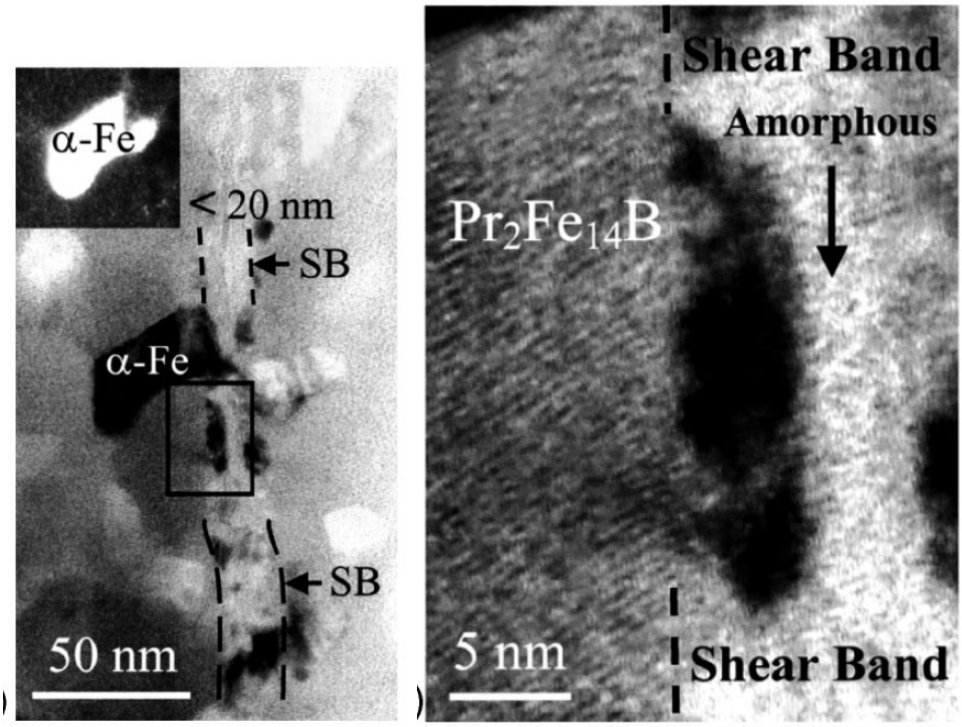

(a) (b)

Figure 35: TEM micrographs of a shear band in shock compacted Pr-Fe-B/α-Fe composite. The lower magnification image in part (a) shows the shear band passing through several Pr-Fe-B grains. The inset is a darkfield image, identifying the dark areas in the brightfield images as α-Fe grains. The higher magnification image in part (b) shows the presence of an amorphous phase in the shear band. [116]

The grain size distribution determined from TEM has shifted to a smaller average grain size relative to the starting materials [16]. The authors attributed this effect to shear bands that cleave the grains into smaller grains. Williamson-Hall analysis of the original powder and shock compacted samples showed that shock compaction also increases the microstrain [15]. This is at odds with TEM observations, which showed no evidence of the presence of dislocations or defects in areas not near a shear band [116].

Post shock compaction annealing performed at 600 ^{o}C, 700 ^{o}C and 800 ^{0}C for 20 minutes resulted in the grain size distribution increasing to near the original size. The saturation magnetization increased when annealed at 600^{0}C, which is attributed to crystallization of the amorphous phase created during the shock event. Annealing

also resulted in an increase in remanence as compared to the original material, which is thought to be due to the refinement in grain size from increased exchange coupling. Annealing at 800^0C decreases remanence, which is thought to be caused by the presence of larger soft grains that are not properly exchange coupled. TEM micrographs showed that grains of up to 50 nm were present in samples annealed at 800 ^{o}C, but not in the original powder. Correspondingly, the hysteresis loop for 800^0C annealed samples showed a small kink. Likewise, the decrease in coercivity is also attributed to increasing grain size.

Similar results were obtained by the authors when extending this work to explosive compaction [117] and underwater shock consolidation [118] on the same powders.

2.4.3 Shock Compaction of SmCo5

Chau et al. [119] performed shock compaction of ball milled $SmCo_5$ powders. A simple compaction set up was used with no momentum traps. The authors attempted to align several of their samples in a 1T static field prior to uniaxial pressing at 8000 psi. Aligned samples had a green density of approximately 50%, while unaligned samples were preloaded to around 62% TMD. Shock pressures of 2-27 GPa were used to compact samples to densities from 50% to 85%. While squareness values, $\frac{B_r}{4\pi M_s}$, for aligned samples were as high as 0.95, the highest anisotropy values, $\frac{B_{rx}}{B_{rz}}$, reported were only 1.4. Several unaligned samples had squareness values well over the 0.5 mark. While not discussed by the authors, the high squareness values reported may be due in part to exchange coupling, instead of grain alignment. The authors show the post milling particle size, but do not discuss the grain size.

2.4.4 Shock Compaction of Sm-Fe-N

Hu et al. [120] performed one of the first investigations using shock compaction to produce bulk $Sm_2Fe_{17}N_3$ magnets. The $Sm_2Fe_{17}N_3$ powder was ball milled and aligned in a 1.5T field prior to explosive compaction. The density of the recovered

compacts were in the 78-89% range of TMD. The microstructure of the starting powder is not shown; however, the microstructure of the recovered compacts shows two distinct regions with differing grain size. Figure 36 a) shows a TEM micrograph of a large defect free grain. The corresponding diffraction pattern, shown in Figure 36 b) matched the $Sm_2Fe_{17}N_3$ phase, while other areas had small, 0.1 μm, grains. The TEM diffraction pattern for the small grain areas match α-Fe and other phases.

Figure 37 shows the hysteresis loops for the shock compacted samples and the as-milled powder. Hu et al. [120] note that the shock compacted sample shows an increased squareness relative to the ball milled powder; however, the squareness, usually defined as M_r/M_s, can not be determined from this portion of the hysteresis loop. Thus, the degree of alignment for the starting powder or the recovered compact can not be determined either. It is possible that ball-milling the Sm-Fe-N powder creates polycrystalline particles that will not be suitable for alignment by magnetic field.

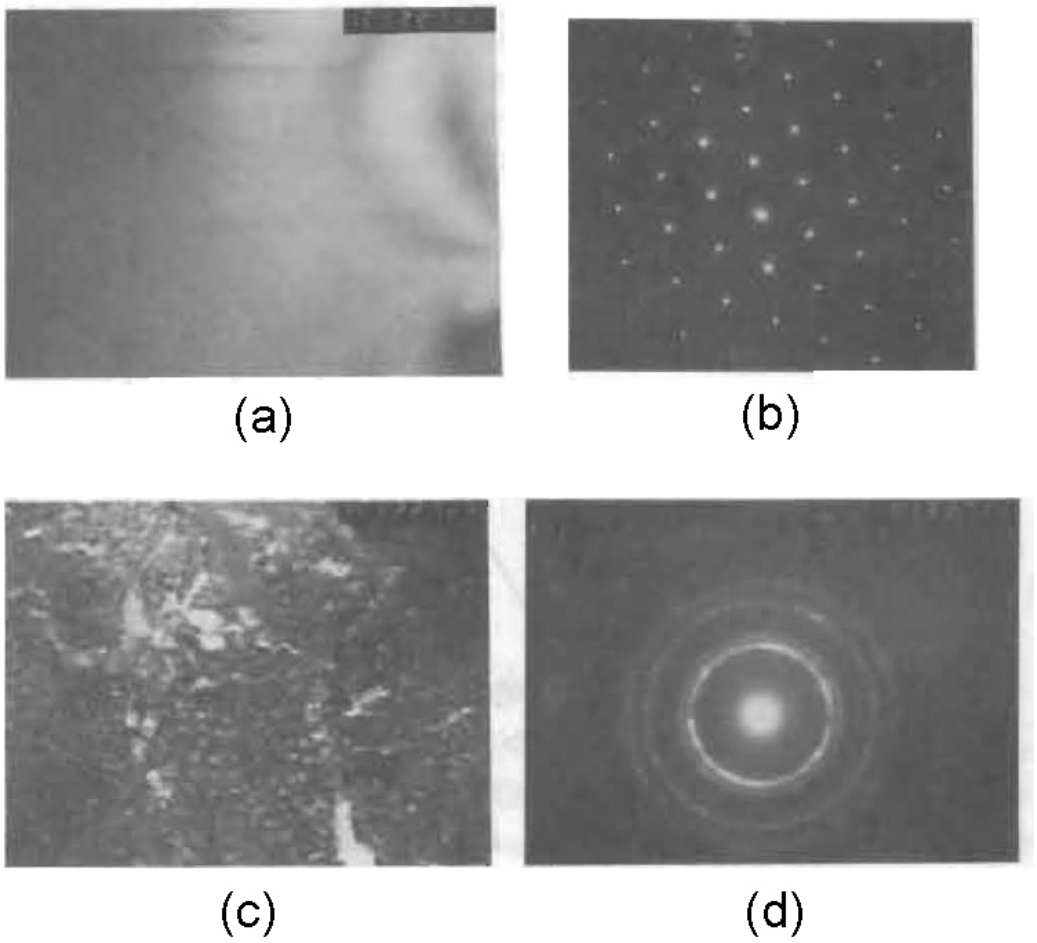

Figure 36: TEM micrographs and diffraction patterns of shock consolidated Sm-Fe-N powder. (a) a large defect free grain (b) diffraction pattern of defect free grain which matches the expected pattern of $Sm_2Fe_{17}N_3$ (c) microstructural region with small grains, approximately 0.1 μm (d) diffraction pattern for small grain area which matches α-Fe and other, unidentified phases. The magnification for the images, (a) and (c), is 10^5. Lλ=3.071 cmÅfor the diffraction patterns, (b) and (d). [120]

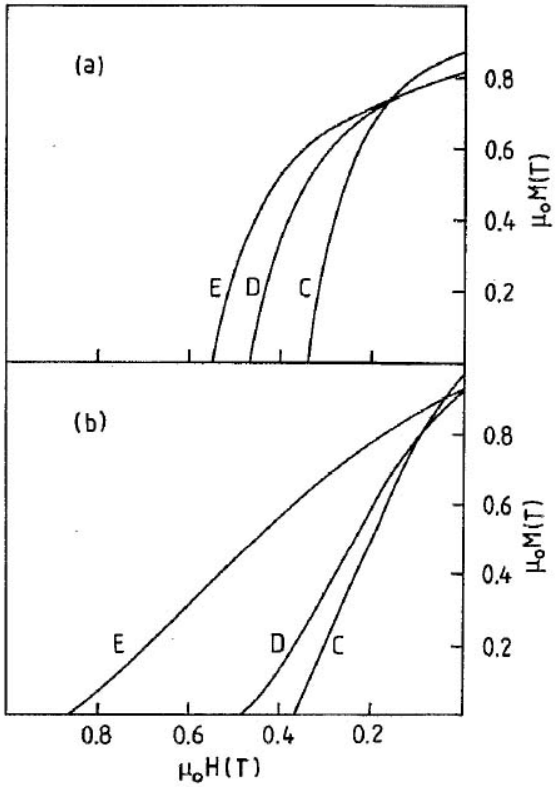

Figure 37: Demagnetization curves for (a) shock compacted $Sm_2Fe_{17}N_3$ and (b) the as-milled powder for three sizes of milled powder, (C) 5 μm (D) 3 μm and (E) 1 μm. [120]

Oda et al. [121] performed a series of shock compaction experiments on Sm-Fe-N using a propellant gun and shock fixtures with momentum traps. The samples were pre-pressed under a 0.55T static magnetic field to a green density of approximately 70% TMD. The compacts were heated to 300^oC for 20 minutes and then sealed in an evacuated capsule. Shock pressures from 20 to 34 GPa were used, and highest compact density, 97%, was achieved at 28 GPa. XRD of the recovered compact showed a large amount of peak broadening as compared to the starting powder. In addition, amorphous regions were detected via TEM imaging.

Mashimo et al. [122, 123, 124] performed a series of shock compaction experiments on Sm-Fe-N . The first study [122] tested various methods of synthesizing the $Sm_2Fe_{17}N_3$ phase, resulting in a range of nitrogen content. Pellets were pressed under a static field of 12 kOe and axial and isostatic pressure, yielding green compacts in the 46% to 52% range. The authors used the porous iron Hugoniot as an approximation for the Hugionot of $Sm_2Fe_{17}N_3$, and calculated a shock pressure of 10-30 GPa in the capsules containing the samples. Shocked compact density was somewhat independent of shock pressure in the region tested; however, samples with higher nitrogen content tended to have lower compact densities. XRD patterns showed that the relative intensity of the α-Fe peak increased for shock pressures above 15 GPa. At 30 GPa, the compact had completely decomposed into SmN and α-Fe. The effects of aligning the pellets in a magnetic field were not discussed in this report.

A subsequent attempt [123] used a similar pressing technique under magnet fields followed by a hydrostatic pressing to a higher initial packing density of 61% to 64% TMD. This produced less decomposition, but a lower remanence was also present, which the authors attributed to scattering of the alignment by the shock wave. Additionally, the compaction capsules were constructed in a way that allowed the shock experiments to be performed in a vacuum. No clear trend was shown between the ambient and vacuum experiments.

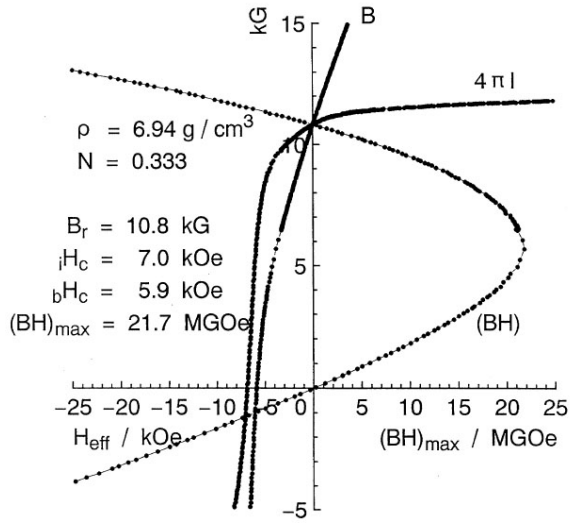

Figure 38: Hysteresis loop of shock compacted Sm-Fe-N samples. [124]

A further study used both a propellant gun and explosive compaction and tested higher initial packing densities [124]. The highest density compact, 7.47 g/cm^3 (97% TMD), was achieved for an impact velocity of 1240 m/s using a 2024-aluminum impactor. Coercivity decreased with increasing impact speed, while volume fraction of α-Fe increased, as shown by the relative intensity of XRD peaks. The highest energy product, 22 MGOe, corresponded to the highest remanence, 11.4 kG, even though other samples had higher coercivity and density. Figure 38 shows the hysteresis loop for one of the high energy product samples. Explosively compacted samples had lower densities and severe cracking in the center. These samples had significantly worse magnetic properties.

Chiba et al. [125, 126] performed explosive compaction experiments on Sm-Fe-N powders. The powders were packed into compaction fixtures at tap densities. Certain samples were oriented in a 5T field normal to the shock propagation direction before detonation using an explosive with a detonation velocity of 2.4 km/s. The XRD pattern for the as-compacted samples were consistent with the starting powder. The compact density was not reported other than to say that it was fully dense. The aligned samples had an energy product of 24 MGOe. Annealing above

200^{o}C decreased the energy product. Non-aligned samples had an energy product approximately 1/4 of the aligned samples. The energy product was the only reported magnetic property

A further report by Chiba et al. [126] examined both Sm-Fe-N and Sm-Fe-N mixed with Ni and Co powders. The authors note that the Ni and Co powders, 40μm or less in diameter, were intended to aide in consolidation, instead of providing an exchange-coupled phase. An explosive with detonation speed of 2.4 km/s was used again, and all samples were over 95% dense. Addition of the metallic powders lowered the energy product achieved from 24 MGOe to 16-17 MGOe. No other magnetic properties were reported.

A third study by this group examined Sm-Fe-N powders coated with an iron-oxide layer [127]. The 3μm diameter particles, once coated, were approximately 15% ferrite. A 1.5T field was used to align the powder, instead of the 5T as in previous reports. The compaction pressure and explosive detonation speed were not reported, but the samples were between 92-94% dense. The energy product of these samples were roughly equivalent to the unaligned samples previously reported, approximately 6 MGOe.

2.4.5 State of the Art of Shock Compaction of Magnetic Materials

Shock compaction has been shown to be a useful technique for consolidating several different magnetic materials to high density. Shock compaction has been applied to Nd-Fe-B [107, 108], $SmCo_5$ [119], and Sm-Fe-N [120, 128]; however, there are relatively few studies of magnetically soft phases. Outside of elemental iron or nickel, studies of high magnetization phases, such as $Fe_{16}N$ or Fe_4N, have been not been performed. For the case of Nd-Fe-B, the magnetic properties of shock compacted materials have been shown to be equivalent to isotropic magnets fabricated by hot pressing [108].

Shock compaction has also been used to consolidate melt-spun composites of Pr-Fe-B / α-Fe, and the magnetic properties of these compacts are also equivalent to the properties of traditional, rare earth rich isotropic magnets [15]. However, there have been no attempts to make exchange-coupled composites of Sm-Fe-N, whose high anisotropy would make it an ideal candidate for use as the hard magnetic phase. In addition, there have been no attempts to make an anisotropic Nd-Fe-B magnetic material through shock compaction.

Several studies of Sm-Fe-N have made an attempt to align the magnetic particles prior to shock compaction [120, 121, 128, 125]; however, none of these report the degree of alignment prior to shock compaction. As discussed in §2.2.2, relatively high field strengths are required to achieve a well aligned green compact, and pulsed fields create a better alignment than static fields for the same field strength. Most studies reported using static magnetic fields of 1.5T or less. It is also important to note that polycrystalline powders will produce less texture from magnetic field alignment. Therefore, in many studies it is unclear what degree of alignment is achieved prior to shock compaction. This severely complicates any evaluation of how the shock compaction process affects the alignment.

Mashimo et al. [123] notes in one study that the shock consolidated samples had a lower remanence than the starting materials and suggested that this effect is due to the shock wave disturbing the alignment. Without knowing the degree of alignment present in the starting materials, it is difficult to know to what extent shock compaction alters the alignment. Regardless, the compaction process will most likely alter the texture of the green compacts in some way, but the degree to which any alignment is changed will depend on the mechanism of deformation. Diffusional processes, such as sintering and die-upsetting, can potentially increase the texture of magnetic materials, whereas mechanical deformation processes such as plastic slip, twinning, and shear banding will most likely decrease the texture if the degree of

initial alignment is large. There has been very little attention paid to the types of deformation mechanisms that occur in these magnetic materials during shock compaction. Hard magnetic materials such as Nd-Fe-B and Sm-Fe-N are very brittle, and thus may have limited plastic slip during shock compaction. Only the studies performed by Jin et al. [15] and Li et al. [116] examined the mechanism of deformation, however, the results were conflicting, with Williamson-Hall analysis suggesting significant microstrain [15] and TEM micrographs showing evidence of shear banding but no indications of dislocations [116].

As the study of shock compaction of magnetic materials progresses, more emphasis needs to be placed on studying the structure of both the green compacts and the shock consolidated compacts. Many shock compaction studies focus on the magnetic properties of the recovered compact. While this is an important aspect, a lack of texture or decomposition of the magnetic phase is the main factor limiting the energy product in many cases. In order to understand how shock compaction affects a material, it is necessary to well characterize the pre-shock compacted material and to understand the process of deformation. This will aide in evaluating the development of texture, by defining the initial amount of texture, and in studying decomposition, by determining the purity of the starting materials. Additionally, more study is needed on the effects of shock compaction on soft magnetic phases such as $Fe_{16}N_2$.

CHAPTER III

PROCEDURE

This chapter will outline the material systems studied in this work and describe the techniques used. The materials section will describe the characteristics of the various magnetic powders in their as-received form, followed by an accounting of the methods used to characterize the materials. A brief description of powder pretreatment techniques used prior to shock compaction is provided. The impact experiments section discusses shock compaction, high strain forging, and time-resolved measurement experiments used to examine the compaction behavior, mechanical texture development, and the equation of state of the magnetic materials. The final section describes the approach for modeling shock compaction experiments, including calculations of important state variables.

3.1 Magnetic Materials Systems Investigated

A range of magnetic material systems were studied, listed in Table 4, in order to determine which systems are suited for use in processing through shock compaction. Soft magnetic materials based on α-Fe, γ'-Fe_4N, and α''-Fe_16N_2 and hard magnetic materials based on $Nd_2Fe_{14}B$ and $Sm_2Fe_{17}N_3$ were investigated. Composite materials including Sm-Fe-N/Fe_4N, Sm-Fe-N/$Fe_{16}N_2$, and Nd-Fe-B/α-Fe were formed by mechanical alloying or simple mixing of two kinds of magnetic particles. Pr-Fe-B/α-Fe composite materials, provided by Magnaquench, Inc., were fabricated from melt-spun ribbons. This section will describe the materials in their as-received form, while §3.3 will discuss methods for powder pretreatment and producing composites.

Table 4: Summary of material systems investigated

Hard	Soft	Composite
Sm-Fe-N	Fe_4N	Sm-Fe-N/Fe_4N
Nd-Fe-B	$Fe_{16}N_2$	Sm-Fe-N/$Fe_{16}N_2$
	α-Fe	Nd-Fe-B/α-Fe
		Pr-Fe-B/α-Fe

3.1.1 Fe_4N

γ'-Fe_4N powder, supplied by AMC, was synthesized from freshly prepared iron oxyhydroxide, Fe(OOH). A few grams of Fe(OOH) were loaded into a fluidized bed reactor and reduced to fine crystallites of *bcc* iron by heating the sample at 440 ^{o}C under flowing hydrogen. The temperature is then lowered to 350^{o}C and the sample is reacted with a flowing mixture of ammonia and nitrogen for several hours. The sample is then cooled to room temperature.

Figure 39(a) shows the morphology of the as-received powder. The average diameter of the typical particle is approximately 3 μm. The particles appear to be polycrystalline, as shown by the fractured particle with smaller subgrains of approximately 300 nm in diameter. Figure 39(b) shows the XRD trace for the as-received powder. All major peaks correspond to the γ'-Fe_4N peaks, and are indexed as shown in the Figure.

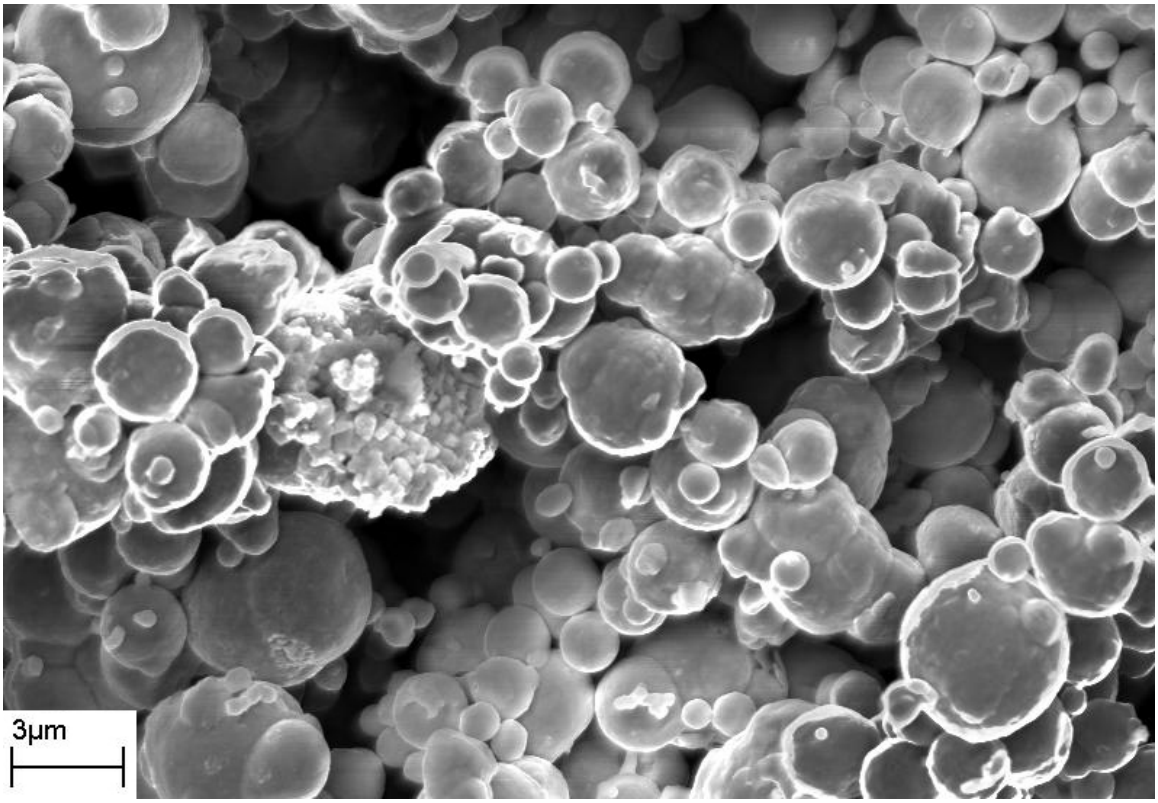

(a) SEM micrograph of the Fe_4N starting powder.

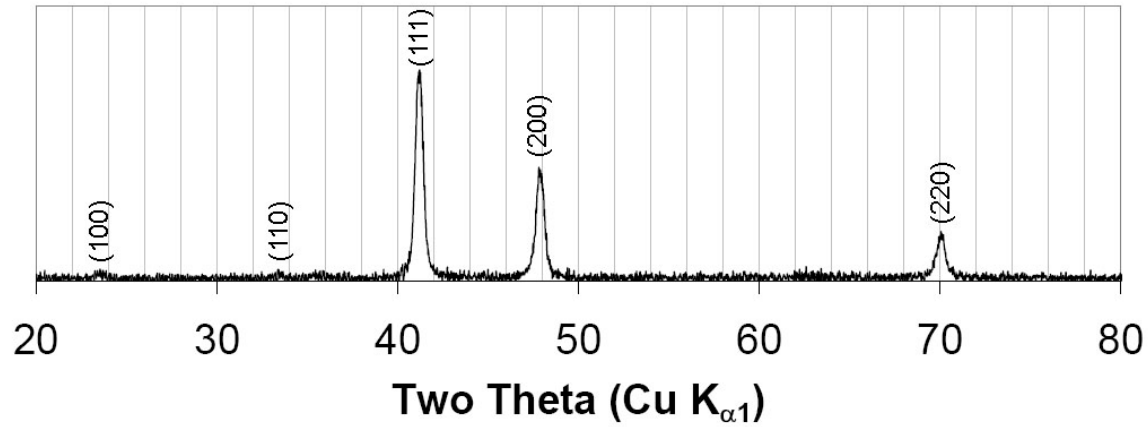

(b) XRD trace of the Fe_4N starting powder.

Figure 39: SEM micrograph (a) and XRD trace (b) of the Fe_4N starting powder as-received from AMC.

3.1.2 $Fe_{16}N_2$

α''-$Fe_{16}N_2$ particles were synthesized at Advanced Materials Corporation through a proprietary process. The starting material for this process is Fe(OOH) which is loaded into a fluidized bed reactor. It is reduced to fine crystallites of *bcc* iron by heating the sample at 440 ^{o}C under flowing hydrogen. The temperature is then reduced to a fixed value between 140 and 300 ^{o}C and then the sample is reacted with a flowing mixture of ammonia and nitrogen for several hours. The sample is cooled to room temperature, then the surface of the powder is passivated with a measured, small quantity of oxygen (air) after which the sample is removed from the reactor. Several reactions were performed to optimize the conditions for the synthesis of bulk single phase α''-$Fe_{16}N_2$.

Figure 40(a) shows an SEM micrograph of the as-received powder. The particles have a fairly uniform size distribution of 50-100 nm diameter. Figure 40(b) shows the XRD trace of the as-received powder. No impurity phases were detected with XRD, other than the presence of a small amount of α-Fe in some batches. On average, the batches contained $\sim$ 5% α-Fe, but ranged from 0-14%.

The α'-$Fe_{16}N_2$ phase has a similar structure to α''-$Fe_{16}N_2$, but with nitrogen occupying the octahedral sites in a disordered manner. Previous studies have differentiated the two phases by measuring the ratio of the $\alpha''(002)$ peak to the $\alpha''(004) + \alpha'(002)$ combined peak, with a ratio 0.125 corresponding to a perfect ordering [36, 37]. The XRD pattern for the starting powder shown in Fig. 40(b) has an integrated intensity ratio of 0.2. Even though this value is higher than the theoretical value for 100% α'', These peaks are much smaller in the XRD pattern of a powder sample than for the epitaxial films studied in other reports [36, 37], and so this ratio can be considered to coincide with the 100% α'' value to within expeirmental error.

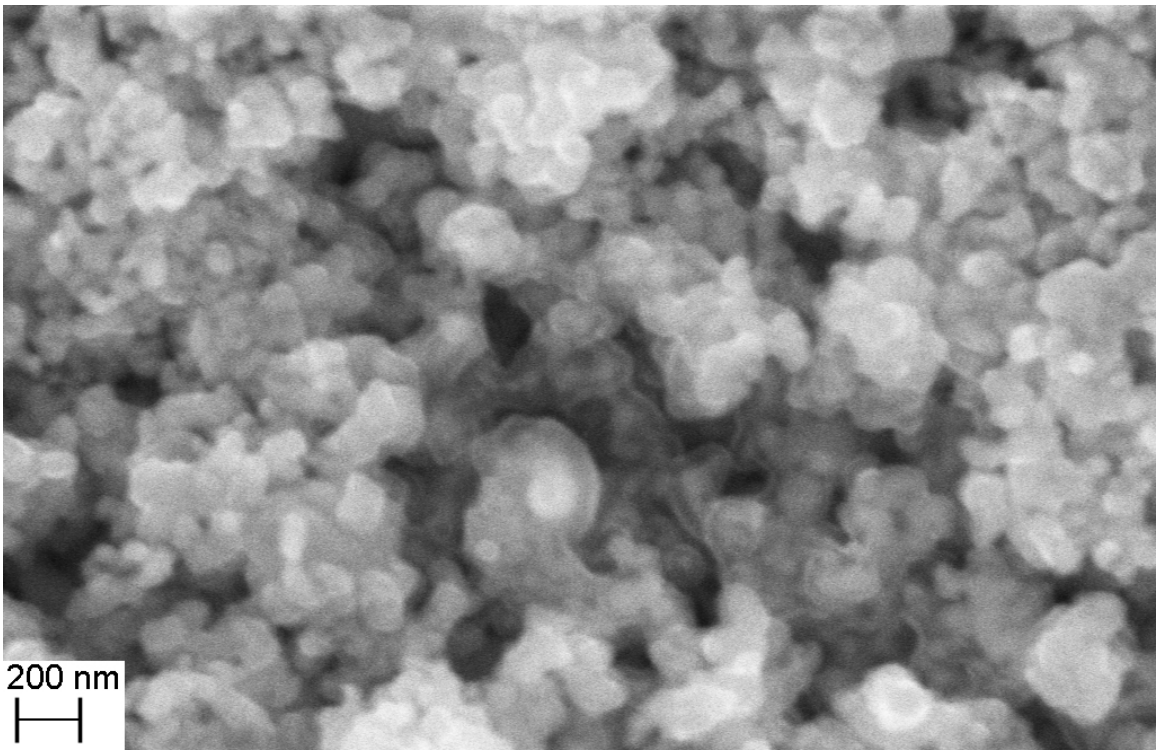

(a) SEM micrograph of the $Fe_{16}N_2$ starting powder.

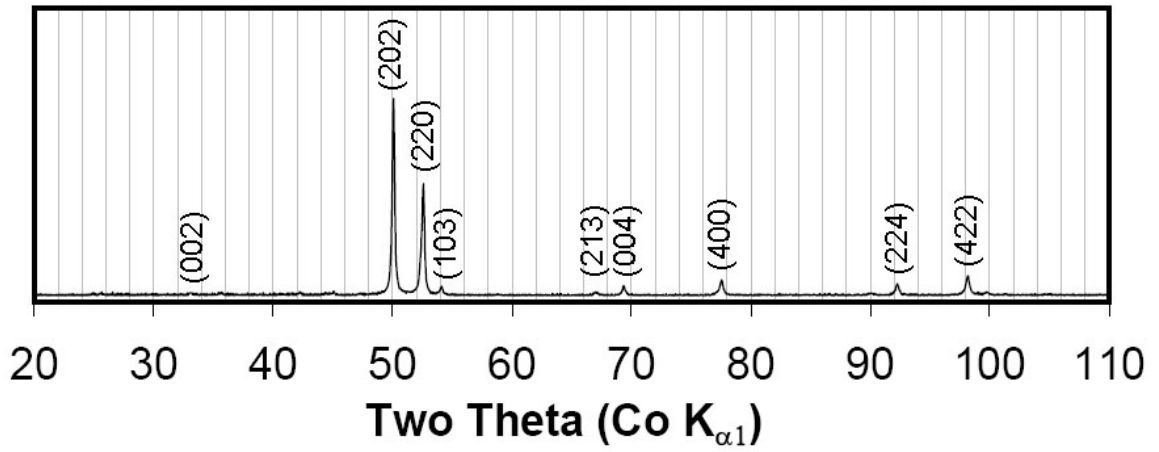

(b) XRD trace of the $Fe_{16}N_2$ starting powder.

Figure 40: SEM micrograph (a) and XRD trace (b) of the $Fe_{16}N_2$ starting powder as-received from AMC.

3.1.3 Sm-Fe-N

Sm-Fe-N powder was fabricated by Advanced Materials Corporation (AMC) through a process of casting a SmFe alloy, ball milling, annealing and nitrogenation. Three types of powders, labeled 677, 804, and 816, were received with differing microstructures. Figure 41 shows the as received morphology of powders 677 and 816. While

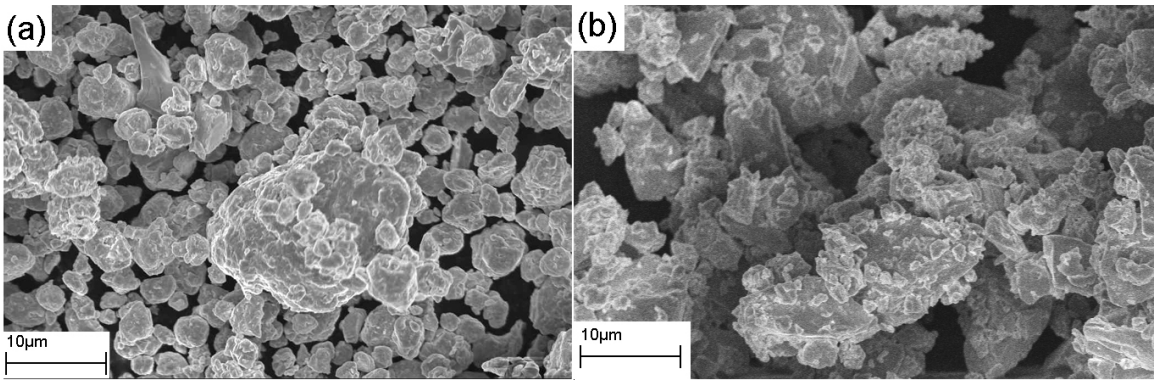

Figure 41: SEM micrographs of two batches of as-received Sm-Fe-N powder, 677 (a)) with spheroidal morphology and 816 (b) with a wider size distribution and angular morphology.

the average particle size of the two powders are similar, the 677 powder, shown in part (a), has a more uniform size distribution. Powder (a) also has a more spheroidal morphology than the 816 powder shown in part (b), which has sharper corners. The 804 powder has a similar particle morphology to the the 816 powder (Figure 41(b)).

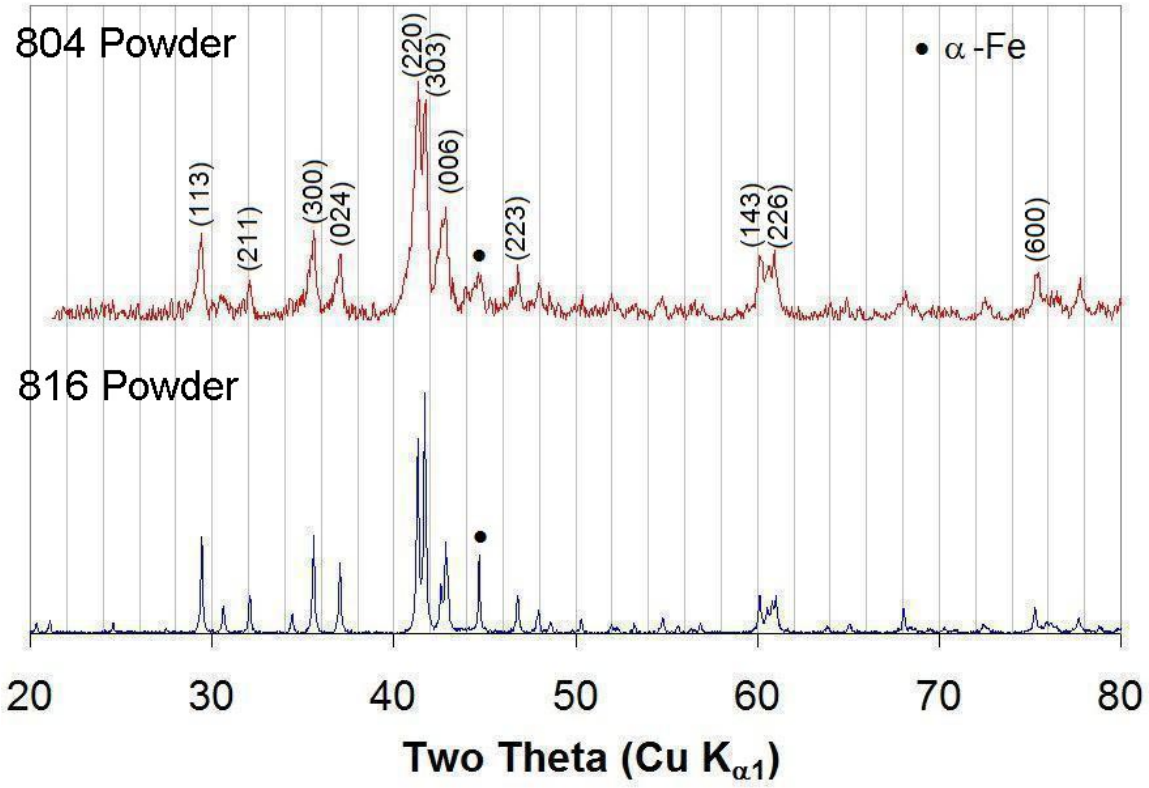

Figure 42: XRD traces for two batches of Sm-Fe-N powder as received from AMC and shock compacts 677, 804, and 816

Figure 42 shows the XRD traces for the 804 and 816 powders. Both Sm-Fe-N powders contained small amounts of α-Fe. The relative amount of α-Fe, estimated by comparing the relative integrated intensities of the 100% lines for the α-Fe phase and the Sm-Fe-N phase, is approximately 4% for both samples. The XRD pattern for the 677 powder is not avaiable. The XRD scans show that while the 804 and 816 powders have a similar particle morphology, they have different microstructures, since the XRD scan for the 804 shows considerably broader diffraction peaks as compared to the 816 powder. The influence of this characteristic will be discussed further in §4.3.

3.1.4 Nd-Fe-B

Several forms of $Nd_2Fe_{14}B$ based materials were studied in this work. The Nd-Fe-B powder, fabricated by hydrogenation-decomposition-desorption-recombination (HDDR), was supplied by Magnaquench, Inc. The powder had an approximate composition of $(Nd,Dy)_{15}(Fe,Co)_{79}B_6$. Energy dispersion spectroscopy (EDS) performed on the powder showed that the ratio of iron to cobalt content was approximately 3:1. Figure 43(a) shows the XRD trace of the as-received powder with *hkl* indices of several prominent peaks. The morphology of the powder is shown in Figure 43(b), while the microstructure is shown in Figure 43(c). The powder has an irregular particle morphology and size distribution ranging from a few microns to a few hundred microns. The grain structure is fairly regular, spheroidally shaped, and has a typical diameter of 300-500 nm.

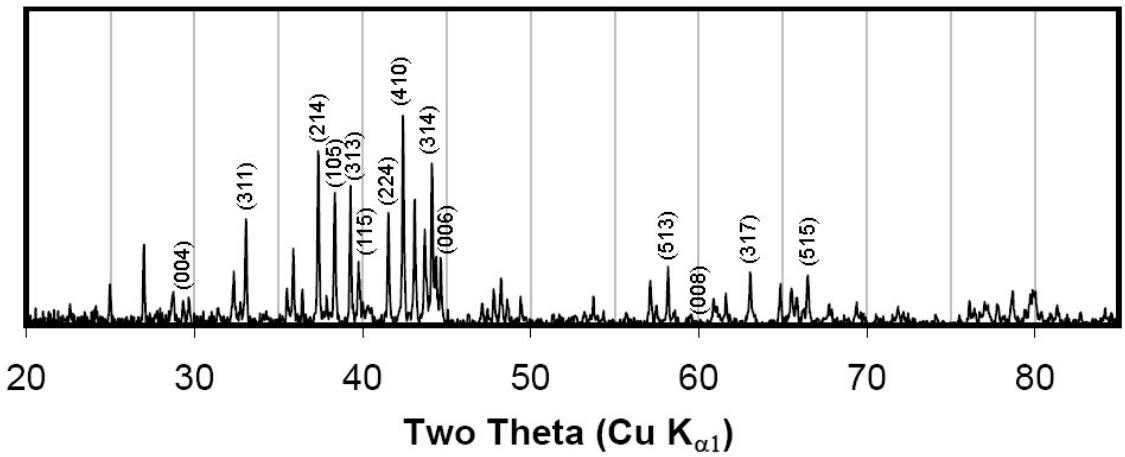

(a) XRD trace of as-received HDDR powder

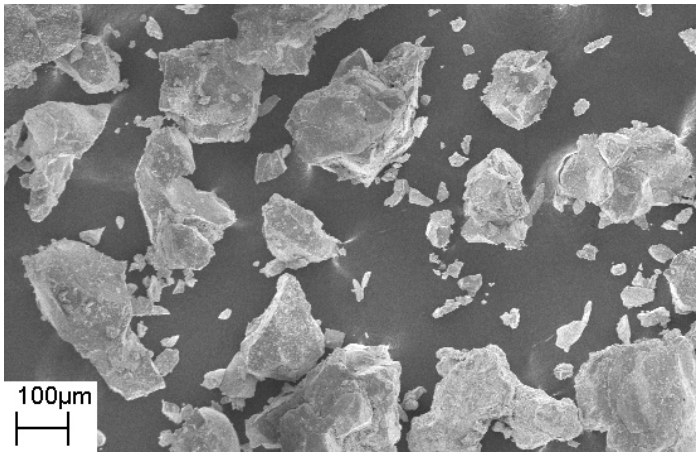

(b) Morphology of Nd-Fe-B starting powder

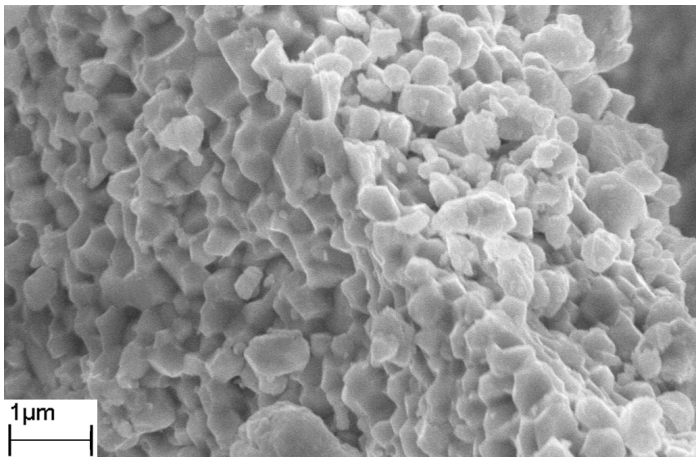

(c) Grain structure of Nd-Fe-B starting powder

Figure 43: XRD trace (a) and SEM images of HDDR Nd-Fe-B starting powder showing (b) morphology and (c) grain structure.

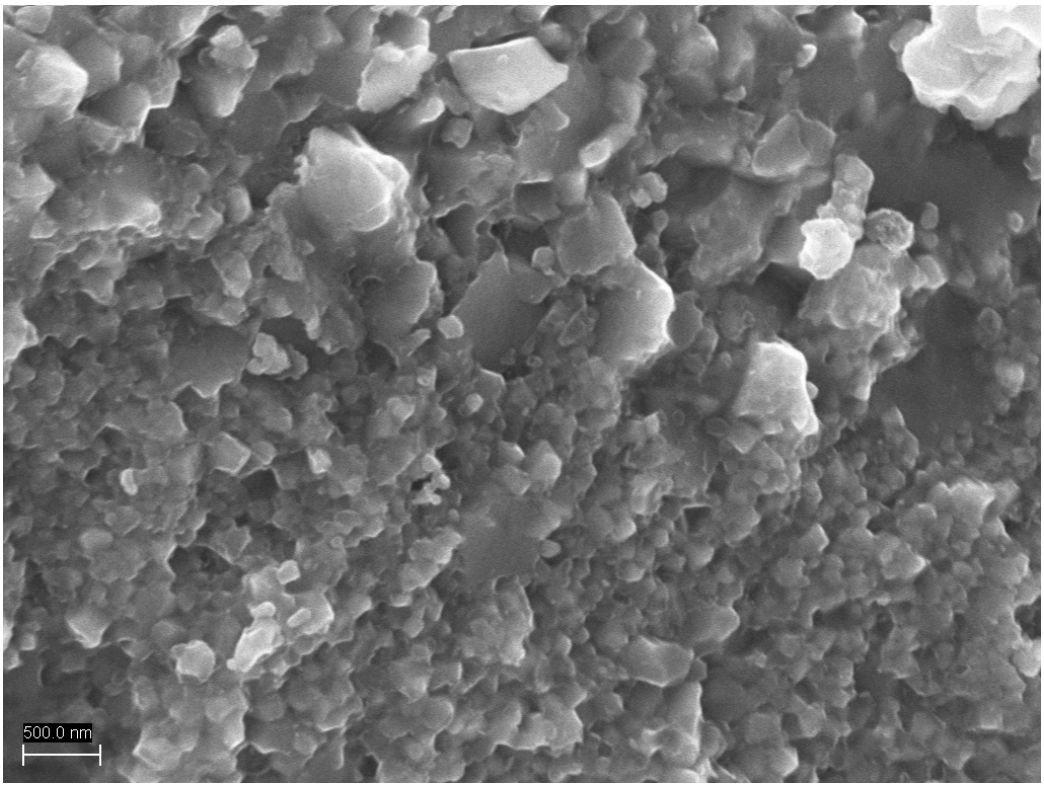

Figure 44: SEM micrograph of the NRL melt-spun Nd-Fe-B powder showing two regions with differing grain sizes.

Melt spun Nd-Fe-B ribbons were provided by the Naval Research Laboratory (NRL) with a composition of $Nd_{15}Fe_{79}B_6$. The ribbons were crushed into powder form using a mortar and pestle. Figure 44 shows the grain size of the powder, which varies from region to region. While the 100-200 nm grain size shown in the bottom region of the figure is more common, several areas have the 300-500 nm grain size shown in the upper region. Figure 45 shows the XRD trace for the crushed powder. The width of the diffraction peaks are larger for the NRL powder (Figure 45) than for the HDDR powder (Figure 43(a), most likely due to the smaller grain size.

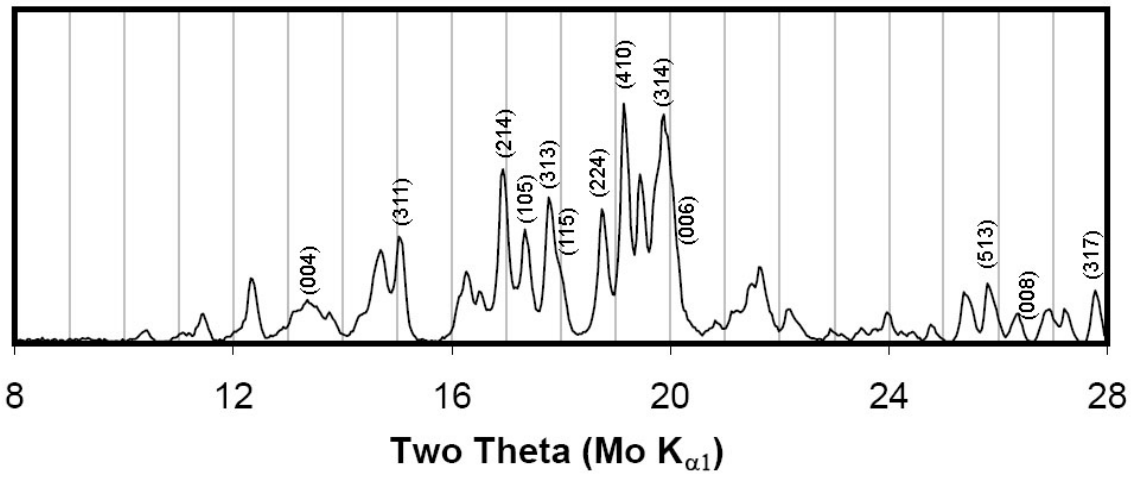

Figure 45: XRD of melt-spun Nd-Fe-B powder provided by NRL

Impact experiments were also performed on non-porous, commercial samples of Nd-Fe-B. The XRD patterns for two different grades, N52 and N42, are shown in Figure 46. The $(00c)$ family of diffraction peaks and the (105) peak have a larger intensity compared to other diffraction peaks than would be expected for isotropic samples, such as the powder diffraction patterns shown in Figures 45 and 43(a). The N52 grade material has a greater degree of raised intensity of the $(00c)$ peaks than the N42 material. Figure 47 shows SEM micrograph of a fracture surface of the N52 grade material. The microstructure, having equiaxed grains several microns in diameter, is consistent with a sintered Nd-Fe-B material.

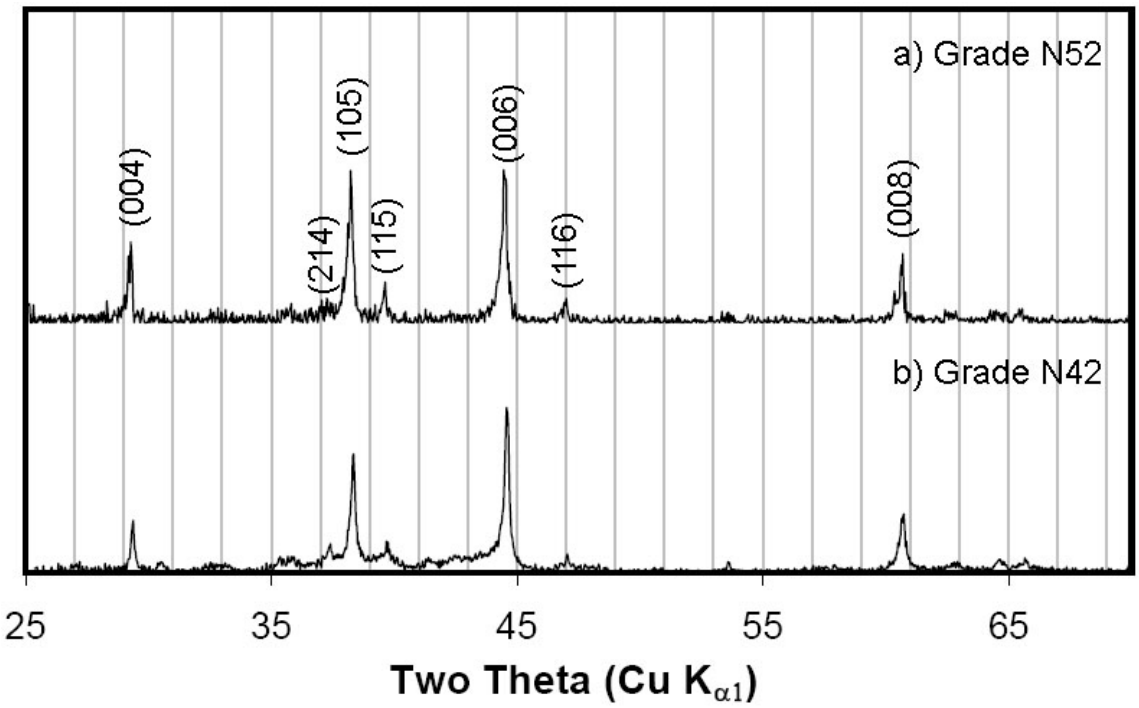

Figure 46: XRD of commercial Nd-Fe-B

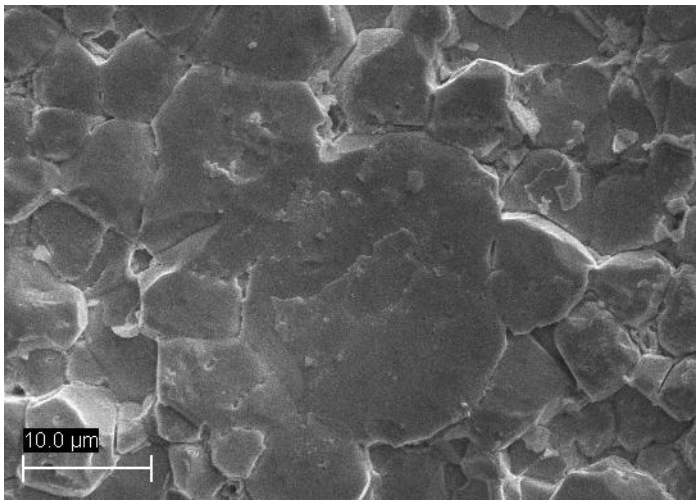

Figure 47: SEM micrograph of the microstructure of non-porous commercial Nd-Fe-B.

3.1.5 Pr-Fe-B/Fe Composite

Composite powder consisting of 80% Pr-Fe-B/ 20% α-Fe was provided by Magnaquench, Inc. The material was produced by melt-spinning of an ingot of composition $Pr_9Fe_{85}B_6$. While the details of the process are proprietary, the material was overquenched, meaning a faster than optimal wheel speed was used, followed by annealing. Figure 48 shows the particle morphology and grain structure of the as-received powder.

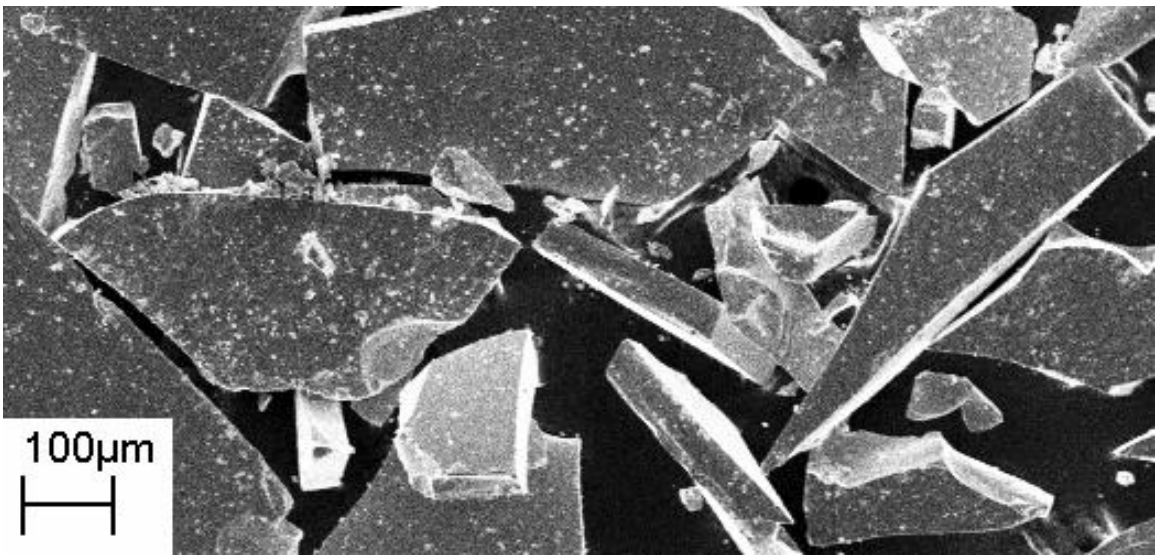

(a) Pr-Fe-B/α composite particle morphology

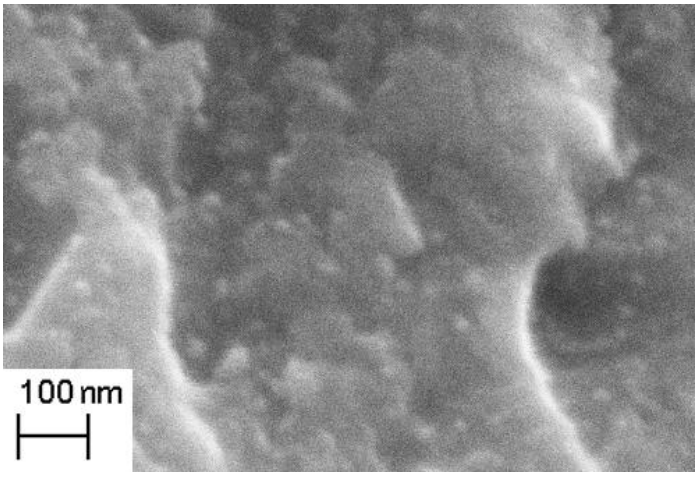

(b) Pr-Fe-B/α composite particle grain structure

Figure 48: SEM images of Magnaquench Pr-Fe-B/α-Fe composite. (a) micrograph of particle morphology and (b) grain structure.

3.2 Materials Characterization

The magnetic materials were characterized through several methods. SEM images, recorded using a LEO thermal field emission SEM, were used to determine particle morphology, grain size and structure of the starting powders, and evidence of cracking and interparticle bonding, etc. of the shock consolidated compacts. Grain structure images, unless other wise noted, were taken on a fracture surface without any sputter coating. Density measurements were performed on the compacts using the immersion method.

The magnetic properties of selected samples were measured either by AMC, using a closed loop hysteresis graph, or at Georgia Tech, using a vibrating sample magnetometer (VSM). The source of the measurements will be noted in each case. The closed loop hysteresis graph data is not affected by a demagnetizing field. VSM samples will have a demagnetizing field, and therefore only the saturation magnetization measurement can be considered valid for soft magnetic materials. VSM samples were embedded in epoxy in an argon atmosphere to prevent oxidation. The hard magnetic powder samples were die-pressed to a nominal density of ∼60% prior to being embedded in the epoxy, in order to prevent the particles from rotating in the magnetic field.

X-ray diffraction (XRD) was used to determine the phase composition of starting powders and shock consolidated compacts. XRD analysis of the recovered compacts was typically performed on both the front and back surfaces of the recovered sample; however, only the scan for the front side is shown unless there are significant difference between the two. Occasionally XRD analysis was performed on cross sections of the sample that are crushed into a powder. A range of x-ray sources were used and are noted for each XRD trace. The as-recovered samples are typically not flat and may have some contamination from the steel recovery capsules, so a small amount of the outer sample was removed by sanding. Processing of the XRD data was done using

the commercially available Jade XRD analysis software. The Jade software was used to remove background, $K_{\alpha 2}$radiation, and to fit diffraction peaks using a combined Gaussian-Lorentzian (pseudo-Voight) curve.

In order to determine the relative amount of each phase present, the integrated intensity (total area) of the fitted curves were compared with the expected percent intensity for that peak and the I/I_c value for each phase. Peak widths, B, were measured using the full width of the fitted peaks at half maximum intensity. The two major sources of diffraction peak broadening, including microstrain and small crystallite size, were separated by a Williamson-Hall approach, in which $Bcos(\theta)$ is plotted versus $sin(\theta)$. The slope of the plot gives an indication of the microstrain in the material, while the y-intercept is related to the grain (crystallite) size, t, by Equation 26,

$$t \sim \frac{0.9}{\lambda * B_0} \tag{26}$$

where B_0 is the peak width at the y-intercept of the Williamson-Hall plot [129]. Diffraction peak broadening due to the instrumental error was measured using a LaB_6 standard. The instrumental diffraction peak broadening was subtracted from the measured width using Equation 27.

$$B^n_{measured} = B^n_{instrumental} + B^n_{actual} \tag{27}$$

The fitted curves had an equal Gaussian and Lorentzian character, which corresponds to a exponent, n, of 1.5. Williamson-Hall linear trend lines were calculated using a least-squares fit in which each point is weighted relative to the uncertainty of the fitted curve, as reported by the Jade software. The Williamson-Hall analysis is known to ignore several minor contributions to the peak broadening[130], such as the shape and size distribution of crystallites. Hence, in the present work it was used to estimate changes in the grain size and degree of microstrain due to the effects of shock-compression.

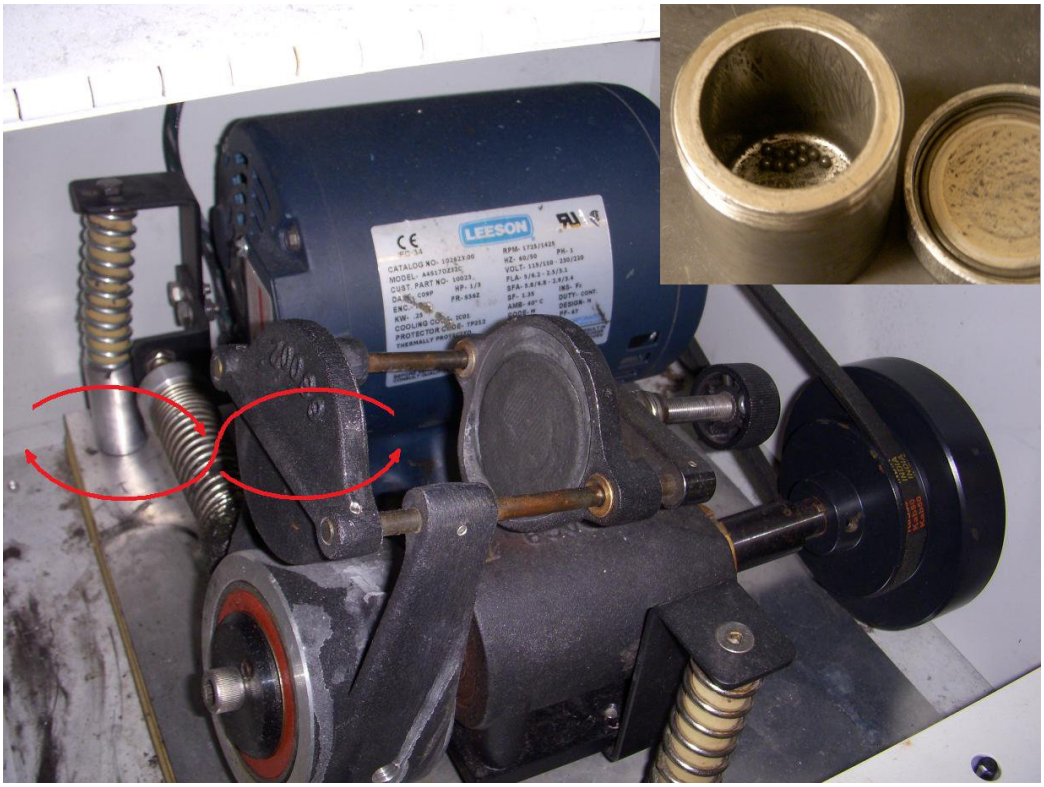

Figure 49: High energy ball mill (SPEX 8000) wih figure eight shaking motion marked. Inset shows the steel milling vial wih 1/8" steel ball milling media.

3.3 Powder Pretreatment Methods

3.3.1 Powder Milling/Mixing

While several shock experiments were performed on as-received powder, in some cases a smaller particle size or a mixture of powders was desired. In these cases pre-shock treatment was performed through different mixing/milling techniques. High energy ball milling was performed using a SPEX 8000 series mixer/miller (Figure 49). The mill shakes the vial in a three dimensional version of a figure eight. The figure inset shows the mill vial with 1/8" steel balls used as the milling media. While a range of steel ball sizes can be used, 1/4" and 1/8" balls were typical. The powder and milling media were handled and sealed inside a glove box with an argon environment.

Attrition milling was performed using a Union Process Model 01 attritor mill. Figure 50 shows the setup of the milling vial. A polypropylene jar, shown in Figure

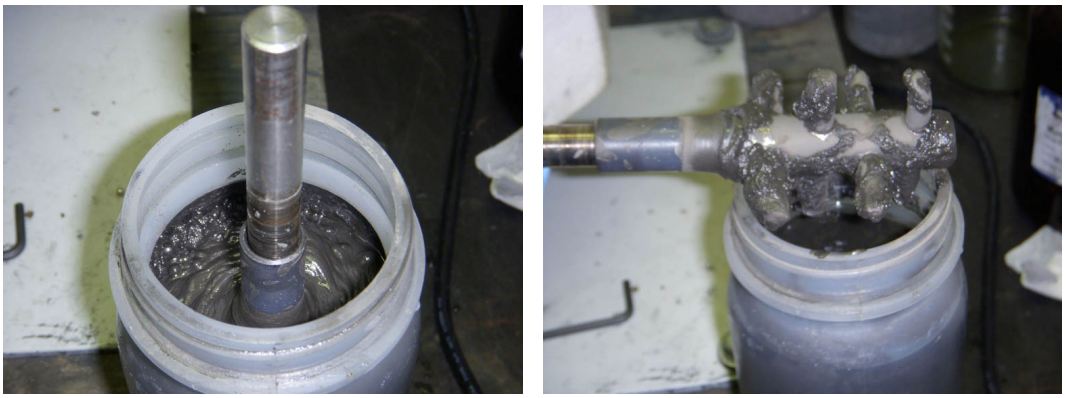

(a) (b)

Figure 50: Attrition milling setup showing polypropylene jar (a) and stirring rod (b).

50(a), is used with 1/8" steel balls in a 1:1 ball to powder mass ratio, along with a toluene slurry to minimize oxidation. For the jar size shown, 0.5-1.0 kilograms of powder and 0.5-1.0 kilograms of steel balls are typically used. Toluene is added until it completely covers the powder and milling media. The stirring rod, shown in Figure 50(b), rotates with a speed of ∼4 Hz, creating the milling action. Toluene was removed from samples of the milled powder by placing them in a vacuum for 24 hours.

Two methods were used in cases in which a simple mixture of two kinds of powders was desired. Short run times can be used with the high energy ball mill to mix powders. This is typically performed by using 1/8" steel balls and a higher powder to ball mass ratio. Alternatively, mixtures can be made by placing the powder in a sealed polypropylene jar with a single steel ball and placing the jar in a rotating mixer for 24 hours. The rotating mixer creates a simple end-over-end motion for the jar.

3.3.2 Field Alignment of Powders

Texture can be introduced into single crystal magnetic powders through alignment in a magnetic field. The powders were pressed by hand into a 0.5" polyurethane die

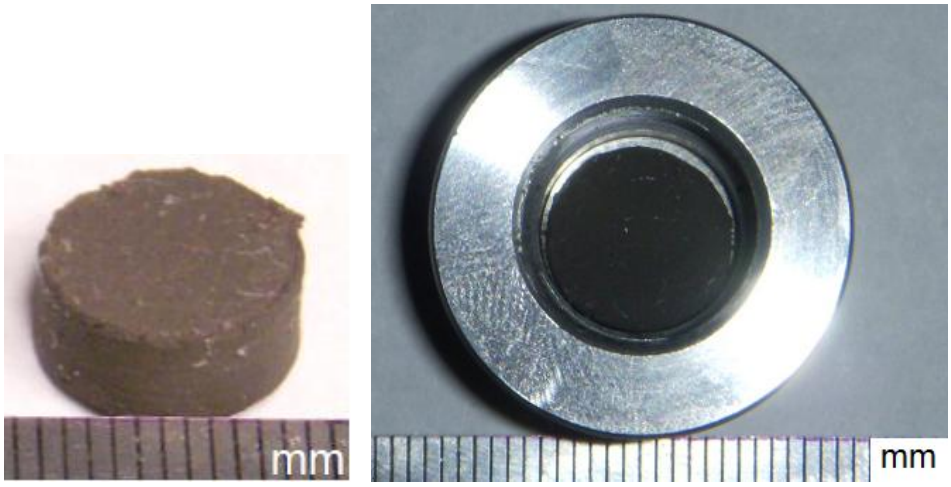

(a) Typical aligned and isostatic pressed sample

(b) Isostatic pressed sample inside a steel shock-recovery capsule

Figure 51: Pictures of aligned and isostatic pressed samples (a) and misfit between the isostatic pressed samples and shock-recovery capsule (b)

and sealed inside a rubber bag. Three 10 T magnetic field pulses of ∼50 ms duration were applied to each sample followed by isostatic pressing at 30-34 ksi. The resulting samples are roughly cylindrical and the degree of alignment may vary from sample to sample, depending on the the properties of the powder and the die. A typical example is shown in Figure 51(a). The irregular shape of the samples makes measuring the exact density difficult, but each sample had an approximate post-isostatic pressing density of 60-70%.

Because the samples are pressed outside of the capsules, there is necessarily some misfit between the pressed pellet and the shock-recovery capsule. Figure 51(b) illustrates this misfit. Gaps between the capsule and the sample would cause shock wave reflections and tensile waves to arise. To mitigate these effects, loose tungsten powder was poured into the gaps. Tungsten was chosen because of its high density, such that, even in a loose form, it has a shock impedance (ρU_s) roughly equivalent to the magnetic powder pellet.

3.4 Shock Compaction and Impact Experiments

Shock compaction was utilized as the primary technique for producing bulk magnets. Rod-on-anvil impact experiments were used to study the ability of magnetic materials to create texture through mechanical deformation at high strain rates. This section will describe the setup of both types of impact experiments as well as time-resolved measurements on parallel plate impact experiments.

Figure 52(a) illustrates the scheme of the shock compaction experiments employing a parallel plate on plate impact configuration. In these experiments, a steel flier plate and sabot was accelerated by expansion of compressed helium in the 80 mm bore, single stage gas gun at Georgia Tech. An impact velocity of 700-1000 m/s was typically used. The powder was uniaxially pressed into steel capsules at pressures of up to 0.8 GPa. The target fixture, shown in Figure 52(b), can accommodate three samples at time.

As shown in the Figure 52(b), an air gap surrounded each capsule, which serves to mitigate but not completely eliminate radial wave focusing due to the impedance mismatch between the powder and the surrounding steel. The target fixture also contained linear and radial momentum traps that serve to reduce tensile release waves and aide in the recovery of the capsules. Both the capsule and flier plate (impactor) were made of SS17-4PH. Impact surfaces were lapped to flatness on a lapping wheel with variations less than .0003 inch. Following impact, the capsules were recovered and the samples removed by machining. Care was taken during machining to minimize heating of the sample.

The temperature of the samples can be cooled below room temperature at the time of impact. For these experiments, a coil of copper tubing was attached to the back (non-impact side) of the target fixture. Liquid nitrogen was made to flow through the coil until the temperature was slightly lower than the desired temperature, as monitored by a thermocouple attached to the side opposite the cooling coil. The

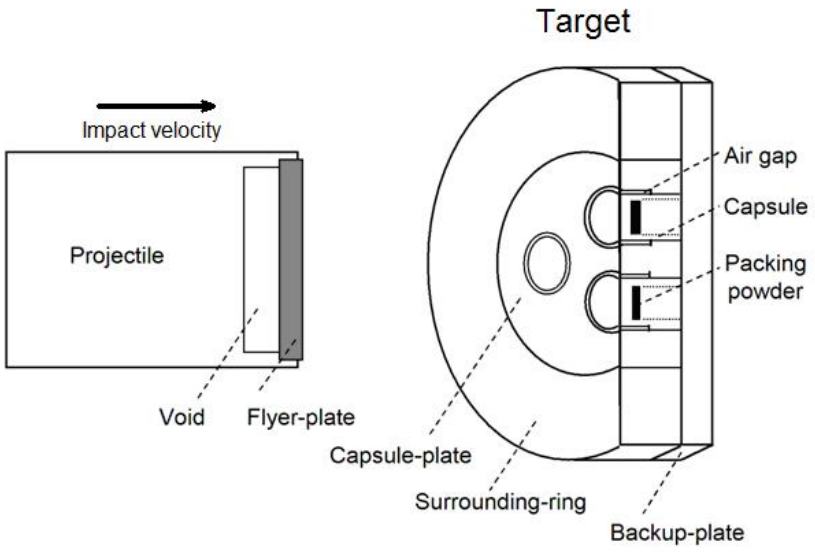

(a) Schematic of shock compaction setup

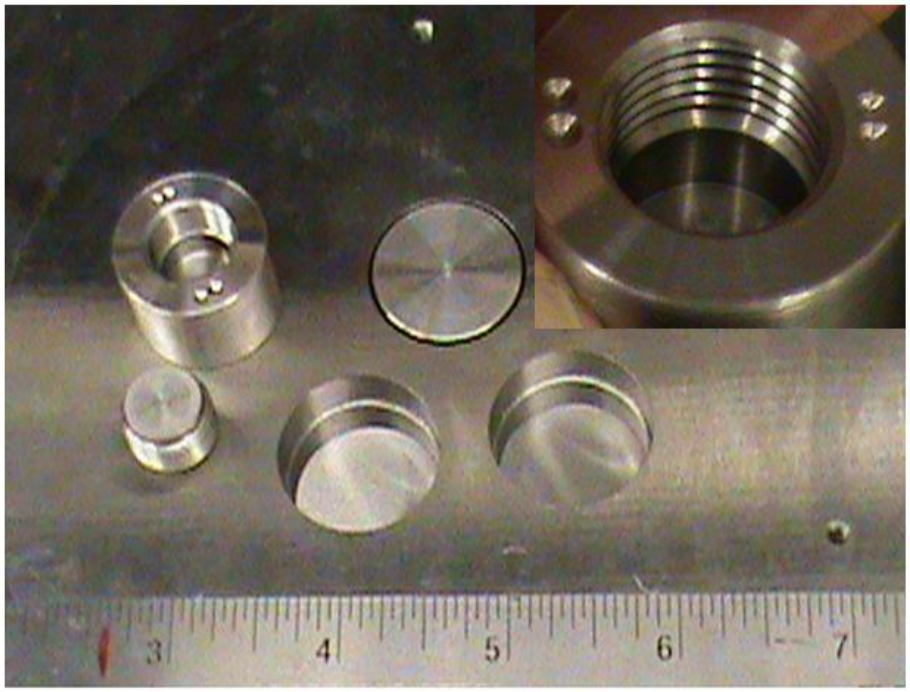

(b) Shock recovery fixture and steel capsule. Inset shows close up view of recovery capsule.

Figure 52: (a) Schematic of shock compaction and (b) image of compaction target showing an open steel capsule and a capsule inserted into the fixture. Inset shows a close up view of the recovery capsule.

target was then allowed to equilibrate and warm slightly to the desired temperature.

High-rate forging (rod-on-anvil) impact experiments were used to explore the high strain rate behavior of porous magnetic materials. In these experiments, a die-pressed pellet of magnetic powder is mounted on the front of a cylindrical projectile (rod), and this assembly impacts a rigid anvil. This experiment attempts to create a uni-axial stress condition on a bulk scale, although a porous material will have a much more complicated local stress state. In contrast, the shock compaction experiments discussed previously have a tri-axial stress state, dominated by a hydrostatic stress component.

The pellets of magnetic powder are die pressed to $\sim$85% density at a nominal uniaxial pressure of 1.5 GPa. The pellet is attached to the front of a projectile, typically made of copper, by a ring of epoxy around the base of the pellet, as shown in Figure 53(a). Figure 53(b) shows a series of high speed camera images (time increases left to right) which depict the forging process with deformation occurring under uniaxial stress. The pellet of magnetic powder deforms so that that height decreases and the diameter increases at the impact surface.

Parallel plate impact experiments employing VISAR measurements were performed on N52 grade commercial Nd-Fe-B. The experiments were performed using Nd-Fe-B as both the flier plate and sample to ensure that the particle velocity is one-half of the impact velocity. Both materials had their *c*-axis texture oriented along the impact direction. A sapphire window was also used with the combined thickness of the window and the Nd-Fe-B sample being approximately equal to the Nd-Fe-B flier plate. The diameter to thickness ratio of the sample is approximately 8:1. A schematic of the VISAR setup is shown in Figure 54, with the VISAR providing a direct measure of the particle velocity.

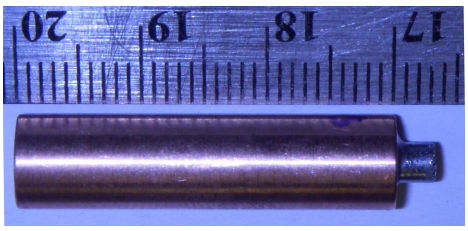

(a) High rate forging projectile

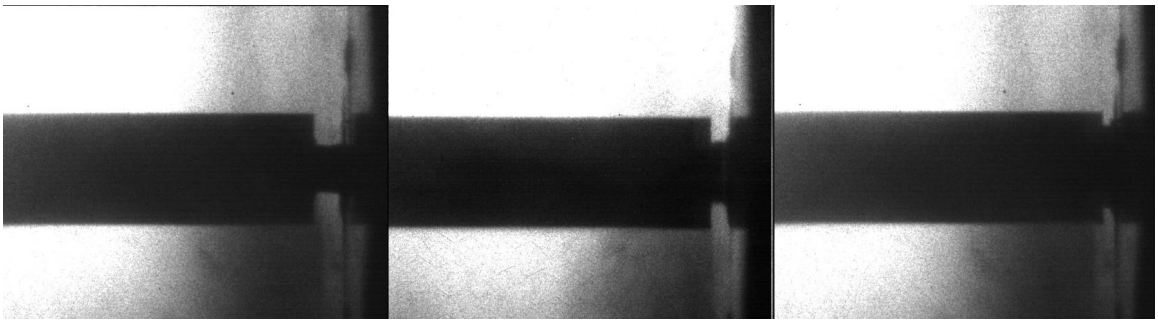

(b) Example of high speed forging experiment

Figure 53: (a) Picture of a high rate forging projectile, a 1/8" diameter sample pellet mounted on a copper cylinder. (b) Time-sequenced high speed camera images of an example high rate forging experiment. Projectile is moving left to right.

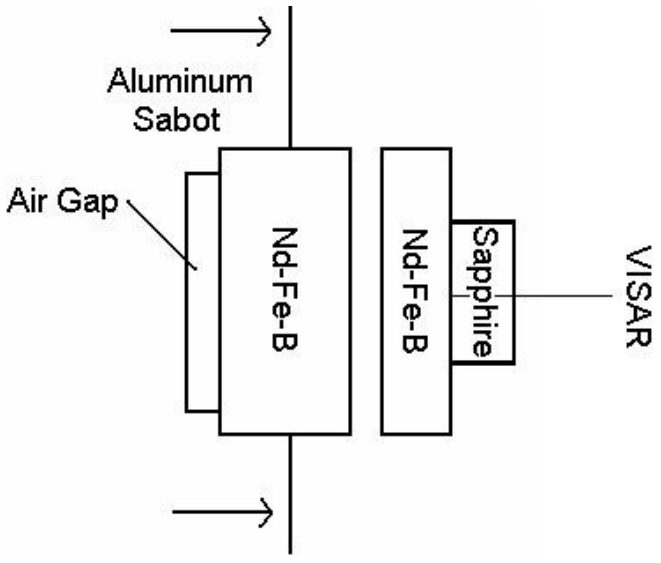

Figure 54: Schematic of VISAR setup

3.5 Modeling Shock Compaction Conditions

The three capsule compaction experiments described in §3.4 employ robust fixtures to allow recovery of the compacts. However, use of such fixture does not allow direct measurement of the compaction pressure. The pressure, temperature, or other compaction conditions are, therefore, estimated based on the pressure-volume or shock-velocity-particle-velocity relationships. This section will discuss how the shock compaction conditions are estimated.

The pressure-volume compressibility (P-V Hugoniot), pressure-temperature relationship (P-T Hugoniot), or other shock state relationships can be calculated from the shock speed versus particle speed relationship ($U_s - U_p$) using the jump conditions (Eqs. 13 and 14) described in §2.3.1. The $U_s - U_p$ relationship is linear for many solid materials, and if the relationship is unknown, an estimate of the relationship can be obtained from the mass weighted averages of the constituents [77].

Table 5 summarizes the U_s-U_p relationships for the materials studied in this work. For materials with an unknown Hugoniot, the values of the constituents used in mass averaging are shown. For Sm-Fe-N and Nd-Fe-B, the mass % of nitrogen and boron respectively is very low and ignored in the calculations. Iron under goes an α-*bcc* to ϵ-*hcp* transition at 13 GPa, however, the Hugoniot of the ϵ-phase was used for estimating the Sm-Fe-N Hugoniot in the region below 13 GPa. This is due to the rhombohedral lattice of the Sm-Fe-N being more closely related to the hexagonal lattice of ϵ-Fe than α-Fe. By similar reasoning, the Hugoniot for austenitic (γ-Fe based) SS304 was used to estimate the Hugoniot of γ'-Fe_4N.

The original report of α''-$Fe_{16}N_2$ by Jack[35] noted that the peak hardness of nitrogen alloyed steels corresponds to the nitrogen content of the α''-$Fe_{16}N_2$ phase, suggesting that the high hardness was due to the presence of α''. Lach et al.[137] reported the $U_s - U_p$ relationship for a 1045 iron-carbon steel that had been nitrided to high hardness (called 1045N) and this relationship is assumed to be similar to the

Table 5: Hugoniot parameters for materials studied

	Mass %	C_0 (km/s)	S	Source	Notes
Sm	24	2.23	0.8	[131, 132, 133]	
ϵ-Fe	76	3.6	1.9	[77]	Extended to Low Pressure
Sm_2Fe_{17}		3.3	1.6	Mass Average	
Nd	32	2.24	0.69	[131]	
Fe	51	4.63	1.33	[134]	P < 13 GPa
Co	17	4.59	1.56	[135, 133]	P < 30 GPa
$Nd_{15}(Fe,Co)_{85}$		3.9	1.2	Mass Average	
$Nd_2Fe_{14}B$		3.7	1.1	[136]	19 < P < 79 GPa
$Fe_{16}N_2$		2.65	2	[137]	High Nitrogen Steel
Fe_4N		4.6	1.5	[133]	Austenitic SS304
α-Fe		4.63	1.33	[134]	P < 13 GPa

$U_s - U_p$ relationship for α''.

Li et al. [136] reported the $U_s - U_p$ equation of state for Nd-Fe-B to be $U_s = 3.686 + 1.059U_P$, in the pressure range of 19 to 38 GPa. This pressure range is considerably higher than the pressure expected for the present experiments; however, the reported EOS roughly agrees with that estimated from mass averaging. Therefore, the Li et al. [136] EOS was used after rounding to two significant digits.

3.5.1 Prediction of Compaction Pressure

As noted above, P-V Hugoniot can be calculated from the $U_s - U_p$ relationship using the jump conditions (Eqs. 13 and 14). Several methods can be used to estimate the P-V response of a porous material from the solid P-V curve. The Mie-Grüneisen equation of state (EOS) is a popular isochoric method; however, it cannot be used when the compression, V_0/V, is greater than $2/\gamma + 1$, which was reached in some cases due to a high value of the Grüneisen constant, γ, and to a high initial volume (i.e. low initial density). The Wu-Jing method [138], which calculates the porous Hugoniot using an isobaric approach, was used for such cases in which the powder

were pressed at a low initial density.

Both the Wu-Jing and Mie-Grüneisen EOS assume that the porous material has negligible strength, meaning the crush up of the powder to the equivalent solid density occurs at zero pressure. The P-α model, shown in Eq. 24, was used to estimate the P-V response in the partial compaction region. The material was assumed to have an effective yield strength, P_y, equal to the pressure of green pressing, typically 0.8 GPa. P_c, the crush strength, is the pressure at which the porous material reaches the equivalent solid density. The Grüneisen parameter, γ, is estimated by assuming that γ/V is a constant, and γ_0 is approximated by considering $\gamma_0 \approx 2S_1 - 1$, where S_1 is constant in the linear Hugoniot shown in Eq. 16.

An upper bound to the crush strength can be estimated by assuming that the relative density of shock compressed samples will not increase after unloading from the shock state. The relative density of the recovered sample will be at least the same as the samples under shock loading, meaning $\alpha \leq \frac{1}{\rho_{recovered}}$. The P-$\alpha$ curve was then constructed such that it is self-consistent with the (α,P) point, whose pressure is found in an iterative manner from impedance matching. Figure 55 shows an example P-V Hugoniot for shock compaction of $Fe_{16}N_2$ using both the Wu-Jing and P-α approaches. The P-α curve shown is plotted using the upper bound of the crush strength.

The iterative method was utilized by choosing an arbitrarily high value of the crush strength, P_{c1}, to calculate the P-α curve, and the resulting curve was used as a first approximation to calculate the shock pressure in the powder, P_1, from impedance matching. However, the point (α,P)=($\frac{1}{\rho_{recovered}}$,$P_1$) will likely not fall on the P-α curve found using a crush strength of P_{c1}. The crush strength is adjusted to a new value, P_{c2}, such that the new P-α curve does contain the (α,P_1) point. The new P-α curve will yield a new shock pressure from impedance matching, P_2, and the point (α,P_2) will lie closer to the new P-α. The method was repeated until the shock pressure and crush strength converge to their respective values.

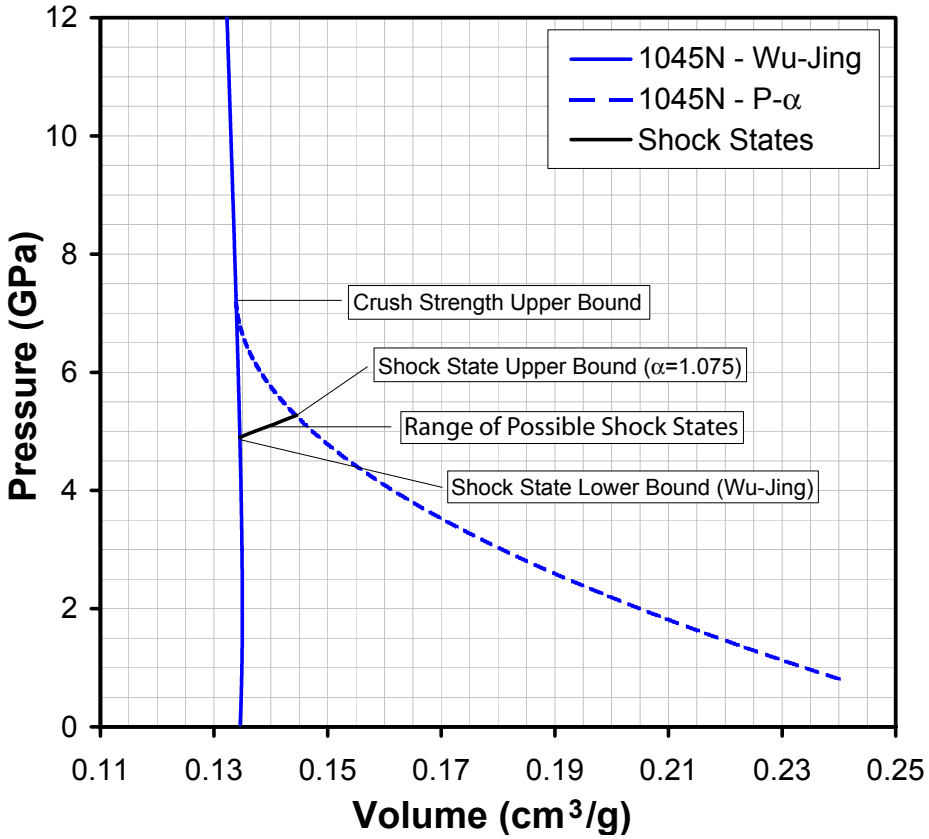

Figure 55: Calculated P-V Hugoniot for $Fe_{16}N_2$ assuming a $U_s - U_p$ response similar to that of 1045 steel treated with nitrogen to high hardness (1045N). Both the Wu-Jing and P-α methods are shown.

In previous work on shock compaction of Fe_3O_4 nanoparticles [139], the crush strength was determined from fitting static loading data to the P-α curve and was estimated to be 1.2-1.4 GPa. The Wu-Jing curve was used with the impedance matching technique, since the shock pressure would be significantly higher than this estimated crush strength. The recovered compacts were only 70-80% dense, and the difference in porosity was attributed to debonding of the particles that occurrs after loading to full density.

Some or all of the porosity seen in recovered compacts can be attributed to debonding, meaning the samples reached a higher relative density (lower α) while under shock loading and then partially debonded upon release from the high pressure state. The pressure calculated assuming $\alpha \leq \frac{1}{\rho_{recovered}}$, therefore, serves as an upper bound. The

lower bound of the shock pressure is found using the Wu-Jing or Mie-Grüneisen curves with impedance matching. If the crush strength is below this value, its exact value will not affect the shock response. The shock state can take any value on the line connecting the upper bound to the lower bound.

3.5.2 Prediction of the Shock Associated Temperature Rise

Estimation of the mean bulk temperature rise can be performed by assuming that all the energy deposited by the shock wave, given by Eq. 15, is converted to internal energy which goes into heating. The temperature rise, ΔT, is given by Equation 28,

$$\Delta T \;=\; \frac{1}{2} P(V_{00} - V_s)/C_p \tag{28}$$

where P and V_s represent the pressure and volume in the shock state, V_{00} is the initial volume, and C_p is the specific heat at constant pressure. For solid materials, such as the steel capsules in the shock fixtures, V_{00} is equal to the specific volume of the solid at ambient temperature. This implies that the temperature rise associated with shock compaction is typically smaller for solid materials than for porous materials.

The bulk temperature calculated from Equation 28 persists while the material is in the shock state, which typically lasts for a few microseconds. The material is expected to cool slightly when unloaded from the shock pressure, with the ratio of temperatures given by Equation 29,

$$\frac{\Delta T_R}{\Delta T_S} \;=\; exp(-\frac{\gamma_0}{V_R}(V_R - V_S)) \tag{29}$$

where S refers to the shock state value and R refers to the residual state value that occurs after unloading. For powder compacts, the difference in T_R and T_S is typically small, since the volume change for unloading is considerably smaller than the volume change volume change for loading and the crush up to solid density. The cooling expected from unloading from the shock state is typically more significant for solid materials, such as the steel capsules surrounding the compacts.

The thermal history after unloading will be dominated by thermal conduction and is therefore geometry dependent. In order to study the thermal behavior, a simple heat conduction model was

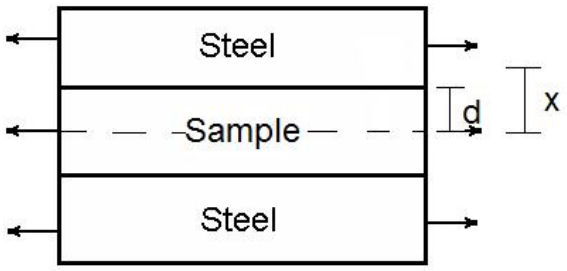

Figure 56: Schematic of thermal conduction model which ignores energy transfer along the circumference of the sample. The sample is modeled as an infinite plane of thickness d in contact on both sides by planes of steel of semi-infinite thickness.

used which ignores edge effects. The shock consolidated compact was considered to be a plane of high temperature material in contact on both sides by the lower temperature steel. Figure 56 shows a schematic of the thermal conduction model. For this model, any internal energy transfer occurring at the interface between the circumference of the samples and the capsules was ignored. Many of the magnetic materials studied here are composed mainly of iron, and their thermal conductivities will be close to that of the steel capsules. If one assumes a uniform thermal conductivity, this problem is then identical to the classical example of conduction along a well insulated bar [140]. The temperature-time-position relationship is given by Equation 30,

$$T(x,t) = T_{st} + \frac{1}{2}(T_{sample} - T_{st})(erf\frac{\frac{d}{2} - x}{2c\sqrt{t}} + erf\frac{\frac{d}{2} + x}{2c\sqrt{t}}) \tag{30}$$

where T is temperature, t is time, x is the distance from the center of the shocked compact, and d is the thickness of the compact. c is given by $c = \sqrt{k/(C_p\rho)}$ where k is the thermal conductivity and ρ is the density. T_{st} and T_{sample} are the bulk shock temperatures found for the steel and sample respectively, as calculated from Eq. 28. In most cases, T_{st} will be significantly lower than T_{sample} since the steel is nonporous and will therefore have a much smaller change in volume resulting from shock compaction.

3.5.3 AUTODYN simulations of two dimensional shock effects

The pressure-temperature-volume relationships of shock wave interactions discussed in this work, as described above, are based on simplified one-dimensional models. Significant two dimensional effects can arise, since the low density powder compact will have a significantly lower shock impedance compared to the surrounding steel. This gives rise to radial focusing effects that can cause pressure spikes several times higher than the pressure calculated from one-dimensional models. Figure 57(a) shows an ANSYS AUTODYN 2D simulation of shock compaction of Nd-Fe-B powder. Shown in

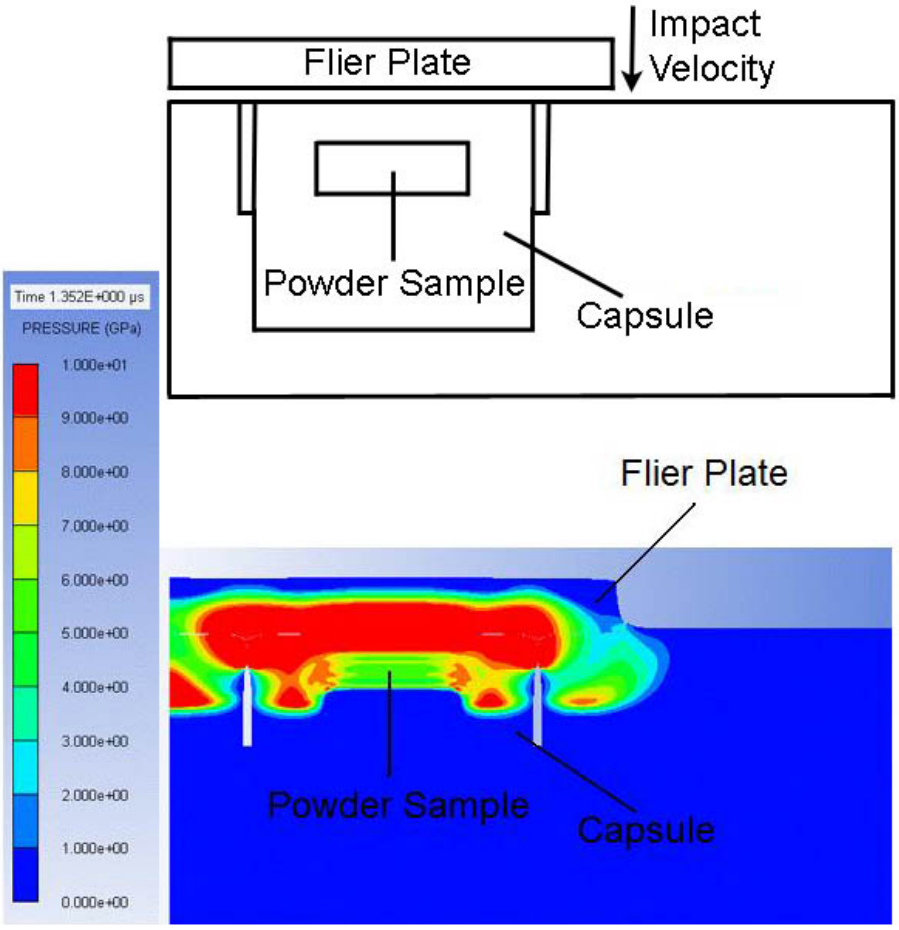

(a) Schematic of Autodyn simulation and simulated pressure outlines.

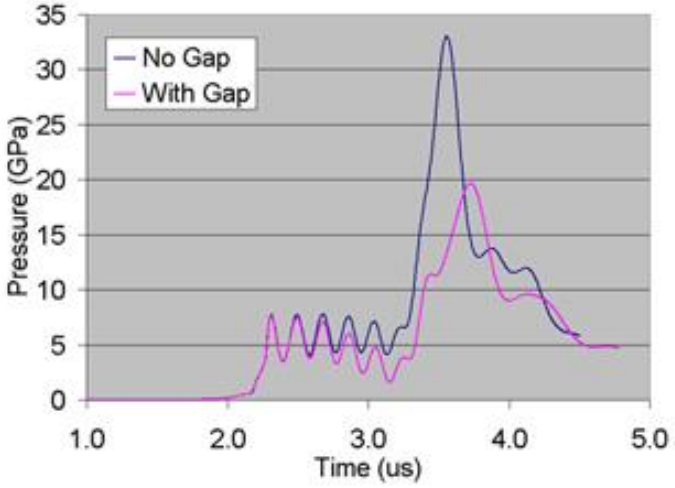

(b) Simulated pressure trace of a shock compaction experiment with and without an air gap

Figure 57: Autodyn simulation of shock compaction experiment (a) and simulated pressure traces with and without air gap (b).

Figure 57(b) are simulated pressure traces for a point near the back of the powder sample with and without an air gap. Both traces have initial pressure oscillations centered around 5 GPa, which corresponds to the pressure calculated from the P-α model for one-dimensional compaction. Short time scale pressure spikes also arise which are several times higher than the primary shock pressure. The air gap helps to reduce the size of the pressure spike. Previous reports on shock compaction of Pr-Fe-B/α-Fe melt-spun powder pressed to 64-78% initial density have shown that the pressure spikes are typically twice as large for the back of the sample as compared to the front of the sample [15]. Without the use of an air gap surrounding the powder containg capsules, the pressure spkes can be as large as an order of magnitude higher than the incident pressure.

CHAPTER IV

RESULTS

As discussed in §2.4, there is relatively little data on shock compaction of permanent magnetic materials. Very few of the studies that do exist carefully characterize the structure of the material before and after shock compaction. In addition, there is no shock compaction data on magnetic materials such as $Fe_{16}N_2$ and Fe_4N. These materials are of particular interest for use in shock compaction since their lower thermal stability limits the use of traditional sintering techniques for making bulk magnets.

This chapter presents the results of several shock compaction experiments that explore a wide range of magnetic materials to determine their suitability for use as exchange coupled composites. Specific attention is paid to shock-induced decomposition and other phase changes, which would negatively impact the performance of permanent magnets. The deformation mechanism of hard magnetic phases is examined in shock compacted samples. Shock compact experiments were also performed on textured green samples of mixtures of Nd-Fe-B and α-Fe nanoparticles. Appendix A includes a summary of all shock compaction experiments performed in this work, along with the starting material characteristics and consolidation conditions.

4.1 Fe_4N

Fe_4N powder was loaded into a steel capsule and uniaxially pressed at 0.79 GPa to approximately 68% of the TMD. The shock compaction experiment was performed at 860 m/s and the samples were cooled to 4^oC at the time of impact. Table 6 summarizes the conditions of the experiment and resulting compact. Following compaction, the sample was not recovered in bulk form, but fragments and loose powder were recovered. Thus the compact density is unknown. The pressure generated during the shock compression experiment was calculated using both the method described in §3.5, providing a one-dimension model, and by the Ansys AUTODYN two-dimensional numerical simulations software. The porous sound speed, used in the AUTODYN simulations, was taken to be 1.3 km/s, which is equal to the porous sound speed of α-Fe at similar porosities [133]. The crush strength was estimated by fitting quasi-static data from uniaxial pressing to the Fishmeister-Artz equation (Eq. 25) for densification of powders.

Table 6: Experimental conditions for shock compaction of Fe_4N

Sample Name	Fe_4N	Fe_3N	Relative Density	Impact Velocity (m/s)	Pressure (GPa)	Temp (^{0}C)
Fe_4N Green	100%	-	68%	-	0.79	4
Fe_4N Compact	57%	43%	-	860 $\pm$ 6	6.4-6.8	420-440

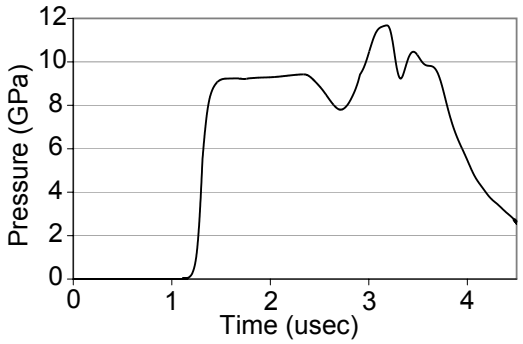

Figure 3. Simulated Pressure-Time trace for the center of the Fe_4N powder sample.

Figure 58: Autodyn-2D simulated pressure-time trace for the center of the Fe_4N powder sample.

The shock pressure found from the AUTODYN simulations is especially sensitive to the crush strength used in the P-α model. Die pressing of Fe_4N powder was only able to achieve up to 70% density. Extrapolating this data to full compaction using the Fishmeister-Artz model gives a wide range of possible values for the crush strength, from 4 to 11 GPa. An example of a simulated pressure trace for the center of the sample, assuming a crush strength of 10 GPa, is shown in Figure 58. Simulations of the shock pressure over the entire range of possible crush strength values yield initial shock pressures of 6.5-10 GPa. The lower end of the simulations match the values predicted by the one dimensional model, 6.4-6.8 GPa. Short duration pressure spikes as high as 23 GPa may arise due to two dimensional radial wave focusing effects, depending upon the crush strength and subsequent compaction behavior.

The XRD pattern for the as received powder is shown in Figure 59 along with the powder pattern for the recovered compact. While the starting powder contains only diffraction peaks for the γ'-Fe_4N phase, the XRD trace for the shocked powder contains both γ'-Fe_4N and ϵ-Fe_3N diffraction peaks. The volume ratio of the γ'-Fe_4N to ϵ-Fe_3N phase is approximately 4:3.

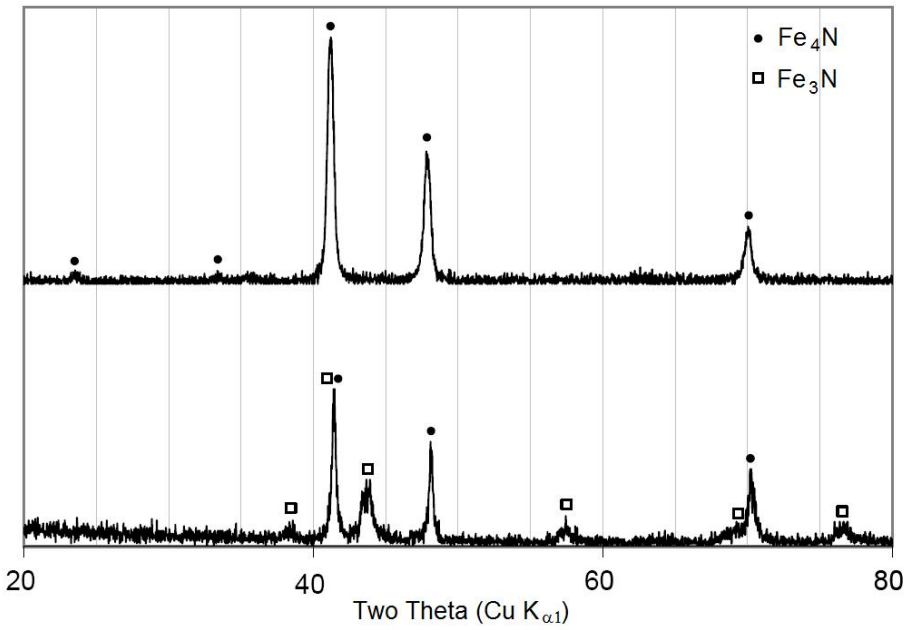

Figure 59: XRD of patterns of pure γ'-Fe_4N powder (top) and shock compressed powder (bottom).

4.2 $Fe_{16}N_2$

Two shock compaction experiments were performed on the the α''-$Fe_{16}N_2$ samples at impact velocities near 850 m/s, while cooling samples at temperatures of -21^{0}C and -126^{0}C, as measured just prior to impact. Table 7 summarizes the experimental conditions and results of XRD scans. The P-V curve for non-porous α''-$Fe_{16}N_2$ was modeled by using the $U_s - U_p$ for high nitrogen 1045 steel, as discussed in §3.5 [137]. The exact choice of $U_s - U_p$ parameters is not crucial to this analysis. Using the $U_s - U_p$ relationship for α-Fe [134] with the initial and solid densities of α-$Fe_{16}N_2$ yields similar results.

As noted in §3.5, the temperature rise from shock compaction was calculated by dividing the entire shock energy by the specific heat, C_p. Variations in C_p values over the range of temperatures expected are relatively small, and so it was assumed to be a constant. The C_p value of a sample of commercially available Fe_xN with $x = 3.8$ was measured by a differential scanning calorimeter to be 0.45 J/g^{o}C, which is equivalent to the C_p of iron. Given the similarity of the specific heat of iron with nitrogen content above and below that of $Fe_{16}N_2$, it is assumed that the C_p of α''-$Fe_{16}N_2$ and its decomposition products will be approximately 0.45 J/g^{o}C.

Figure 60 shows the calculated shock temperature for the sample impacted at -126^{o}C sample. As noted in Table 7, the range of possible shock pressures for the -126^{o}C compact is 4.9-5.3 GPa,

Table 7: Experimental conditions for shock compaction of $Fe_{16}N_2$

Sample Name	$Fe_{16}N_2$	α-Fe	Fe_4N	γ''-FeN	ϵ-Fe	TMD (g/cm^3)
-21C 16-2 Green	95%	5%	-	-	-	7.43
-21C 16-2 Compact	20-22%	41-55%	21-32%	0-3%	4-5%	7.61-7.69
-126C 16-2 Green	95%	5%	-	-	-	7.43
-126C 16-2 Compact	13-17%	18-24%	29-43%	16-27%	6-7%	7.44-7.46

Continued	Relative Density	Impact Velocity (m/s)	Pressure (GPa)	Temp (^{0}C)
-21C 16-2 Green	59%	-	0.79	-21
-21C 16-2 Compact	92-93%	844 ± 42	5.3-5.8	520-540
-126C 16-2 Green	56%	-	0.79	-126
-126C 16-2 Compact	92-93%	866 ± 4	4.9-5.3	430-450

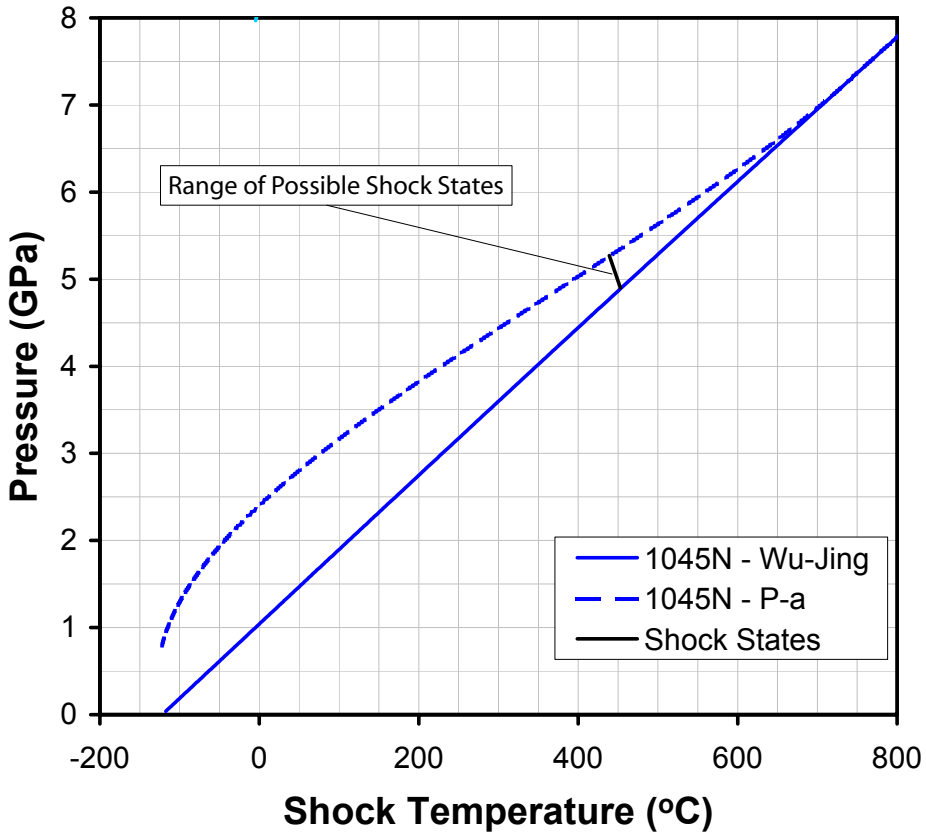

Figure 60: Shock temperature as a function of pressure for compaction of $Fe_{16}N_2$

and the corresponding range of P-T states are marked by the solid black line in Figure 60. The shock temperature is very sensitive to the initial porosity of the material. A larger change in temperature is expected for the -126^{o}C compact than for the -21^{o}C compact because of the slightly higher initial volume in the former. Using the iron shock parameters instead of those for 1045N, however, produces no significant change in the predicted temperatures. Likewise, adjusting the Grüneisen parameter over the typical range for metals, i.e. γ_0 being equal to 1.5-3, makes only small changes, <10%, to the calculated shock temperature.

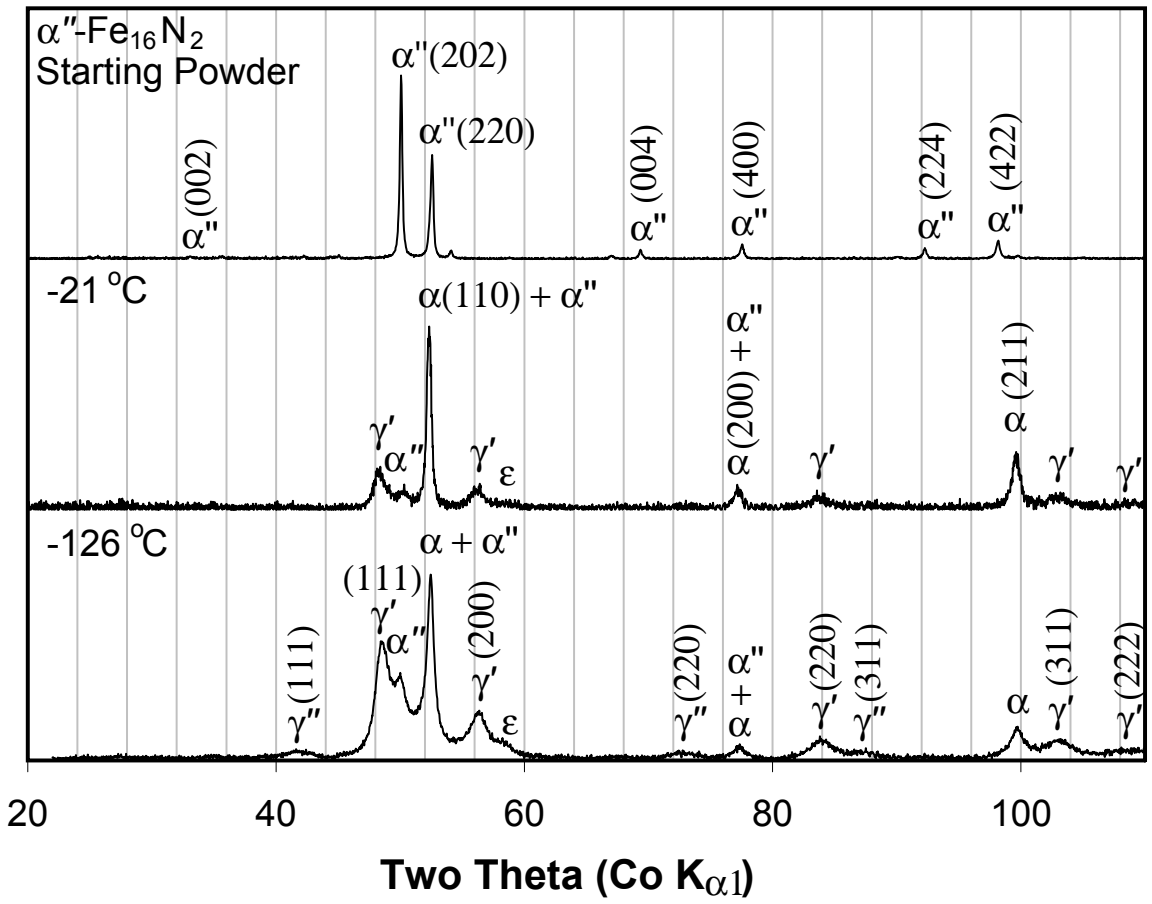

Figure 61: XRD traces of $Fe_{16}N_2$ starting powder (Top), -21^{o}C compact (Middle), and the -126^{o}C compact (Bottom).

The estimated bulk shock temperature, 520-540^{o}C for the -21^{o}C sample and 430-450 for the -126^{o}C sample, is well above the stability range of α''-$Fe_{16}N_2$ for both samples. Thus, at least a partial decomposition is expected, although the extent of decomposition is not known for temperature calculations alone. Figure 61 shows the XRD traces for the starting powder and the recovered compacts. XRD results shown are for a cross section of the material that has been crushed into a powder form. The XRD scans reveal that decomposition has occurred in both samples, as shown by the formation of additional XRD peaks. The powder pattern for the -21^{o}C compact shows that the sample has decomposed, with α-Fe making up roughly half the sample, and γ'-Fe_4N and α''-$Fe_{16}N_2$ making up most of the remainder. A high pressure *hcp* iron phase, ϵ-Fe, may also be present, based on the broad peak at 58.5^o. In the -126^{o}C compact, the α''-$Fe_{16}N_2$ phase has also decomposed; however, a larger amount of γ' has formed. In addition, the zinc-blend structure, γ''-FeN is also present [141]. Quantitative phase analysis was complicated by broad overlapping peaks, giving rise

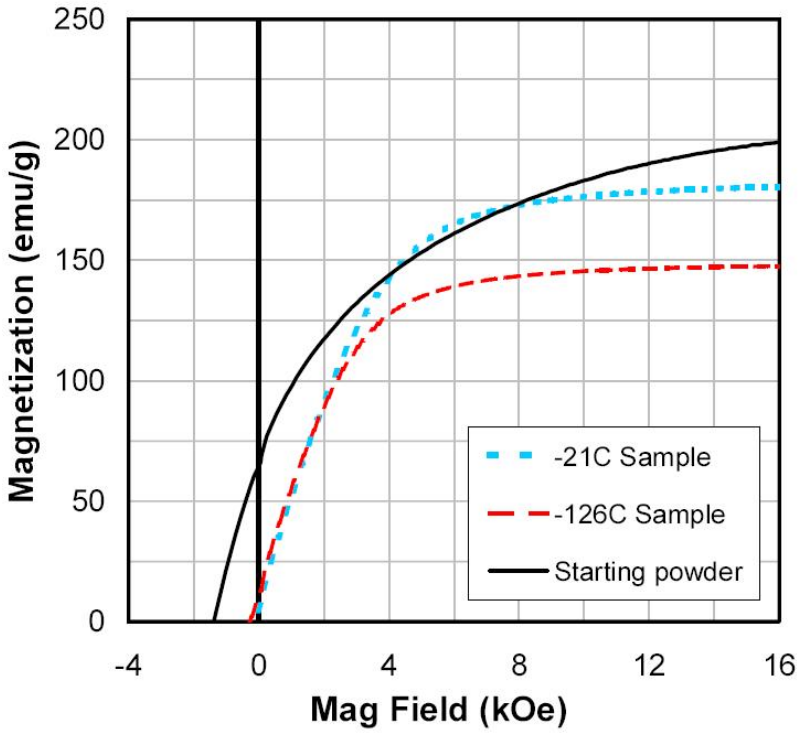

Figure 62: Magnetic hysteresis curves for both recovered compacts.

to considerable uncertainty in the measurements. The ranges shown in Table 7 for the amounts of each phase reflect the difference found when considering only the highest intensity lines for each phase versus those found when including minor peaks.

Figure 62 shows the hysteresis curves for both recovered compacts, as measured on a closed loop hysteresisgraph. The $Fe_{16}N_2$ starting powder has not reached saturation. Using the law of approach, the M_s value is estimated to be 226 emu/g, whereas the -21^{o}C and -126^{o}C compacts have saturation magnetizations of 181 and 152 emu/g respectively, meaning the magnetization has decreased in both samples as compared to the starting powder. The drop in magnetization is most likely due to phase changes that occur following shock compaction. The higher magnetization present in the -21^{o}C compact is attributed to the higher α-Fe content, and the higher coercivity in the -126^{o}C compact is most likely due to the higher amount of Fe_4N.

SEM micrographs of the as-received powder and the -126^{o}C compact are shown in Figure 63 (a) and (b) respectively. The particle size of the starting powder is essentially the same as the grain size seen in the microstructure of the compact. No obvious melted regions are observed in the shock consolidated compact. While Archimedes density measurements indicate 7% porosity, the voids are too small to be seen with SEM imaging.

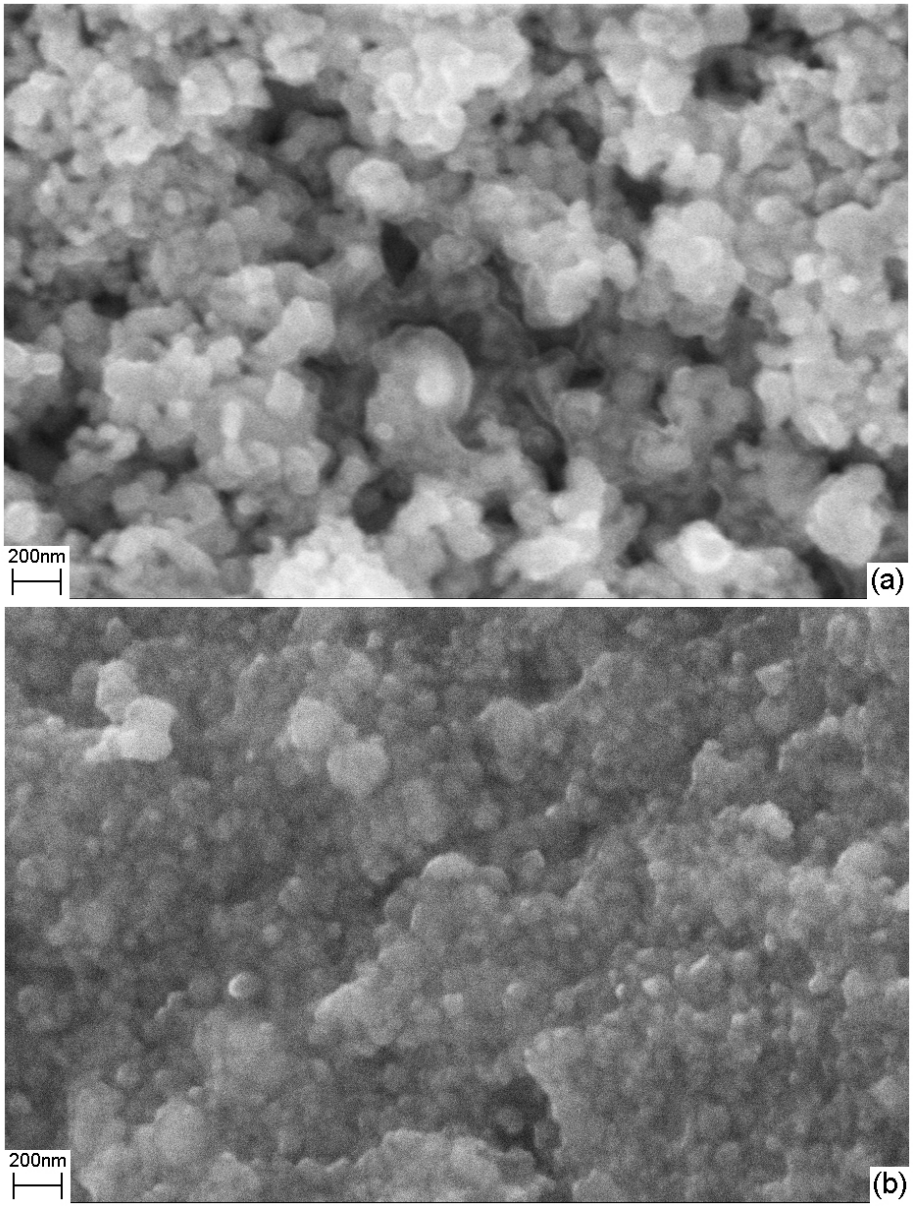

Figure 63: SEM micrographs of (a) $Fe_{16}N_2$ starting powder and (b) the microstructure of shock consolidated Compact B, which was chilled to -126^{o}C prior to impact.

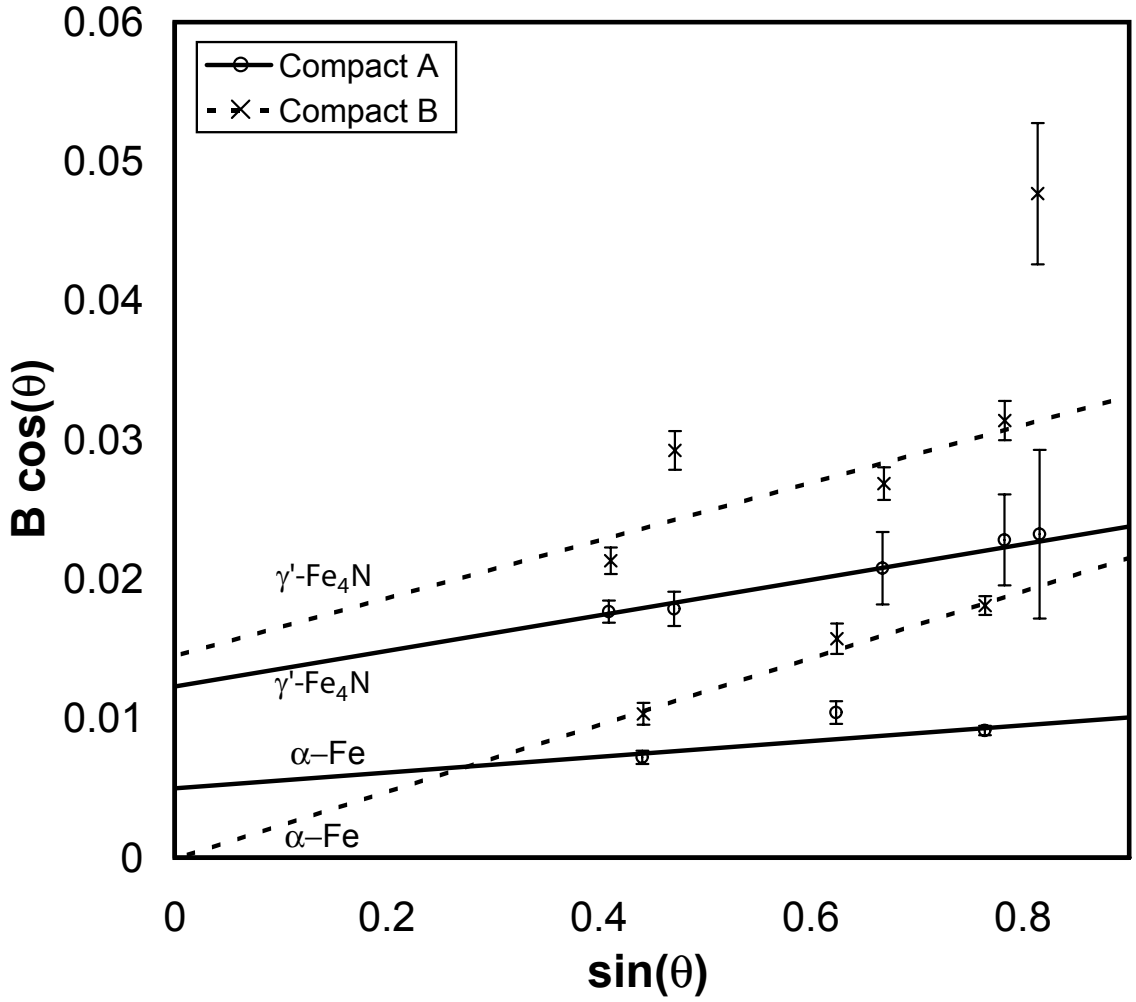

Figure 64: Williamson-Hall analysis of broadening in XRD peaks for both compacts.

The broad X-ray peaks for the compacts shown in Figure 61 suggests a grain size significantly smaller than the particle size seen in SEM micrographs from Figure 63. Williamson-Hall analysis of XRD peak broadening is shown in Figure 64. For the γ'-Fe_4N phase, this analysis suggests both compacts have approximately the same grain size, $\sim$ 10 nm. The γ'-Fe_4N phase in the -126^{o}C compact has a higher degree of strain, as shown by the increased slope of the Williamson-Hall line. The grain size of the α-Fe phase is estimated to be $\sim$ 30nm for the -21^{o}C compact but is too large to be determined accurately in the -126^{o}C compact, meaning it is probably greater than 100 nm.

The heat conduction model for shock compacted materials developed in §3.5 was applied to the -126^{o}C sample. The expected temperature-time curves for three different distances from the center of the α'' sample, x positions of 0.0, 1.0, and 1.8 mm, are shown in Figure 65. The thickness of the compact is 3.7 mm, so $x = 1.8$ represents a point very near the outside edge of the compact. Using

Eqs 29 and 28, the temperature of the steel surrounding the capsule, T_{st}, is estimated to be 150^{o}C for the -21^{o}C compact and 50^{o}C for the -126^{o}C compact.

The outer skin of the material cools rapidly to a temperature near the temperature of the surrounding steel. The inner portions of the sample, represented by the x = 0.0 mm curve, experience a temperature over the stable range of α'' for 1-2 seconds. γ''-FeN is not stable over 342^{o}C [141]; however, a large portion of the sample quickly cools to below this temperature. The temperature-time curves for the -21^{o}C compact have a similar shape. Since the surrounding steel in the -21^{o}C compact is heated to approximately 150^{o}C most of the sample stays above not only the α'' stable temperature, but also the γ'' stable temperature for several seconds.

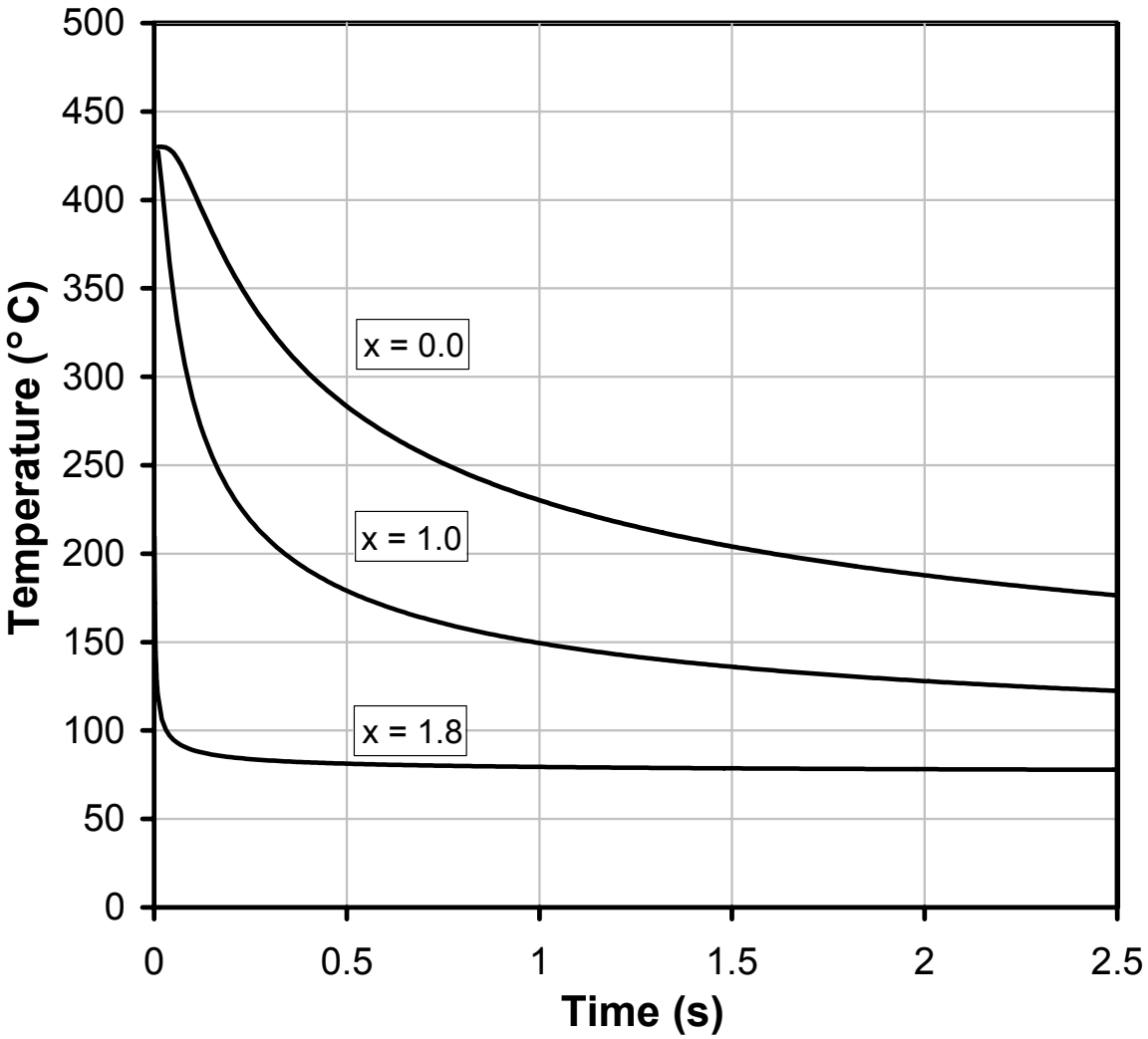

Figure 65: A temperature-time model for the -126^{o}C compact ignoring cooling from the circumference of the sample. Curves for three distances from the center are shown, x = 0.0, 1.0, 1.8 mm, while the distance to the compact-steel interface is 1.85 mm. The outer skin of the material cools rapidly to a temperature near the temperature of the surrounding steel, while the inner portions cool over a period of several seconds.

4.3 Sm-Fe-N

Three shock compaction experiments, numbered 677, 804, and 816, were performed on Sm-Fe-N powders. Table 8 summarizes the experimental conditions for the three experiments. While all three samples were pre-pressed using a nominal pressure of 0.79 GPa, Sample 677 had a lower green density than the sample 804 and 816. This is most likely due to the uniform size and spheroidal morphology of the starting powder, as discussed in §3.1.

Table 8: Experimental conditions for shock compaction of Sm-Fe-N

Exp No	$Sm_2Fe_{17}N_3$	α-Fe	Relative Density	Impact Velocity (m/s)	Pressure (GPa)	Temp (^{0}C)
677 Green	-	-	63%	-	0.79	-6
677 Compact	96%	4%	92%	788 ± 10	4.9-5.4	370-390
804 Green	96%	4%	72%	-	0.79	-21
804 Compact	96%	4%	95%	844 ± 42	7.0-7.4	350-365
816 Green	96%	4%	73%	-	0.79	-122
816 Compact	92%	8%	98%	903 ± 2	7.8-8.1	300-310

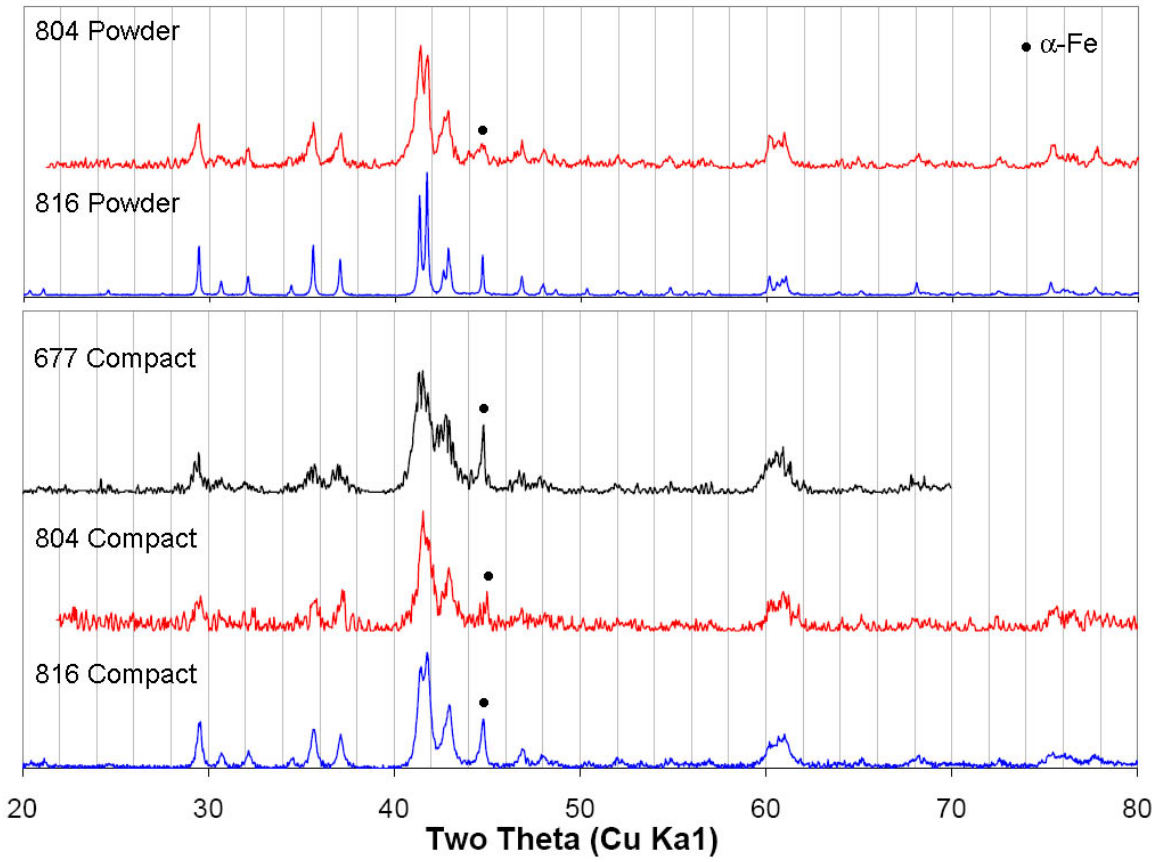

Figure 66: XRD traces for two batches of Sm-Fe-N powder as received from AMC and shock compacts 677, 804, and 816

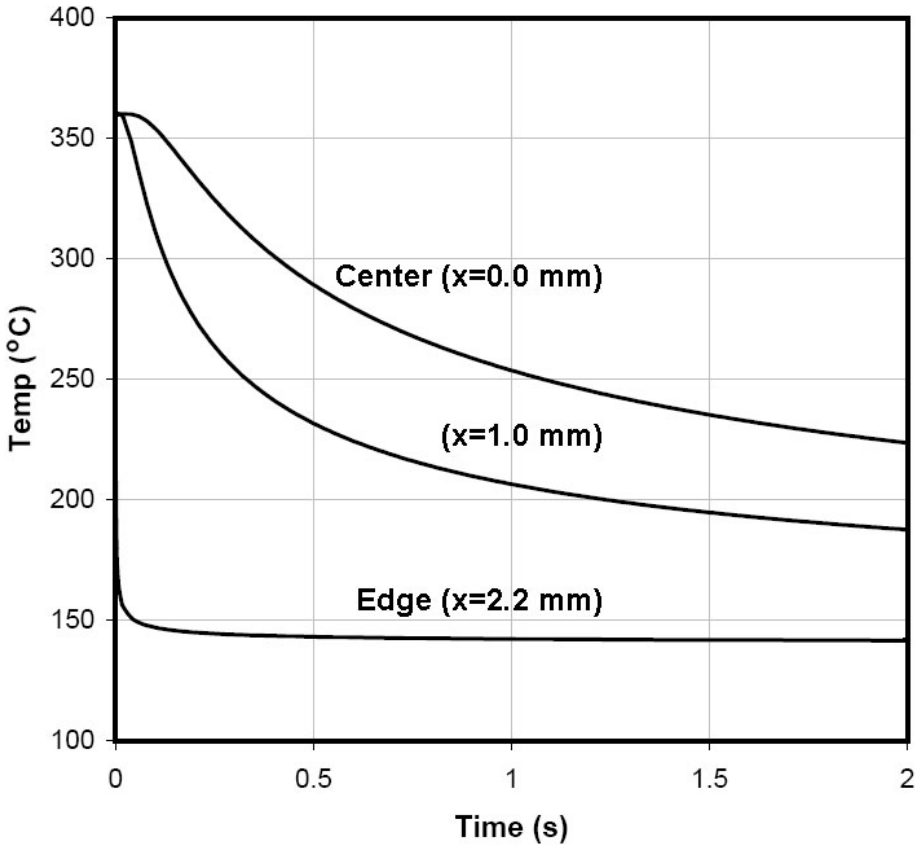

Figure 67: Pressure-Time curve for shock compacted sample 804. Curves are shown for three distances from the center of the 4.47 mm thick sample, x = 0.0, 1.0, and 2.2 mm. The outer edges of the sample quickly cool to the temperature of the surrounding steel, 140^{o}C, while the center of the sample remains at a higher temperature for a few seconds.

Figure 66 shows the XRD traces for the two starting powders and the three shock consolidated compacts. The XRD pattern for the 677 starting powder is not available. All Sm-Fe-N samples contained small amounts of α-Fe. The relative amount of α-Fe remained unchanged following shock compaction for shots 804, and a small amount of α-Fe was formed for shot 816. No other decomposition products, such as SmN or Fe_4N, were detected in any of the recovered compacts, although α-Fe is expected to be the main decomposition product, as shown by Eq. 11.

Figure 67 shows the expected temperature-time curves (from Eq. 30) following shock compaction of sample 804, which is expected to have the highest shock temperature. Curves are shown for three distances from the center of the 4.47 mm thick sample, x = 0.0, 1.0, and 2.2 mm. The outer edges of the sample quickly cool to the temperature of the surrounding steel, 140^{o}C, while the center of the sample remains at a higher temperature for a few seconds.

Williamson-Hall analysis was performed for each XRD trace shown in Figure 66. The traces shown in Figure 66 were measured using different x-ray wavelengths, but each trace was converted to the copper wavelength for ease of comparison. The Williamson-Hall analysis, however, was performed on the original scan for each sample. The scan for 677 used a copper radiation source, while the powder and compact for 804 used a molybdenum source and 816 powder and compact used a cobalt source. A LaB_6 standard was used for each radiation source to estimate the instrumental broadening. Figure 68 shows the Williamson-Hall plots for the compacts and starting powders. As noted previously, the pattern for the 677 starting powder was unavailable. The scatter in the data for compact 677 prevented fitting a trend line with any reasonable certainty.

There exists a significant scatter in the data for both the 804 starting powder and recovered compact. A wide range of slopes could potentially fit the 804 data. Therefore, the Williamson-Hall analysis for this sample was performed by ignoring microstrain. Instead, a rough grain size estimate for these samples was obtained by assuming zero strain. This assumption may not be valid, especially for the recovered compact, but the number of overlapping peaks makes a more accurate analysis unfeasible. The error bars shown in the plots are the uncertainty provided by the Jade analysis software in fitting each peak the pseudo-Voigt curve. A best fit line with zero slope was calculated by weighting each data point relative to its uncertainty, similar to the manner described by Taylor [142]. Thus, points with large error bars, such as the 804 starting powder point with $B\cos(\theta)$=.0107, do not significantly affect the best fit line. Using this method, the approximate grain size is found to be 30-45 nm for the 804 starting powder and 25-35 nm for the compact. The Williamson-Hall plot in Fig. 68(c) shows an increase in diffraction peak broadening from the powder to the compact due mainly to a decrease in grain size. The approximate grain size has decreased from $\sim$150nm to $\sim$40 nm, although it should be noted that a Williamson-Hall analysis is typically not considered accurate for grain sizes larger than 100 nm [129].

Figure 69 shows the microstructure of the recovered compacts 677 and 804. The approximate shape of the original polycrystalline particles is maintained in the microstructure of the resulting compacts. The Williamson-Hall analysis shown in Figure 68 indicates that the grain size of the 804 compact is significantly smaller than the size of the particles seen in the micrographs. Most likely, the grains are too small to be resolved by the SEM image shown in Figure 69.

Although Figure 68 indicates that the grain size for the starting polycrystalline powder of sample 816 is significantly larger than that of sample 804, the particle morphology of the two starting powders was very similar. Figure 70 shows SEM micrographs of the recovered compacts for samples 804 and 816. The outline of the original particles can be seen in 70(a) (Left) for sample 804; however,

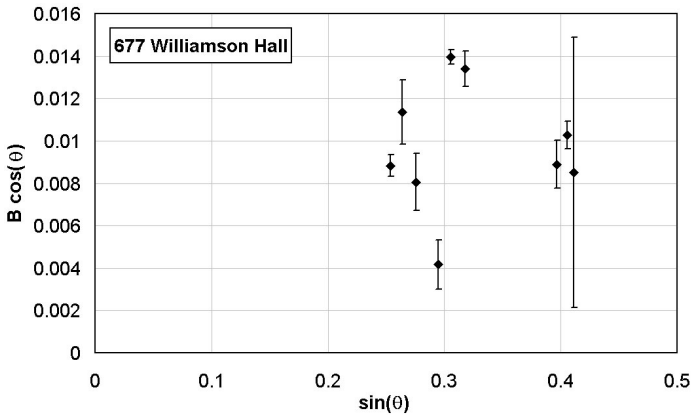

(a) 677 compact

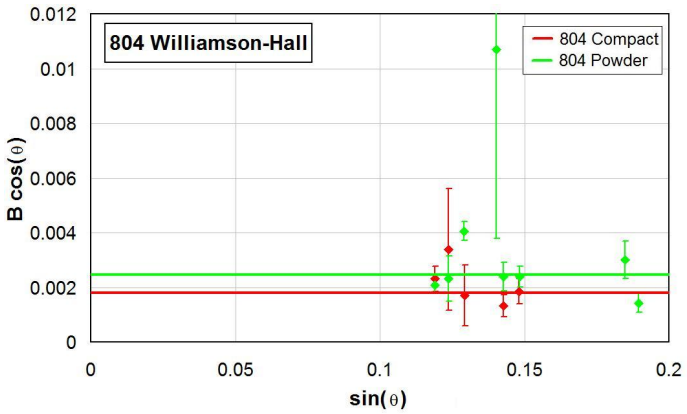

(b) (red) 804 compact (green) starting powder

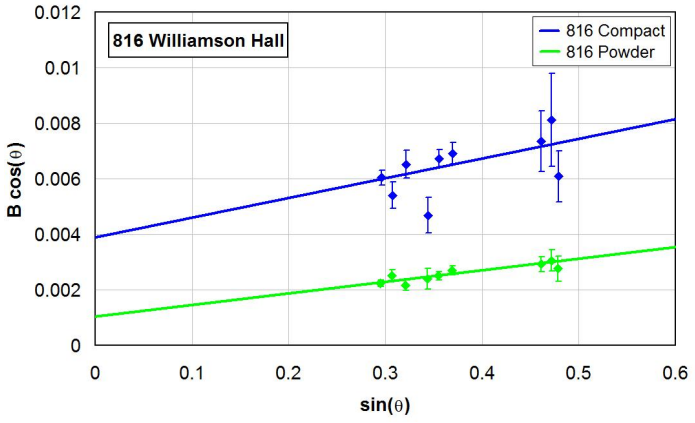

(c) (blue) 816 compact (green) starting powder

Figure 68: Williamson-Hall plots of (a) 677 compact (b) 804 compact and starting powder (c) 816 compact and starting powder. Starting powders are shown in green. The scatter in the data for 677 and 804 prevents drawing a meaningful trend line.

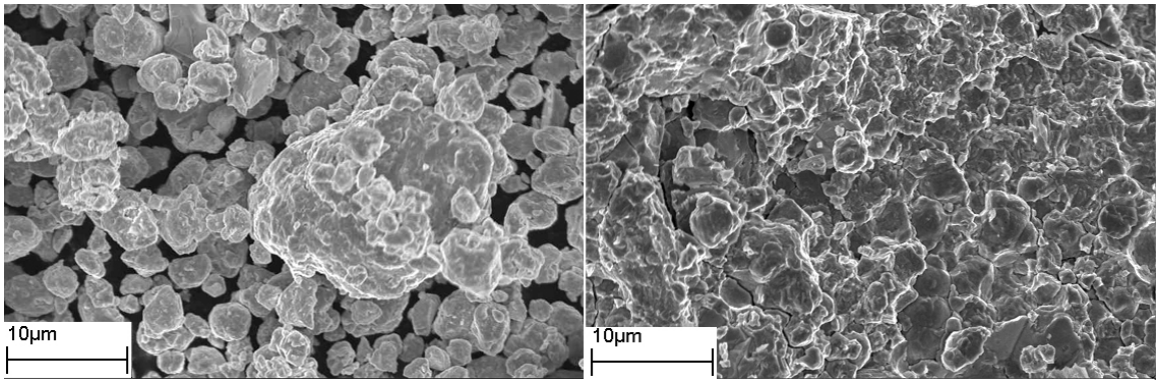

(a) Starting powder (left) and recovered compact (right) for sample 677

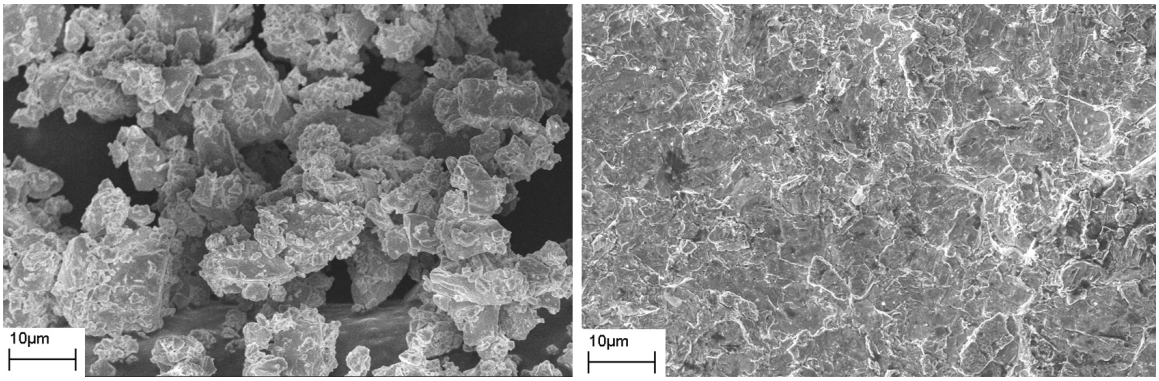

(b) Starting powder (left) and recovered compact (right) for sample 804

Figure 69: SEM micrographs of starting powders and recovered compacts for samples 677 and 804

the micrograph of compact 816 (Right) shows areas of localized deformation where the particles have broken up into smaller grains or grain aggregates. The higher magnification images in Figure 70(b) show that both samples have grains smaller than 100 nm, while compact 816 also has retained some larger grains/aggregates.

4.4 Sm-Fe-N Composites

Sm-Fe-N composites were formed with $Fe_{16}N_2$ and Fe_4N as the soft phase. The appropriate amount of powder for each phase was placed in a plastic vial with a single steel ball and sealed in an argon environment. The vial was placed in a rotating mixer for 24 hours. The resulting powder mixtures were used in a series of shock compaction experiments. The various experimental conditions are summarized in Table 9. The compositional phase percentages shown for composites containing $Fe_{16}N_2$ are the nominal values, and the actual values measured from XRD are in parenthesis.

Figure 71 shows both the green density after uniaxial pressing at 0.79 GPa and the compact density following shock compaction, with varying amounts of $Fe_{16}N_2$. Increasing the $Fe_{16}N_2$ content

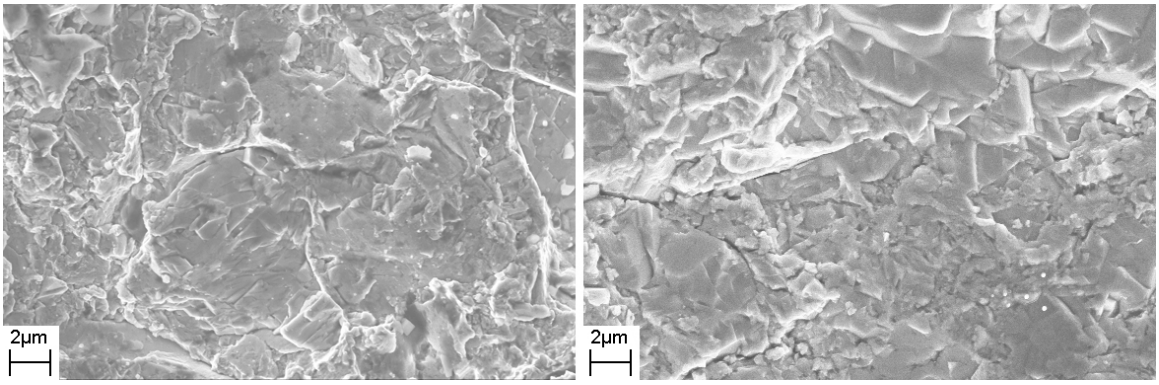

(a) Compact 804 (Left) and 816 (Right) at low magnification

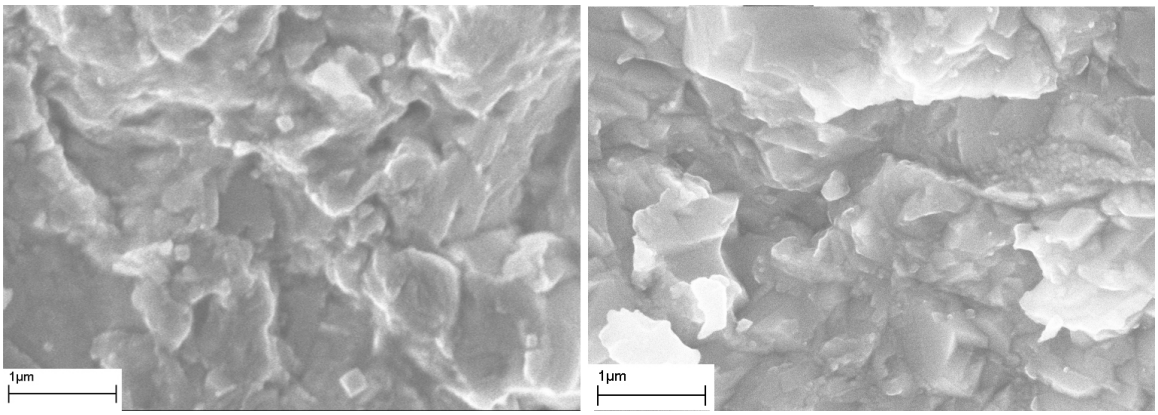

(b) Compact 084 (Left) and 816 (Right) at high magnification

Figure 70: SEM micrographs comparing the fracture surfaces of recovered compacts 804 and 816 at low magnification (a) and high magnification (b)

Table 9: Experimental conditions for shock compaction of Sm-Fe-N composites

Sample Name	$Sm_2Fe_{17}N_3$	$Fe_{16}N_2$	Relative Density	Impact Velocity (m/s)	Pressure (GPa)	Temp (^oC)
Sm-10%16-2 Green	90% (86%)	10%	75%	-	0.79	-122
Sm-10%16-2 Compact	90%	∼0%	∼94%	903 ± 2	8.2-9.1	280-330
Sm-20%16-2 Green	80% (77%)	20%	74%	-	0.79	-122
Sm-20%16-2 Compact	80%	∼0%	∼94%	903 ± 2	8.0-8.7	290-350
Sm-80%16-2 Green	20%	80% (76%)	59%	-	0.79	-126
Sm-80%16-2 Compact	20%	0-15%	∼93%	866 ± 4	5.4-6.0	400-450
Sm-90%16-2 Green	10%	90% (86%)	56%	-	0.79	-126
Sm-90%16-2 Compact	10%	0-15%	∼90%	866 ± 4	5.1-5.6	400-470
Sm-Fe-N/Fe_4N	$Sm_2Fe_{17}N_3$	Fe_4N	Rel. Dens.	Imp. Vel.	Pressure	Temp
Sm10%Fe4N Green	90%	10%	77%	-	0.79	-6
Sm10%Fe4N Compact	-	-	93%	788 ± 10	7.1-8.0	300-350
Sm20%Fe4N Green	80%	20%	79%	-	0.79	-6
Sm20%Fe4N Green	-	-	96%	788 ± 10	7.4-7.9	280-330

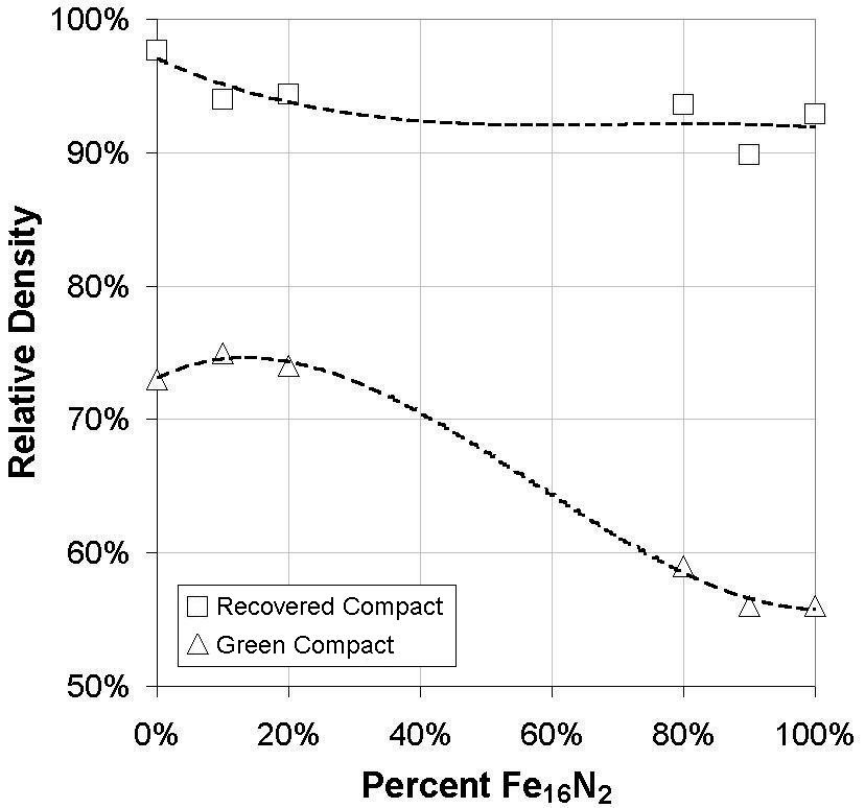

Figure 71: Dependence of green density and recovered compact density of Sm-Fe-N/$Fe_{16}N_2$ composites on $Fe_{16}N_2$ content.

lowers the green density and also the final compact density. The sample containing 10% $Fe_{16}N_2$ (Sm-10%16-2) had the highest relative green density. It is therefore expected to have the lowest shock temperature and be most likely to have no decomposition of the $Fe_{16}N_2$ phase. A temperature range of 280-330^{o}C was estimated for the upper bound of the bulk shock temperature, which is close to the 200-250^{o}C stable range for $Fe_{16}N_2$.

Figure 72 shows the XRD traces for the starting powder and recovered compact of sample Sm-10%16-2. The diffraction peaks for the $Sm_2Fe_{17}N_3$ phase have increased in width, but show no signs of decomposition. This is similar to the results shown previously for the 816 Sm-Fe-N compact in Figure 66. While the starting powder shows two small peaks corresponding to the $Fe_{16}N_2$ phase, no identifiable peaks for the α''-$Fe_{16}N_2$ phase were found in the trace for the recovered compact. The compact was scanned a second time at scan speed four times slower over the 68-70 and 97-99 angle ranges, in order to detect trace amounts of $Fe_{16}N_2$ diffraction peaks. These regions correspond to $Fe_{16}N_2$ peaks (004) and (422), two peaks that do not overlap any $Sm_2Fe_{17}N_3$ peaks; however, no $Fe_{16}N_2$ peaks were found in the rescaned trace.

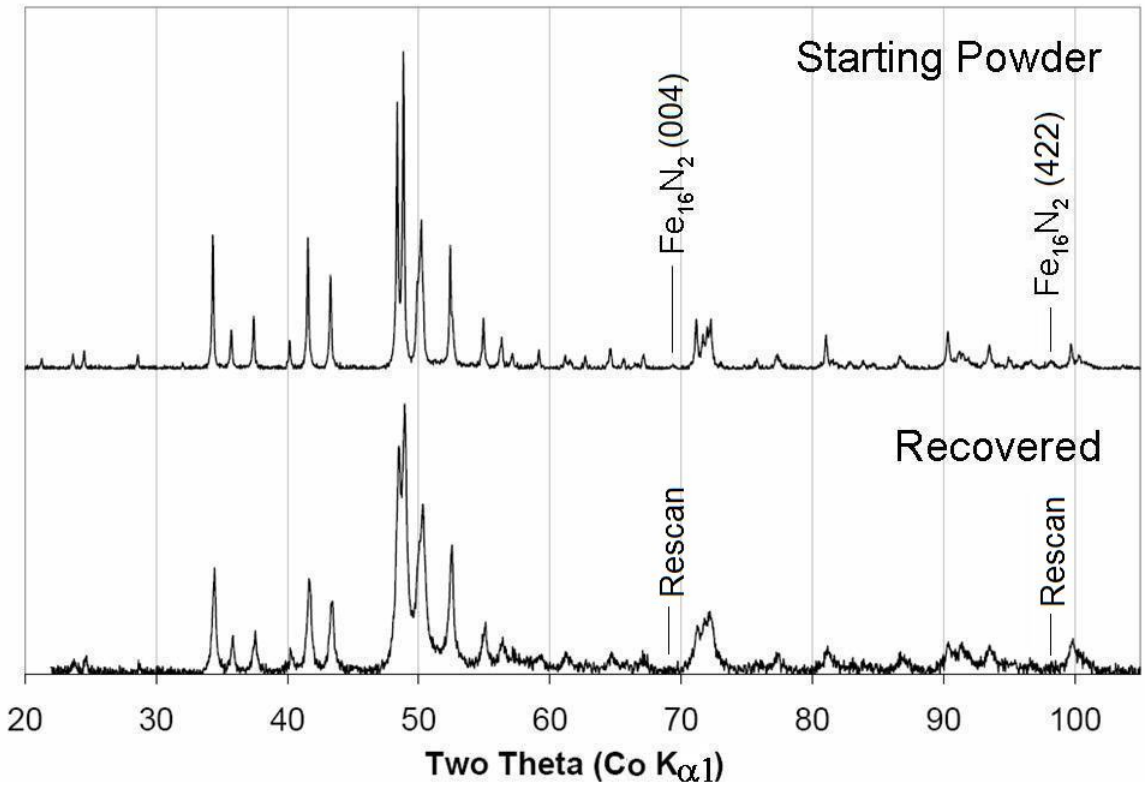

Figure 72: XRD traces of the starting powder, containing 90% $Sm_2Fe_{17}N_3$ and 10% $Fe_{16}N_2$, and the corresponding recovered compact, Sm-10%16-2. Two diffraction peaks belonging to $Fe_{16}N_2$ which do not over lap any peaks corresponding to $Sm_2Fe_{17}N_3$, are indicated.

Figure 73 shows the microstructure of the recovered compact Sm-20%16-2. EDS performed on the pictured area detected two distinct regions. Ignoring lighter elements, one region was determined to contain only iron while a second region had both samarium and iron. The iron only region corresponds to a fine structure similar to $Fe_{16}N_2$. This suggests that clusters of $Fe_{16}N_2$ are present in the microstructure and that the rotational mixing method used prior to compaction may not have produced a well dispersed distribution of the soft phase.

Samples with a higher % of $Fe_{16}N_2$ show a similar behavior in XRD traces. Figure 74 shows the XRD traces for the Sm-80%16-2 and Sm-90%16-2 recovered samples. The $Sm_2Fe_{17}N_3$ peaks show an increase in peak width but show no indications of a phase change. The $Fe_{16}N_2$ peaks have a similar pattern to the unmixed $Fe_{16}N_2$ in that the α-Fe lines have increased in intensity and new diffraction peaks for Fe_4N peaks have appeared. Quantitative phase analysis was performed on these XRD traces using the $\alpha(110)$, assuming the contribution from the α'' (220) peak is small, and the $Sm_2Fe_{17}N_3$ (113) peak, since this peak does not overlap any diffraction peaks for Fe_4N or FeN. This

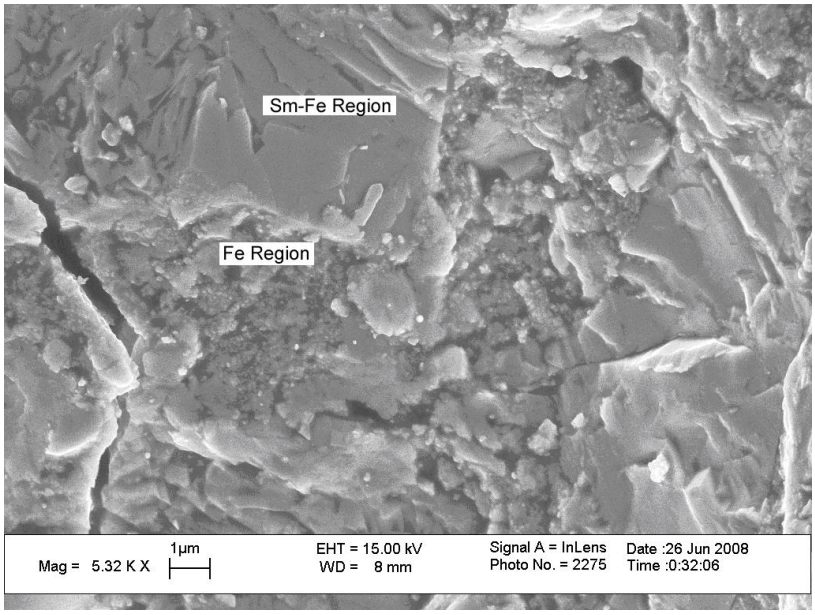

Figure 73: SEM micrograph of shock compact #816-2, containing 80% $Sm_2Fe_{17}N_3$ and 20% $Fe_{16}N_2$. EDS of two regions detected one area with samarium and iron and a second with only iron, corresponding to a fine structure similar to $Fe_{16}N_2$.

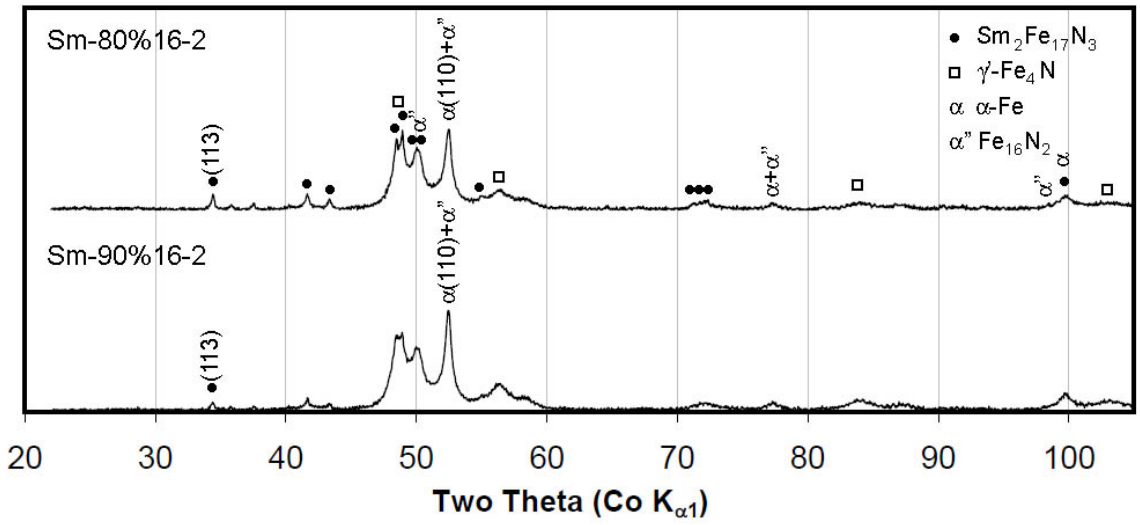

Figure 74: XRD traces of recovered compacts Sm-80%16-2 and Sm-90%16-2 after crushing a section of each sample into a powder.

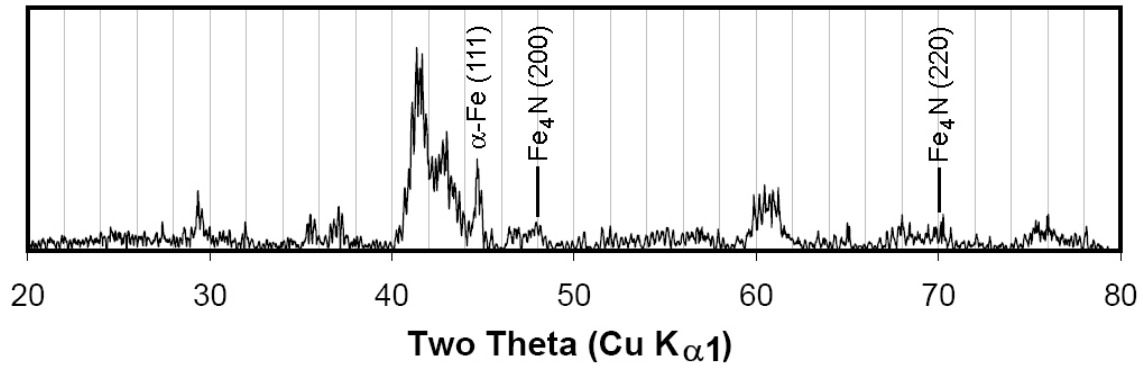

Figure 75: XRD trace of recovered compact 677-1, a Sm-Fe-N / Fe_4N composite containing 20% Fe_4N in the green state. Partial retention of the Fe_4N phase is shown by peaks at 48 and 70 degrees.

analysis shows that the ratio of $Sm_2Fe_{17}N_3$ to α-Fe in the Sm-80%16-2 compact is roughly twice that of the Sm-90%16-2 compact. This result is expected if one assumes that there is little or no decomposition of the $Sm_2Fe_{17}N_3$ phase and that the decomposition of α'' phase produces roughly the same proportion of α-Fe in each compact.

Shock compaction experiments were also performed on mixtures of $Sm_2Fe_{17}N_3$ and Fe_4N. As discussed in Section 4.1, Fe_4N will partially transform during shock compaction into Fe_3N. However, the results shown in Figure 59 reveal that the transformation did not run to completion in that case. The sample was still comprised mostly of Fe_4N. Figure 75 shows the XRD trace of compact Sm-20%Fe4N; however the XRD pattern for the starting material is not available. The XRD trace in Figure 75 contains two minor peaks for Fe_4N, (200) and (220) at 48 and 70 degrees respectively. This indicates at least partial retention of the Fe_4N phase. An estimation of the amount retained is difficult, since the strongest line for Fe_4N overlaps the strongest line for $Sm_2Fe_{17}N_3$. No evidence of Fe_3N in detectable amounts is apparent in the XRD trace.

4.5 Nd-Fe-B

Shock compaction experiments were performed on several different forms of Nd-Fe-B. Table 10 summarizes the different materials tested and the experimental conditions. In addition to the as-received materials described in section §3.1.4 (HDDR, NRL-melt-spun, and nonporous-commercial), shock experiments were also performed on attrition milled powder. For comparison purposes, HDDR powder was processed both by high-energy ball milling and attrition milling. Figure 76(a) shows XRD traces for the as-received material and samples that have been attrition milled for 40 and 185 hours. Attrition milling for 185 hours produces very little increase in the width of the diffraction

Table 10: Experimental conditions for shock compaction of Nd-Fe-B

Sample Name	Description	Relative Density	Impact Velocity (m/s)	Pressure (GPa)	Temp (^{o}C)
826-3 Green	As-Rec HDDR	75%	-	0.79	RT
826-3 Compact	As-Rec HDDR	99%	722 ± 4	5.6-5.7	310-330
1127-2 Green	Attrition Milled Aligned	∼62%	-	0.2	RT
1127-2 Compact	Attrition Milled Aligned	∼90%	700 ± 3	3.9-4.3	350-370
1113-1 Green	Attrition Milled	68%	-	0.79	RT
1113-1 Compact	Attrition Milled	88%	978 ± 9	8.1	550
826-2 Green	NRL Melt Spun	78%	-	0.79	RT
826-2 Compact	NRL Melt Spun	96%	722 ± 4	6.2-6.6	300-320
1127-1 Green	Commercial	100%	-	0	RT
1127-1 Compact	Commercial	100%	700 ± 3	11	160

peaks. Attrition milling was performed up to 400 hours, and the corresponding XRD trace appeared similar to the 185 hour scan. Figure 76(b) displays XRD traces for the high-energy ball milled powder. As milling time increases, diffraction peak width increases as compared to the as-received powder. At 8 hours of milling time, the diffraction pattern resembles that of an amorphous material, lacking clear diffraction peaks.

Figure 77(a) compares SEM images of the Nd-Fe-B starting powder with attrition milled powder. The original grain size shown in the high magnification inset approximately matches the particle size of the attrition milled material. In the high energy ball milled material shown in Figure 77(b), the particle size, 1-4 μm, is significantly larger than the original grain size, 200-400 nm. Thus, attrition milling has produced particles similar in morphology to the original grain size. Given the relatively small amount of diffraction peak broadening in the XRD trace, the attrition milled particles are most likely single crystal particles. High-energy milling produces polycrystalline particles with a typical size of 1-4 μm.

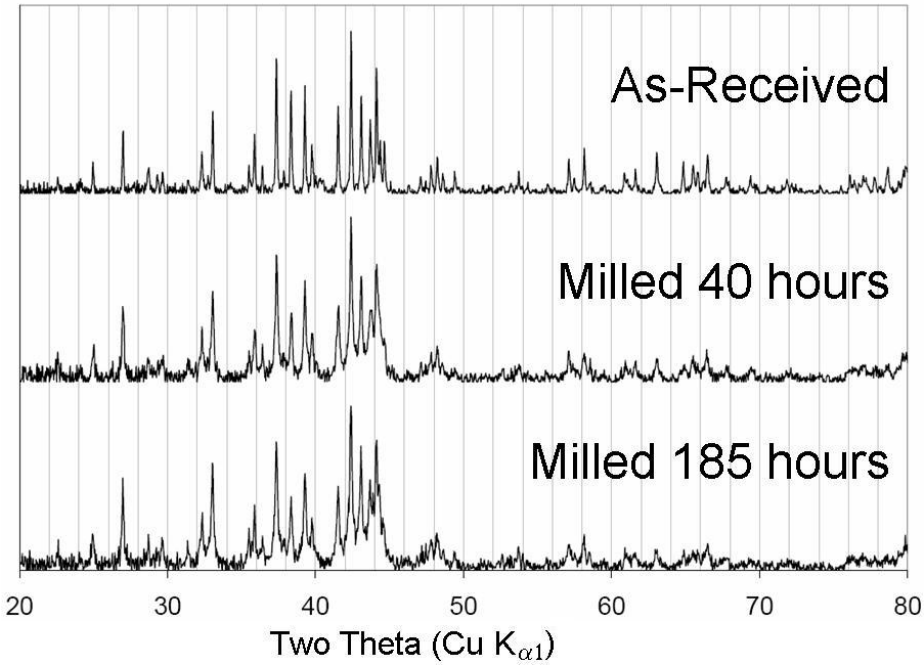

(a) XRD traces of attrition milled HDDR Nd-Fe-B powder (a) as-received (b) milled for 40 hours and (c) milled for 185 hours.

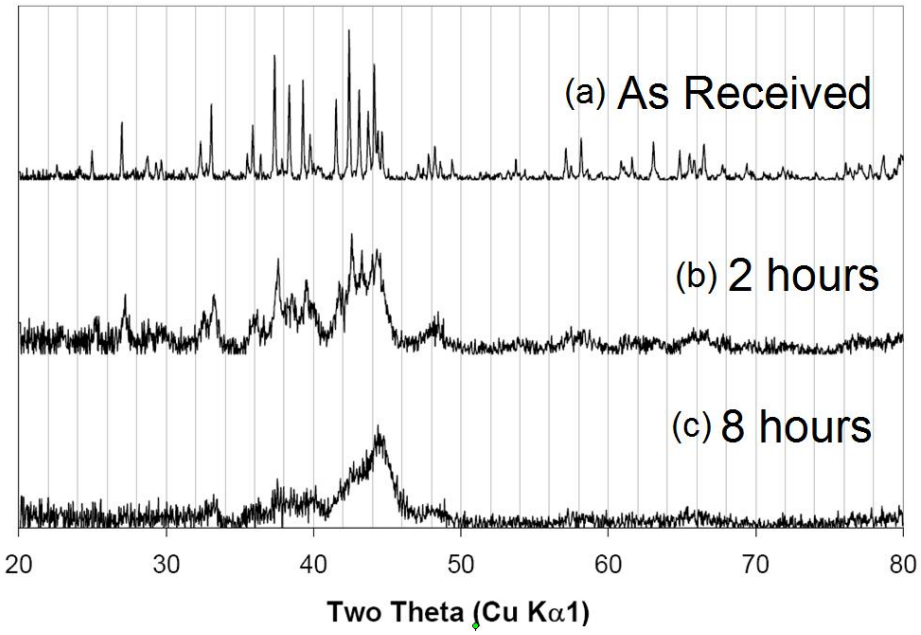

(b) XRD traces of high-energy milled HDDR Nd-Fe-B powder (a) as-received (b) milled for 2 hours and (c) milled for 8 hours.

Figure 76: XRD traces of attrition milled and high-energy ball milled HDDR Nd-Fe-B powder.

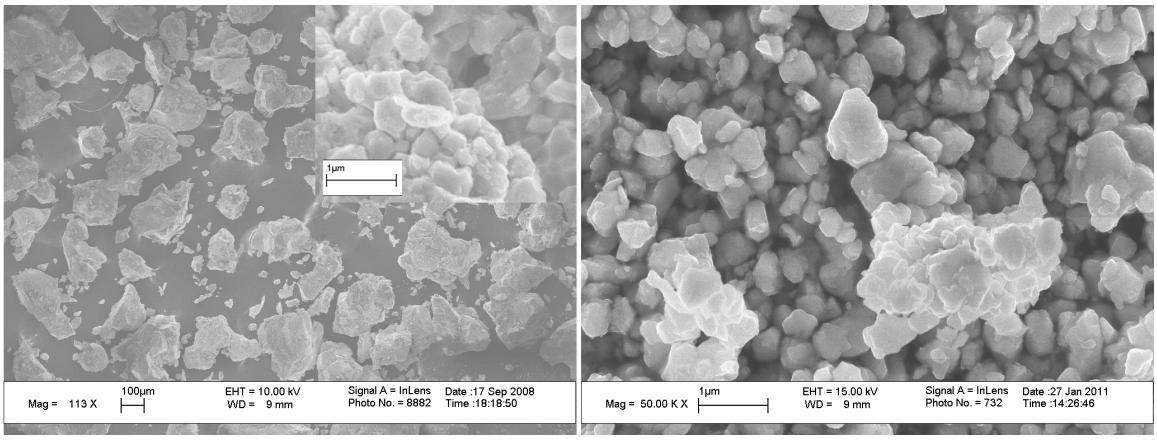

(a) Nd-Fe-B starting powder with high mag inset (left) and attrition milled powder (right)

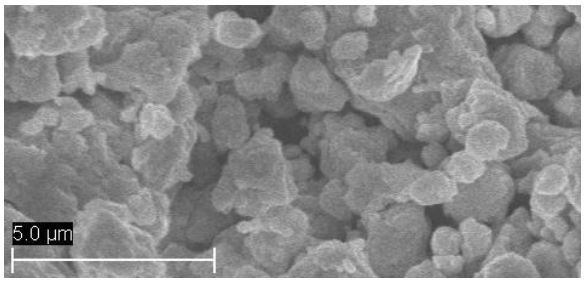

(b) SEM image of HDDR Nd-Fe-B powder high energy ball milled for 12 hours.

Figure 77: (a) SEM images of HDDR Nd-Fe-B starting powder with high magnification inset (left) and powder after 185 hours of attrition milling (right) (b) SEM image of HDDR Nd-Fe-B powder high energy ball milled for 12 hours.

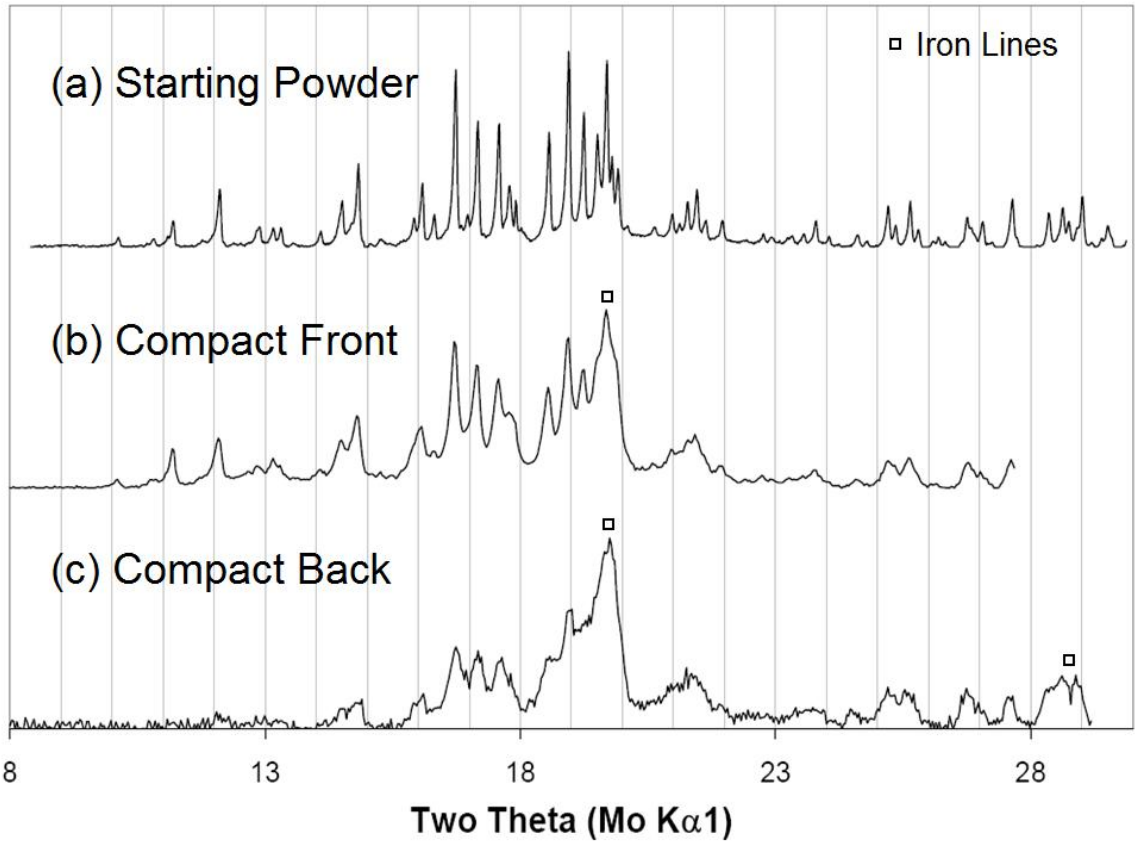

Figure 78: XRD traces of (a) Nd-Fe-B HDDR starting powder (b) front (impact) side of recovered compact (c) back side of recovered compact

Figure 78 shows the XRD traces of the 826-3 starting powder (as-received HDDR powder) and traces of the impact side and back side of the recovered compact. Two effects are seen in the XRD traces of the recovered compact. The width of the diffraction peaks have increased relative to the starting powder, and the peaks which overlap α-Fe (Iron) diffraction lines have increased in intensity relative to the Nd-Fe-B diffraction lines. These effects are even more prominent for the back side of the compact, which is expected to experience a higher pressure due to the effects of radial focusing and wrap-around of the shock waves.

While performing a Williamson-Hall analysis of the XRD scans, it was noted that several of the diffraction peaks for the 826-3 starting powder (HDDR powder) had several peak widths smaller than the LaB_6 standard. Figure 79(a) plots the peak widths verses two theta position for both the starting powder and the LaB_6 standard. The curve shown in the plot is a second order polynomial trend line fit to the LaB_6 standard points. The peak widths for the 826-3 starting powder fall roughly around this line. This indicates that the peak widths measured in the starting powder scan

are due primarily to instrumental broadening and that the points with peak widths smaller than the LaB_6 standard are due primarily to scatter in the data.

The Williamson-Hall plot for 826-3 compact front scan and the as-received powder are shown in Figure 79(b). Peak widths in the as-received scan that are smaller than the LaB_6 standard are plotted as zero. While there is a large amount of scatter in the data, the Williamson-Hall analysis shows that increase in diffraction peak width from the as-received scan to the 826-3 Front scan is due mainly to a decrease in grain size. The intercept of the 826-3 front trend line could reasonable fall in the range of 0.002-0.004, which corresponds to a grain size of 15-30 nm. The large amount of overlap between peaks in the XRD trace for the back side of the compact makes performing a Williamson-Hall analysis difficult and prevents drawing any meaningful conclusions.

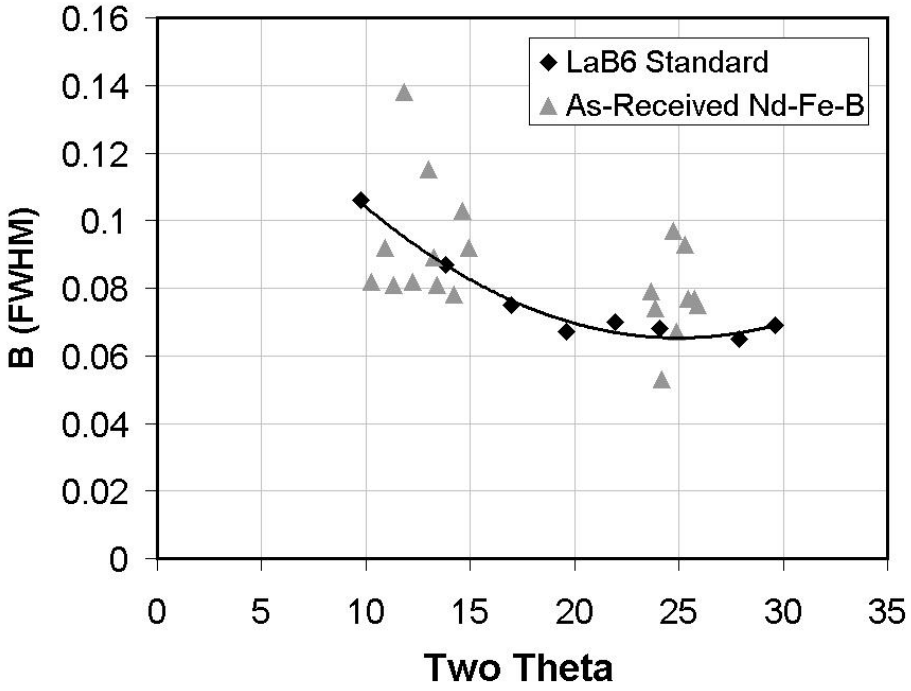

(a) Comparison of diffraction peak widths

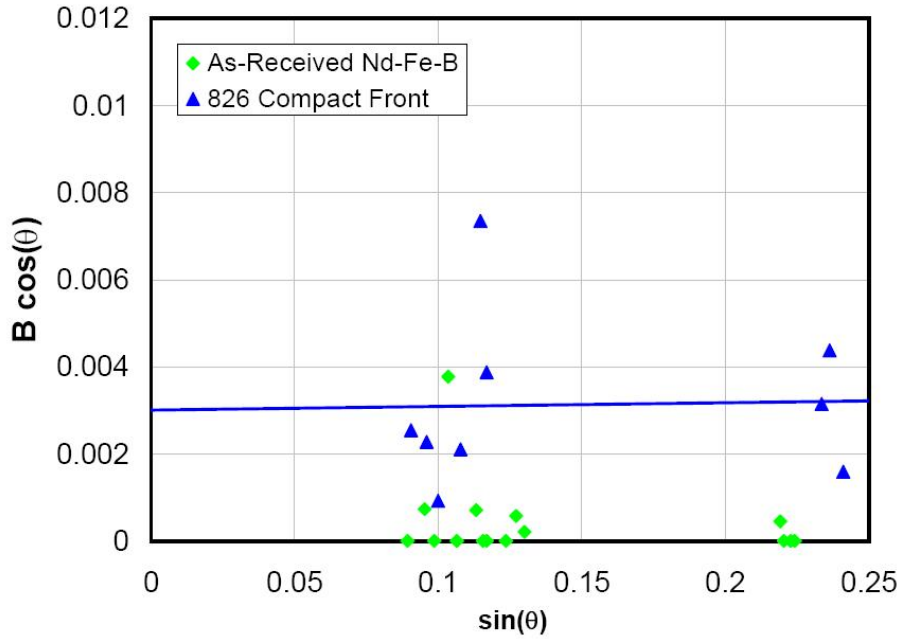

(b) Williamson-Hall plot

Figure 79: (a) Comparison of diffraction peak widths of as-received HDDR Nd-Fe-B and a LaB_6 standard. The trend line shown is the best fit line for the LaB_6 sample. (b) Williamson-Hall plot of the as-received HDDR and the front of compact 826-3. Peak widths which are smaller than the LaB_6 standard are plotted as zero.

Figure 80 shows SEM images of the starting powder and recovered compact 826-3. The HDDR microstructure, shown in part (a) of the figure, has a fairly uniform grain size of approximately 300-400 nm. Part (b) of the figure shows the fracture surface of the recovered compact. While portions of the compact have retained the original microstructure of the starting powder, other portions show regions of localized deformation in which the Nd-Fe-B grains have broken up into much smaller grains. This is most likely the source of the diffraction peak broadening seen in Figure 78.

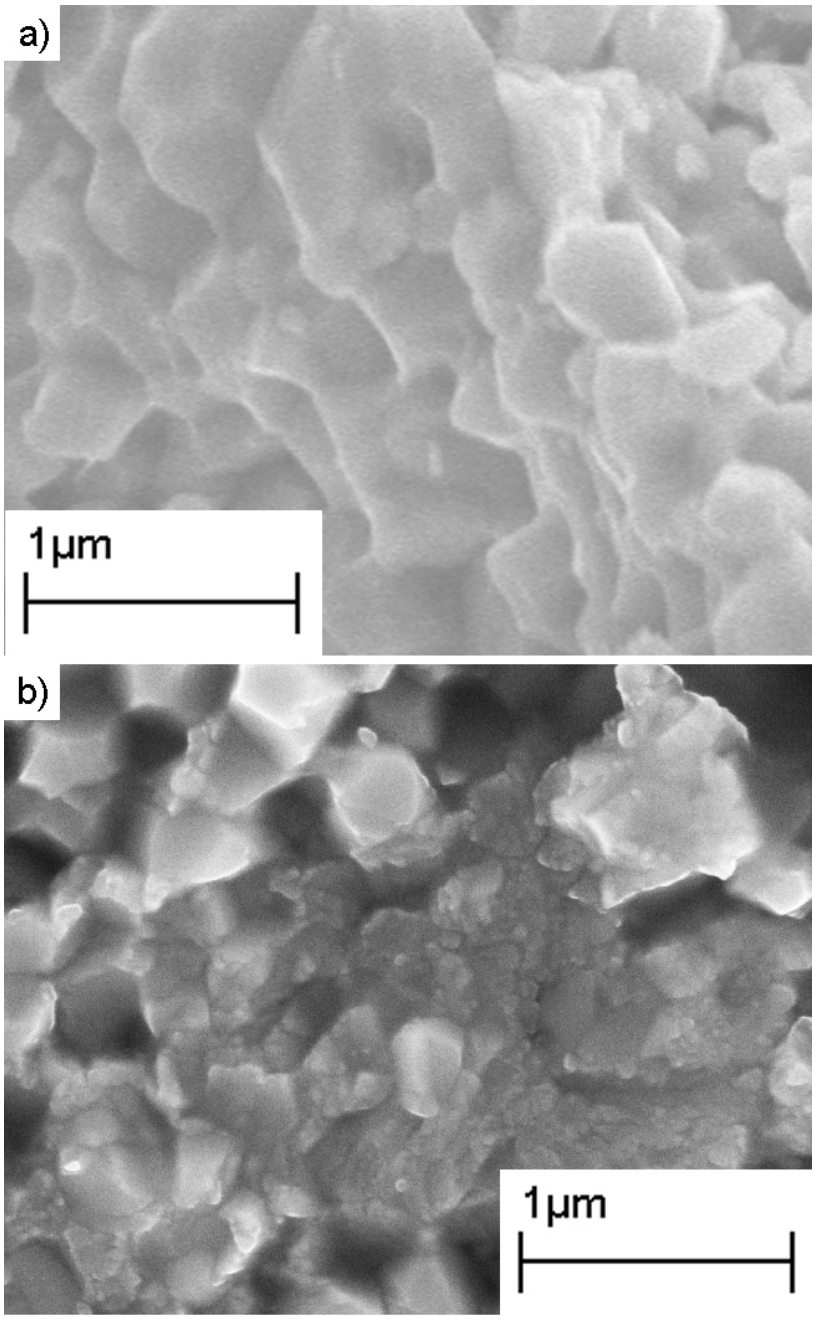

Figure 80: SEM images of HDDR Nd-Fe-B starting powder (a) and fracture surface of recovered compact (b) following shock compaction at 722 m/s.

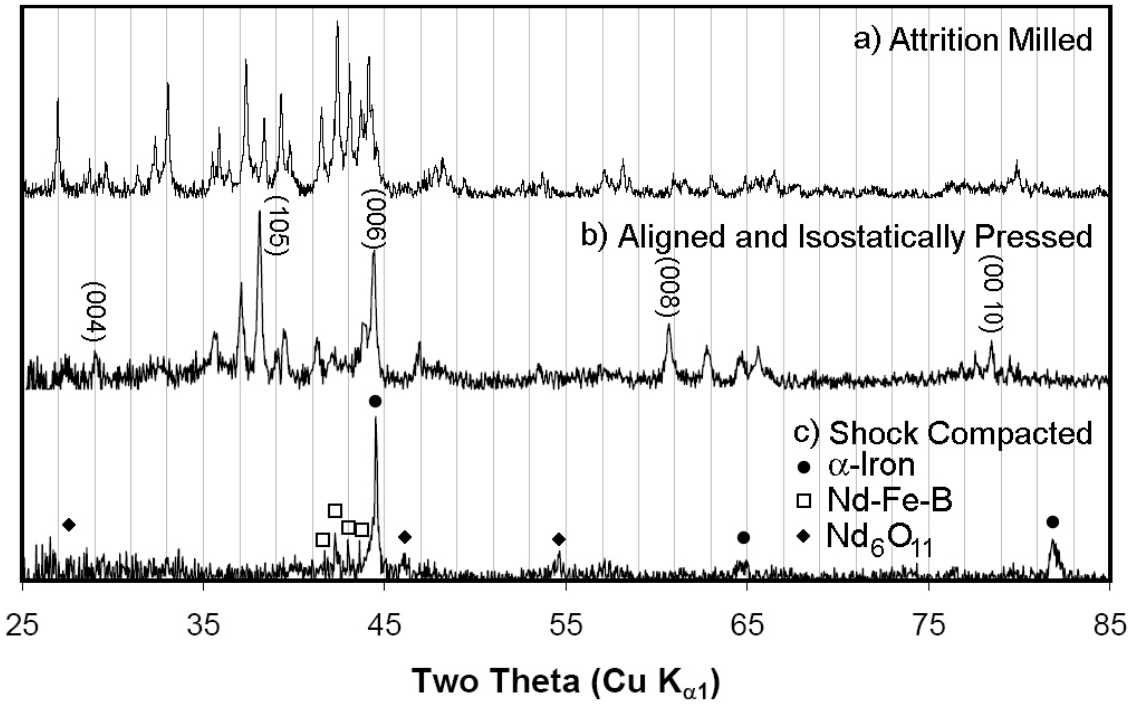

Figure 81: XRD patterns for (a) attrition milled Nd-Fe-B powder, (b) aligned and isostatically pressed pellet 1127-2 Green, and (c) sample 1127-2 following shock compaction.

A subsequent compaction experiment was performed on HDDR Nd-Fe-B powder that had been attrition milled for 185 hours. The attrition milled particles were aligned in a magnetic field and isostatically pressed prior to the shock compaction. Figure 81 shows the XRD traces of the pre-aligned pellet and the recovered shock compact. The XRD trace shown for the shock compacted sample 1127-2 was measured on a cross section of the compact that was then crushed into a powder using a mortar and pestle. The field alignment has increased the $(00c)$ family of peaks. Decomposition has occurred similar to the one observed for the unmilled powder shown in Figure 78. Diffraction lines corresponding to α-Fe have appeared; however, in this case, the α-Fe phase has become the dominant phase. In addition, broad XRD lines for Nd_6O_{11} have formed. Thus it appears that a decomposition has occurred in which the $Nd_2Fe_{14}B$ phase forms α-Fe and an amorphous Nd-Fe phase. The amorphous Nd-Fe phase will quickly oxidize when exposed to air, which occurs when the sample is removed from the capsule via machining.

Figure 82 shows SEM micrographs of the recovered compact 1127-2. Two distinct regions can be observed. The type A regions have 200-400 nm grains, similar to the starting powder. The type B regions correspond to the larger (1-5 μm) dark spots. EDS analysis performed on these these regions

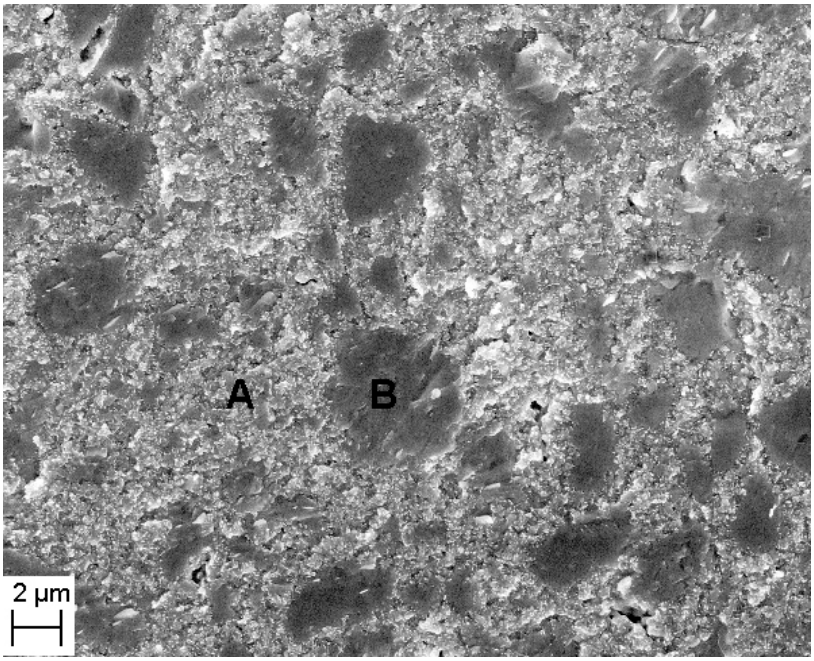

(a) 5kX

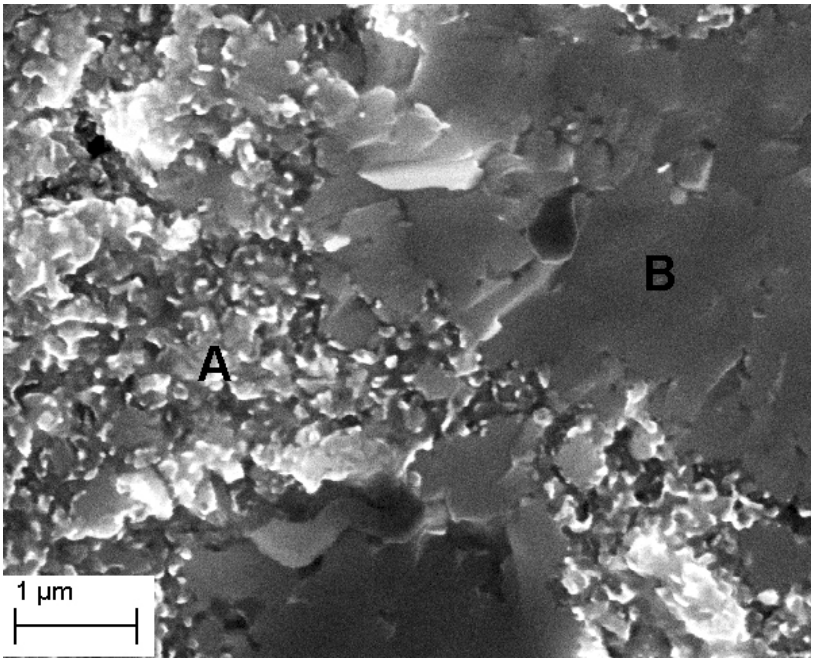

(b) 25kX

Figure 82: SEM micrographs of attrition milled and shock compacted Nd-Fe-B at (a) 5kX and (b) 25kX. Two types of microstructural features are seen. Type A regions, consisting of 200-400 nm grains, and type B regions, corresponding to the larger (1-5 μm) spots.

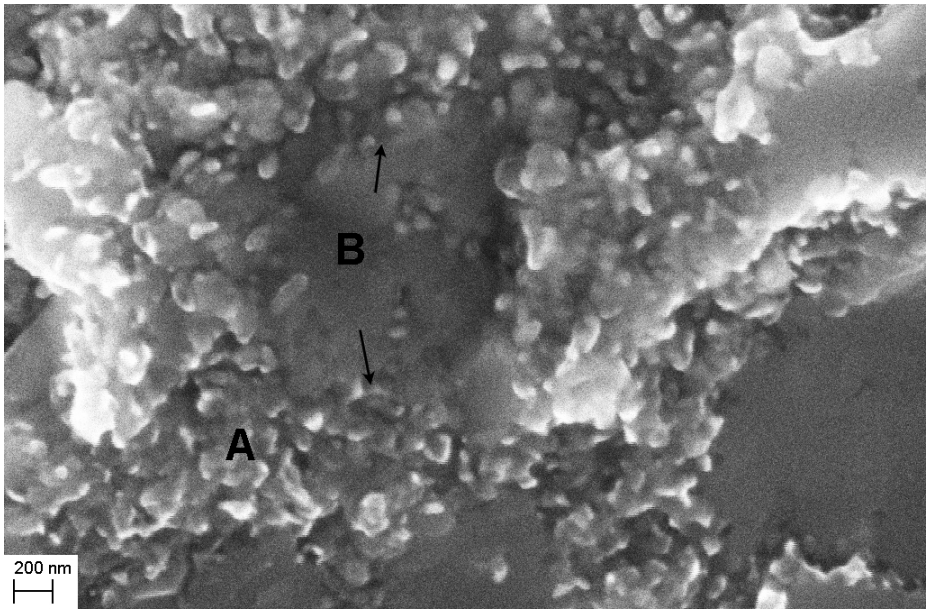

Figure 83: High magnification SEM micrograph of the attrition milled and shock compacted Nd-Fe-B. Areas of localized deformation are seen to blend into areas which retain features of the original particle morphology.

indicated the composition of the larger, darker areas are very similar to the surrounding regions; both contain approximately the same amount of Nd and Fe. The higher magnification image in Figure 82(b) shows that the type A regions, in addition to 200-400 nm grains, also have smaller features $\sim$ 50 nm in size. The type B regions have no distinct grain features, even though they are several times larger than the original particle size.

Figure 83 shows a high magnification image of the recovered compact 1127-2. The micrograph shows two different kinds of microstructural areas (A and B), similar to the previous micrographs; however, in this image the two areas can be seen to blend together at the borders, as indicated by the arrows. Similarly, the small grains in region A, lacking distinct grain outlines, blend together as well.

An additional shock compaction experiment was performed on attrition milled powder at 980 m/s. The powder was not pre-aligned and was pressed directly into the shock capsule. Figure 84 shows the XRD traces for the attrition milled powder and the shock compacted sample 1113-1. A shock pressure and temperature of 8.3 GPa and 570^{o}C were estimated. In this sample, the $Nd_2Fe_{14}B$ has almost completely decomposed; only the highest intensity diffraction line, the (410) line, is observed for the $Nd_2Fe_{14}B$ phase. The α-Fe and neodymium-oxide products match the other identifiable diffraction peaks.

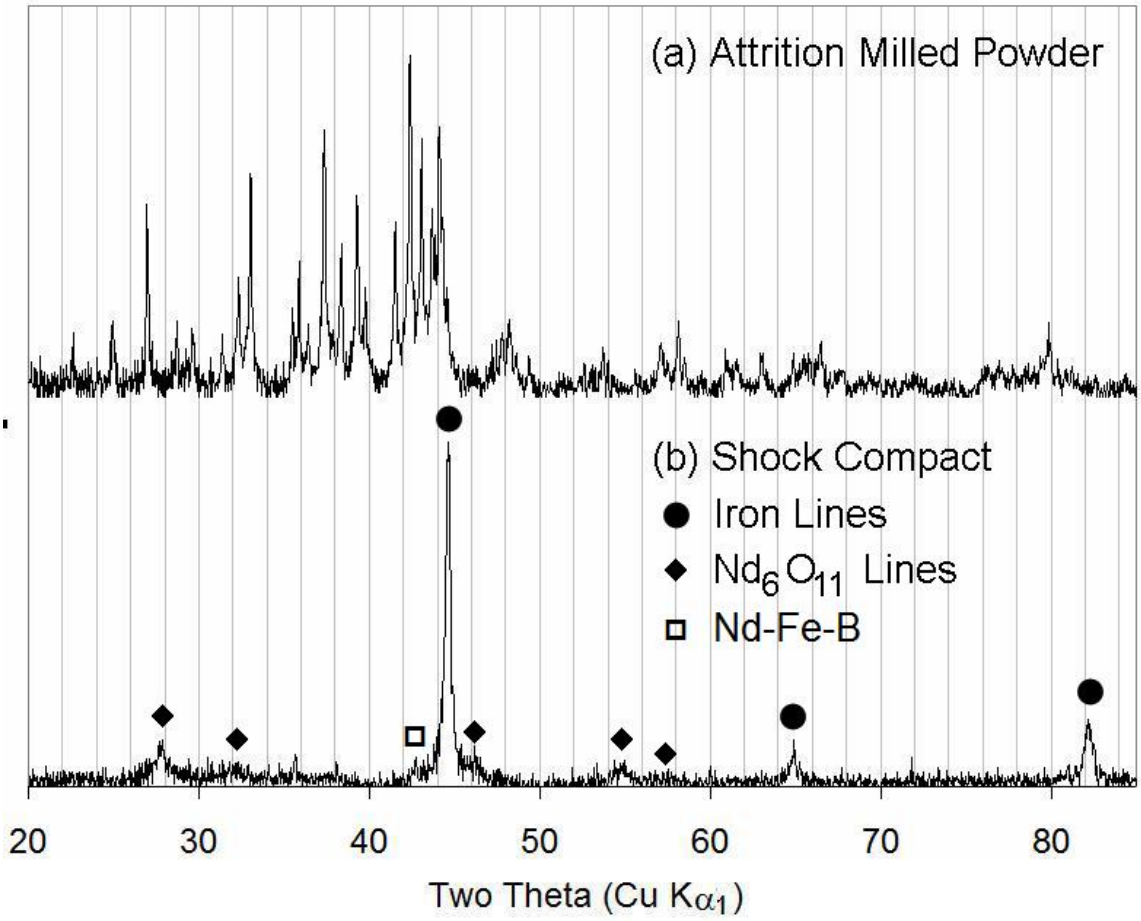

Figure 84: XRD traces of (a) attrition milled Nd-Fe-B powder and (b) the recovered compact. α-Fe diffraction lines are marked with a circle, and neodymium oxide peaks are marked by a diamond.

Effects similar to those observed for the HDDR powder are seen for melt-spun ribbons. Melt-spun Nd-Fe-B ribbons of composition $Nd_{15}Fe_{79}B_6$ were provided by the Naval Research Laboratory. The ribbons were crushed using a mortar and pestle and pressed to a green density of 78%. The sample was shock compacted in the same experiment as the HDDR powder, which was performed at 722 m/s. The recovered compact, called 826-2, was 96% dense. Comparing the as-received grain size to the shock compacted grain size is difficult for this material, because of the non-uniform structure.

Figure 85 shows the XRD traces of the crushed ribbons and the front and the back of the recovered shock compact 826-2. The diffraction pattern of the starting powder already has significant peak width as compared to the HDDR starting powder shown in Figure 78. Therefore, an increase in peak width in the recovered sample would be less noticeable. The pattern for the front of the compact shows no significant difference in peak widths as compared to the staring powder; however,

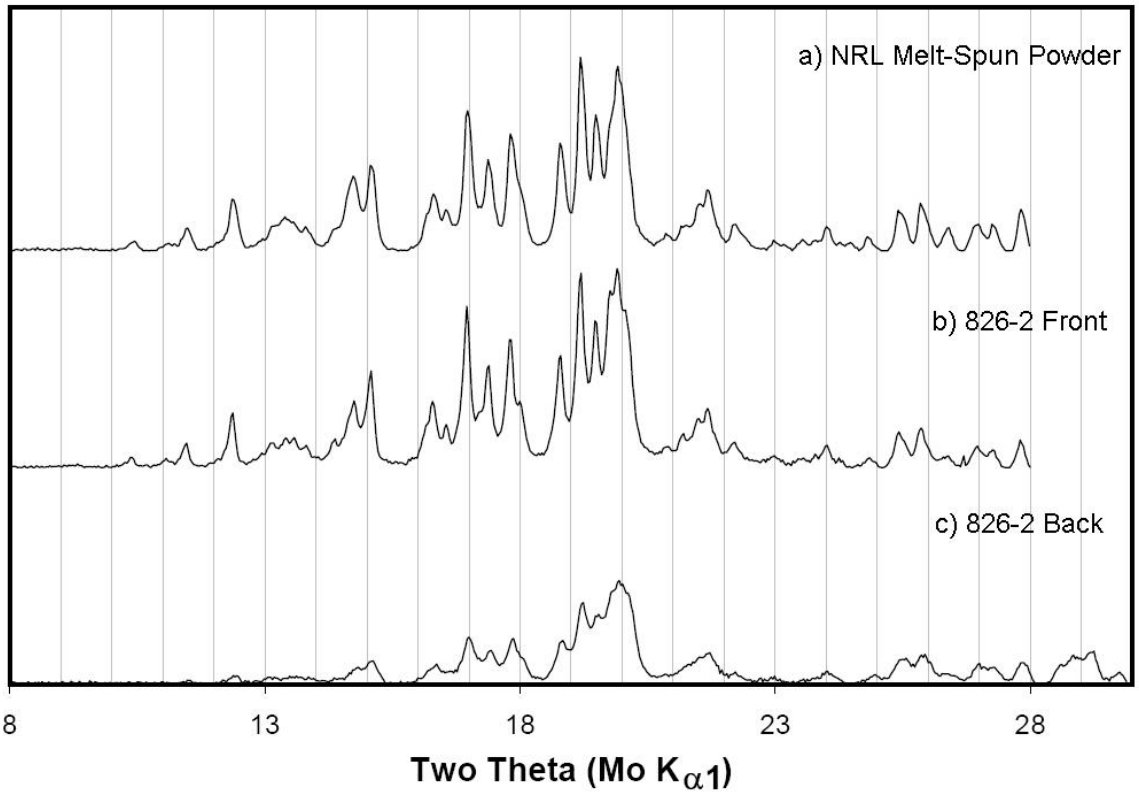

Figure 85: XRD traces of the crushed melt spun Nd-Fe-B ribbons provided by NRL (a) and the front (b) and back (c) of compact 826-2

the back of the sample, which is expected to have a higher pressure due to radial focusing effects, does have significantly broader peaks. Attempts at a Williamson-Hall analysis did not provide meaningful results due to the amount of overlap between peaks. Similar to the results for compact 826-3, the peak at 20^o, which corresponds to the 100% peak for α-Fe, has increased in the scan for both the front and the back of the compact, relative to the starting powder, indicating a partial decomposition.

A shock compaction experiment (1127-1) was performed on the N42 grade commercial and non-porous Nd-Fe-B at 700 m/s. The steel shock capsule was modified so that a 1/2 inch diameter and 3/16 inch thick Nd-Fe-B sample would have a tight slip fit inside. Since the material is non-porous, it will have a higher shock impedance, leading to a higher shock pressure, $\sim$ 11 GPa, than is typically experienced for shock compaction of powders. The shock impedance will more closely match the surrounding steel and therefore will minimize radial focusing pressure spikes. The shock temperature is also be considerably lower, $\sim 160^o$C, due to the higher initial density.

Figure 86 shows the XRD traces of the as-received and shock compressed samples. There is

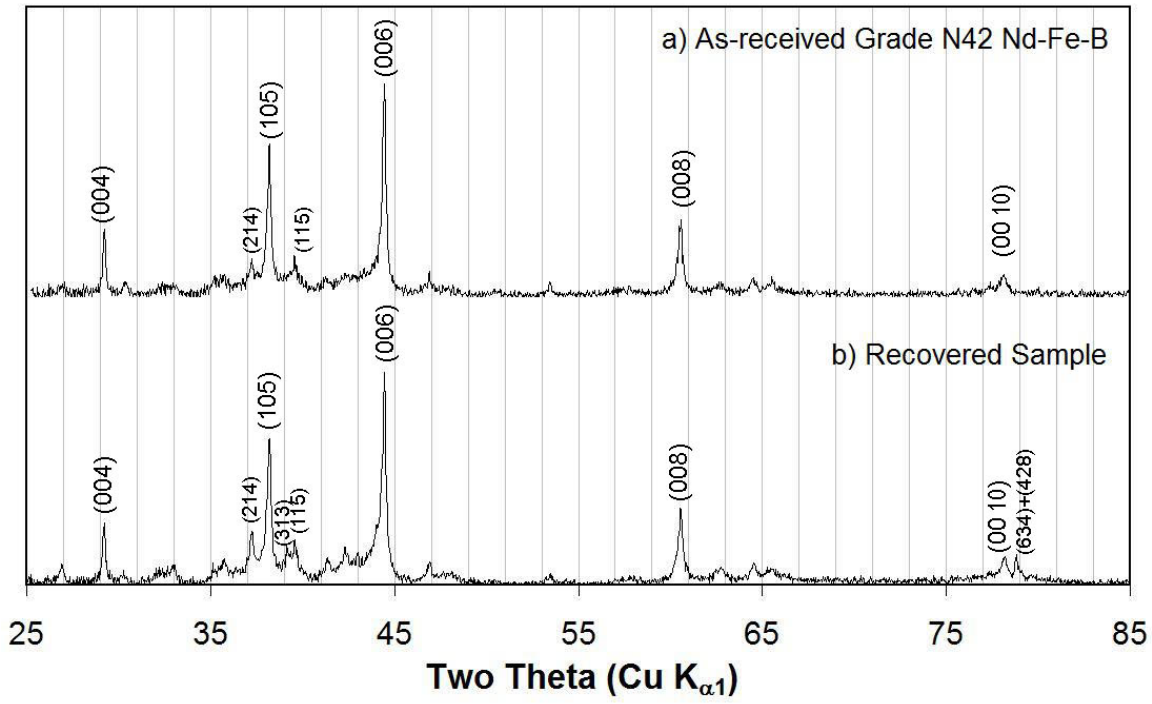

Figure 86: XRD traces of (a) as-received grade N42 non-porous Nd-Fe-B and (b) recovered material

slight decrease in texture for the shock compressed sample, as shown by the relative increase in size of the non-(00c) peaks as compared to the (105) or (00c) peaks, but there is no evidence of decomposition.

Parallel plate VISAR experiments were performed on N52 grade commercial Nd-Fe-B at 420 and 657 m/s. Figure 87 shows the VISAR traces converted from free surface velocity to pressure-time plots. The Nd-Fe-B Hugoniot was used to calculate pressure from the particle velocity measured by the VISAR. Both samples show an elastic-to-plastic transition (HEL) at 1.8 GPa. A second transition is also reveled in the VSAR traces occurs at ∼4.8 GPa.

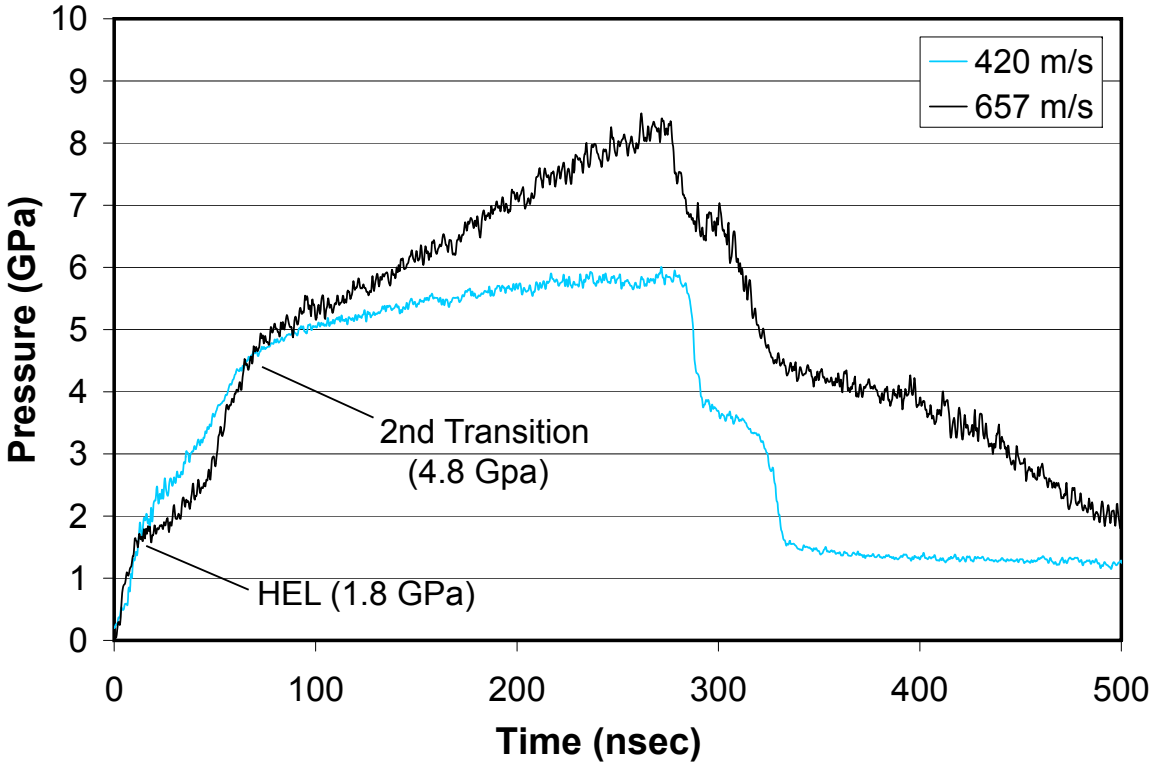

Figure 87: VISAR traces of symmetric parallel plate impact experiments on commercial Nd-Fe-B samples using impact velocities of 420 m/s and 657 m/s. The elastic to plastic transition (HEL) is marked, along with a second transition in mechanical behavior.

Portions of the flier plate and VISAR sample were recovered from the 420 m/s experiment in the form of both loose powder debris and sections of the flier plate embedded in the aluminum sabot, which is shown in Figure 88(a). No Nd-Fe-B material was recovered from the 657 m/s experiment. The XRD traces for both types of recovered sample are shown in Figure 88(b) along with the XRD pattern of the starting material. The XRD pattern of the loose debris shows no indication of texture and no evidence of a decomposition. This result is similar to what would be expected if one had ground the starting material into a powder without shock compression. The pattern for material embedded in the aluminum sabot shows a large degree of diffraction peak broadening, but also no clear indication of decomposition. Since this experiment was performed at a low impact velocity, it is possible that only a small percentage of the material experienced any decomposition.

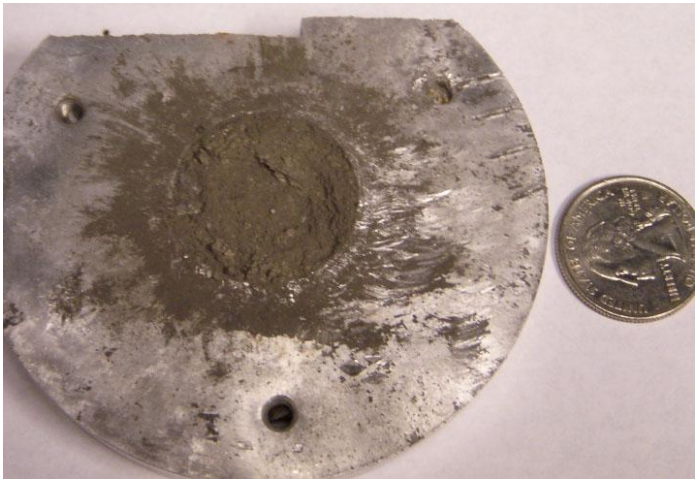

(a) Recovered flier plate from 420 m/s VISAR experiment

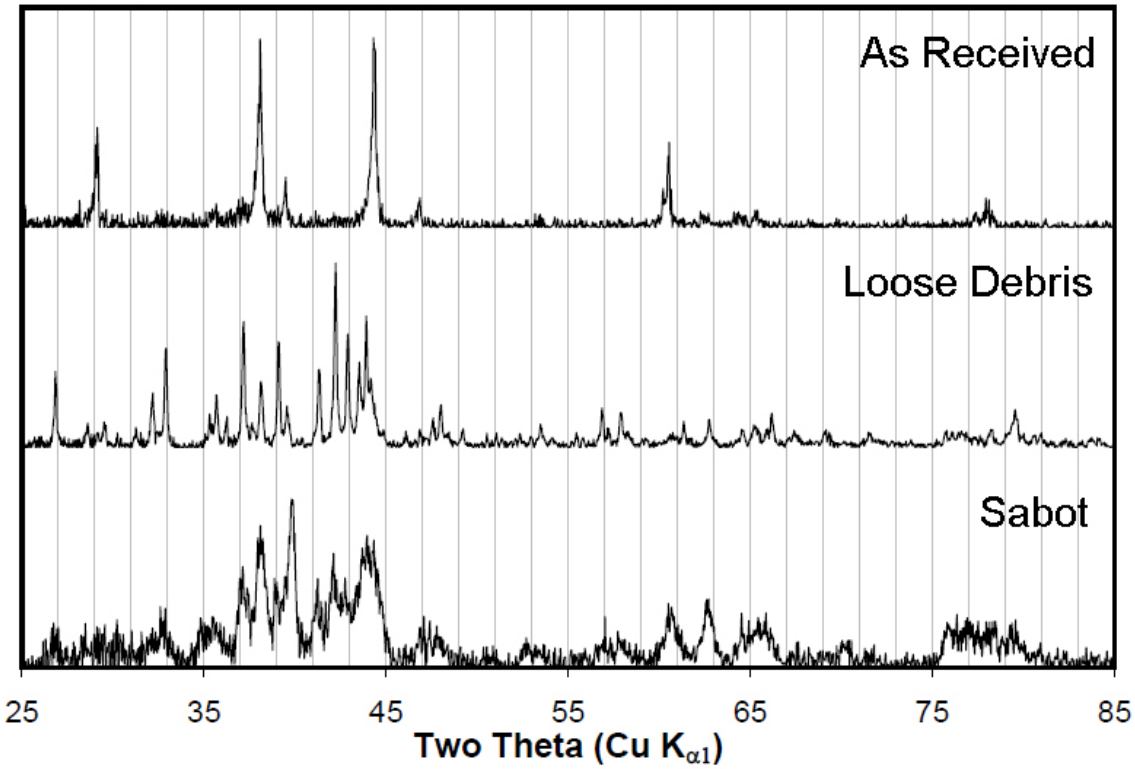

(b) XRD traces of as-received commercial Nd-Fe-B, recovered loose debris, and recovered sample embedded in the sabot.

Figure 88: (a) Image of recovered Nd-Fe-B flier plate material embedded in an aluminum sabot and (b) corresponding XRD traces starting material, loose debris, and material embedded in the sabot.

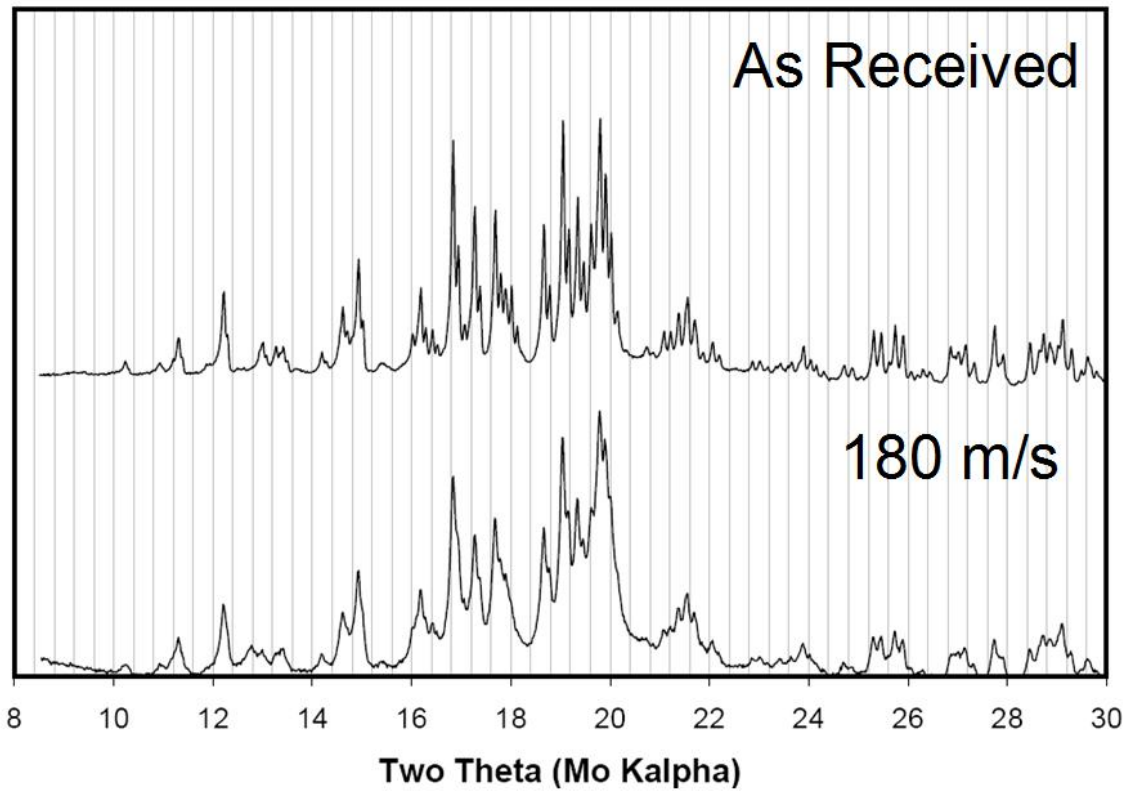

Figure 89: XRD traces of (top) as-received HDDR Nd-Fe-B powder and (bottom) compact forged at 180 m/s.

4.5.1 High Rate Forging of Nd-Fe-B

High-rate forging experiments were performed on HDDR Nd-Fe-B powder. Figure 89 shows the XRD traces of the as-received powder and a powder compact forged at 183 m/s. Forging produces a broadening in the XRD peaks; however, no increase in the intensity of the (00c) family of diffraction peaks is detected.

Figure 90(a) shows an SEM micrograph of an HDDR compact forged at 198 m/s that has been cross sectioned perpendicularly to the impact face and polished. Significant porosity can be seen in the cross section, and the back (non-impact) side of the compact has more free particle surfaces than the impact side, which is most likely a product of the non uniform pressure and strain rate of the forging processes. The higher magnification micrograph shown in Figure 90(b) shows the microstructure of the forged compact. There is no indication of elongated grains perpendicular to the forging direction, suggesting an isotropic microstructure.

While the powder compact became embedded in the copper for high velocity forging experiments on Pr-Fe-B/α-Fe composites, higher velocity forging experiments on the HDDR powder were fused

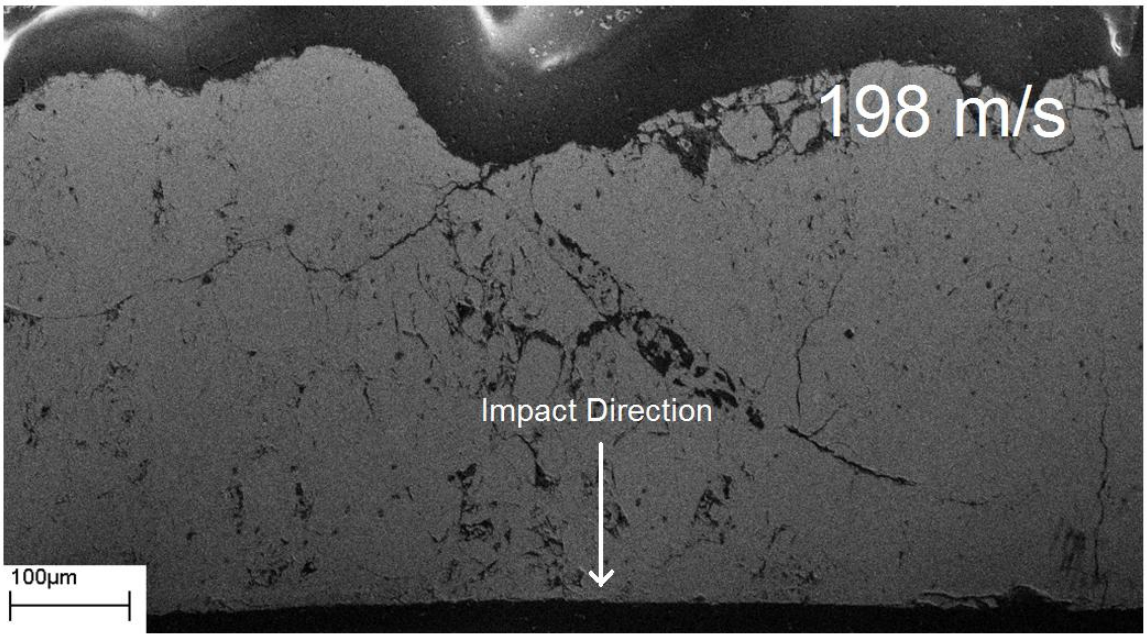

(a) Polished cross section of HDDR compact forged at 198 m/s

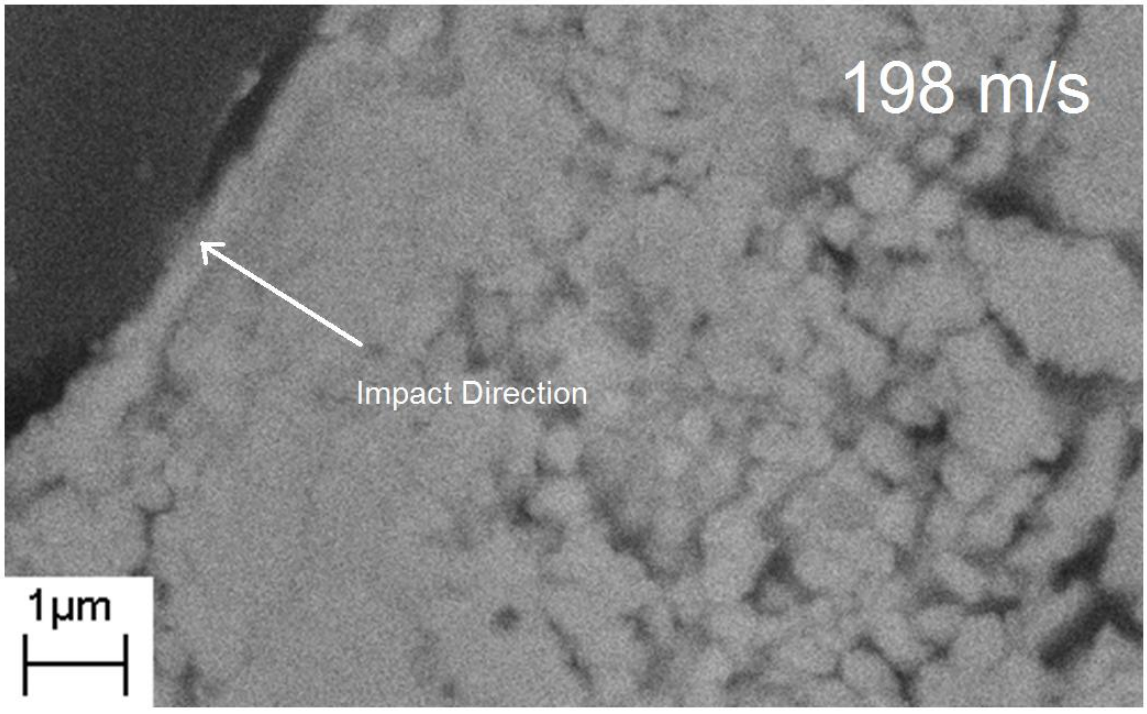

(b) Close up image of cross section

Figure 90: SEM images of polished cross section of HDDR compact forged at 198 m/s at (a) low magnification and (b) high magnification. Impact direction is marked on each micrograph.

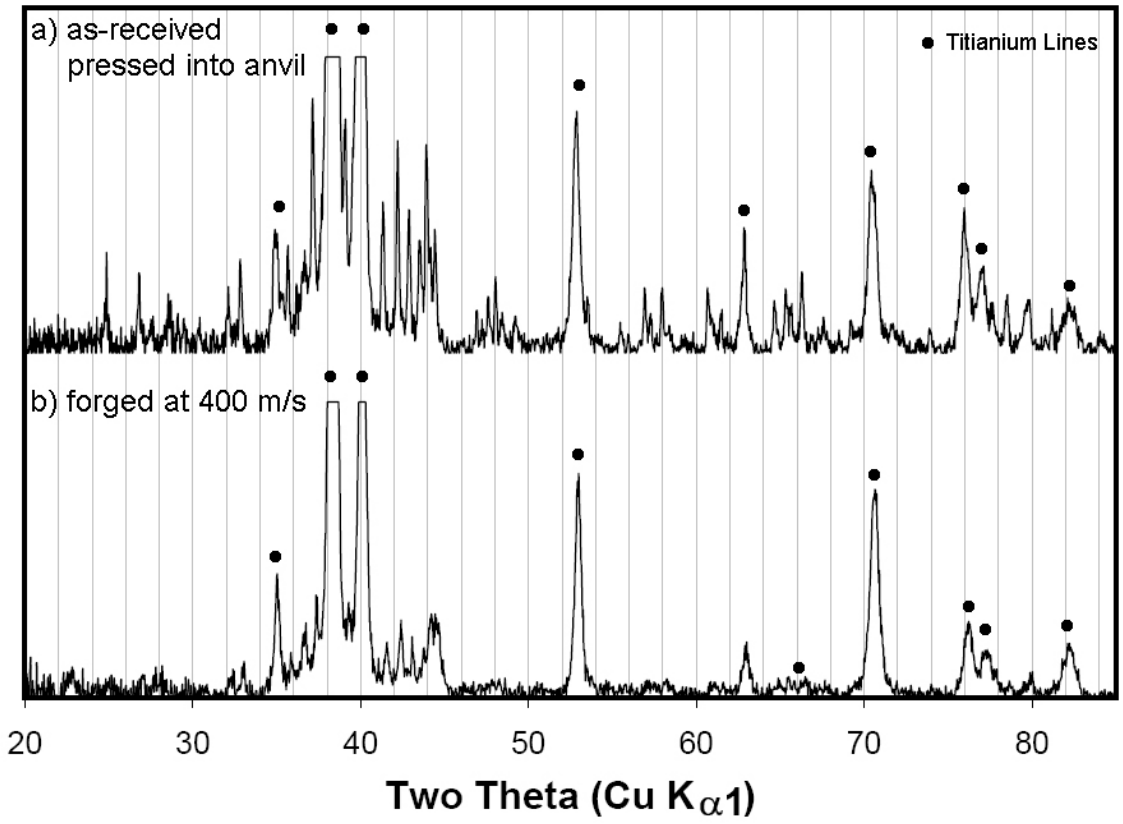

Figure 91: XRD traces of as-received Nd-Fe-B powder pressed into a hole in a machined hole in a titanium anvil (a) and a Nd-Fe-B compact forged on to a titanium anvil

on to the anvil. Therefore, titanium anvils were used for forging at high speed for the HDDR material as well. Titanium does not have any diffraction lines in the 42-50^o range where the largest diffraction lines for Nd-Fe-B are expected. Figure 91 shows the XRD traces of a forged compact and as-received HDDR powder pressed into a hole machined into the titanium anvil. A similar trend is seen at the higher speeds used for the titanium anvil experiments. The diffraction peaks show an increase in the peak breadth, but no indication of texture formation.

Table 11: Experimental conditions for shock compaction of Nd-Fe-B/α-Fe composites

Sample Name	Description	Relative Density	Impact Velocity (m/s)	Pressure (GPa)	Temp (^{o}C)
1023-1 Green	Nd-Fe-B Ball Milled	64%	-	0.79	-83
1023-1 Compact	Nd-Fe-B Ball Milled	98%	820 ± 60	5.8-6.0	370-380
1023-2 Green	15% α-Fe Ball Milled	67%	-	0.79	-83
1023-2 Compact	15% α-Fe Ball Milled	99%	820 ± 60	6.2-6.3	400-410
1023-3 Green	25% α-Fe Ball Milled	69%	-	0.79	-83
1023-3 Compact	25% α-Fe Ball Milled	96%	820 ± 60	6.7-7.0	320-330
1113-2 Green	15% α-Fe Nanoparticle Mix	∼69%	-	0.79	RT
1113-2 Compact	15% α-Fe Nanoparticle Mix	∼90%	980 ± 3	8.0-8.2	530-550
1127-3 Green	15% α-Fe Nanoparticle Mix	∼62%	-	0.2	RT
1127-3 Compact	15% α-Fe Nanoparticle Mix	∼90%	700 ± 3	3.4-4.1	260-330

4.6 Nd-Fe-B and Pr-Fe-B composites

§2.4.2 summarized the reports of shock compaction of Nd-Fe-B or Pr-Fe-B composites with α-Fe. While there are several reports of shock compaction of melt-spun Pr-Fe-B/α-Fe, none of the studies have examined the shock compaction of powders fabricated via high-energy ball milling. In addition, this section will explore the new technique of forming composites by mixing of nanoparticles. Table 11 summarizes the properties of the Nd-Fe-B/α-Fe composites and the experimental condition for shock compaction. This section will also present the results of high-rate forging experiments on Pr-Fe-B/α-Fe composites.

4.6.1 Shock compaction of High-energy ball milled Nd-Fe-B/alpha-Fe composites

Shock compaction experiments were performed to study the response of ball-milled Nd-Fe-B/α-Fe composites. The starting materials for the ball milled composites were HDDR Nd-Fe-B and pure α-Fe powder purchased from Alfa-Aesar. The unmixed Nd-Fe-B powder was first milled for four hours before adding the α-Fe powder. The mixtures were then milled for an additional four hours. Three compositions were tested: 100% Nd-Fe-B (1023-1), 85% Nd-Fe-B / 15% α-Fe (1023-2), and 75% Nd-Fe-B / 25% α-Fe (1023-3).

Figure 92 shows the microstructures of the milled and shock compacted samples for the 15% alpha-Fe mixtures. Nano-scaled grains are visible in both the milled and shock compacted micrographs.

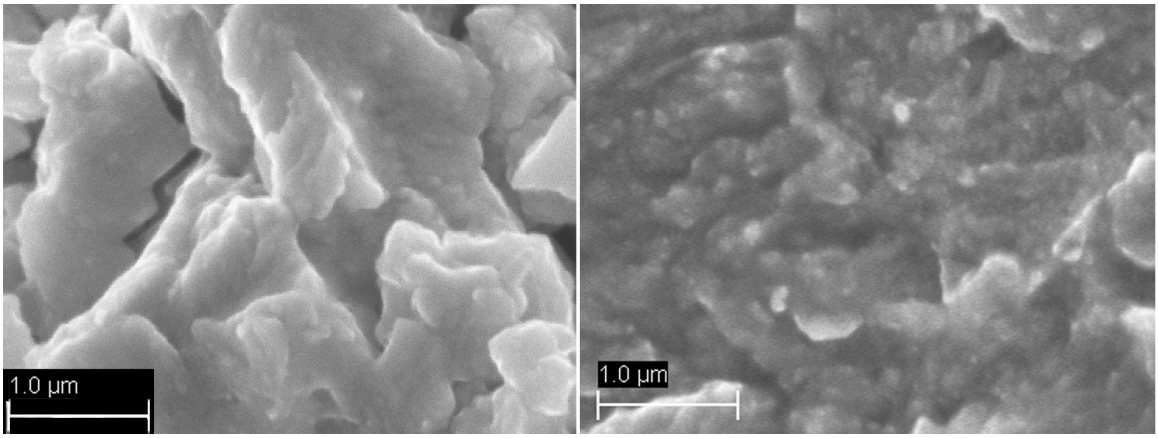

Figure 92: SEM micrographs of the 85% MQA-T/15% alpha-Fe mixture in the milled state (left) and shock compacted state (right)

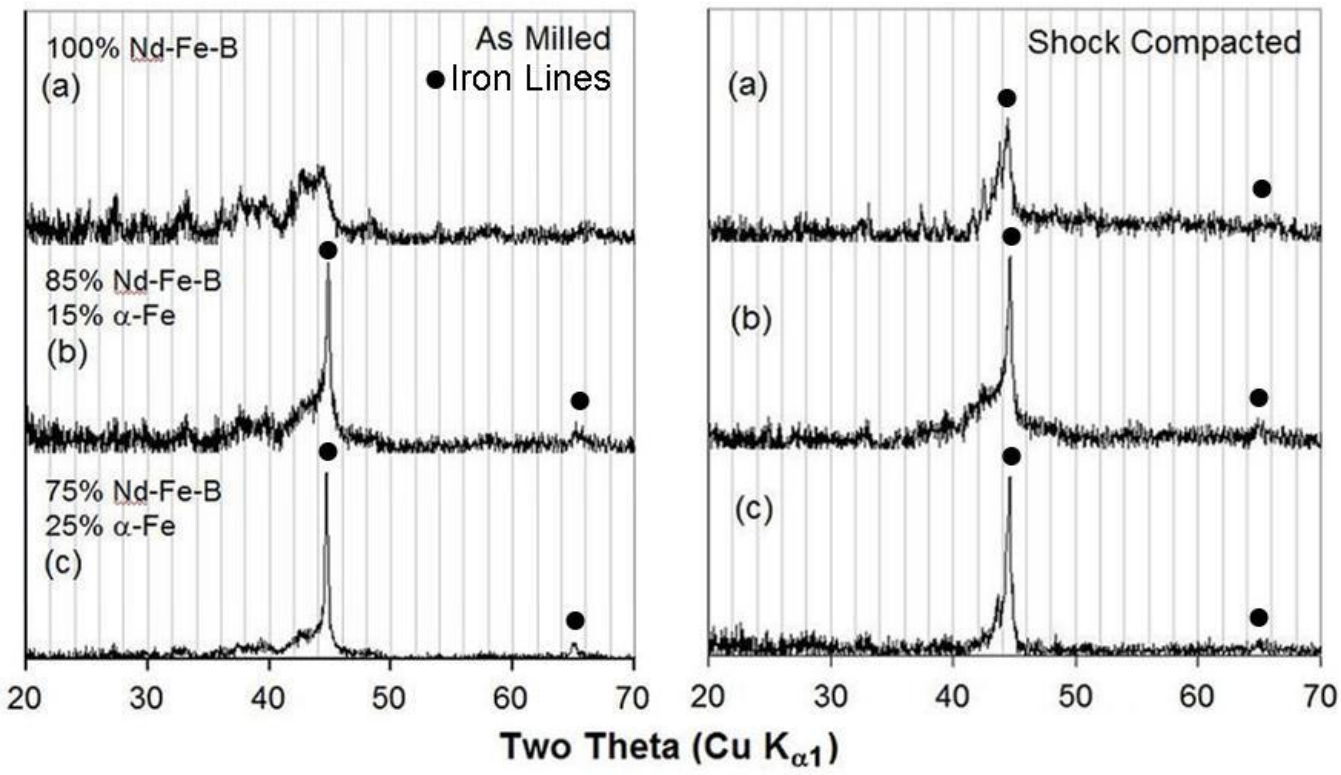

Figure 93: XRD traces for as milled (left) and shock compacted (right) samples of 100% MQA-T (a), 85% MQA-T/15% alpha-Fe (b), and 75% MQA-T/25% alpha-Fe (c)

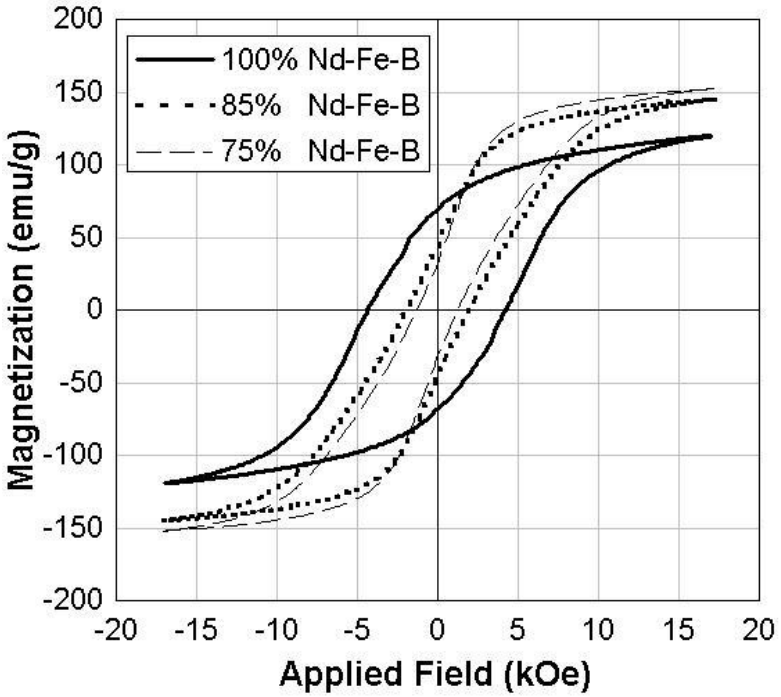

Figure 94: Magnetic hysteresis curves of the recovered compacts.

Figure 93 shows the XRD traces of the as-milled powders and the recovered compacts for each sample. The XRD traces of the as-milled powders show that composites with additional iron have larger α-Fe diffraction peaks, as expected. All peaks in the 1023-1 (100% Nd-Fe-B) trace match the $Nd_2Fe_{14}B$ phase. Some amount of amorphous phase is expected in all samples, although the exact amount is difficult to quantify. XRD patterns of the recovered samples are similar to the as-milled powders. The most notable difference is that the main diffraction line for α-Fe has increased in the 100% Nd-Fe-B sample, similar to other shock compacted samples.

Figure 94 shows the magnetic hysteresis curves of the shock compacted samples, as measured on the closed loop hysteresis graph at AMC. The magnetic saturation, M_s, increases with additional iron. The M_r/M_s ratio is above 0.5 for the 100% Nd-Fe-B sample and below 0.5 for the two composites. The XRD traces for the composite materials of both the as-milled and shock compacted samples have very broad or unidentifiable diffraction lines, indicating a large amount of material maybe amorphous or have a highly disturbed, nearly amorphous structure. Thus, one would expect these materials to be somewhat magnetically soft and have a low coercivity, with limited hardening from exchange coupling.

One hour heat treatments were performed at 450^{o}C, 550^{o}C, and 600^{o}C in an argon environment. Table 12 summarizes the magnetic properties of the as-recovered and heat treated samples. Heat

Table 12: Summary of sample densities and magnetic properties of shock compacted Nd-Fe-B/α-Fe composites. Magnetic saturation, M_s, is given in units of emu/g. Coercivity, H_c, is given in units of kOe.

Sample	Green Density	Compact Density	As-Recovered		450^{o}C		550^{o}C		600^{o}C	
			M_s	H_c	M_s	H_c	M_s	H_c	M_s	H_c
100%NdFeB	64	98	119	4.3	117	4.7	109	5.9	110	5.3
85%NdFeB - 15%Fe	67	99	143	2.0	140	2.4	133	4	132	3.6
75%NdFeB - 25% Fe	69	96	151	1.3	167	1.7	145	2.5	142	2.2

treatment at 550^{o}C and above is expected to crystallize the $Nd_2Fe_{14}B$ phase and increase the coercivity [46]. While a slight increase is observed, the coercivity of the heat treated samples remains low. Figure 95 shows the XRD traces of the 550^{o}C heat treated samples. The traces show an increase in size and breadth of the α-iron lines, but no evidence of crystallization of the $Nd_2Fe_{14}B$ phase. This differs from other reports in which crystallization of the $Nd_2Fe_{14}B$ phase occurs at 550^{o}C [46]. This is the most likely the cause of the low coercivity measured in the heat treated samples; the high coercivity $Nd_2Fe_{14}B$ phase has not crystallized. In the case of 100% Nd-Fe-B sample, it appears that the $Nd_2Fe_{14}B$ diffraction lines have diminished.

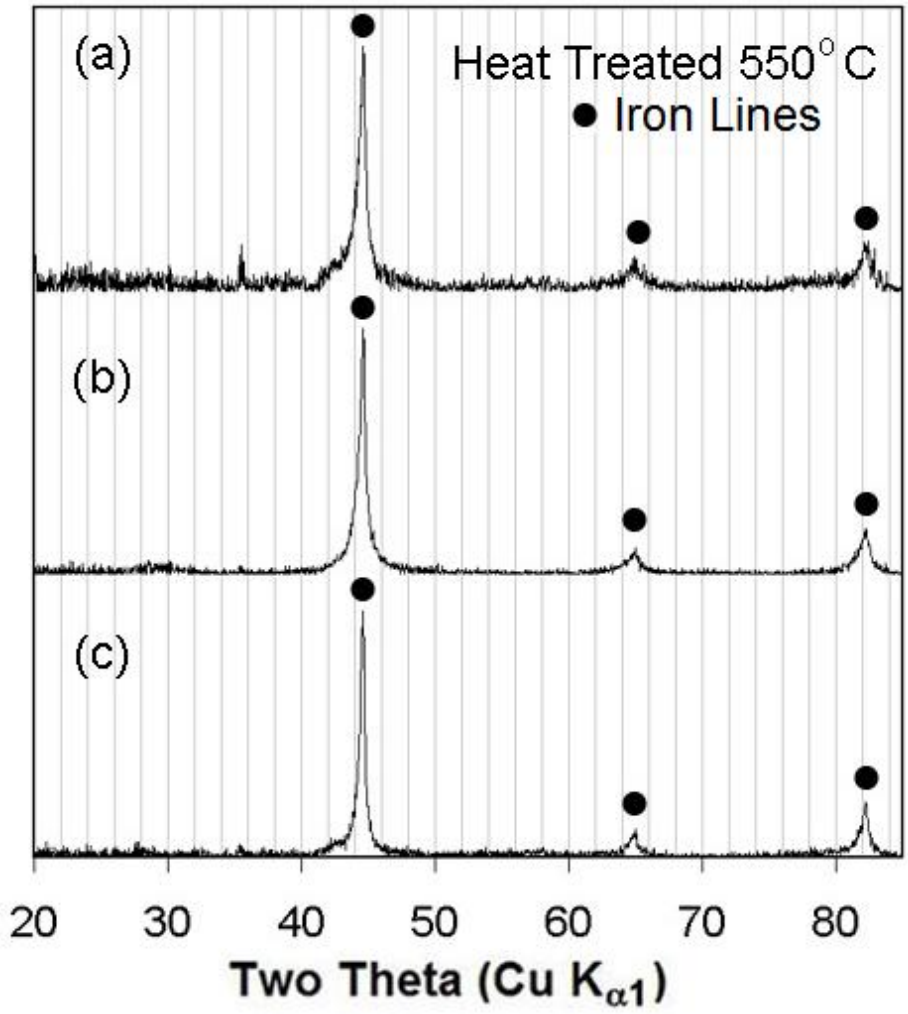

Figure 95: XRD traces of ball milled and shock compacted samples after heat treatment at 550°C for one hour.

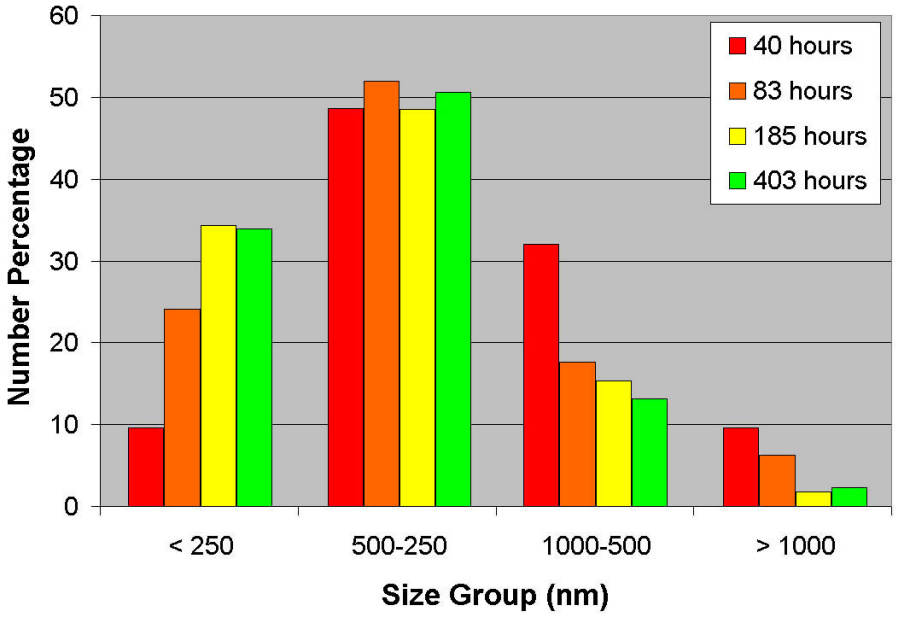

Figure 96: Size distribution of attrition milled Nd-Fe-B powder. Number percentages are shown for size groups of $>$ 1000 nm, 1000-500 nm, 500-250 nm, and $<$ 250 nm. The size distribution decreases with milling time up to 183 hours of milling time.

4.6.2 Shock compaction of Nd-Fe-B/nano-Fe mixtures

Nd-Fe-B/α-Fe nanocomposites were formed in a bottom-up fashion by mixing Nd-Fe-B submicron particles with α-Fe nanoparticles. As discussed in §4.5, attrition milling is capable of producing submicron sized single crystal particles of Nd-Fe-B. Figure 96 shows the size distribution of attrition milled particles for several milling times. The number percentage for four size groups of particles, $>$ 1000 nm, 1000-500 nm, 500-250 nm, and $<$ 250 nm, were measured from multiple SEM images. The size distribution moves towards smaller particle sizes with increasing milling time, up to 185 hours. Further milling beyond 185 hours does not significantly impact the size distribution, as shown by similarities in the distributions of samples milled for 185 hours and 403 hours.

Iron nanoparticles were mixed with the attrition milled Nd-Fe-B to make a hard/soft composite. Several commercially available nanoparticles were evaluated. Iron nanoparticles were purchased from Alfa Aesar with a size range of 10-30 nm, from Sun Innovations with an average diameter of 25 nm, and from US Research with an average diameter of 40 nm. XRD was performed on the nanopowders by sealing each sample between two layers of kapton inside an argon atmosphere glove box to prevent oxidation. The reflected x-ray intensity was limited by the low apparent density of the nanopowders, and so the powders were pressed into discs to increase the relative density. All three powder samples had some degree of oxidation. Figure 97 shows the XRD traces the three

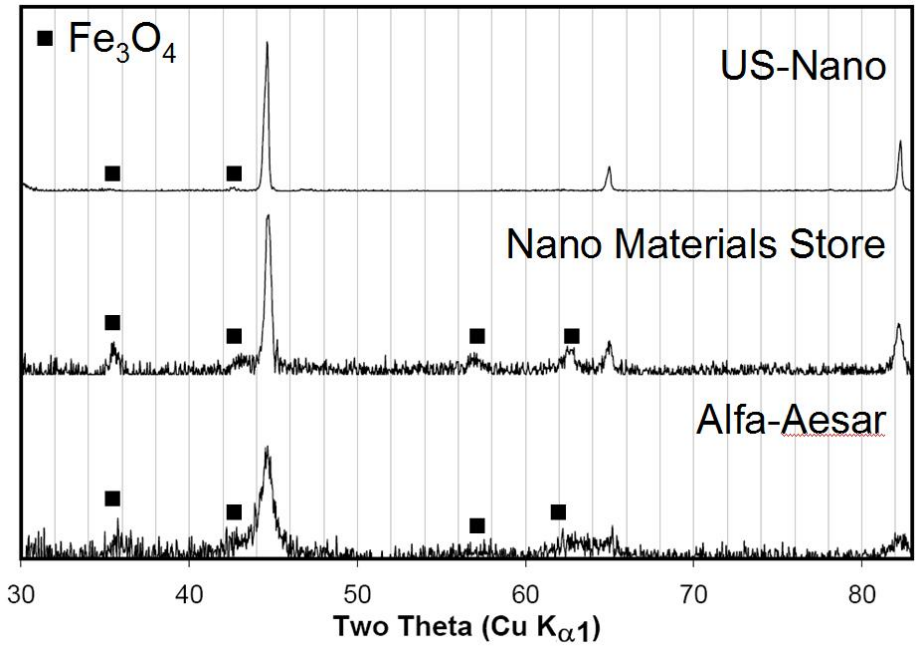

Figure 97: XRD traces for three commercially available nano-iron powders.

nanopowders with the kapton background removed. All types of iron powder showed some evidence of oxidation from the XRD traces. The amount of oxide roughly correlates with small particle size. US Research, the largest nanoparticles of the three types, had the least amount of oxidation.

VSM loops, performed at Georgia Tech, were measured on all three types of nanoparticles. Figure 98 shows the M-H hysteresis curves for the three iron powders along with the curve for the attrition milled Nd-Fe-B. Since the maximum field used for the VSM measurements (1.2T) is low, the Nd-Fe-B sample did reach saturation. The M-H curves shown are not corrected for demagnetizing fields, and the small remanence and coercivity values of the iron nanoparticles are particularly susceptible to this error; however, the saturation magnetization, M_s, measurements should not be significantly affected. The M_s value for the Alfa Aesar sample is lower than the M_s value for the Nd-Fe-B, even for the minor loop measured in this instance. Thus, adding the Alfa-Aesar nanoparticles to the Nd-Fe-B particles is not expected to increase the magnetization of the bulk magnet.

The U.S. Research (USR) nanoparticles have the highest M_s value, 203 emu/g, most likely due to the lack of oxidation seen from the XRD trace. Therefore, the US Research nanoparticles were selected for use in shock compaction experiments. Figure 99 shows the morphology of the as-received nanoparticles purchased from US Research. While the 30-40 nm particle size is typical, a few micron sized particles are also seen.

The iron nanoparticles were first ball milled separately from the Nd-Fe-B in order to study the

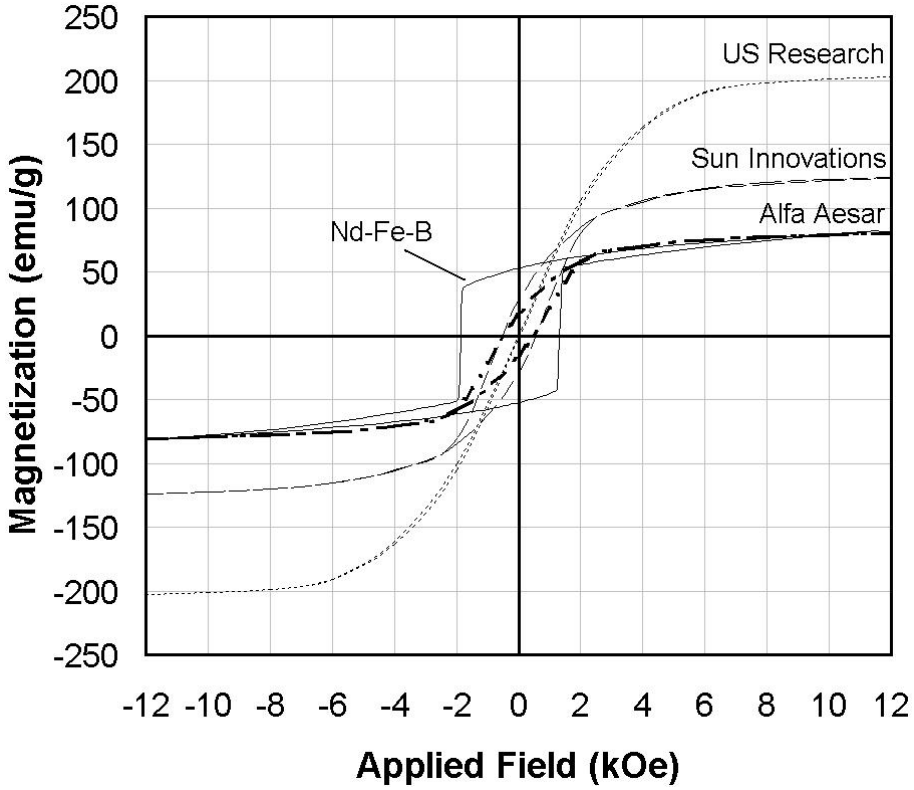

Figure 98: VSM curves for three commercially available nano-iron powders and attrition milled Nd-Fe-B.

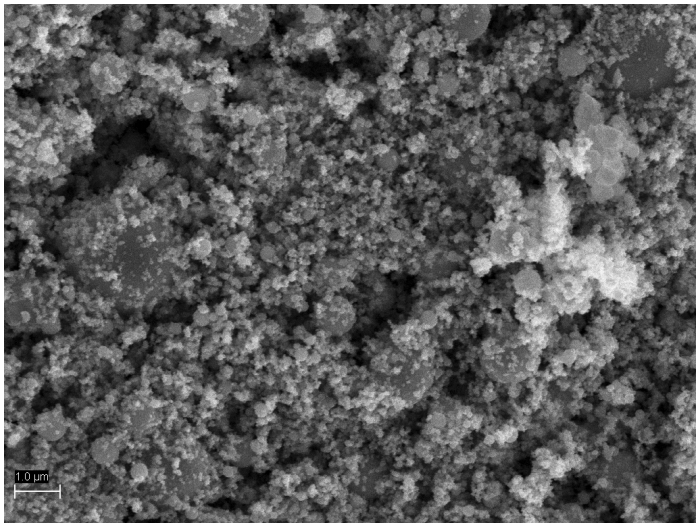

Figure 99: SEM micrograph of iron nanoparticles purchased from U.S. Research Nanomaterials with an average size of 30-40 nm. The powder also contains some large particles with diameter up to 1-2 μm.

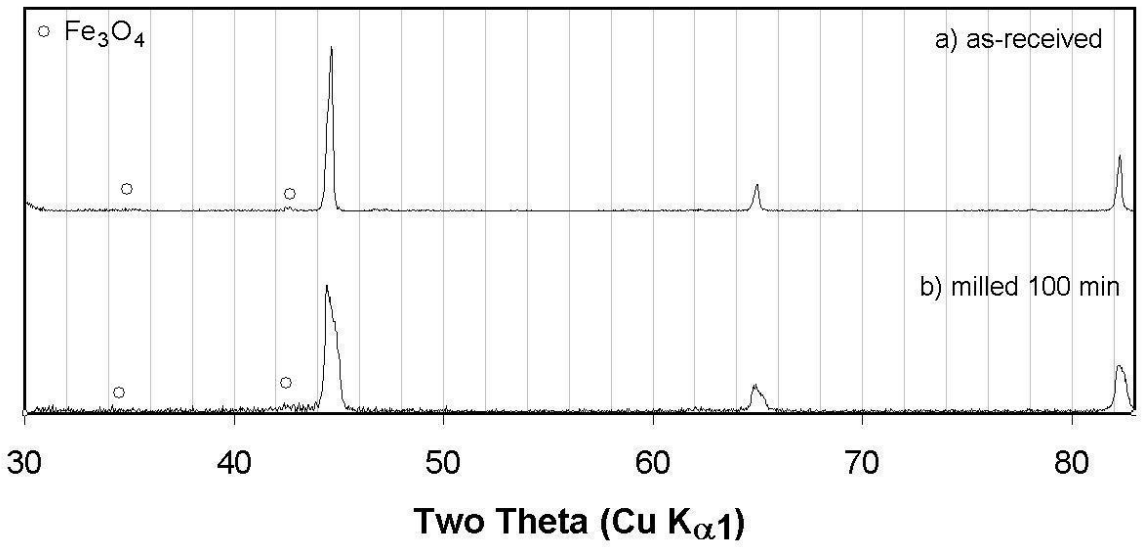

Figure 100: XRD patterns for (a) as-received US Research iron nanoparticles and (b) nanoparticles milled for 100 minutes.

effect of the deformation due to milling. The US Research nanoparticles were milled in anhydrous toluene for 100 minutes using a 1:3 ball to powder mass ratio. Figure 100 shows XRD traces for the as-received nanoparticles and milled powders. There is no significant increase in oxide, as shown by the size of the oxide peak at 43 degrees. Likewise, the saturation magnetization value, as measured by VSM, has decreased only slightly from 203 to 200 emu/g.

The attrition milled Nd-Fe-B particles and the nanoparticles were mixed by high-energy ball milling in a toluene slurry. The 15% nano-iron mixtures were milled using 10 1/8" diameter steel balls, which corresponds to a 1:3 ball mass to powder ratio. Smaller balls and a lower ball to powder mass ratio were used as compared to the experiments described in §4.5 in order to limit the deformation introduced into the Nd-Fe-B. Figure 101 shows SEM micrographs of mixtures of the Sun Innovations nanoparticles and attrition milled Nd-Fe-B after high-energy mililng for 10, 100, and 1000 minutes. A significant amount of clustering of nanoparticles is present in the 10 minute mixed powder. The 100 minute mixed powder shows a fairly even dispersion of iron nanoparticles with only a few clusters. The 1000 minute mixed powder, while having well dispersed iron nanoparticles, also has significant contamination from the milling media. There are many larger particles, ∼10 μm diameter, present in the powder. EDS performed on these particles indicates that these large particles are mainly iron with some silicon and light elements, suggesting that they are formed from chipping of the steel balls or steel container.

Shock experiment, 1113-2, was performed on unaligned mixture of Nd-Fe-B with 15% nano-iron

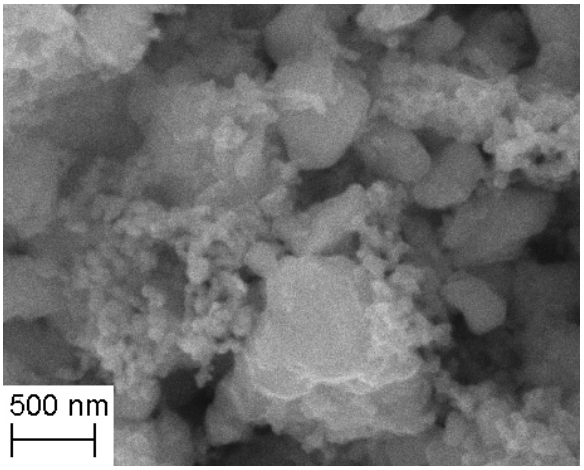

(a) 10 minutes

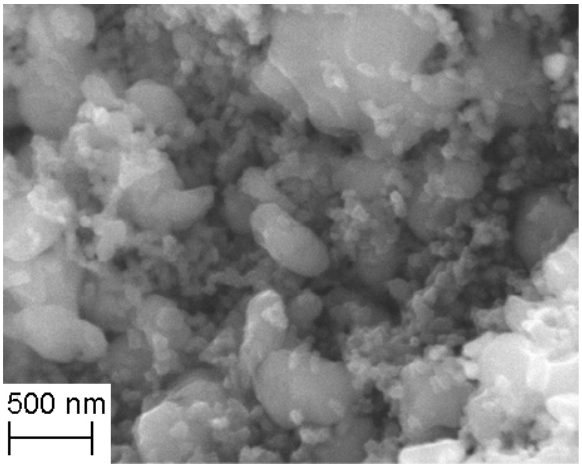

(b) 100 minutes

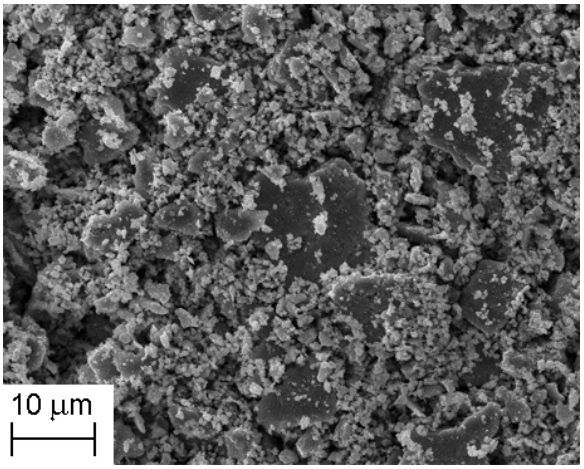

(c) 1000 minutes

Figure 101: SEM micrograph of mixtures of 15% nano-iron powder with attrition milled Nd-Fe-B powder. The powders are mixed by high-energy ball milling for 10, 100, 1000 minutes.

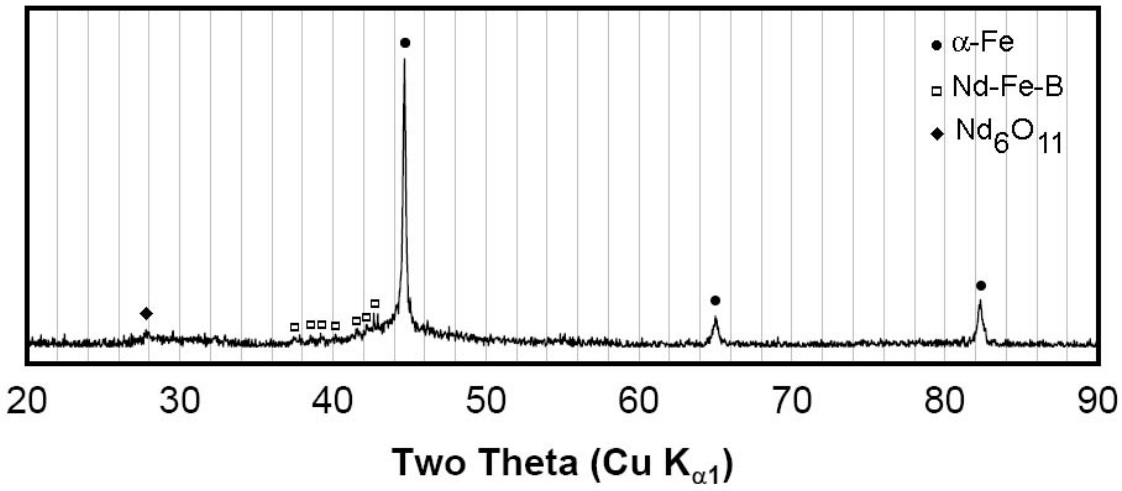

Figure 102: XRD pattern for shock compacted sample 1113-2.

particles. Figure 102 shows the XRD trace of the recovered compact. While the Nd-Fe-B has mostly decomposed in α-Fe, small peaks corresponding to the $Nd_2Fe_{14}B$ phase are present in the trace for the recovered compact. This differs from the results for sample 1113-1 (unmixed Nd-Fe-B submicron particles) shown in Figure 84, which showed no retention of the $Nd_2Fe_{14}B$ phase.

Because α-Fe is a main decomposition product, detecting the iron-nanoparticles by XRD is not feasible. Nevertheless, some areas of the compact show retention of the nanoparticles, as seen by SEM microscopy. Figure 103 shows SEM micrographs of the starting material, a mixture of attrition milled Nd-Fe-B and USR nanoparticles, and the recovered compact. Both types of particles in the mixture can be seen in Figure 103(a). The larger particles, 200-2000 nm in diameter, are the Nd-Fe-B particles, while the 30-50 nm particles are the nano-iron particles. In the shock compact, the decomposition of the Nd-Fe-B phase creates a matrix material around the nanoparticles, making them appear less distinct in SEM images. Figure 103(b) shows an area of the compact with grains of similar size to the iron nanoparticles, indicating possible retention of the size of the nanoparticles. However, some heterogeneities exist in the compact, as other areas have grain sizes in between the size of the typical iron nanoparticle or Nd-Fe-B particle, as shown in Figure 103(c). These areas may be regions in which grain growth has occurred in the α-Fe phase, although the wide size distribution of the original nanoparticles makes this difficult to determine with any certainty.

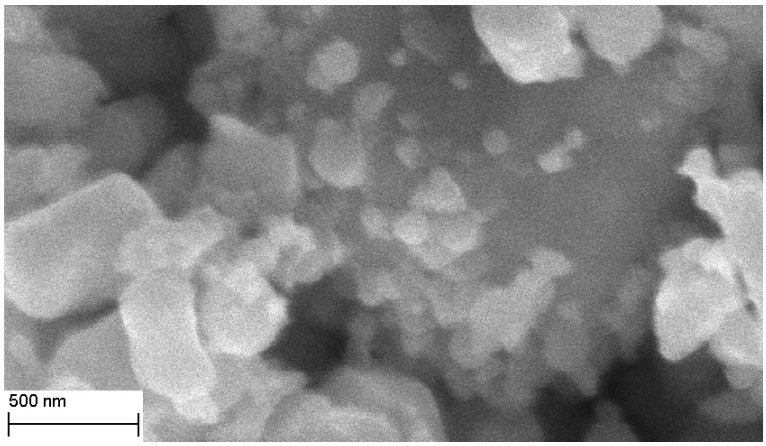

(a) Mixture of attrition milled Nd-Fe-B and USR iron nanoparticles.

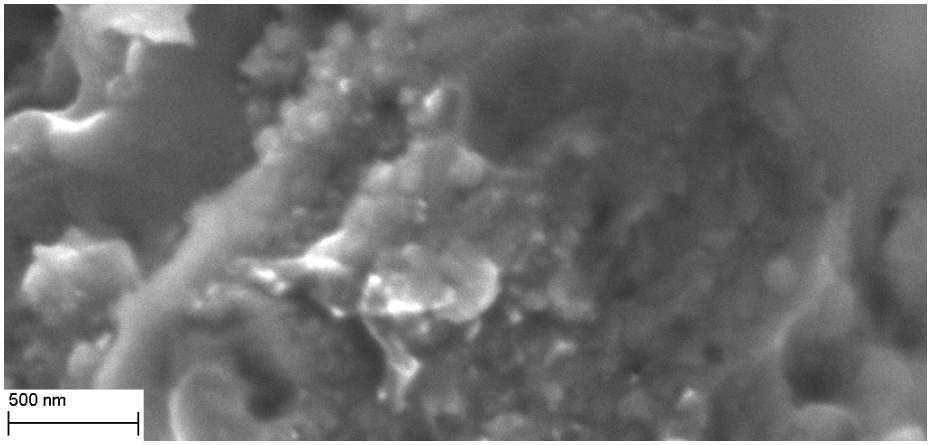

(b) Area of shock compact showing retention of the grain size of the iron nanoparticles.

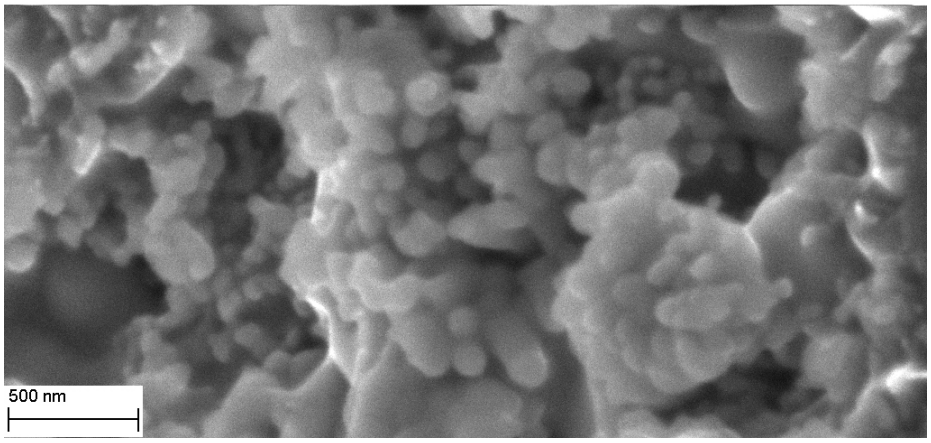

(c) Area of shock compact showing possible growth in size of the nanoparticles.

Figure 103: SEM micrographs of a) mixture of attrition milled Nd-Fe-B and USR iron nanoparticles, and recovered compact showing b) region with little or no growth in the size of the nanoparticles and c) area with possible growth in the size of the nanoparticles.

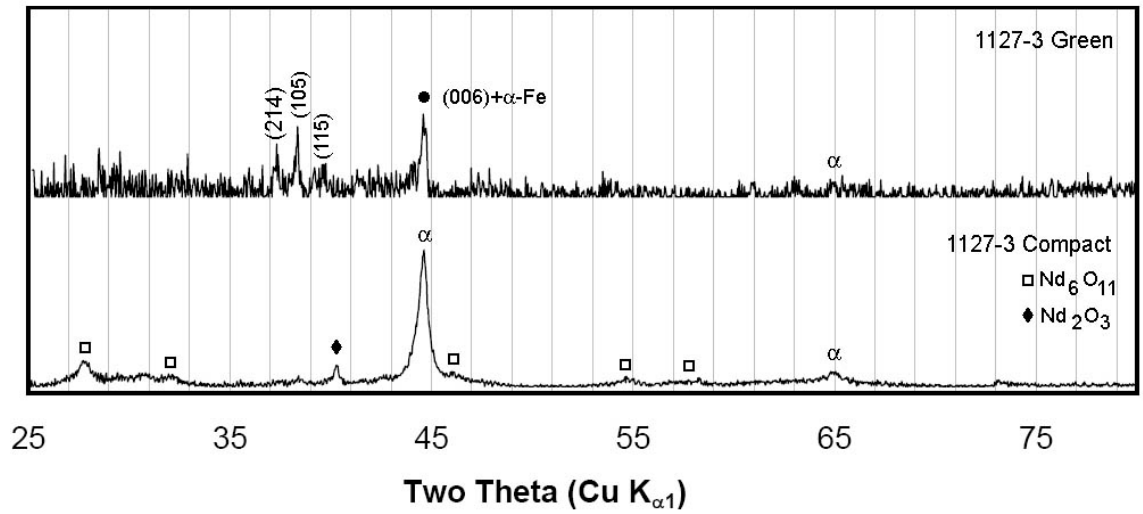

Figure 104: XRD traces of 1127-3 green (α-Fe and Nd-Fe-B nanoparticle mixture) and recovered compacts.

Samples of the attrition milled Nd-Fe-B and 85% Nd-Fe-B / 15% US Research nano-iron powder were sent to Advanced Materials for alignment by magnetic field. XRD traces of the nanoparticle mixture and the shock consolidated compact, sample 1127-3, are shown in Figure 104. The XRD traces showed similar decomposition of $Nd_2Fe_{14}B$ phase as the 1127-2 compact, which contained only the attrition milled Nd-Fe-B particles. Figure 105 shows SEM micrographs of the 1127-3 starting powder and recovered compact. Similar to compact 1113-2, retention of the nanoparticles can be seen in the SEM micrograph. No obvious areas of grain growth were observed, although proving a lack of grain growth in the iron nanoparticles is very difficult to achieve by microscopy. The lower shock temperature associated with this experiment, as compared to the 1113-2 experiment, may have slowed grain growth.

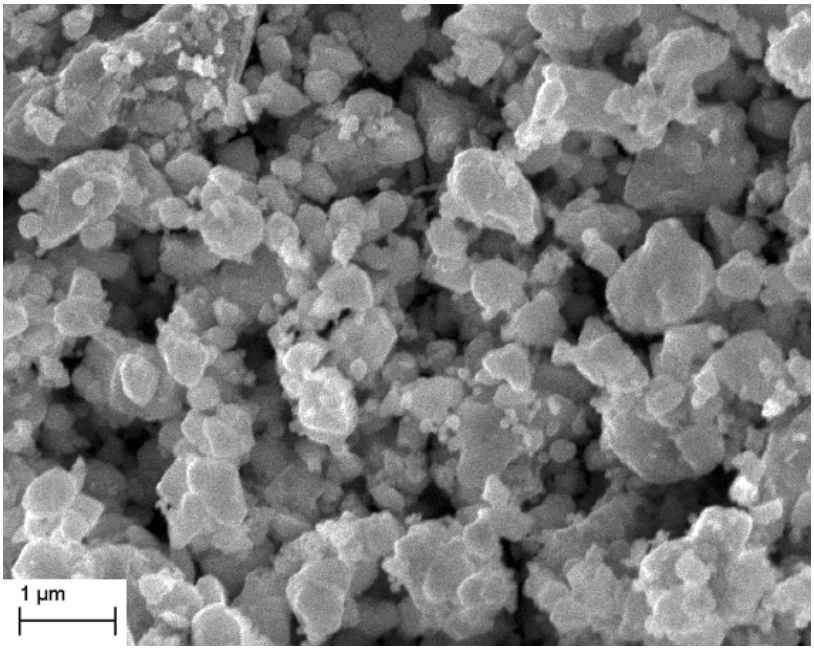

(a) Mixture of attrition milled Nd-Fe-B and iron nanoparticles

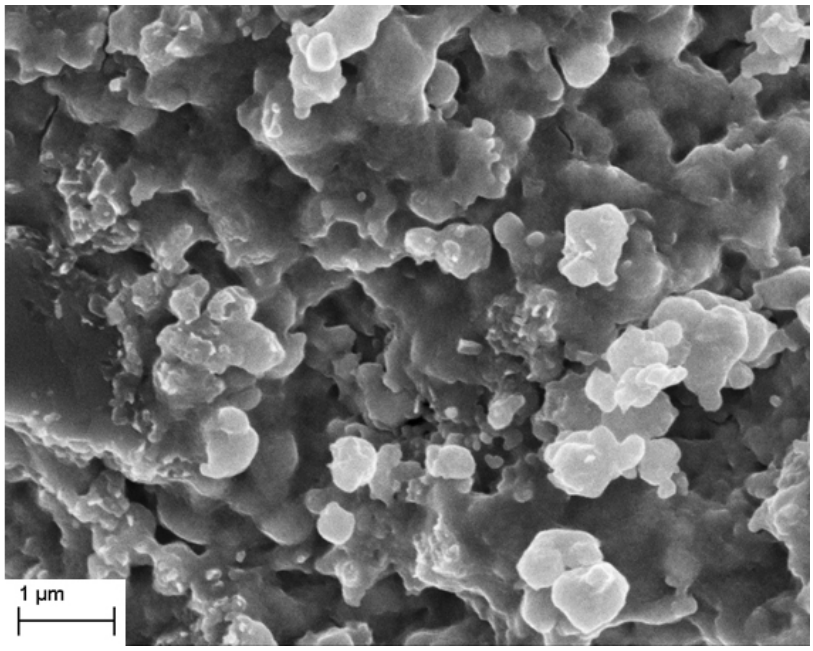

(b) Shock compacted mixture of aligned Nd-Fe-B and iron particles

Figure 105: SEM micrographs of (a) starting material composed of a mixture of attrition milled Nd-Fe-B particles and iron nanoparticles and (b) the microstructure of the recovered shock compact.

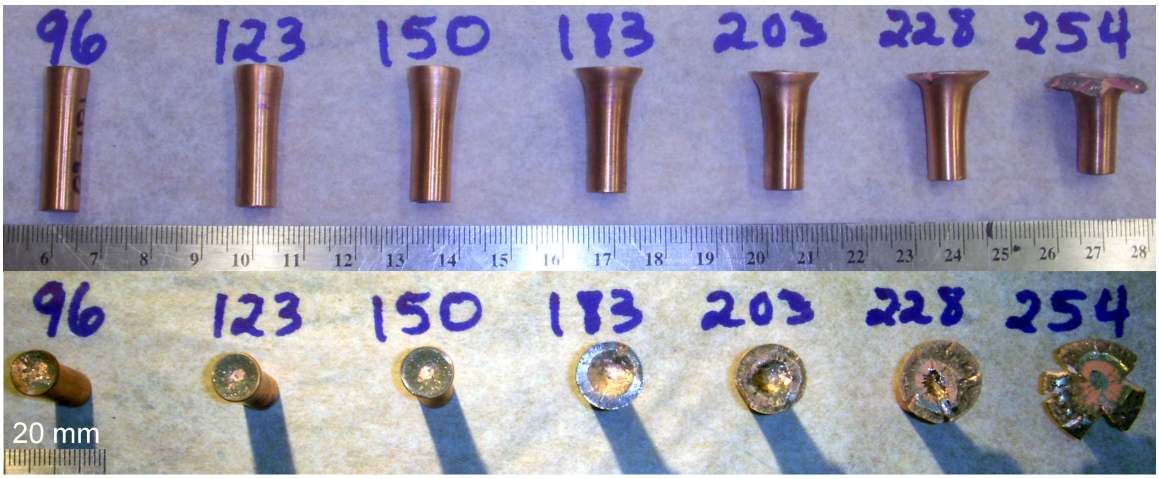

Figure 106: Small gun forging projectiles recovered after impacting a hardened steel anvil at impact velocities ranging from 96 to 254 m/s. The impact speed is written above each projectile.

4.6.3 High rate forging of Pr-Fe-B/alpha-Fe composites

A series of high-rate forging experiments were performed in which the pellet of the Magnaquench Pr-Fe-B/α-Fe powder was mounted on a copper projectile and impacted a hardened steel anvil at a range of speeds from 73 to 417 m/s. Figure 106 shows several of the recovered copper projectiles from these experiments with the impact speed labeled above each one. The radial and axial strain in the copper projectile increases with increasing impact speed. An indentation can be seen in each projectile indicating the approximate size of the forged pellet.

The size of the indentation is significantly smaller for the 228 m/s and 254 m/s projectiles than for slower speed projectiles, with not much change in size between the two. Shots with impact velocities of 315 m/s and 417 m/s show a similar pattern: larger amounts of deformation and tearing in the copper, but similar sized small powder compacts embedded in the center of the copper. It is possible that, at these speeds, the center portion of the powder compact increases in density and hardness until its flow strength surpasses the flow strength of the copper. The copper then begins to flow around the powder compact instead of producing additional compaction or deformation. Therefore, increasing the impact velocity above 228 m/s is not expected to significantly change the deformation behavior.

Powder compacts were recovered for all experiments at 73 m/s to 254 m/s. Figure 107 shows an image of a typical forged compact. The small size of the recovered compacts makes measuring their density difficult. The immersion test will be more sensitive to errors associated with any bubbles that form on the compact or any contaminants attached to the compact, such as residual copper.

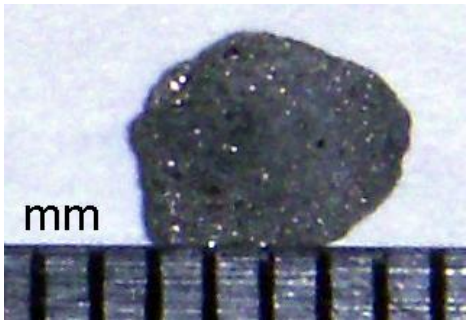

Figure 107: Image of a typical forged compact

Figure 108 shows the measured densities of several recovered compacts. The error bars shown in the figure are the standard deviation of at least three measurements or a minimum of +/- 0.5 g/cm^3. These results suggests that no significant amount of densification is taking place during the forging event.

Figure 109 shows the XRD patterns for the impact face for several of the recovered compacts. The (00c) family of peaks occur at 29.1^o, 44.3^o, and 60.4^o for XRD $Pr_2Fe_{14}B$ with copper $K_{\alpha 1}$ radiation. The 44.3^o peak overlaps the 100% peak for α-Fe and so an estimate of the texture must focus on the other two peaks. The two traces from forged compacts shown in Figure 109 have no significant change in intensity relative to other diffraction peaks as compared to the unforged pellet. Instead, there is some broadening that occurs in the peaks; however, analysis of the peak broadening is difficult due to the number of overlapping peaks.

Additional experiments above 254 m/s were performed using a titanium anvil and projectile. For comparison purposes, a hole was machined in a titanium anvil and the as-received powder was pressed inside. Figure 110 shows the XRD traces for a forging experiment performed at 400 m/s and the as-received powder pressed into a titanium anvil. These forging experiments show a similar result as the lower velocity experiments. The deformation creates an increase in the diffraction peak width but no indications of texture development.

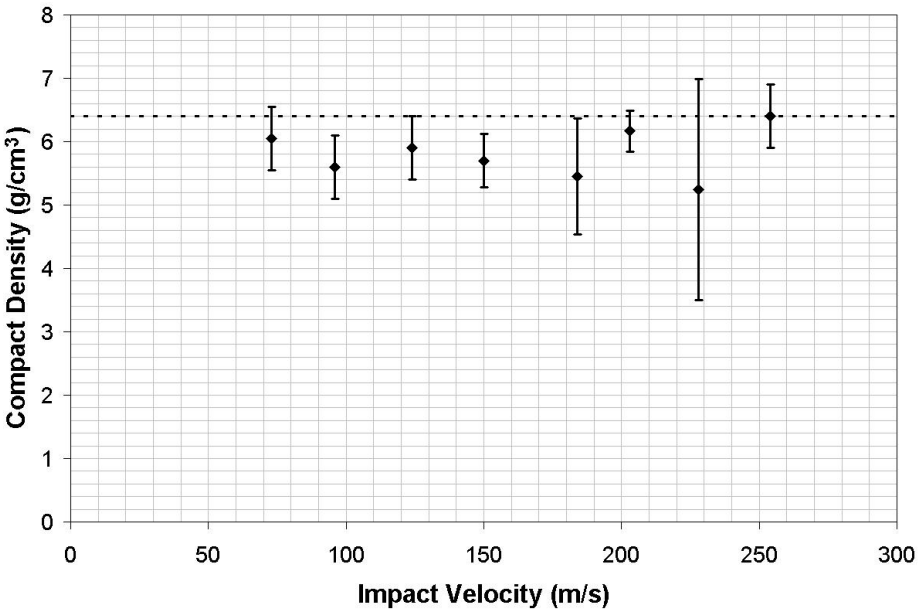

Figure 108: Density of Pr-Fe-B/α-Fe composite powder compacts forged at a range of impact velocities. Density is measure by the Archimedes method and error bars represent the standard deviation or a minimum error of +/- 0.5 g/cm^3. The dashed line indicates the initial density of the unforged compacts, 6.4 g/cm^3.

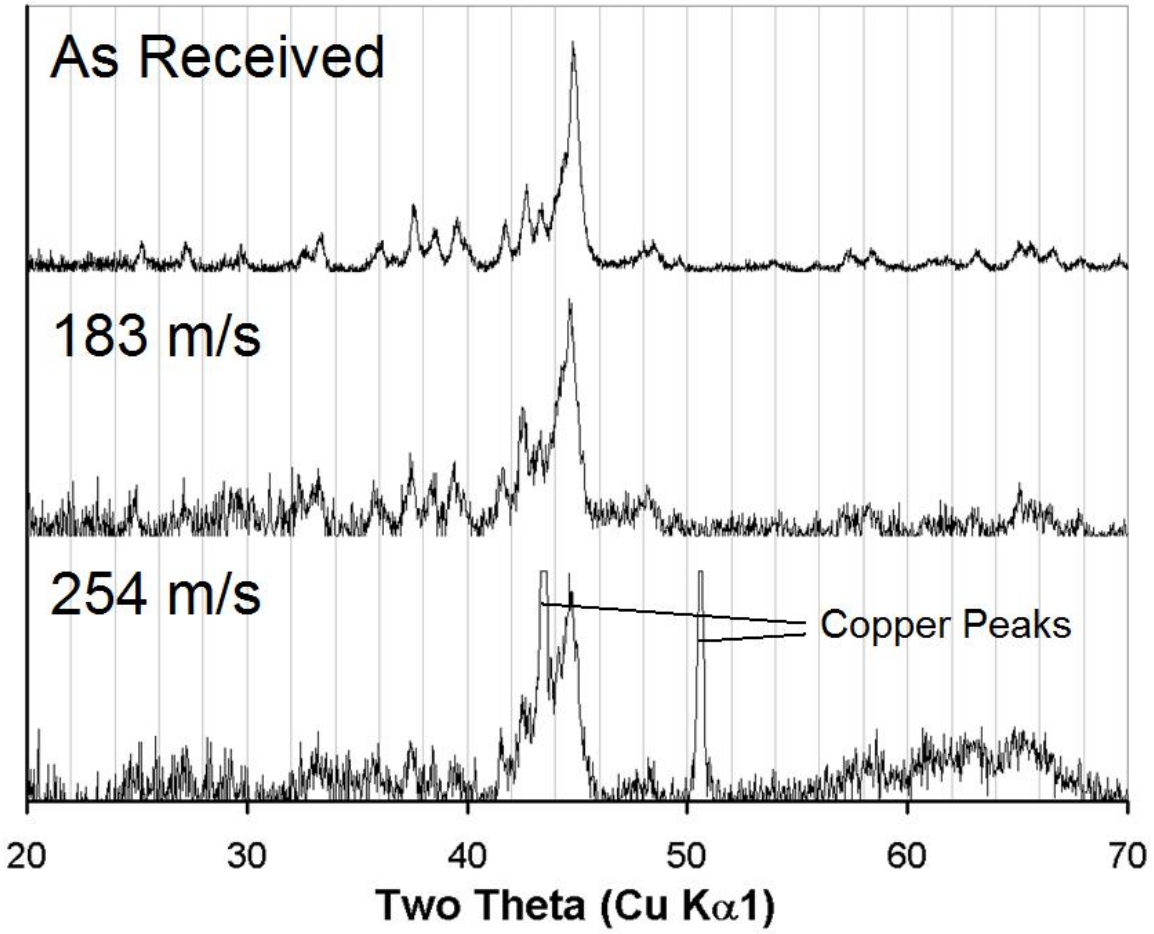

Figure 109: Pr-Fe-B/α-Fe XRD traces of (a) pressed pellet prior to forging (b) compact forged at 183 m/s (c) compact forged at 254 m/s.

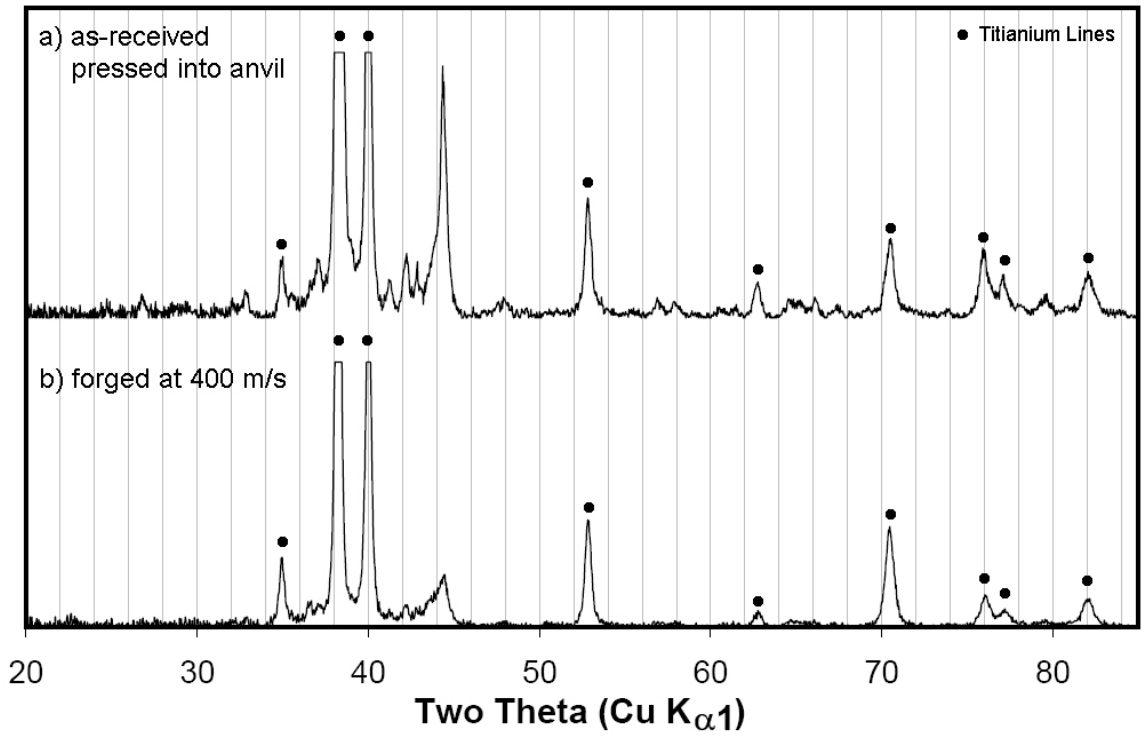

Figure 110: Pr-Fe-B/α-Fe composite powder XRD traces (a) pressed into the anvil and (b) after forging at 400 m/s.

CHAPTER V

DISCUSSION

This chapter will analyze key results presented in Chapter 4. The magnetic properties, phase transformations, and deformation mechanisms observed in the shock compacted samples are discussed and compared among the various systems. The possibility of developing texture through plastic deformation and alignment by magnetic field prior to shock compaction is also discussed.

5.1 Magnetic Properties of Shock Consolidated Materials

Magnetic property measurements are only available for a few shock compacted samples. The hysteresis loops for $Fe_{16}N_2$ samples shown in Figure 62 reveal that the saturation magnetization has decreased for both shock compacted samples relative to the starting powder, which is most likely due to the thermal decomposition of the α''-$Fe_{16}N_2$ phase. Comparing the two compacts, the -21^{o}C compact has a higher saturation magnetization than the -126^{o}C compact, due to the higher percentage of α-Fe present. The slightly higher coercivity in the -126^{o}C compact is most likely due to the higher Fe_4N content.

Table 12 (§4.6.1) shows the magnetic properties for the series of Nd-Fe-B/α-Fe composites formed by ball milling and shock compaction. While the saturation magnetization of the recovered compacts increases with increasing nominal iron content, the coercivity significantly decreases. The XRD traces in Figure 93 show that diffraction peaks for the $Nd_2Fe_{14}B$ phase are very broad or unidentifiable in the recovered samples. This means that there is relatively small amount of crystalline $Nd_2Fe_{14}B$ phase present or that the $Nd_2Fe_{14}B$ phase that is present is highly disordered, and this is most likely the cause of the low coercivity. The lack of crystalline $Nd_2Fe_{14}B$ phase is due in part to the ball milling, since the as-milled traces in Figure 93 also show very broad peaks; however, shock compaction increases the relative size of the α-Fe peaks, indicating a decrease in the relative amount of $Nd_2Fe_{14}B$.

The magnetic measurements from these samples indicate that phase transformations can negatively affect the magnetic properties of shock compacted samples. Developing high performance magnets through shock compaction will require careful control of the starting material and compaction conditions in order to minimize potential phase transformations. The following section, §5.2

will discuss the phase transformations observed in shock compacted materials more thoroughly.

5.2 Phase transformations in Shock Consolidated Materials

As discussed in §2.3.4, phase transformations in shock compacted materials can be caused by a variety of mechanisms. Allotropic transformations can be driven by a shock-induced mechanism in which the new phase is formed from coordinated short range movement of atoms, similar to martensitic transformations [97, 94, 95], in the time scale of the high pressure state. The deformation associated with shock compaction can aide certain transformations, such as mixing and alloying in intermetallic reactions [102, 101] and crystallite size reduction in crystalline-to-amorphous transitions [100, 104]. The work of shock compression and plastic deformation can result in bulk temperature increases and promote defect-enhanced solid state diffusion reactions in time scales of temperature equilibration. [99, 143]. In the phase transformations observed in the shock compacted magnetic materials studied in this work, there are examples for each of these transformation mechanisms in certain cases.

Phase transformations are observed to occur in several of the magnetic materials studied in this work, summarized in Table 13, and these will be discussed in further detail in the following sections. For the partial transformation of Fe_4N to Fe_3N, there is evidence that the transformation is shock

Table 13: Summary of phase transformations observed in magnetic materials.

Soft Phase Magnets			
γ'-Fe_4N	shock →	γ'-Fe_4N + ε-Fe_3N	shock (stress) induced/defect driven
	ball milling →	ε-Fe_3N	defect driven transition
α''-$Fe_{16}N_2$	T = -126°C →	α-Fe + γ'-Fe_4N + α''-$Fe_{16}N_2$ + γ''-FeN	Thermally aided decomposition
	T = -21°C →	α-Fe + γ'-Fe_4N + α''-$Fe_{16}N_2$	
Hard Phase Magnets			
$Nd_2Fe_{14}B$	shock →	$Nd_2Fe_{14}B$ + α-Fe + amorphous-NdFeB	defect driven decomposition
	ball milling →	α-Fe + amorphous-NdFeB	
$Sm_2Fe_{17}N_3$	shock →	$Sm_2Fe_{17}N_3$	stable (no decomposition)
	ball milling →	$Sm_2Fe_{17}N_3$ + α-Fe	stable for short milling times α-Fe forms for long milling times

(stress)-induced and that the defects generated during shock compaction aide the transformation. The decomposition of $Fe_{16}N_2$ appears to be thermally driven, although the formation of γ''-FeN may be linked to defects created during shock compaction. Decomposition to α-Fe and an amorphous Nd-Fe-B phase is observed in shocked compacted samples of $Nd_2Fe_{14}B$. Shock compacted samples of $Sm_2Fe_{17}N_3$ have little or no evidence of decomposition, since only small changes in the relative amount of α-Fe were observed. The deformation generated from shock compaction aides the decomposition of the magnetic phase in several of these material systems. Ball milling serves as an alternate method of introducing deformation in the powder samples, and decomposition reactions are observed in ball milled samples similar to those observed in shock compacted samples. This section will discuss the mechanism for phase transformation in each material system in more detail.

5.2.1 Fe_4N

As shown in Figure 59, the shock compaction of *FCC* γ'-Fe_4N results in partial transformation to a *HCP* ϵ-Fe_3N phase. While iron nitride will form a mixture of Fe_4N and Fe_3N for nitrogen content between 19-26% [144, 145], Yao et al. [146] showed that the ϵ-Fe_3N phase is the main stable iron nitride phase at high pressures. The authors showed that iron-rich nitride (Fe_xN with x=3.5-4.5) will form Fe_3N when annealled in a high pressure tungsten-carbide anvil cell. They attribute this phenomena to the lower molar volume of Fe_3N compared to Fe_4N over this composition range and identify the critical pressure for 20% nitrogen content (Fe_4N) as approximately 3 GPa. It is therefore not unexpected to see a γ' to ϵ transition in the shock compacted sample, since the lower bound of the shock pressure (6.3 GPa) is considerably higher than this critical pressure. This suggests that the transformation of Fe_4N to Fe_3N is stress induced.

The formation of Fe_3N is also possible due to plastic deformation of the powder during shock compression. In order to study the effect of plastic deformation on the phase transformation, ball milling experiments were preformed on Fe_4N powder. Ball milling was performed on Fe_xN (x=3.8) powder obtained from Alfa Aesar for milling times up to 48 hours. Figure 111 shows the XRD traces for the unmilled powder and powder milled using a 1:1 ball mass to powder mass ratio . Bragg diffraction peaks for both γ'-Fe_4N and ϵ-Fe_3N phases are observed in the pattern for the unmilled powder (pattern *a*). Based on the ratio of the area of the main peak for each phase, the unmilled powder contains γ'-Fe_4N and ϵ-Fe_3N in the ratio of of approximately 6:1. Milling quickly increases the relative intensity of the ϵ-Fe_3N peaks, as seen in the (b) and (c) patterns. The milled structure eventually reaches a steady state structure (pattern *d*) after approximately 24-36 hours. In the (d) pattern the ϵ-Fe_3N peaks have broadened and shifted to higher angles while the

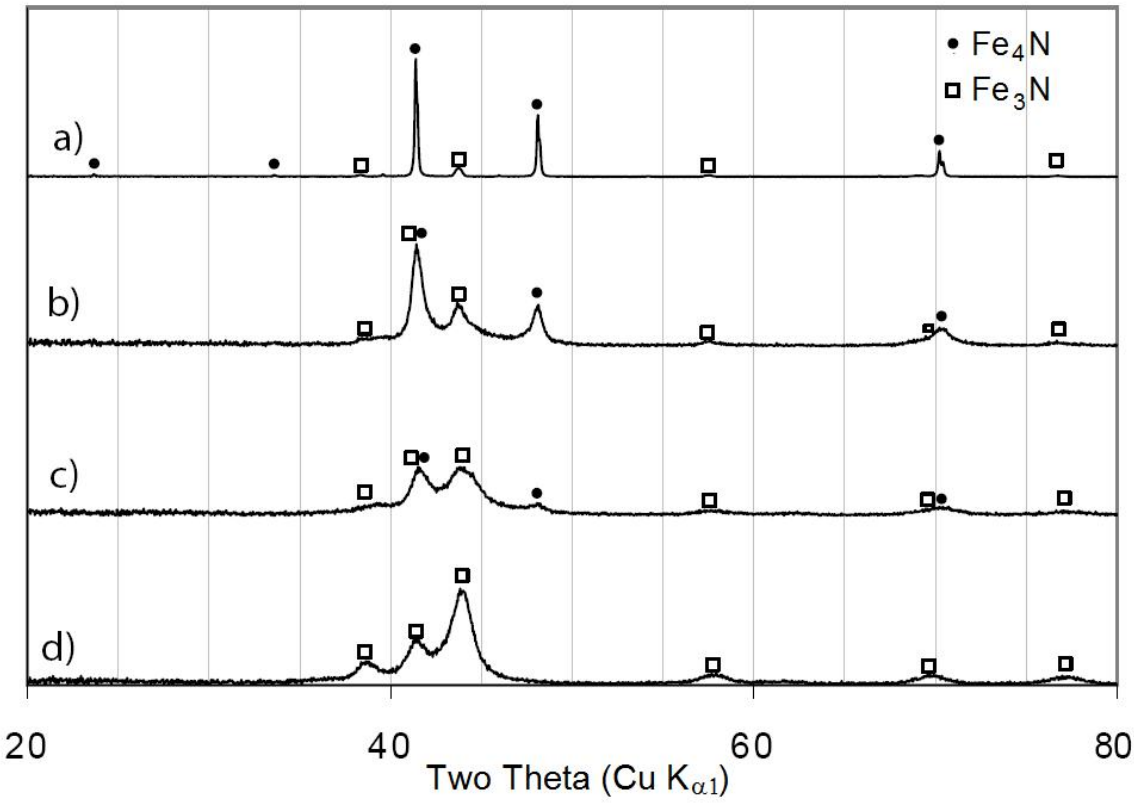

Figure 111: XRD of ball milled powders (a) as received (b) 1 hr (c) 6 hrs (d) 36 hrs.

γ'-Fe_4N peaks have disappeared or diminished to the point where they are not distinguishable from the ϵ-Fe_3N peaks and background noise. Milling up to 48 hours produces no significant changes in the XRD pattern. Using a 12:1 ball to powder mass ratio, however, achieves a structure similar to the one in pattern (d) after 2 hours of milling. Chilling the vial with dripping liquid nitrogen produced no changes in the XRD pattern of the milled powder for corresponding milling times. Both temperatures take approximately 24 hours to achieve the steady state structure and produce nearly identical XRD traces for corresponding milling times.

Transformation of γ'-Fe_4N to ϵ-Fe_3N has been linked to deformation in previous reports of high-energy ball milling [144]. Sumiyama et al. [144] suggest that the γ' to ϵ transformation is not a martensitic formation of a BCT structure, as had been previously suggested [147]. They theorize the phase change from FCC to HCP arises from a build up of stacking faults caused by the milling deformation. The difference between the material composition Fe_xN (x=3.6) and the stoichiometry of the ϵ-Fe_3N is accounted for with additional unoccupied interstitial sites.

The stacking fault mechanism proposed by Sumiyama et al. [144] may be applicable to the shock compacted samples from this work. As the pores in the compact collapse, pockets with

extensive deformation will develop around the closed pore. These highly deformed regions would be more likely to produce ϵ-Fe_3N. The XRD traces of shock compacted Fe_4N in Figure 59 show only a partial transformation to the ϵ-Fe_3N structure even though the shock pressure was well above the critical pressure for stress-induced formation of Fe_3N. The short duration of the pressure pulse, approximately 4 microseconds as estimated by the simulations, may have halted a stress-induced transformation prior to completion. The partial transition may also be explained by the staking fault mechanism, since areas near a collapsed void may undergo more deformation than surrounding areas.

5.2.2 $Fe_{16}N_2$

Decomposition is clearly observed in shock compacted α''-$Fe_{16}N_2$, and the process appears to be thermally driven. The XRD traces shown in Figure 61 reveal that the shock compacted sample with an initial temperature of -21^{o}C forms primarily Fe_4N and α-Fe, which are the expected thermal decomposition products. In addition, the grain size estimates obtained from the Williamson-Hall analysis are achievable by diffusion given the bulk heating generated by shock compaction.

The rate limiting process for decomposition of α'' is diffusion of nitrogen in γ' [148]. Fall et al. [148] reported that the activation energy for the formation of γ'-Fe_4N from α'', 94 kJ/mol, is equivalent to the the activation energy for diffusion of nitrogen in Fe_4N. In addition, the diffusivity of nitrogen in α-Fe, $D_\alpha^N = (5.2 \text{ x } 10^{-8} \text{ m/s})\exp[(\text{-}72 \text{ kJ/molK})/RT]$, is much larger than for γ', for which $D_{\gamma'}^N = (6.8 \text{ x } 10^{-10} \text{ m/s})\exp[(\text{-}94 \text{ kJ/molK})/RT]$ [149, 150, 148].

An approximate diffusion distance can be found by using the $X \approx \sqrt{Dt}$ approximation and numerical integration of the time-temperature curves in Figure 65. For nitrogen diffusion in γ', this process gives a diffusion distance estimate of $\sim$20 nm for the center of the -126^{o}C compact and close to 0 nm for the outside of the sample. In the -21^{o}C compact the center portion of the sample will have a diffusion distance in excess of 100 nm. It should be noted that these numbers represent an overestimate, since thermal conduction from around the circumference of the samples was ignored. Williamson-Hall analysis of the XRD peaks estimates the grain size of the γ' phase to be roughly 10 nm for both compacts. Given the assumptions made in calculating the diffusion distance and the error associated with the Williamson-Hall technique, these values can be considered to roughly agree with each other for the -126^{o}C compact. While the expected diffusion distance is significantly larger the grain size in the -21^{o}C compact, XRD analysis suggests the additional shock induced bulk heating aides in completing the transformation of γ''-FeN to γ'-Fe_4N and α-Fe and decreasing the microstrain, instead of increasing the grain size.

Given the above analysis, it is probable that the phase changes detected in the shock compacted samples of $Fe_{16}N_2$ are a result of bulk heating that persists after passage of the shock wave. The retained α''-$Fe_{16}N_2$ most likely resides in the outer sections of the compacts, while the inner portions produce a diffusional transformation to α-Fe and γ'-Fe_4N. In §5.2.1, it was shown that γ'-Fe_4N partially transforms to ϵ-Fe_3N_x under shock loading. The lack of an ϵ-Fe_3N phase in the XRD traces suggests that the γ'-Fe_4N phase is not formed during the primary shock wave, but primarily as a result of thermal effects.

Despite the evidence for a thermally driven solid-state diffusion reaction, it is possible that plastic deformation during shock compaction also plays a role. Weighting the nitrogen content by the relative amount of each phase listed in Table 7, the starting powder has roughly the same amount of nitrogen as the -21^{o}C sample. However, if one assumes no nitrogen vacancies, then the -126^{o}C sample has considerably higher nitrogen content than $Fe_{16}N_2$, due to the presence of the γ''-FeN phase. A higher degree of microstrain was found from the Williamson-Hall analysis of the -126^{o}C sample, as shown in Figure 64. The additional microstrain in the -126^{o}C sample may indicate a higher dislocation density in the -126^{o}C sample, and these dislocations may help accommodate additional nitrogen vacancies. As discussed in §2.3.3, dislocations formed during shock compression can create an especially large number of vacancies. The longer thermal excursion of the -21^{o}C sample helps to remove dislocations by annealing and serves to further the decomposition reaction.

5.2.3 Nd-Fe-B

Shock compaction of $Nd_2Fe_{14}B$ was observed to create a decomposition reaction in which α-Fe and Nd-oxides are formed. The oxides are most likely the result of oxidation of an amorphous Nd-Fe-B phase that occurs after recovery of the shock compacted samples. The decomposition is most readily detected by an increase in the α-Fe (110) diffraction line, which overlaps the (331) diffraction line for $Nd_2Fe_{14}B$. The overlap of the diffraction peaks can make the decomposition products difficult to detect unless careful analysis of the XRD pattern is performed. In the case of $Nd_2Fe_{14}B/\alpha$-Fe composites, there is already a larger than normal $Nd_2Fe_{14}B$ (331) + α-Fe (110) peak, which makes detecting the decomposition even more difficult. Evidence of this decomposition can be seen in the XRD traces for all shock compacted samples, but shock compacted samples 1113-1 (Figure 84) and 1127-2 (Figure 82) show the greatest degree of decomposition.

A decomposition process similar to the one seen in shock compacted Nd-Fe-B is also observed to occur in high-energy ball milled Nd-Fe-B powders. XRD traces for ball milled HDDR powder are shown in Figure 76(b). The effects seen in the XRD traces of ball-milled powders are similar to

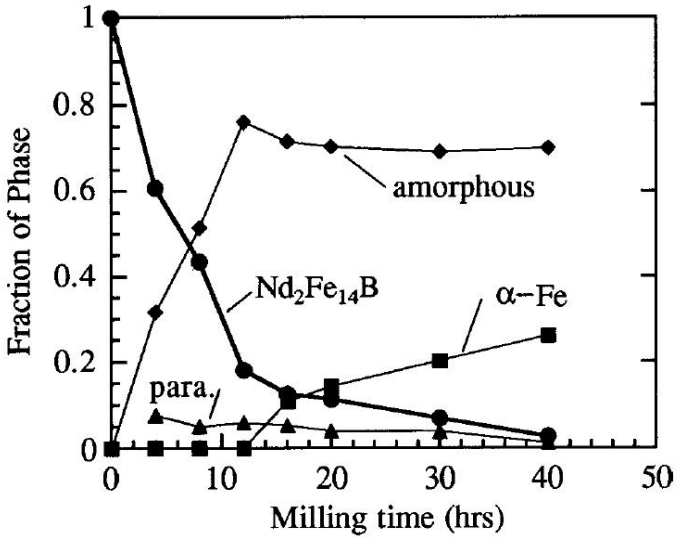

Figure 112: Fraction of phases present in ball milled Nd-Fe-B as a function of milling time. [46]

the ones seen in shock compacted samples 826-3 (Figure 78) and 826-2 (Figure 85), the $Nd_2Fe_{14}B$ diffraction peaks broaden and diminish while the α-Fe diffraction lines increase. Previous reports have studied the decomposition of Nd-Fe-B during ball milling [46, 151]. Figure 112 shows the relative amount of $Nd_2Fe_{14}B$ and it's decomposition products as a function of milling time, as reported by McCormick et al. [46]. The figure shows that the α-Fe and amorphous Nd-Fe-B are the main constituents in samples with extended milling times. The McCormick et al. [46] study used a combination of XRD, Mössbauer, and TEM to determine the relative amounts of phases. Determining the amount of amorphous phase from XRD alone is difficult.

Deformation clearly plays a crucial role in the decomposition of shock compacted Nd-Fe-B. The XRD traces for front and back of the 826-3 compact (as-received HDDR starting powder) in Figure 78 and for the 826-2 compact (NRL-melt spun starting powder) in Figure 85 show the same pattern. The back side trace shows more peak broadening and a larger increase in the size of the α-Fe peak than the front side. While the back side of the sample will experience a larger shock pressure due to radial wave focusing, it will also see a less uniform shock wave. Deviations from a planar shock wave will increase the non-hydrostatic portions of the loading condition and increase localized deformation. The results of shock compression experiment 1127-1 (Figure 86) on nonporous Nd-Fe-B stand in contrast to the shock compaction of powder experiments. The lack of initial porosity in the sample will significantly reduce the severe plastic deformation created during shock compression. As a result, there is no indication of decomposition, despite the higher shock pressure expected for

the experiment.

It is worthwhile examining the possibility that the decomposition of the $Nd_2Fe_{14}B$ phase is caused by melting. Figure 5(a) shows a two-dimensional section of the phase diagram passing from the pure iron corner through the stoichiometric $Nd_2Fe_{14}B$ point. The melt temperature is 1155-1300^{o}C for the typical Nd content (12-15%); however, the $Nd_2Fe_{14}B$ phase (T1 in the phase diagram) is not stable above 1155^{o}C. Between the melt temperature and 1155^{o}C, crystalline γ-Fe (FCC) and liquid are present. Below 1155^{o}C the peritectic reaction shown in Eq. 31 occurs for materials with composition near the stoichiometric point (Nd=11.8%) [24].

$$L + \gamma Fe \rightleftharpoons Nd_2Fe_{14}B \tag{31}$$

However, this peritectic reaction is reversible. Hence, one would expect crystallization of the $Nd_2Fe_{14}B$ phase to occur unless the material was rapidly quenched.

Bulk melting is unlikely to have occurred in any of the shock compacted samples. The bulk shock temperature for each experiment is shown in Table 10 and the calculated bulk temperature is significantly lower than 1155^{o}C for all experiments. However, localized deformation at the interfaces between particles can cause temperature spikes along the outer shells of particles and subsequent rapid quenching as the temperature equilibrates with the inner core of the particle. Gourdin [91] estimated the temperature rise profile for a range of shock compacted metal powders. The rise in surface temperature was estimated to be 2-3 times the bulk temperature, depending on the type of powder and whether the latent heat of melting was considered. Applying similar ratios to the Nd-Fe-B shock compaction experiments in this work, only the 1113-1 compact ($\sim$550 bulk shock temperature) would be expected to experience significant surface melting; however, this sample shows extensive decomposition that would likely require melting in the bulk of the material. In addition, Gourdin [91] notes that the energy flux is independent of surface area for monosized spheres; therefore, the surface temperature will increase with increasing particle size. In the present work, samples with a smaller particle size achieved through attrition milling, such as 1113-1 and 1127-2, show a greater degree of decomposition than compacts with a larger initial particle size, such as 826-3 and 826-2. This would indicated that the decomposition is most likely not caused by melting and rapid quenching.

In addition, the results of the VISAR experiments serve as evidence that the decomposition reaction is a shock-induced phase transition. Two transition points are seen in the VISAR trace showin in Figure 87. The first transition, occurring at 1.8 GPa, is mostly likely the dynamic yield strength in compression, also known as the Hugoniot Elastic Limit (HEL). Deformation above this

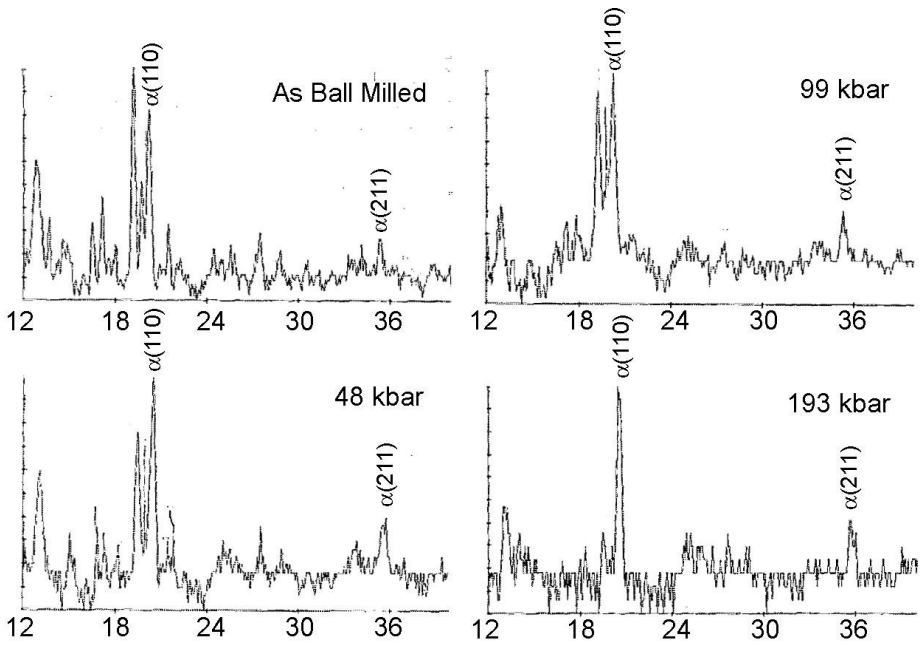

Figure 113: XRD traces of Nd-Fe-B shock compacted at three different pressures. [107]

pressure occurs mainly by fracture and grain size reduction. The second transition (4.8 GPa), may indicate the onset of decomposition. An alternate interpretation is that $Nd_2Fe_{14}B$ undergoes a high pressure phase transition. The phase transition may be reversible upon unloading and the new phase may decompose into the products seen in the recovered samples. Regardless of the nature of the second transition, its presence in the VISAR traces indicates that the phase transformation or decomposition occurs while in the shock loaded state. This provides further evidence that the decomposition is not caused by melting, since both bulk heating and surface heating will be limited in the nonporous samples used in the VISAR experiments.

All of the shock compacted Nd-Fe-B samples studied in this work had some degree of decomposition, although the amount of decomposition varied. This is striking since no previously published studies of shock compaction of Nd-Fe-B note any decomposition. However, reexamination of the reports in the literature that provided XRD traces of recovered samples shows that there is indeed evidence of decomposition in these samples as well.

Figure 113 shows the XRD traces of three shock compaction experiments performed by Chandramouli et al., along with the trace of the as-milled powder [107]. While a small amount of α-Fe is present in the as milled samples, the size of the α-Fe peaks has increased relative to the Nd-Fe-B peaks for the samples compacted at 48 kbar (4.8 GPa) and 99 kbar. The 193 kbar sample has

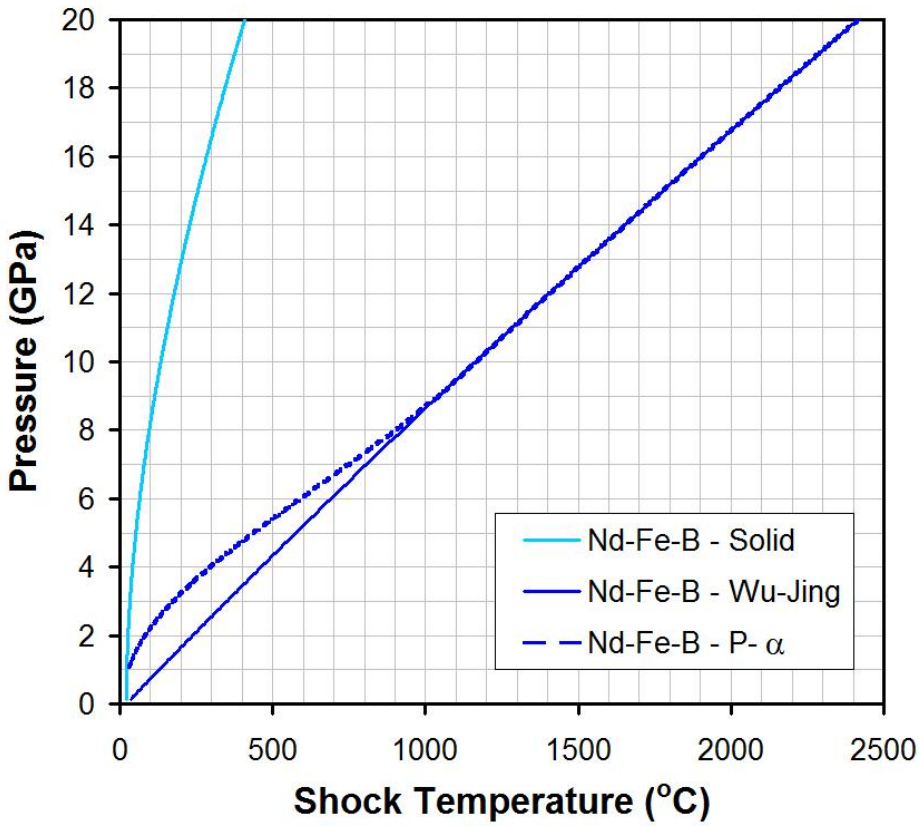

Figure 114: Pressure-Temperature relationship for Nd-Fe-B with an $\sim$ 60% initial density.

undergone a near complete decomposition, with only the α-Fe phase showing in the XRD trace. The authors estimate the initial packing density at $\sim$ 50-60%. For this initial density, one can use the Nd-Fe-B Hugoniot shown in Table 5 to calculate an approximate shock temperature. The resulting pressure-temperature dependence is shown in Figure 114 for 55% initial density. The authors attribute the transformation seen in the 193 kbar sample to melting, noting that melting of $Nd_2Fe_{14}B$ produces liquid and crystalline Fe. The 193 kbar (19.3 GPa) experiment corresponds to an approximate bulk shock temperature of $\sim$2000-2600^{o}C, which clearly exceeds the 1155^{o}C melt temperature. As noted above, the sample will have to undergo rapid quenching in order to prevent recrystallization of the $Nd_2Fe_{14}B$ phase. It is possible that some portions of the samples reported by Chandramouli et al. [107] may have undergone rapid quenching, while other sections may experience a slower cooling. Due to the large amount of noise in XRD pattern shown in Figure 113 for the sample tested at 193 kbar, a small amount of $Nd_2Fe_{14}B$ phase formed in the slower quenched areas may have gone undetected.

The pressures reported for the other two experiments, 48 and 99 kbar, correspond to shock

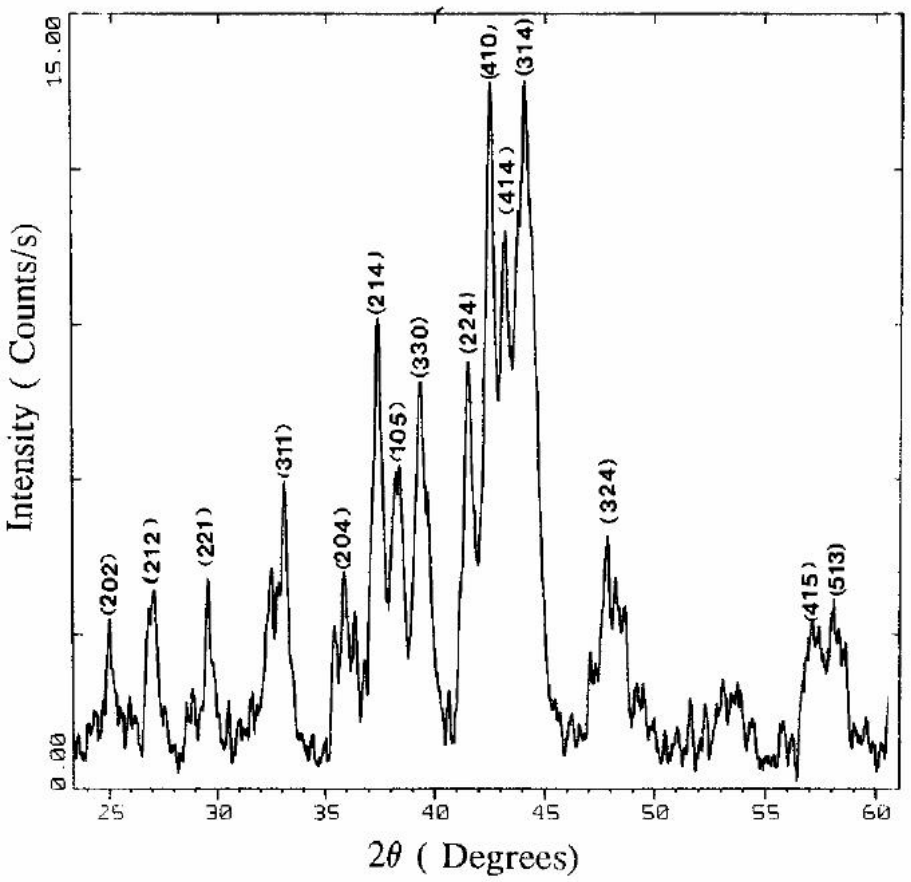

Figure 115: XRD trace of explosive shock compacted Nd-Fe-B sample reported by Guruswamy et al. [108].

temperatures of 340-620^{o}C and 960-1300^{o}C respectively over the 50-60% range of intial densities. The authors do not describe how they calculate the shock pressure, so the uncertainty in the shock temperature may be even greater. While the 99 kbar experiment may have experienced some melting, the shock temperature for the 48 kbar experiment is signficantly below the melt temperature, yet both the 99 and 48 kbar experiments have indications of an increase in the amount of α-Fe relative to the starting powder. This indicates that the sample may have experienced decomposition due to mechanical deformation instead of melting and rapid solidification.

Guruswamy et al. [108] performed explosive driven shock compaction of melt-spun Nd-Fe-B powder. They estimated the shock pressure to be approximately ~6GPa. Figure 115 shows the XRD trace reported for one of the shock compacted samples. The XRD trace for the starting powder was not reported, but the powder was produced by Magnaquench, Inc. and was type MQP-B, which has Nd content of ~12.5%. For compositions with Nd content above the stoichometric

point of 11.8%, no α-Fe phase is expected [24]. For this case, one would expect the (410) peak to the be the largest peak, whereas the pattern in Figure 115 shows the (410) peak as being of equal height to the (314) peak. Since the (314) peak overlaps the 100% intensity α-Fe diffraction peak (110), a partial decomposition would appear as an increase in the height of the (314) peak. Without the diffraction pattern of the starting material, it is difficult to discern if a partial decomposition has occured, but this XRD trace shows that it is a possiblity.

5.2.4 Sm-Fe-N

In contrast to the other magnetic phases, Sm-Fe-N is fairly stable during shock compaction. Although the decomposition temperature is debated [25, 26], thermal decomposition of $Sm_2Fe_{17}N_3$ produces α-Fe, Fe_4N, and SmN, as shown in Equation 11. Therefore, any decomposition of the $Sm_2Fe_{17}N_3$ phase would mostly likely be detected as an increase in the relative amount of α-Fe in the XRD trace. The 804 and 816 samples, shown in Figure 66, have no change or very small changes in the amount of α-Fe. While the initial amount of iron in the 677 sample is not known, the recovered compact also has a small fraction ($\sim$4%) of iron. The temperature estimates listed in Table 8 show that the bulk shock temperature never reaches the 400-475 range that Katter et al. [26] identified as the point at which magnetic properties begin to degrade. The temperature-time curves shown in Figure 67 indicate that the stable long term operating temperature estimated by Skomski [25], 250-300^{o}C, is only exceeded for $\sim$ 1 second for the center of the sample and for even shorter times for the outer portions of the sample.

Previous reports have demonstrated the stability of $Sm_2Fe_{17}N_3$ under shock compression [122, 124, 126]. Figure 116 shows the XRD traces for several shock compacted Sm-Fe-N samples and the starting powder as reported by Mashimo et al. [122]. XRD traces are presented for shock compaction experiments performed at 12.8, 15.5, 19.2, and 29.0 GPa, and the impactor material and impact velocity for each experiment are also indicated. The XRD traces show increased diffraction peak broadening but no increase in α-Fe for experiments (b) and (c) performed at 12.8 and 15.5 GPa respectively. The $Sm_2Fe_{17}N_3$ phase begins to decompose for shock compaction pressures above 15.5 GPa, as shown by an increase in the α-Fe diffraction line. In a subsequent report, Mashimo et al. [124] found no decomposition in shock compacted samples with a shock pressure of 14.6 and 14.7 GPa but an increase in the amount of α-Fe in samples compacted with a shock pressure of 15.8 and 15.9 GPa. While Mashimo et al. [122, 124] tested other factors, such as compacting the samples in vacuum or air, their results indicate that decomposition in shock compacted samples is mainly pressure dependent and begins at shock pressures greater than $\sim$15.5 GPa. Their results

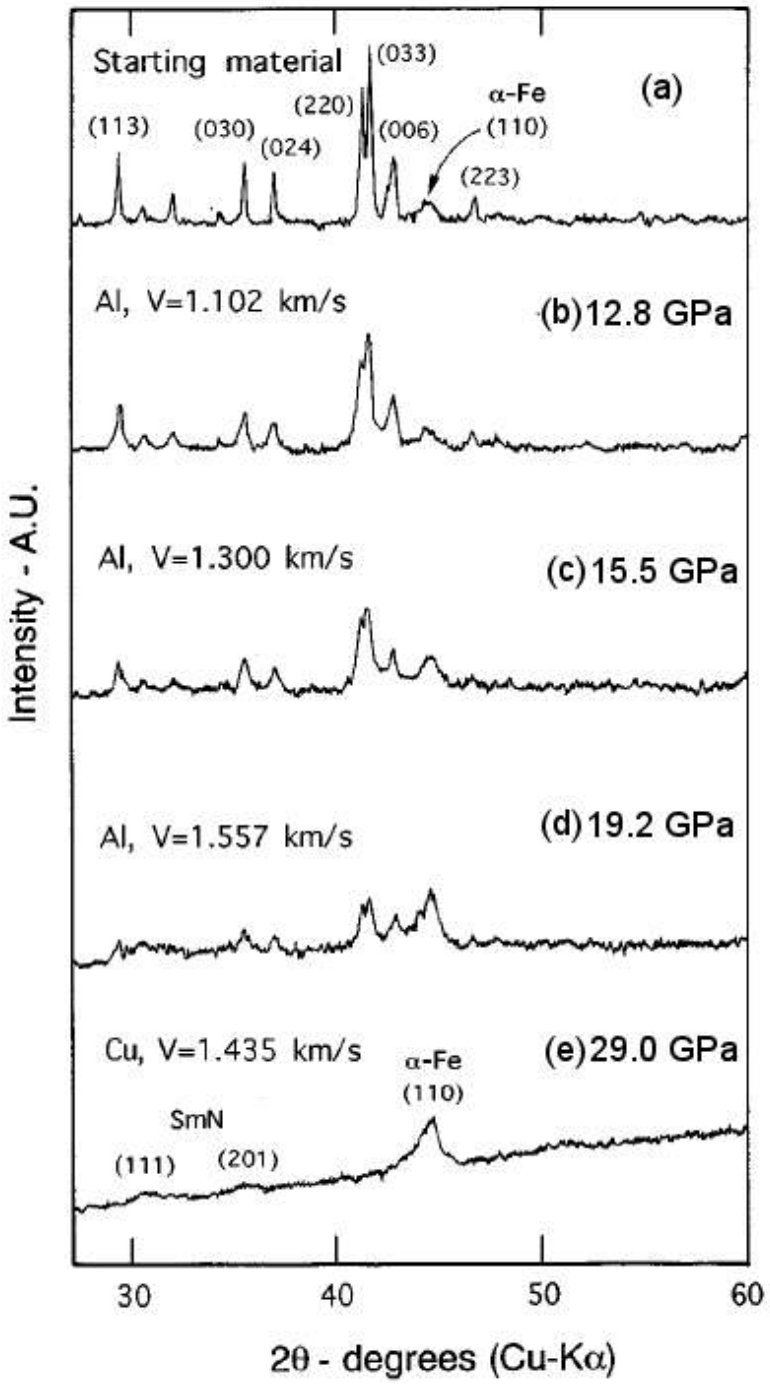

Figure 116: XRD traces of (a) Sm-Fe-N starting powder and shock compacted samples with primary shock pressure of (b) 12.8 GPa (c) 15.5 GPa (d) 19.2 GPa and (e) 29.0 GPa. The impactor plate material and impact velocity are also indicated for each experiment. [122]

are consistent with the results from the shock compaction experiments performed in this work. The samples from this work had a shock pressure (∼5-8 GPa) that is well below the 15.5 GPa critical point, and these samples show little or no decomposition.

Figure 117(a) shows the XRD traces for ball milled samples of Sm-Fe-N with different milling times. While ball milling increases the diffraction peak width, decomposition, as shown by an increase in α-Fe, occurs only for long milling times. This is shown more clearly in Figure 117(b), which shows the α-Fe content for various milling times. As milling time increases, the overlap in the Sm-Fe-N peaks increase, making quantitative analysis more difficult. This is the reason for the increasing size of the error bars in Figure 117(b). A more detailed explanation for estimating the size of the error bars is provided in Appendix B.

The XRD traces for ball milled samples shown in Figure 117(a) share many similarities with the XRD traces for shock compacted samples in Figures 66 and 116. Increasing milling time or increasing shock pressure produces additional diffraction peak broadening, but formation of α-Fe only begins for long milling times and high shock pressures. This indicates that decomposition of shock compacted $Sm_2Fe_{17}N_3$ is linked to the deformation produced by shock compaction. The $Sm_2Fe_{17}N_3$ S phase is stable for small amounts of deformation; however, large amounts of deformation causes decomposition, resulting in the formation of the α-Fe decomposition product.

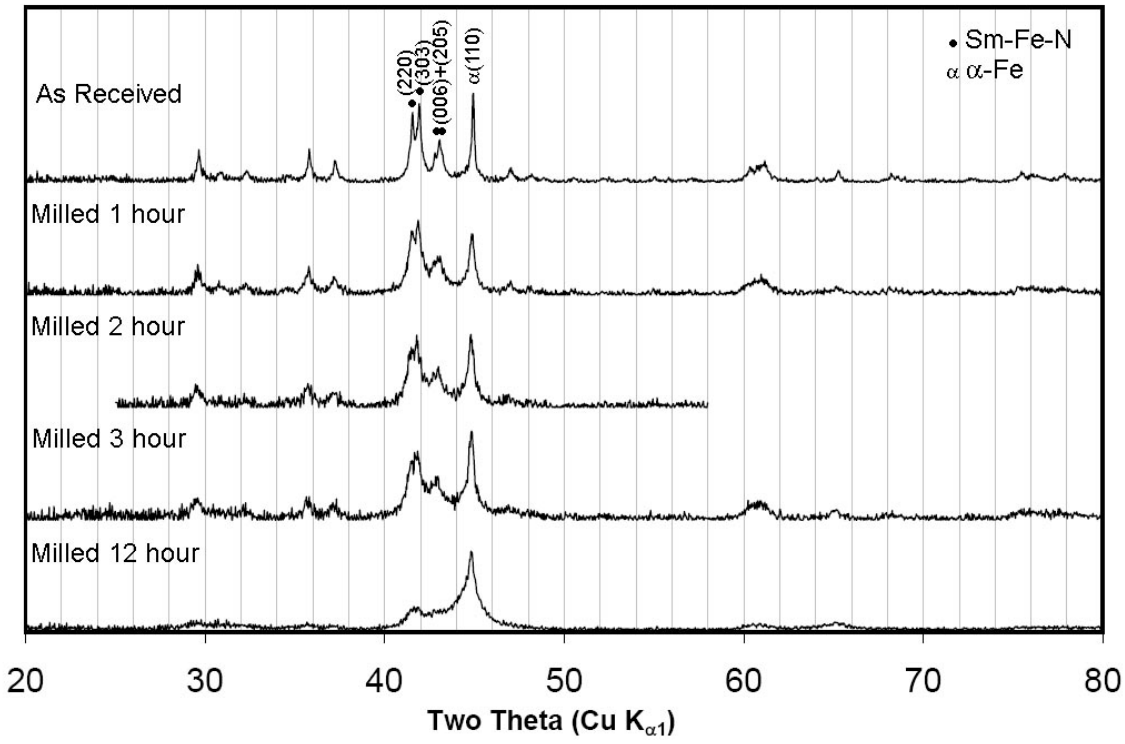

(a) XRD traces of ball milled Sm-Fe-N

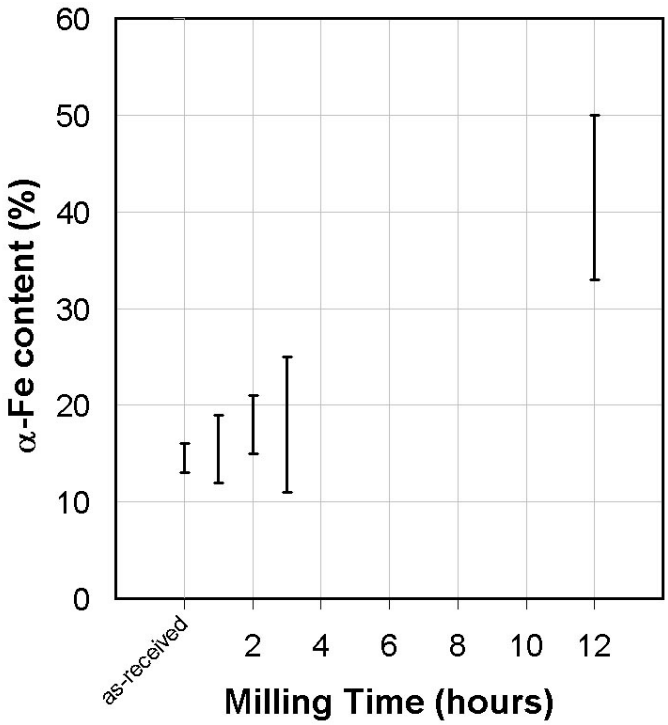

(b) Iron content of ball milled Sm-Fe-N

Figure 117: (a) XRD traces of ball milled Sm-Fe-N powder with milling times up 12 hours. (b) α-Fe content in each sample as determined from XRD analysis.

5.2.5 Composite Systems

While forming composites from the magnetic materials discussed above would alter the local stress condition and potentially change the compaction behavior, it does not seem to significantly alter the stability of any of the magnetic phases. XRD traces of shock compacted Sm-Fe-N/$Fe_{16}N_2$ composites shown in Figure 72 and Figure 74 show that the $Fe_{16}N_2$ phase decomposes in all cases. For the Sm-10%16-2 sample, the expected shock temperature is near (but just above) the stable temperature for the $Fe_{16}N_2$, yet decomposition still occurs, as shown by the lack of the α'' diffraction peaks (004) and (422). The samples with a higher percentage of $Fe_{16}N_2$, displayed in Figure 74, show that similar $Fe_{16}N_2$ products are produced in the composite. The XRD trace for Sm-Fe-N/Fe_4N composite shown in Figure 75 show that the Fe_4N phase is at least partially retained. The small initial percentage of Fe_4N and the overlap of diffraction peaks means that detecting the formation of Fe_3N is not possible for this sample.

Detecting decomposition of the $Nd_2Fe_{14}B$ phase in Nd-Fe-B/α-Fe composites is difficult since the α-Fe decomposition product is already present. The XRD traces of compact 1023-2 and 1023-3 of ball milled Nd-Fe-B/α-Fe in Figure 93 may have some increase in the α-Fe diffraction peak, but a lack of other diffraction peaks makes comparison difficult. The Nd-Fe-B/α-Fe composites made by mixing nanoparticles (1113-2 and 1127-3) demonstrate more clearly that the $Nd_2Fe_{14}B$ phase will decompose in composite form, as shown in Figure 102 and Figure 104.

Jin et al. published several reports of shock compaction of melt-spun Pr-Fe-B/α-Fe composites [15, 16]. Figure 118 shows the XRD traces for the front and back of recovered compacts after impact at 880 m/s. The trace for the front of the sample has an increase in peak width compared to the starting powder, and the back of the sample has both increased width and an increase in the α-Fe diffraction lines. The authors report the peak pressure calculated from 2D AUTODYN simulations, instead of the primary pressure, but indicate that the back of the sample experiences a pressure roughly twice that of the front of the sample. The difference seen for XRD traces of the front and back of the samples are similar to those in Figures 78 and 85 for non-composite Nd-Fe-B.

5.3 Deformation Behavior

Deformation of $Sm_2Fe_{17}N_3$ bears some similarity to $Nd_2Fe_{14}B$. In both types of materials, deformation is accommodated primarily by a reduction in grain size for large grained samples. Williamson-Hall plots for Sm-Fe-N compact 816 (Figure 68(c)) and Nd-Fe-B compact 826-3 (Figure 79(b)) show similar trends. Shock compacted samples have increased diffraction peak width, and most of the

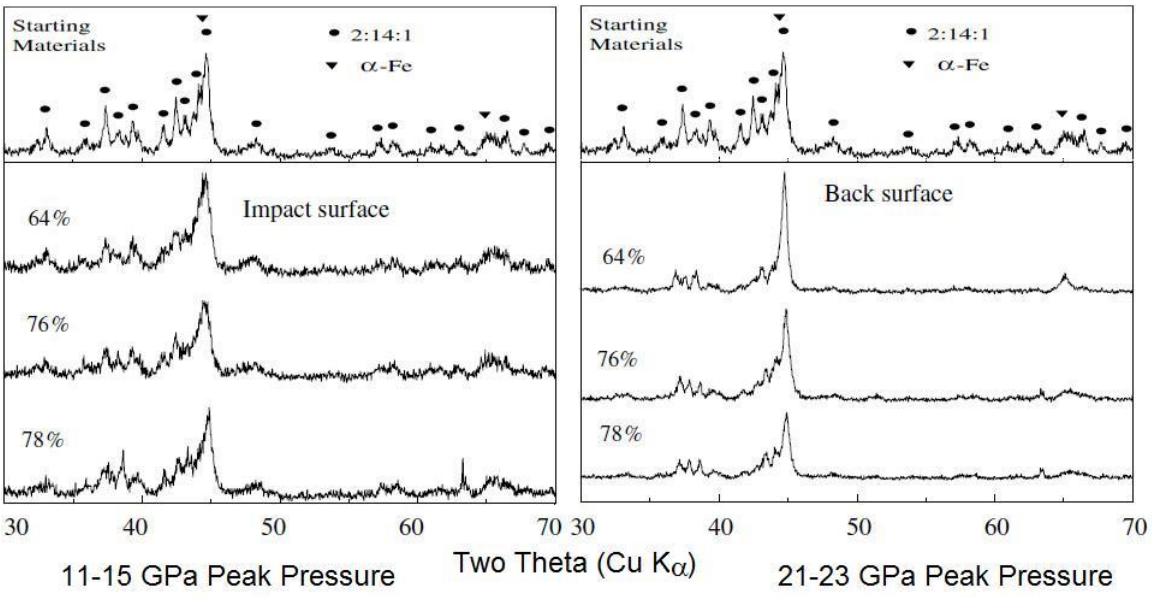

Figure 118: XRD traces of traces of melt-spun Pr-Fe-B/α-Fe composites and the front and back of recovered compacts with different initial densities. [15]

increase width is accounted for by a decrease in grain size. The SEM images for both types of materials agree with the Williamson-Hall analysis, as shown by Figure 70 (Sm-Fe-N) and Figure 80 (Nd-Fe-B). Both micrographs show that larger grains have broken up into smaller ones.

The similarity in deformation behavior of Nd-Fe-B and Sm-Fe-N most likely arises from the availability of limited plastic slip in both of these systems. This means that large grained samples of Nd-Fe-B and Sm-Fe-N will tend to deform by fracture, which appears as a reduction in grain size in shock compacted samples. Mishra et al. [58] noted that $Nd_2Fe_{14}B$ has only one primary slip plane (001) and only two primary slip directions on this plane. This is essentially a result of the low symmetry of the crystal system, a characteristic shared with the rhombohedral $Sm_2Fe_{17}N_3$ phase.

The main difference in mechanical behavior of Sm-Fe-N and Nd-Fe-B is that Sm-Fe-N can accommodate significantly more deformation before it begins to decompose. Comparing the XRD traces of ball milled samples of Sm-Fe-N (Figure 117(a)) and Nd-Fe-B(Figure 76(b)), decomposition occurs even in short milling times for Nd-Fe-B, while only long milling times produce decomposition in Sm-Fe-N.

McCormick et al. [46] suggested that milling decreases the $Nd_2Fe_{14}B$ grain size and the transformation to an amorphous phase is driven by the large surface energy of the nanocrystalline grains. SEM micrographs of compacts 826-3 and 1127-2 have microstructural features that may correspond to areas of decomposition. Figure 80 of 826-3 shows areas of highly localized deformation with

smaller grain and grain aggregates. The SEM image of compact 1127-2 in Figure 82 shows two types or microstructural regions: type A, with grain morphology roughly similar to the starting powder particle morphology, and type B, which appear as dark spots 1-5 μm in size. Both types had similar Nd and Fe composition, as measured by the EDS. It is possible that the type B regions are large areas of decomposition formed from an aggregate of many grains. The type B regions in the images of compact 1127-2 may be regions similar to the areas of localized deformation in compact 826-3, but with more severe deformation. The increased deformation produces decomposition, leaving only areas of amorphous phase and tiny α-Fe grains (too small to resolve in SEM micrographs).

The SEM image in Figure 83 shows that the particles in the type A regions of the 1127-2 sample lack distinct particle outlines. The particles blend together in a manner that appears similar on a smaller scale to the type B regions. This indicates that localized deformation is occurring at particle interfaces, producing a microstructure with amorphous intergranular regions which appear in the SEM as these smooth looking regions. This suggests that the type A areas are regions with partial decomposition and the type B areas are regions of nearly complete decomposition.

This view of deformation and decomposition helps to explain why the compact 1127-2, which had a lower shock pressure than compact 0826-3, showed such a greater degree of decomposition. While the 1127-2 green compact had a slightly lower initial density, the biggest difference between the two starting materials is the surface area of the particles. Attrition milling, used in pretreatment of the 1127-2 powder, does not significantly increase diffraction peak width, indicating only a small amount of microstrain is introduced into the material through creation of dislocations; however, attrition milling does significantly increase the surface area. This means that the 1127-2 compact will have an increased amount of deformation at particle interfaces and generate additional decomposition.

An alternate view of the increased decomposition in the 1127-2 sample relative to the 826-3 samples is that the attrition milling may have the effect of stripping off excess Nd from the $Nd_2Fe_{14}B$ particles. The unmilled powder has approximately 15% rare earth content (combined Nd and Dy, with a majority being Nd). Since $Nd_2Fe_{14}B$ is a line compound, the excess Nd will be segregated to the grain boundaries [24]. This amorphous Nd rich grain boundary phase much more easily accomodates dislocations and dislocation motion than the $Nd_2Fe_{14}B$ grains [12]. If the softer Nd-rich coating on the $Nd_2Fe_{14}B$ particles is removed by ball milling, more of the deformation must be accomadated by the $Nd_2Fe_{14}B$ phase, leading to additional decomposition.

The shock compaction experiments discussed previously have a tri-axial stress state, dominated by a hydrostatic stress component. The high rate forging experiments, discussed in §4.5.1 and §4.6.3,

attempt to create a uni-axial stress condition to mimic the die-upsetting process. As discussed in §2.2.3, the die-upsetting process, in which texture is introduced into Nd-Fe-B by uniaxial pressing at high temperature, is a compositionally dependent diffusional process. Excess Nd creates a low melting point grain boundary phase that provides a fast diffusion path at high temperatures. Increasing the strain rate or decreasing the temperature means that a higher pressure is needed to reach the flow stress of the material. Applying this premise to high rate forging experiments means that a very high pressure would be needed. While it is unlikely that a diffusion dominated process, such as die-upsetting, can occur on the time scales available for high rate forging experiments, the high strain rate behavior of Nd-Fe-B under uniaxial stress bears further investigation.

Numerous high rate forging experiments were performed on HDDR Nd-Fe-B powder and Pr-Fe-B/α-Fe composite powder. The XRD traces in Figure 89 and Figure 91 reveal that high-rate forging of HDDR powder causes an increase in diffraction peak width, but no increase in the $(00c)$ family of peaks. Similar results were obtained for high-rate forging experiments on the Pr-Fe-B/α-Fe powder, as shown in Figure 109 and Figure 110. The effects on the XRD traces from forging are similar to those seen for shock compacted Nd-Fe-B samples 826-2 and 826-3, although little or no decomposition is observed in high-rate forging samples. The smaller amount of decomposition may be due to the lower impact velocity used in the forging experiments. These results indicate that uniaxial stress loading experiments do not significantly alter the mechanical behavior of Nd-Fe-B, as compared to the tri-axial stress shock compaction experiments.

The above discussion of deformation in Nd-Fe-B has assumed that limited plastic slip is available in this material system. A study by Jin et al. [15] reported a significant amount of microstrain in shock compacted Pr-Fe-B/α-Fe melt-spun composites, as shown by Williamson-Hall plots, which would seem to contradict the assumption of limited plastic slip. Figure 119 shows the Williamson-Hall plot for the starting powder and recovered samples with different initial densities [15]. It indicates that the starting powder has no significant microstrain, while the increase in the slope of the trend line for the shock compacted samples indicates an increase in retained microstrain. This differs from the results for compact 826-3 in Figure 79(b) of the present work, which show that shock compaction decreases grain size but produces only a small increase in the microstrain.

Previous TEM studies by Mishra et al. [58, 12] have shown very little indications of dislocations in Nd-Fe-B following die-upsetting. A small number of Nd-Fe-B grains contained twin dislocations, but no other types of dislocations were observed. Likewise, TEM micrographs of the shock compacted samples reported by Jin et al. [15] did not find any dislocations in the Pr-Fe-B grains, although minor twinning and shear banding was observed in some of the samples.

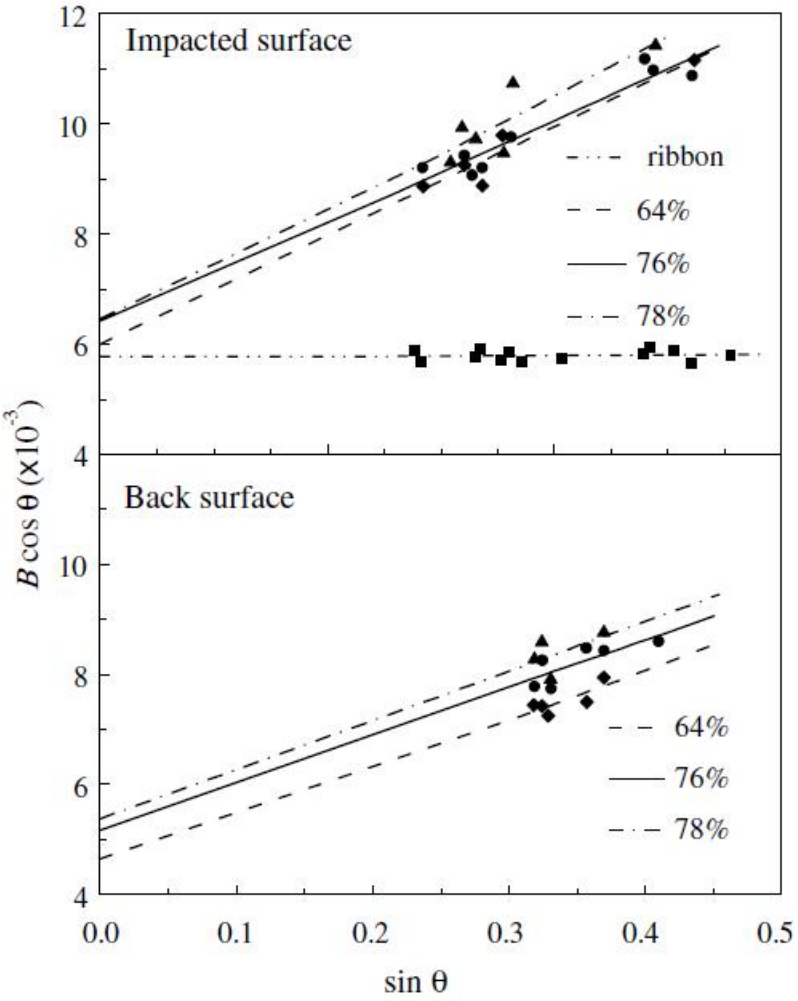

Figure 119: Williamson-Hall plot for XRD traces of shock compacted Pr-Fe-B/α-Fe composites as reported by Jin et al. [15]

The exact method used to determine the peak width for the Williamson-Hall plot in Figure 119 is not described by Jin et al. [15]. In addition, the values for the $\sin(\theta)$ axis are not given, which makes replicating the analysis difficult. The original Williamson-Hall plot shows all three samples on the same plot, which clouds the analysis. Figure 120 shows only the 76% initial denisty sample, which has the most number of peak widths plotted. For comparison purposes, Figure 120 shows a replotted Williamson-Hall plot in which the peak widths, as shown in the XRD trace from the paper, are estimated by eye. The replotted data roughly matches the original plot in some cases, but some peaks shown do not lie with the trend and do not allow for a clear conclusion as to the primary deformation mechanism.

The large number of overlapping peaks present in the XRD trace complicates any measurement

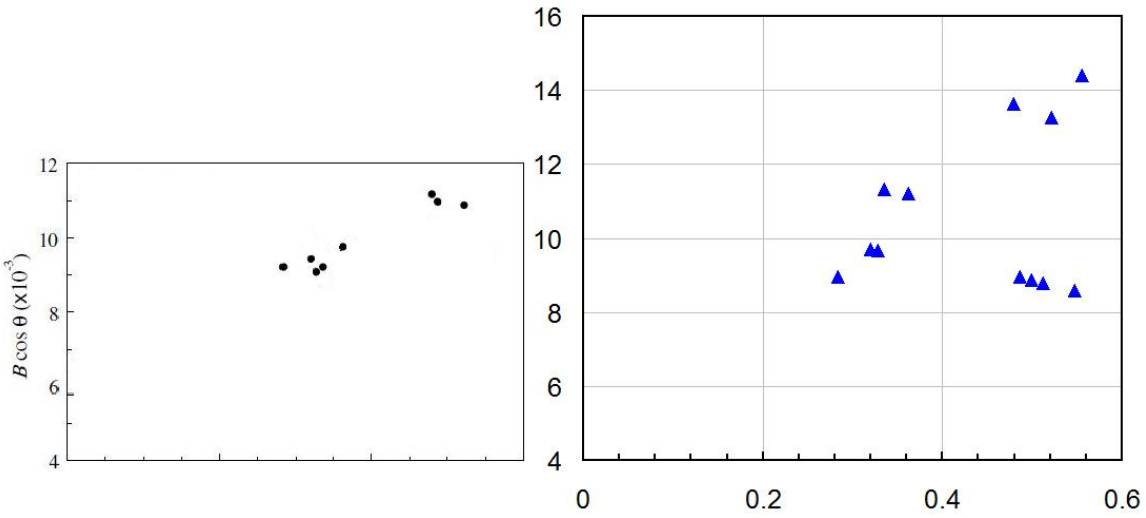

Figure 120: Williamson-Hall plots for (left) published XRD trace of shock compacted Pr-Fe-B/α-Fe composites with initial density of 76% [15] and (right) replotted data when measuring peak width by eye.

of the peak width. A proper analysis of the XRD pattern needs to separate the effects of overlapping peaks by fitting the pattern with superimposed peaks. The 76% XRD trace was digitized and fit to a combined gaussian-lorentzian curves (psuedo-Voigt) using the Jade XRD analysis software. Figure 121 shows the resulting Williamson-Hall plot. While there is considerable scatter in the plot, the best fit trend line has shifted up and there is little evidence of an increase in the slope. This suggests the the deformation is occurring primarily by grain size reduction, instead of generation and motion of dislocations. This is in agreement with both the TEM micrographs shown in the Jin et al. [15] paper and is consistent with the results shown for shock compacted Nd-Fe-B in Figure 79(b) from the present work.

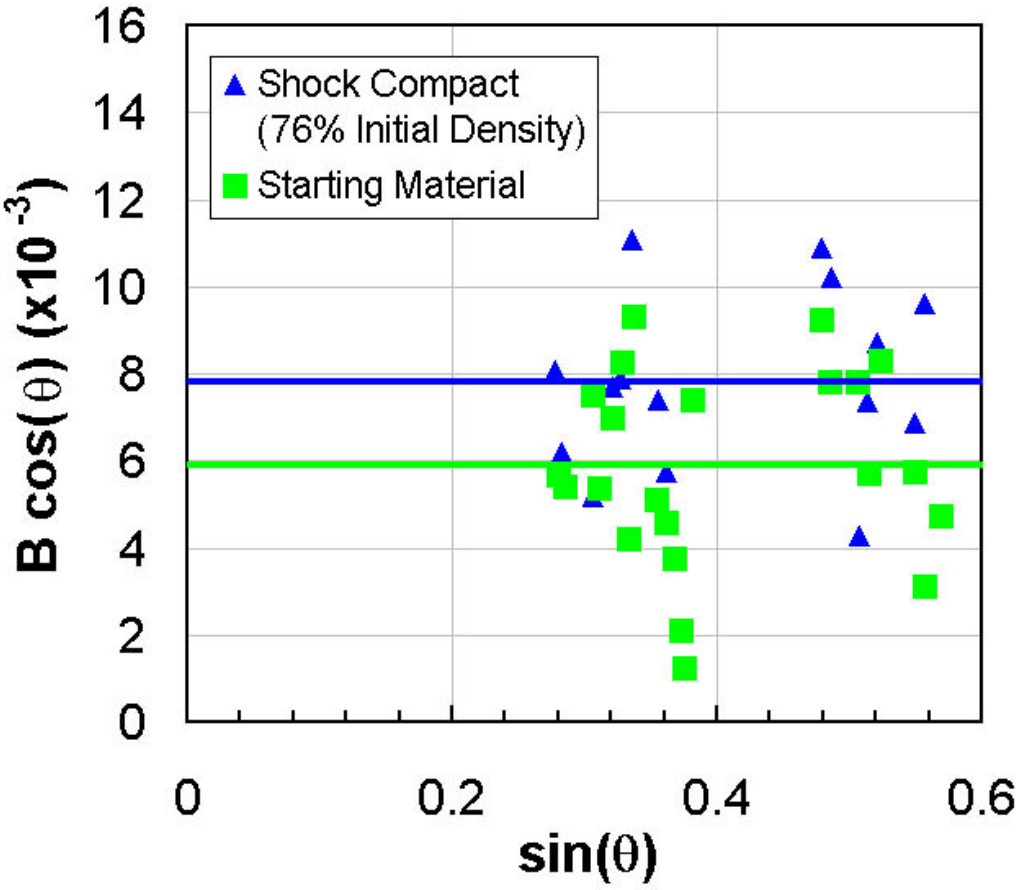

Figure 121: Williamson-Hall plots for (a) starting materials and (b) shock compacted Pr-Fe-B/α-Fe composites from Jin et al.'s report [15] replotted using pseudo-Voigt curves to fit the XRD pattern.

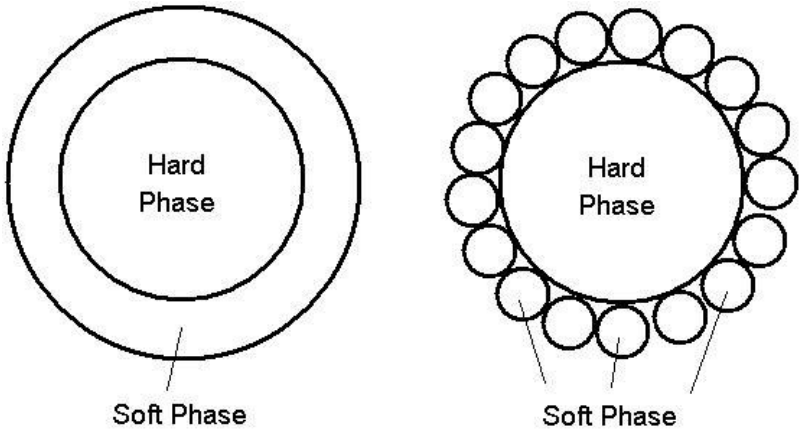

Figure 122: Schematic of optimal distribution of soft particles around a larger hard particle

5.4 Development of Texture by Magnetic Field Alignment

The use of a magnetic field to rotate magnetic particles into alignment prior to sintering is one of the most successful techniques for fabricating highly textured permanent magnets [66, 8]. Adapting a similar technique for use with shock consolidation of nanocomposite magnetic materials requires a new method of fabricating composite powders. The commonly used fabrication methods of melt-spinning and high-energy ball milling typically produce isotropic polycrystalline particles. Since these particle are individually isotropic, using a magnetic field to rotate them into alignment will not produce an anisotropic sample.

A possible solution is to develop a composite by mixing together different types of single crystal particles. In order to construct a bottom-up composite in this fashion, it necessary to control the size distribution of both powders. If the grain size of the hard magnetic phase is large, then clusters of the soft phase particles must necessarily form if there is a significant fraction of soft phase. This is mostly likely the cause of the clustering of $Fe_{16}N_2$ particles seen in the Sm-20%16-2 compact in Figure 73.

The maximum soft phase that can be added without forming clusters of soft particles can be estimated by assuming that the soft phase forms a uniform coating around the hard particles. Alternatively, a uniform coating can be used to approximate a single layer of soft phase particles surrounding a hard phase particle. Figure 122 displays a schematic which illustrates the idea. If a hard phase particle of diameter d has a soft phase coating of thickness t, the volume fraction of soft phase will be given by:

$$Vol\% \;=\; 1 - \frac{d^3}{(d+2t)^3} \tag{32}$$

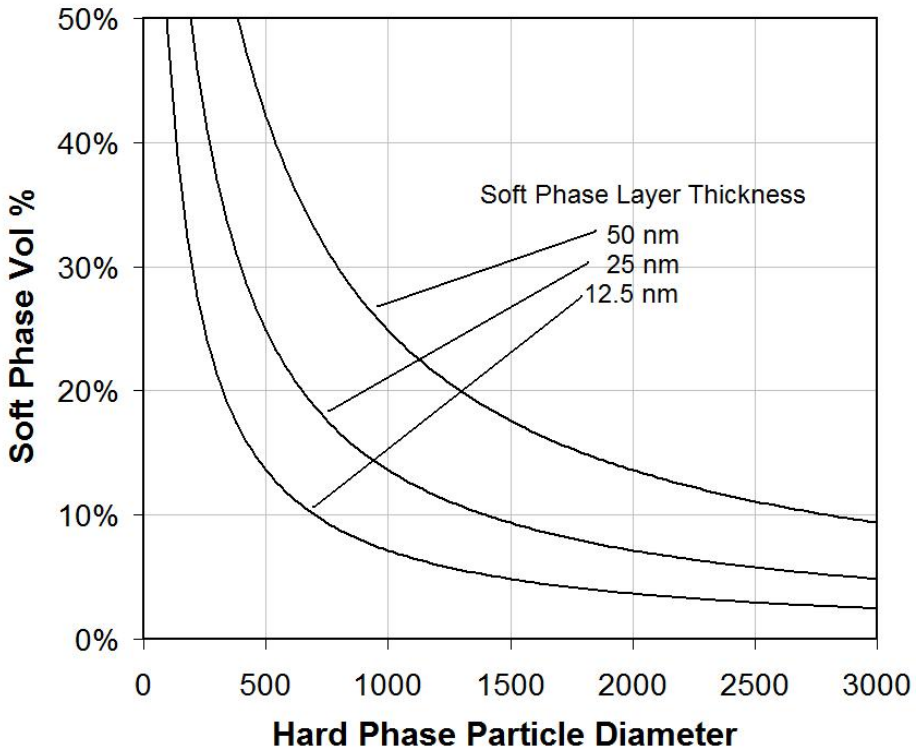

Figure 123: Dependence of maximum possible soft phase volume fraction on hard phase particle diameter. Curves are shown for soft phase layer thicknesses of 50, 20, and 12.5 nm.

For a soft phase thickness of 25 nm, the hard phase particle must have a diameter of approximately 900 nm in order to have a 15% volume of the soft phase. Figure 123 plots the allowable soft phase percentage verses the hard phase particle diameter for three different thicknesses of soft phase coatings. While the soft phase grain size must be approximately ∼10-30 nm in order to take advantage of exchange coupling, the hard phase grain size need only be small in order to allow a significant amount of soft phase to be added [4]. For 10-20% soft phase, the necessary particle size shown in Figure 123 is in the range achievable by attrition milling of Nd-Fe-B powders, which was shown in §4.5 to produce primarily single crystal particles.

Equation 32 is obviously a simplified model of the grain structure of a bottom up composite formed by mixing nanoparticles. Real powders have some distribution of particle sizes, and a few larger particles can significantly skew a volume weighted average. To achieve a suitable microstructure, it will be necessary to achieve a size distribution with very few large particles. Using the size distributions shown in Figure 96, one can get a better estimate of the volume fraction of soft phase that can be added to the mixture. Assuming a 25 nm coating on an average sized particle in each

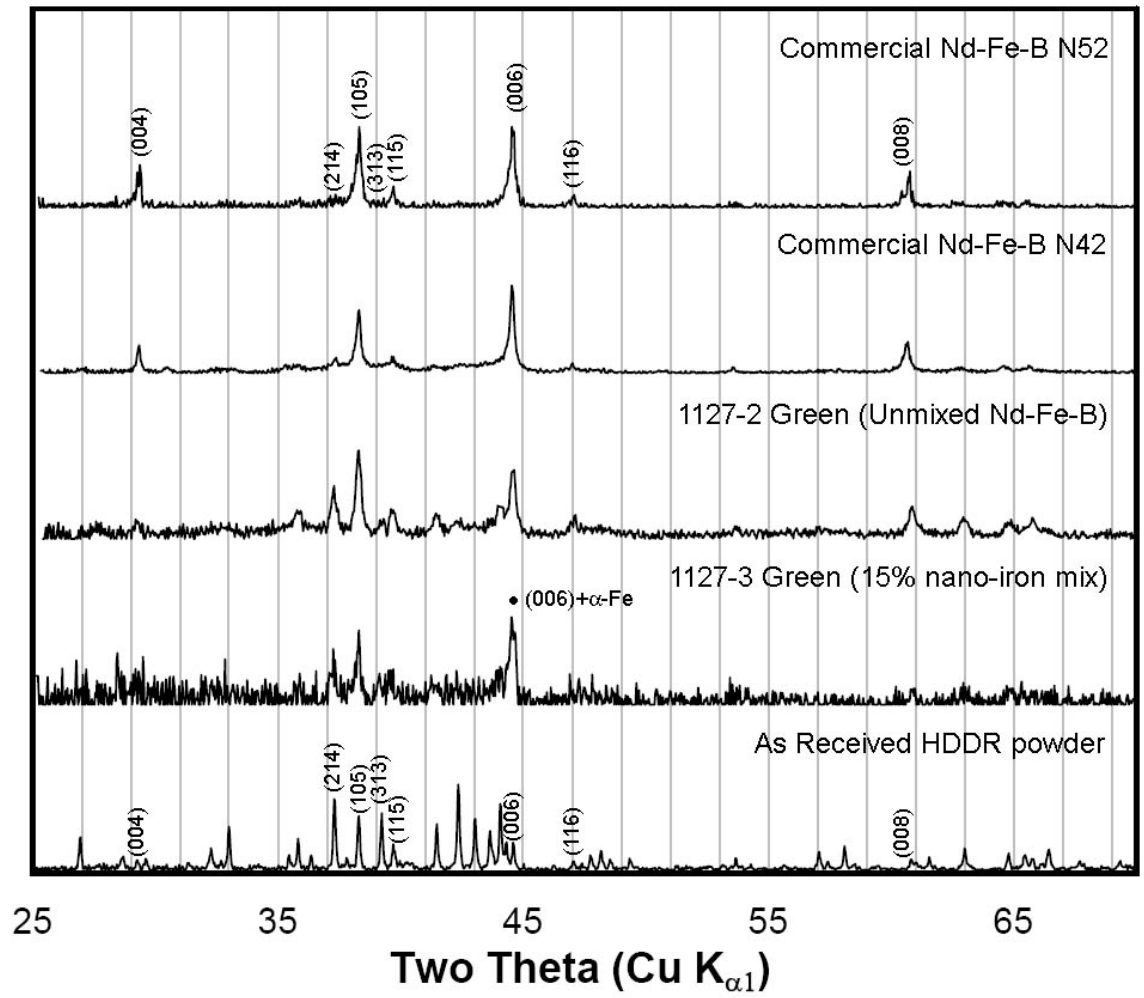

Figure 124: XRD patterns for HDDR Nd-Fe-B powder and textured Nd-Fe-B samples N52, N42, 1127-2, and 1127-3.

size range, then 17% soft phase could be added to the powders milled for 185 and 403 hours.

As discussed in §4.6.2, samples of attrition milled particles were mixed with commercially available iron nanoparticles, and these powders were aligned and isostatically pressed at Advanced Materials Corporation. Figure 124 shows the XRD traces of the aligned pellets for both the unmixed Nd-Fe-B powder (1127-2 Green) and the powder mixed with iron nanoparticles (1127-3 Green). Also shown are the two types of commercial Nd-Fe-B magnets, grades N52 and N42, and as-received HDDR powders. The mixed green compact was sealed inside a two layers of kapton film to prevent oxidation of the iron nanoparticles. This leads to the greater amount of noise present in this scan. The α-Fe lines over lap the Nd-Fe-B lines, and so the presence of the iron nanoparticles is difficult to detect in small amounts. The HDDR powder serves as an isotropic sample for comparison to the other four traces, which all have high intensity for the (00c) family peaks (plus the (105) peak)

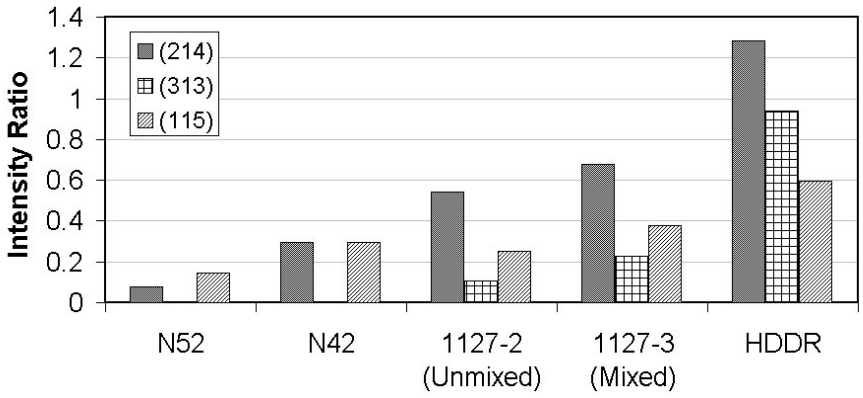

Figure 125: Intensity ratios of the (105) peak to neighboring peaks (214), (313), and (115) for several forms of textured Nd-Fe-B and HDDR Nd-Fe-B powder (isotropic).

relative to other peaks.

The intensity ratio of the enlarged peaks to the surrounding peaks provides a rough estimate of the amount of texture present [152]. Figure 125 shows the intensity ratios for the (105) peak at 38.3^o and three neighboring peaks (214), (313) and (115). The samples are arranged with decreasing texture from left to right. The N52 grade commercial sample shows the greatest degree of texture, with very small (214) and (115) peaks and the (313) peak too small to be seen in the trace. For the grade N42 material, the intensity ratios for these peaks show a slight increase, although the (313) peak is still too small to be seen. The intensity ratios for the unmixed (1127-2) and mixed (1127-3) green compacts show they have less texture than the sintered commercial materials (N52 and N42), which is expected since liquid phase sintering tends to increase texture in Nd-Fe-B magnets [152]. The *c*-axis texture will also increase the (115) peak, but not to the same extent as the (105) peak. This is the reason the (313) peak is larger than the (115) peak in the HDDR sample (isotropic), but not in the textured samples. Relative to the isotropic sample, both green samples have significant *c*-axis texture, although the unmixed sample has less texture than the mixed sample. The addition of the iron nanoparticles may help form aggregates that inhibit rotation of the particles. The higher surface area of the nanoparticles may mean that additional toluene is retained, despite its removal in vacuum, and the toluene residue may serve to entangle the particles. While green compacts 1127-2 and 1127-3 show significant texture, evaluating the effect of shock compaction on the alignment in these samples is not possible, due to the decomposition that occurs in the $Nd_2Fe_{14}B$ phase.

CHAPTER VI

SUMMARY AND CONCLUSION

The shock compression response of soft (Fe_4N and $Fe_{16}N_2$) and hard ($Nd_2Fe_{14}B$ and $Sm_2Fe_{17}N_3$) magnetic phases has been investigated in this work to determine their thermo-mechanical stability and explore the possibility of formation of textured bulk nanocomposite magnets. A prominent result encountered in this work is the wide range of phase transformations observed in the shock compacted magnetic materials. Phase transitions or decomposition were observed in Fe_4N, $Fe_{16}N_2$, and $Nd_2Fe_{14}B$, while shock compacted $Sm_2Fe_{17}N_3$ samples showed very little or no decomposition. The results indicate that use of shock compaction to develop a high performance permanent magnet will require careful control of the material and compaction conditions to minimize the effects of phase transformations.

Utilizing the ferromagnetic iron nitrides, and $Fe_{16}N_2$ in particular, as the soft phase in an exchange coupled permanent magnet is especially difficult, due to their thermo-mechanical instability. Shock compaction of *FCC* Fe_4N created a partial transformation to *HCP* Fe_3N. This mirrors previous reports of tungsten-carbide anvil cell experiments, which establish the transition point as a pressure of $\sim$3 GPa. Shock compaction of $Fe_{16}N_2$ produces decomposition due to thermal effects. The main products, α-Fe and Fe_4N, are the typical thermal decomposition products of $Fe_{16}N_2$, and the estimated diffusion distance of nitrogen in the sample matches the Fe_4N grain size.

Decomposition of Nd-Fe-B, producing α-Fe and amorphous Nd-Fe-B, was observed in several shock consolidated samples. The decomposition process is attributed to deformation associated with shock compaction, similar to decomposition reported in ball milled Nd-Fe-B. SEM micrographs of shock compacted samples suggest that decomposition occurs primarily in areas of localized deformation. Shock compaction of attrition milled samples, which have a significantly higher initial surface area, leads to nearly complete decomposition of the $Nd_2Fe_{14}B$ phase, and this may be due to increased deformation at particle interfaces. Previous reports have shown evidence of decomposition, but the formation of α-Fe was attributed to melting or was not directly discussed. Estimates of the shock temperature and VISAR experiments performed in the present work indicate that the decomposition is not due to melting. Observation of decomposition in shock compacted Nd-Fe-B and Pr-Fe-B composites with α-Fe can also go undetected, since α-Fe is already present in the starting

materials.

Previous reports have demonstrated the stability of $Sm_2Fe_{17}N_3$ under shock compression [124, 126]. The present work helps to describe the deformation occurring during shock compaction more thoroughly. Sm-Fe-N was shown to accommodate deformation primarily by grain size reduction, especially in large grained materials. The phenomena of grain size refinement is likely linked with low plasticity, as very little increase in microstrain is observed in any of the Williamson-Hall plots. Similar effects, deformation by grain refinement and limited microstrain, are seen in shock compacted samples of Nd-Fe-B. The low symmetry of the rhombohedral (Sm-Fe-N) and tetragonal (Nd-Fe-B) systems limits the number of active slip planes, which is most likely the cause of the limited plasticity.

While many questions remain, the use of magnetic fields to pre-align magnetic particles holds promise for development of texture in exchange coupled permanent magnets. Composites were formed by mixing single crystal particles of Nd-Fe-B with iron nanoparticles, and the alignment-by-magnetic-field technique was able to introduce significant texture into green compacts of this mixture. Problems with decomposition of the $Nd_2Fe_{14}B$ phase, as discussed above, prevent fabricating bulk compacts from the aligned green compacts; however, SEM micrographs show that the grain growth in the iron nanoparticles is limited during shock compaction. Thus, if the decomposition problem can be overcome, then the technique has potential to produce a textured nanocomposite magnet.

While consolidating mixtures of nanoparticles into bulk form without decomposition or grain growth is a challenge, fabricating single crystal particles of sufficiently small size is also an issue. If the hard phase particles are large, then either a very small fraction of soft phase can be used or there must necessarily be clusters of soft phase particles. The use of attrition milling to process Nd-Fe-B is therefore an important technique, since it can be used to create single crystal particles of sufficiently small size.

In conclusion, the present work on shock compaction has revealed the importance of detailed characterization of microstructure as a function of loading conditions. A wide range of phase transitions were observed in shock compacted materials due to a combination of deformation, thermal, or stress induced effects. Unwanted or uncontrolled phase transformations can be detrimental to the properties of permanent magnets. Many previous studies on shock compaction of magnetic materials do not pay attention to the phase stability aspects, and simply focus on measured magnetic properties. Without providing detailed characteristics of the microstructure, the effects of shock compaction can be difficult to discern. Careful analysis of the microstructure and phase stability, through XRD or TEM analysis, and their correlation with processing (compaction) conditions, will be crucial to developing high performance permanent magnets.

CHAPTER VII

FUTURE WORK

The combination of magnetic field alignment and shock compaction has great potential for developing a textured and exchange-coupled nanocomposite magnet; however, the decomposition of Nd-Fe-B is a critical problem. The decomposition is driven by localized deformation; however, the deformation mechanism of Nd-Fe-B changes at elevated temperatures. At 1000^oC and above, Nd-Fe-B can accommodate significant plastic slip. Shock compaction experiments performed at an elevated temperature may be able to consolidate the material through enhanced plastic slip instead of decomposition. A combination of the heating from shock compaction and conventional heating of the shock fixture at the time of impact can be used to achieve the optimal thermal conditions for good consolidation.

An alternative is to replace Nd-Fe-B with a more mechanically stable hard magnetic phase. Future work in this area will need to develop techniques for fabricating submicron sized hard phase magnetic particles, and attrition milling appears to be a promising technique. Sm-Fe-N may be an ideal candidate, since this work and several other studies have shown it to be relatively stable under shock loading. $SmCo_5$ is another possible choice. It's high anisotropy maybe useful in maintaining a high coercivity while adding a larger volume fraction of soft phase. An exchange coupled magnet based on $SmCo_5$ will be unlikely to significantly surpass the energy product of a conventional Nd-Fe-B magnet, due to the low magnetization of $SmCo_5$; however, Sm-Co magnets are still the best available high temperature permanent magnets. An exchange-coupled Sm-Co magnet may improve the energy product of magnets used in high temperature applications. In addition, shock compaction of $Fe_{16}N_2$ alloyed with cobalt should be explored, since the cobalt additions may raise the temperature stability and allow for the use of this high magnetization phase in a nanocomposite permanent magnet.

Despite the alignment achieved in green compacts of nanoparticle mixtures, it is unclear how shock compaction will affect the alignment. While the loading condition is mainly hydrostatic, shock compaction is unlikely to produce a true isostatic compaction. Varying the shape of the wave front or altering the character of the pulse, such as using a ramp wave, may be beneficial to maintaining the alignment.

Even if a textured nanocomposite is developed through shock compaction, there are other significant challenges to developing a high performance exchange-coupled magnet. Maintaining a high coercivity while adding a large fraction of soft grains may be difficult. The presence of defects and the character of the grain boundaries also have a significant influence on the magnetic behavior. The development of texture in bulk form, however, has so far been the biggest problem in fabricating these types of next generation magnets.

APPENDIX A

SUMMARY OF SHOCK COMPACTION EXPERIMENTS

This appendix provides a single chart of all shock compaction experiments presented in this work. Several important characteristics are listed, however, additional details are presented for each experiment in the appropriate section. The compositional phase percentages shown for $Fe_{16}N_2$ composites are the nominal values with the actual values measured from XRD in parenthesis. The overlapping peaks and low signal to noise ratio of the XRD scans of the Sm-Fe-N/Fe_4N composites prevented any meaningful quantitative phase analysis, so these phase percentages were left blank. Since most samples of shock compacted Nd-Fe-B contained significant amounts of amorphous phase, the relative phase percentages are not listed. Instead a description of the processing steps used to prepare the pre-shock powder are listed.

Table 14: Summary of shock compaction experiments for all materials

Sm-Fe-N	$Sm_2Fe_{17}N_3$%	α-Fe%	Relative Density	Impact Velocity (m/s)	Pressure (GPa)	Temp (^{o}C)
677 Green	-	-	63%	-	0.79	-6
677 Compact	96%	4%	92%	788 ± 10	4.9-5.4	370-390
804 Green	96%	4%	72%	-	0.79	-21
804 Compact	96%	4%	95%	844 ± 42	7.0-7.4	350-365
816 Green	96%	4%	73%	-	0.79	-122
816 Compact	92%	8%	98%	903 ± 2	7.8-8.1	300-310
Fe_4N	Fe_4N	Fe_3N	Rel. Dens.	Imp. Vel.	Pressure	Temp
Fe_4N Green	100%	-	68%	-	0.79	4
Fe_4N Compact	57%	43%	-	860 ± 6	6.4-6.8	420-440
$Fe_{16}N_2$	$Fe_{16}N_2$	α-Fe	Fe_4N	γ''-FeN	ϵ-Fe	TMD
-21C 16-2 Green	95%	5%	-	-	-	7.43
-21C 16-2 Compact	20-22%	41-55%	21-32%	0-3%	4-5%	7.61-7.69
-126C 16-2 Green	95%	5%	-	-	-	7.43
-126C 16-2 Compact	13-17%	18-24%	29-43%	16-27%	6-7%	7.44-7.46
$Fe_{16}N_2$ Contin.	-	-	Rel. Dens.	Imp. Vel.	Pressure	Temp
-21C 16-2 Green	-	-	59%	-	0.79	-21
-21C 16-2 Compact	-	-	92-93%	844 ± 42	5.3-5.8	520-540
-126C 16-2 Green	-	-	56%	-	0.79	-126
-126C 16-2 Compact	-	-	92-93%	866 ± 4	4.9-5.3	430-450
Sm-Fe-N/Fe_4N	$Sm_2Fe_{17}N_3$	Fe_4N	Rel. Dens.	Imp. Vel.	Pressure	Temp
Sm10%Fe4N Green	90%	10%	77%	-	0.79	-6
Sm10%Fe4N Compact	-	-	93%	788 ± 10	7.1-8.0	300-350
Sm20%Fe4N Green	80%	20%	79%	-	0.79	-6
Sm20%Fe4N Green	-	-	96%	788 ± 10	7.4-7.9	280-330
Sm-Fe-N/$Fe_{16}N_2$	$Sm_2Fe_{17}N_3$	$Fe_{16}N_2$	Rel. Dens.	Imp. Vel.	Pressure	Temp
Sm-10%16-2 Green	90% (86%)	10%	75%	-	0.79	-122
Sm-10%16-2 Compact	90%	∼0%	∼94%	903 ± 2	8.2-9.1	280-330
Sm-20%16-2 Green	80% (77%)	20%	74%	-	0.79	-122
Sm-20%16-2 Compact	80%	∼0%	∼94%	903 ± 2	8.0-8.7	290-350
Sm-80%16-2 Green	20%	80% (76%)	59%	-	0.79	-126
Sm-80%16-2 Compact	20%	0-15%	∼93%	866 ± 4	5.4-6.0	400-450
Sm-90%16-2 Green	10%	90% (86%)	56%	-	0.79	-126
Sm-90%16-2 Compact	10%	0-15%	∼90%	866 ± 4	5.1-5.6	400-470
Nd-Fe-B	Description		Rel. Dens.	Imp. Vel.	Pressure	Temp
826-3 Green	As-Rec HDDR		75%	-	0.79	RT
826-3 Compact	As-Rec HDDR		99%	722 ± 4	5.6-5.7	310-330
1127-2 Green	Attrition Milled Aligned		∼62%	-	0.2	RT
1127-2 Compact	Attrition Milled Aligned		∼90%	700 ± 3	3.9-4.3	350-370
1113-1 Green	Attrition Milled		68%	-	0.79	RT
1113-1 Compact	Attrition Milled		88%	978 ± 9	8.1	550
1127-1 Green	Commercial		100%	-	0	RT
1127-1 Compact	Commercial		100%	700 ± 3	11	160
826-2 Green	NRL Melt Spun		78%	-	0.79	RT
826-2 Compact	NRL Melt Spun		96%	722 ± 4	6.2-6.6	300-320
Nd-Fe-B/α-Fe	Description		Rel. Dens.	Imp. Vel.	Pressure	Temp
1023-1 Green	Nd-Fe-B Ball Milled		64%	-	0.79	-83
1023-1 Compact	Nd-Fe-B Ball Milled		98%	820 ± 60	5.8-6.0	370-380
1023-2 Green	15% α-Fe Ball Milled		67%	-	0.79	-83
1023-2 Compact	15% α-Fe Ball Milled		99%	820 ± 60	6.2-6.3	400-410
1023-3 Green	25% α-Fe Ball Milled		69%	-	0.79	-83
1023-3 Compact	25% α-Fe Ball Milled		96%	820 ± 60	6.7-7.0	320-330
1113-2 Green	15% α-Fe Nanoparticle Mix		∼69%	-	0.79	RT
1113-2 Compact	15% α-Fe Nanoparticle Mix		∼90%	980 ± 3	8.0-8.2	530-550
1127-3 Green	15% α-Fe Nanoparticle Mix		∼62%	-	0.2	RT
1127-3 Compact	15% α-Fe Nanoparticle Mix		∼90%	700 ± 3	3.4-4.1	260-330

APPENDIX B

CALCULATION OF RELATIVE PHASE PERCENTAGES IN BALL MILLED SM-FE-N.

For the XRD traces shown in Figure 117(a), a combined gaussian-lorentzian curve was fit to the (220),(303),(006), and (205) peaks of $Sm_2Fe_{17}N_3$ and the α-Fe (110) peak. The relative amount of iron was calculated in three ways. First, the 100% intensity peaks for each phase (Sm-Fe-N(330) and α-Fe(110)) were divided by their respective relative intensity ratios (Sm-Fe-N = 2.5, α-Fe = 11.9). The ratio of the resulting values was assumed to be equivalent to the ratio of Sm-Fe-N to α-Fe. The powder diffraction file (PDF) #01-089-7985 lists the ratio of the of the (220) to the (303) peak for Sm-Fe-N as $\sim$0.7. Since the overlap between these peaks can increase the fitting error, an alternate method was used in which the intensity of the (220) and (303) peaks were added together and divided by 1.7 in order to give an equivalent intensity of the 100% peak. The third method fit a single curve to the (220) and (303) peaks and divided the intensity by 1.7 to find an equivalent 100% intensity value. In most cases, the first method (using only the Sm-Fe-N (303) peak) gave the lowest percentage of α-Fe and the third method (fitting the (220) and (303) peaks with a single curve) yielded the highest precentage of α-Fe. The error bars shown in Figure 117(a) represent the highest and lowest values found for all three methods. As milling time increases, the overlap between the (220) and (303) peaks increase. This results in a widening gap between the values found from the different methods.

REFERENCES

[1] Coey, J. *Rare-Earth Iron Permanent Magnets*, chapter Preface. Clarendon, Oxford (1996).

[2] Skomski, R. and Coey, J. M. D. *Phys. Rev. B* **48**, 15812 (1993).

[3] Drajem, M. and Ratnam, G. October (2010). http://tinyurl.com/275jxss.

[4] Coey, J. *Rare-Earth Iron Permanent Magnets*, chapter 1: Introduction. Clarendon, Oxford (1996).

[5] Fischer, R., Schrefl, T., Kronmüller, H., and Fidler, J. *Journal of Magnetism and Magnetic Materials* **153**, 35–49 (1996).

[6] Wecker, J., Schnitzke, K., Cerva, H., and Grogger, W. *Applied Physics Letters* **67**, 563–565 (1995).

[7] Lee, D., Hilton, J. S., Chen, C. H., Huang, M. Q., Zhang, Y., Hadjipanayis, G. C., and Liu, S. *IEEE Transactions on Magnetics* **40**, 2904–2906 (2004).

[8] Rodewald, B., Katter, W. M., and Uestuener, K. *IEEE Transactions on Magnetics* **38**, 2955–2957 (2002).

[9] Lee, D., Hilton, J. S., Liu, S., Zhang, Y., Hadjipanayis, G. C., and Chen, C. H. *IEEE Transactions on Magnetics* **39**, 2947–2949 (2003).

[10] Gabay, A. M., Zhang, Y., and Hadjipanayis, G. C. *Applied Physics Letters* **85**, 446–448 (2004).

[11] Gabay, A., Zhang, Y., and Hadjipanayis, G. *Journal of Magnetism and Magnetic Materials* **302**, 244–251 (2006).

[12] Mishra, R. K., Chu, T.-Y., and Rabenburg, L. *Journal of Magnetism and Magnetic Materials* **84**, 88–94 (1990).

[13] Grünberg, W., Hinz, D., Kirchner, A., Müller, K., and Schultz, L. *Journal of Alloys and Compounds* **257**, 293–301 (1997).

[14] Schwarz, R. B., Kasiraj, P., and Vreeland, J. *Metallurgical applications of shock-wave and high-strain-rate phenomena*, chapter 15: Temperature Kinetics During Shock-Wave Consolidation, 313–328. Marcel Dekker, New York (1986).

[15] Jin, Z. Q., Chen, K. H., Li, J., Zeng, H., Cheng, S. F., Liu, J. P., Wang, Z. L., and Thadhani, N. N. *Acta Materialia* **52**, 2147–2154 (2004).

[16] Jin, Z. Q., Thadhani, N. N., McGill, M., Li, J., Ding, Y., Wang, Z. L., Zeng, H., Chen, M., Cheng, S., and Liu, J. P. *Journal of Applied Physics* **96**, 3452–3457 (2004).

[17] Cullity, B. *Introduction to Magnetic Materials*. Addison-Wesley, Reading, Mass., (1972).

[18] Skomski, R. *Simple Models of Magnetism*, chapter 2: Models of exchange. Oxford, New York (2008).

[19] Skomski, R. and Coey, J. *Permanent Magnetism*. Institute of Physics Publishing, London, (1999).

[20] Stoner, E. and Wohlfarth, E. *Phil. Trans. Roy. Soc. (London)* **240A**, 599 (1948).

[21] Skomski, R. and Coey, J. *Permanent Magnetism*, chapter 3: Anisotropy and coercivity. Institute of Physics Publishing, London (1999).

[22] Herbst, J. F., Croat, J. J., Pinkerton, F. E., and Yelon, W. B. *Phys. Rev. B* **53**, 4176 (1984).

[23] Herbst, J. F. *Reviews of Modern Physics* **63**, 819–904 (1991).

[24] Sagawa, M., Hirosawa, S., Yamamoto, H., Fujimura, S., and Matsuura, Y. *Japanese J of App Phys.* **26**, 785–800 (1987).

[25] Skomski, R. *Rare-Earth Iron Permanent Magnets*, chapter 4: Interstitial modification. Clarendon, Oxford (1996).

[26] Katter, M., Wecker, J., Kuhrt, C., and Schultz, L. *Journal of Magnetism and Magnetic Materials* **117**, 419–427 (1992).

[27] O'Handley, R. In *Modern Magnetic Materials*. Wiley, New York (2000).

[28] Tremolet de Lacheisserie, E., Gignoux, D., and Schlenker, M. *Magnetism: Fundamentals*.

[29] Hall, R. *Journal of Applied Physics* **31**, 157S–158S (1960).

[30] Coey, J. and Smith, P. *Journal of Magnetism and Magnetic Materials* **200**, 405–424 (1999).

[31] Takahashi, M. and Shoji, H. *Journal of Magnetism and Magnetic Materials* **208**, 145–157 (2000).

[32] Huang, M., W.E., W., Simizu, S., Pedziwiatr, T., Obermyer, R., and Sankar, S. *Journal of Applied Physics* **75**, 6574–6576 (1994).

[33] Jack, K. *Acta Crystallographic* **5**, 404–411 (1952).

[34] Bao, X., Metzger, R., and Carbucicchio, M. *Journal of Applied Physics* **75**, 5870–5872 (1994).

[35] Jack, K. *Proceedings of the Royal Society of London. Series A, Mathematical and Physical Sciences* **208**, 216–224 (1951).

[36] Sugita, Y., Takahashi, H., Komuro, M., Mitsuoka, K., and Sakuma, A. *Journal of Applied Physics* **76**, 6637–6641 (1994).

[37] Takahashi, M., Takahashi, H., Nashi, H., Shoji, H., and Wakiyama, T. *Journal of Applied Physics* **79**, 5564–5569 (1994).

[38] Kneller, E. F. and Hawig, R. *IEEE Trans. Magn.* **27**, 3588 (1991).

[39] Skomski, R. and Zhou, J. In *Advanced Magnetic Nanostructures,* Sellmyer and Skomski, editors, chapter 3. Springer, New York (2006).

[40] Fischer, R., Schrefl, T., Kronmüller, H., and Fidler, J. *Journal of Magnetism and Magnetic Materials* **150**, 329–344 (1995).

[41] Leineweber, T. and Kronmüller, H. *Physica Status Solidi (b)* **201**, 291–301 (1997).

[42] Lee, D., Bauser, S., Higgins, A., Chen, C., and Liu, S. *Journal of Applied Physics* **99**, 08B516 (2006).

[43] Gabay, A. and Hadjipanayis, G. *Journal of Applied Physics* **101**, 09K507 (2006).

[44] Theilsch, J., Hinz, D., Schultz, L., and Gutfleisch, O. *Journal of Magnetism and Magnetic Materials* **322**, 3208–3213 (2010).

[45] Hirosawa, S. *Handboof of Advanced Magnetic Materials. Vol. III: Fabrication and Processing*, chapter Processing and Properties of Nanocomposite $Nd_2Fe_{14}B$-Based Permanent Magnets, 88–114. Springer, New York (2006).

[46] McCormick, P., Miao, W., Smith, P., Ding, J., and Street, R. *Journal of Applied Physics* **83**, 6256–6271 (1998).

[47] Chen, Z., Zhang, Y., Hadjipanayis, G., Chen, Q., and Ma, B. *Journal of Magnetism and Magnetic Materials* **206**, 8–16 (1999).

[48] Bowman, R. Master's thesis, Georgia Institute of Technology, August (1985).

[49] McLean, M. *Directionally Solidified Materials for High Temperature Service*, 51. Metals Society, London (1983).

[50] Campbell, P. In *Permanent Magnet Materials and Their Applications*. Cambridge U.P., Cambridge (1994).

[51] Chen, Z., Zhang, Y., Ding, Y., Hadjipanayis, G., Chen, Q., and Ma, B. *Journal of Magnetism and Magnetic Materials* **195**, 420–427 (1999).

[52] Jin, Z., Okumura, H., Wang, H. L., and Hadjipanayis, G. C. *Journal of Applied Physics* **91**, 8165 (2002).

[53] Gilman, P. S. and Benjamin, J. S. *Annual Review of Materials Science* **13**, 279 (1983).

[54] Rong, C., Nandwana, V., Poudyal, N., Liu, J. P., Kozlov, M. E., Baughman, R. H., Ding, Y., and Wang, Z. L. *J. Appl. Phys.* **102**, 023908 (2007).

[55] Rong, C., Zhang, Y., Poudyal, N., Xiong, X., Kramer, M. J., and Liu, J. P. *Applied Physics Letters* **96**, 102513 (2010).

[56] Yue, M., Wang, Y. P., Poudyal, N., Rong, C. B., and Liu, J. P. *Journal of Applied Physics* **105**, 07A708 (2009).

[57] Akdogan, N. G., Li, W., and Hadjipanayis, G. C. *Journal of Applied Physics* **109**, 07A759 (2011).

[58] Mishra, R. K. *Journal of Applied Physics* **62**, 967–971 (1987).

[59] Kuhrt, C., Schultz, L., Schnitzke, K., Hock, S., and Behrensmeier. *Applied Physics Letters* **59**, 1418–1420 (1991).

[60] Li, L. and Grahm Jr., C. *IEEE Transactions on Magnetics* **28**, 2130–2132 (1992).

[61] Bunge, H. J. In *Quantitative Texture Analysis,* Bunge, H. J. and Esling, C., editors. Deutsche Gesellschaft fur Metallkunde, Germany (1982).

[62] Randle, V. and Engler, O. *Texture Analysis: Macrotexture, Microtexture, and Orientation Mapping.* Gordon and Breach, Australia, (2000).

[63] Eichele, K., October (2007). http://tinyurl.com/4t4e8en.

[64] Fidler, J., Schrefl, T., Hoefinger, S., and Hajduga, M. *J. Phys.: Condens. Matter* **16**, S455–S470 (2004).

[65] Sagawa, M. and Nagata, H. *IEEE Transactions on Magnetics* **29**, 2747 (1993).

[66] Kaneko, Y. *IEEE Transactions on Magnetics* **36**, 3275–3278 (2000).

[67] Wang, Q., Zhao, Z., Liu, W., Sun, X. K., Chuang, Y., and De Boer, F. R. *Journal of Magnetism and Magnetic Materials* **109**, 59–63 (1992).

[68] Yang, J., Mao, O., Girt, E., Altounian, Z., and Strom-Olsen, J. O. *Appl. Phys. Lett.* **70**, 1176–1178 (1997).

[69] Rodewald, W., Katter, M., Wall, B., Blank, R., Reppel, G. W., and Zilg, H. D. *IEEE Transactions on Magnetics* **36**, 3279–3281 (2000).

[70] Fernengel, W., Lehnert, A., Katter, M., Rodewald, W., and Wall, B. *Journal of Magnetism and Magnetic Materials* **157/158**, 19–20 (1996).

[71] Li, L. and Grahm Jr., C. *Journal of Applied Physics* **67**, 4756–4758 (1990).

[72] Yang, L. and Zhang, N. In *10th Internation Workshop on Rare Earth Magnets and their Applications*, number 19, 1–2 (, Kyoto, Japan, 1989).

[73] Sprengel, W., Herth, S., Barve, V., Schaefer, H., Wejrzanowski, T., Gutfliesch, O., and Wüsrschum, R. *Journal of Applied Physics* **98**, 074314 (2005).

[74] Leonowicz, M. and Davies, H. *Materials Letters* **19**, 275–279 (1994).

[75] Liu, Y., Xu, L., Wang, Q., Li, W., and Zhang, X. *Applied Physics Letters* **94**, 172502 (2009).

[76] Liu, Y., Xu, L., Guo, D., Li, W., Wang, Q., and Zhang, X. *Journal of Applied Physics* **106**, 113918 (2009).

[77] Meyers, M. *Dynamic Behavior of Materials.* John Wiley and Sons, Inc., New York, (1994).

[78] Rice, M. H., McQueen, R. G., and Walsh, J. M. In *Solid State Physics, volume VI,* Seitz, F. and Turnbull, D., editors, 1–63. Academic Press, New York (1958).

[79] Herrmann, W. *Journal of Applied Physics* **40**, 2490–2499 (1969).

[80] Borg, J., Chapman, D., Tsembelis, K., and Proud, W. *Journal of Applied Physics* **98**, 073509 (2005).

[81] Fischmeister, H. F. and Artz, E. *Powder Metallurgy* **26**, 82–88 (1983).

[82] Helle, A., Easterling, K., and Asby, M. *Acta Metall.* **33**, 2163–2174 (1985).

[83] Meyers, M. A. *Scripta Met.* **12**, 21 (1978).

[84] Murr, L. E. *Shock Waves in Condensed Matter.* Elsevier, Amsterdam (1988).

[85] Kressel, H. and Brown, N. *J. Applied Physics* **38**, 138 (1967).

[86] Meyers, M. A. and Murr, L. E. *Shock Wave and High-Strain-Rate Phenomena in Metals.* Plenum, New York (1981).

[87] Wang, Y. and Mikkola, D. E. *Shock Wave and High-Strain Phenomena in Materials.* Dekker, New York (1992).

[88] Yest, C. S. and Harris, L. A. *Shock Waves and High-Strain Phenomena in Metals.* Plenum, New York (1981).

[89] Graham, R. A., Morosin, B., Horie, Y., Venturini, E. L., Boslough, M., Carr, M. J., and Williamson, D. L. In *Shock Waves in Condensed Matter,* Gupta, Y. M., editor, 693 (Plenum, New York, 1986).

[90] Thadhani, N. *Advanced Materials and Manufacturing Processes* **3**, 493 (1988).

[91] Gourdin, W. *Journal of Applied Physics* **55**, 172 (1983).

[92] Meyers, M., Benson, D., and Olevsky, E. *Acta Materiala* **47**, 2089–2108 (1999).

[93] Akashi, T. and Sawaoka, A. B. *J. Material Science* **22**, 3276 (1987).

[94] DeCarli, S. and Jamieson, J. C. *Science* **133**, 1821 (1961).

[95] Al'tshuler, L. V. *J. Appl. Mech. Phys.* **4**, 93 (1978).

[96] Jamieson, J. C. and Lawson, A. W. *Journal of Applied Physics* **33** (1962).

[97] Duvall, G. E. and Graham, R. A. *Rev. Mod. Phys.* **49**, 523 (1977).

[98] Thadhani, N. N. and Meyers, M. A. *Acta Met.* **34**, 1625 (1986).

[99] Thadhani, N. N. *J. Applied Physics* **76**, 2129 (1994).

[100] Lange, M. A. and Ahrens, T. J. *Earth and Planetary Science Letters* **77**, 409 (1986).

[101] Thadhani, N. N. *Progress in Material Science* **37**, 117 (1993).

[102] Dremin, A. N. and Breusov, O. N. *Russ. Chem. Rev.* **37**, 392 (1968).

[103] Batsanov, S. S. and Bokarev, V. P. *Inorganic Materials* **16**, 1131 (1980).

[104] Batsanov, S. S. *Propellants, Explosives, and Pyrotechnics* **12**, 206–208 (1987).

[105] Batsanov, S. S. *Russian Chemical Reviews* **75**, 601–616 (2006).

[106] Petrie, M. W. and Page, N. W. *Acta Metall. Mater.* **40**, 3195 (1992).

[107] Chandramouli, M., Thomas, G., and Nellis, W. J. *J. Appl. Phys.* **73**, 6494–6496 (1993).

[108] Guruswamy, S., McCarter, M., Shield, J., and Panchanathan, V. *Journal of Applied Physics* **79**, 4851–4854 (1996).

[109] Ando, S., Mine, Y., Takashim, K., Itoh, S., and Tonda, H. *Journal of Materials Processing Technology* **85**, 142–147 (1999).

[110] Liu, W., Cao, L., Wu, J., and Li, T. .

[111] Lin, J., Nien, M., and Chang, L. In *Proceedings of IPACK*, 1849–1855, (2005).

[112] Kawano, K., Kim, Y., Hamashima, H., and Itoh, S. In *Proceedings of Pressure Vessels and Piping Division - ASME*, 195–200, (2006).

[113] Leonowicz, M., Kaszuawara, W., Jezierska, E., Januszewski, D., Mendoza, G., Davies, H., and Paszula, J. *Journal of Applied Physics* **83**, 6634–6636 (1998).

[114] Kaszuwara, W., Leonowicz, M., Januszewski, D., Mendoza, G., Davies, H., and Paszula, J. *Journal of Material Science - Materials in electronics* **9**, 17–23 (1998).

[115] Saito, T. *IEEE Transactions on Magnetics* , 2561–2563 (2001).

[116] Li, J., Jin, Z. Q., Liu, J. P., Wang, Z. L., and Thadhani, N. N. *Applied Physics Letters* **85**, 2223–2225 (2004).

[117] Jin, Z. Q., Thadhani, N. N., McGill, M., Ding, Y., Wang, Z. L., Chen, M., Zeng, H., Chakka, V. M., and Liu, J. P. .

[118] Jin, Z. Q., Rockett, C., Liu, J. P., Hokamoto, K., and Thadhani, N. N. *Materials Science Forum* (2004).

[119] Chau, R., M. M. B. and Nellis, W. J. *Journal of Applied Physics* **79**, 9236–9244 (1996).

[120] Hu, B. P., Rao, X. L., Xu, J. M., Liu, G. C., and Wang, Y. Z. *Journal of Applied Physics* **74**, 489–494 (1993).

[121] Oda, H., Kondo, K., Uchida, H., Matsumura, Y., Tachibana, S., and Kawanabe, T. *Japanese Journal of Applied Physics* **34**, L35 (1995).

[122] Mashimo, T., Tashior, S., Hirosawa, S., and Mkita, K. *J. Appl. Phys.* **80**, 356–361 (1996).

[123] Mashimo, T., Huang, X., Hirosawa, S., Makita, K., Mitsudo, S., and Motokawa, M. *Journal of Materials Processing Technology* **85**, 138–141 (1999).

[124] Mashimo, T., Huang, X., Hirosawa, S., Makita, K., Kato, Y., Mitsudo, S., and Motokawa, M. *Journal of Magnetism and Magnetic Materials* **210**, 109–120 (2000).

[125] Chiba, A., Ooyabu, K., Morizono, Y., Maeda, T., Sugimoto, S., T, K., Kakimoto, E., Kawahara, K., and Watanabe, T. *Material Science Forum* **449**, 1037–1040 (2004).

[126] Chiba, A., Hokamoto, K., Sugimoto, S., Kozuka, T., Mori, A., and Kakimoto, E. *Journal of Magnetism and Magnetic Materials* **310**, e881–e883 (2006).

[127] Imaoka, N., Koyama, Y., Nakao, T., Nakaoka, S., Yamaguchi, T., Kakimoto, E., Tada, M., Nakagawa, T., and Abe, M. *Journal of Applied Physics* **103**, 07E129 (2008).

[128] Mashimo, T. *High-Pressure Shock Compression of Solids III*, chapter Effect of shock compression on ceramic materials, 101–146. Springer-Verlag, New York (1998).

[129] Cullity, B. *Elements of X-ray Diffraction.* Addison-Wesley, Reading, Mass., 2nd edition, (1976).

[130] Scardi, P., Leoni, M., and Delhez, R. *Journal of Applied Crystallography* **37**, 381–390 (2004).

[131] Carter, W. J., Fritz, J. N., Marsh, S. P., and McQueen, R. G. *J. Phys. Chem. Solids* **36**, 741–752 (1975).

[132] Al'tshuler, L. V., Bakanova, A. A., and Dudoladov, I. P. *Sov. Phys. - JETP* **26**, 1115–1120 (1968).

[133] Marsh, S. P., editor. *LASL Shock Hugoniot Data.* University of California Press, Berkeley and Los Angeles, CA (1980).

[134] Barker, L. M. *Journal of Applied Physics* **46**, 2544–2547 (1975).

[135] Walsh, J. M., Rice, M. H., McQueen, R. G., and Yarger, F. L. *Physical Review* **108**, 196–216 (1957).

[136] Li, Q.-Y., Shi, S.-C., Yang, J.-W., and Sun, Y. *Chinese Journal of High Pressure Physics* **21**, 210–214 (2007).

[137] Lach, E., Nahme, H., and Rohr, I. *Journal de Physique, IV* **110**, 857–862 (2003).

[138] Wu, Q. and Jing, F. *Journal of Applied Physics* **80**, 4343–4349 (1996).

[139] Dai, C. and Thadhani, N. *Acta Materiala* **59**, 785–796 (2011).

[140] Kreyszig, E., editor. *Advanced Engineering Mathematics*, chapter 12: Partial Differential Equations, 564–565. Wiley, New Jersey, 9th edition (2006).

[141] Suzuki, K., Morita, H., Kaneko, T., Yoshida, H., and Fujimori, H. *Journal of Alloys and Compounds* **201**, 11–16 (1993).

[142] Taylor, J. *An Introduction to Error Analysis- The Study of Uncertainties in Physical Measurements*. University Science Books, Sausalito, CA, (1997).

[143] Hammetter, W. F., Graham, R. A., Morosin, B., and Horie, Y. In *Shock Waves in Condensced Matter,* Schmidt, S. C. and Holmes, N. C., editors, 431 (Elsevier, Amsterdam, 1988).

[144] Sumiyama, K., Onodera, H., Suzuki, K., Ono, S., Kim, K. J., Gemma, K., and Nishi, Y. *Journal of Alloys and Compounds* **282**, 158–163 (1999).

[145] Jack, K. H. *Acta Crystallographica* **5**, 404–411 (1952).

[146] Yao, B., Liu, L., Liu, S., Hu, X., and Su, W. *Journal of Materials Research* **16**, 2583–2590 (2001).

[147] Kim, K., Sumiyama, K., Onodera, H., and Suzuki, K. *Journal of Alloys and Compounds* **203**(1-2), 169–176 JAN 4 (1994).

[148] Fall, I. and Genin, J. *Metallurgical and Material Transactions A* **27A**, 2160–2177 (1996).

[149] Wasz, M. and McLellan, R. *Scripta Metallurgica et Materialia* **28**, 1461–1463 (1993).

[150] Somers, M. and Mittemeijer, E. *Metallurgical and Materials Transactions A* **26A**, 57–74 (1995).

[151] Miao, W. F., Ding, J., McCormick, P. G., and Street, R. *J. Phys. D: Appl. Phys* **29**, 2370–2375 (1996).

[152] Chin, T. S., Hugn, M. P., Tsai, D. S., Wu, K. F., and Chang, W. C. *Journal of Applied Phsyics* **64**, 5531 (1988).